

Jet energy measurement with the ATLAS detector in proton-proton collisions at $\sqrt{s} = 7$ TeV

The ATLAS Collaboration

December 30, 2011

Abstract. The jet energy scale (JES) and its systematic uncertainty are determined for jets measured with the ATLAS detector at the LHC in proton-proton collision data at a centre-of-mass energy of $\sqrt{s} = 7$ TeV corresponding to an integrated luminosity of 38 pb^{-1} . Jets are reconstructed with the anti- k_t algorithm with distance parameters $R = 0.4$ or $R = 0.6$. Jet energy and angle corrections are determined from Monte Carlo simulations to calibrate jets with transverse momenta $p_T \geq 20$ GeV and pseudorapidities $|\eta| < 4.5$. The JES systematic uncertainty is estimated using the single isolated hadron response measured *in situ* and in test-beams, exploiting the transverse momentum balance between central and forward jets in events with dijet topologies and studying systematic variations in Monte Carlo simulations. The JES uncertainty is less than 2.5% in the central calorimeter region ($|\eta| < 0.8$) for jets with $60 \leq p_T < 800$ GeV, and is maximally 14% for $p_T < 30$ GeV in the most forward region $3.2 \leq |\eta| < 4.5$. The uncertainty for additional energy from multiple proton-proton collisions in the same bunch crossing is less than 1.5% per additional collision for jets with $p_T > 50$ GeV after a dedicated correction for this effect. The JES is validated for jet transverse momenta up to 1 TeV to the level of a few percent using several *in situ* techniques by comparing a well-known reference such as the recoiling photon p_T , the sum of the transverse momenta of tracks associated to the jet, or a system of low- p_T jets recoiling against a high- p_T jet. More sophisticated jet calibration schemes are presented based on calorimeter cell energy density weighting or hadronic properties of jets, providing an improved jet energy resolution and a reduced flavour dependence of the jet response. The JES systematic uncertainty determined from a combination of *in situ* techniques are consistent with the one derived from single hadron response measurements over a wide kinematic range. The nominal corrections and uncertainties are derived for isolated jets in an inclusive sample of high- p_T jets. Special cases such as event topologies with close-by jets, or selections of samples with an enhanced content of jets originating from light quarks, heavy quarks or gluons are also discussed and the corresponding uncertainties are determined.

Contents

1	Introduction	3	14	Jet energy scale uncertainties for jet calibrations based on cell weighting	61
2	The ATLAS detector	4	14.1	Energy density as input to the global cell weighting calibration	61
3	Introduction to jet energy calibration methods	5	14.2	Cluster properties inside jets as input to the local cluster weighting calibration	61
4	Monte Carlo simulation	6	14.3	Jet energy scale uncertainty from <i>in situ</i> techniques for jets based on cell weighting	66
4.1	Event generators	6	15	Summary of jet energy scale uncertainties of various calibration schemes	74
4.2	Simulation of the ATLAS detector	7	16	Jet reconstruction efficiency	76
4.3	Nominal Monte Carlo simulation samples	7	16.1	Efficiency in the Monte Carlo simulation	76
4.4	Simulated pile-up samples	7	16.2	Efficiency <i>in situ</i> validation	76
5	Data sample and event selection	7	16.3	Summary of jet reconstruction efficiency	77
5.1	Data taking period and LHC conditions	7	17	Response uncertainty of non-isolated jets	77
5.2	Event selection	8	17.1	Evaluation of close-by jet effects	78
5.3	Data quality assessment	8	17.2	Non-isolated jet response	78
6	Jet reconstruction	8	17.3	Non-isolated jet energy scale uncertainty	79
6.1	Reconstructed calorimeter jets	8	17.4	Summary of close-by jet uncertainty	81
6.2	Reconstructed track jets	9	18	Light quark and gluon jet response and sample characterisation	81
6.3	Monte Carlo truth jets and flavour association	9	18.1	Data samples for flavour dependence studies	81
7	Jet quality selection	10	18.2	Flavour dependence of the calorimeter response	81
7.1	Criteria to remove non-collision background	10	18.3	Systematic uncertainties due to flavour dependence	81
7.2	Evaluation of the jet quality selection efficiency	10	18.4	Average jet flavour determination	85
7.3	Summary of the jet quality selection	12	18.5	Systematic uncertainties of average flavour composition	86
8	Jet energy calibration in the EM+JES scheme	12	18.6	Flavour composition in a photon-jet sample	88
8.1	Pile-up correction	12	18.7	Flavour composition in a multijet sample	88
8.2	Jet origin correction	14	18.8	Summary of jet response flavour dependence	88
8.3	Jet energy correction	14	19	Global sequential calibrated jet response for a quark sample	88
8.4	Jet pseudorapidity correction	17	20	JES uncertainties for jets with identified heavy quark components	89
9	Jet energy scale uncertainties for the EM+JES scheme	17	20.1	Selection of identified heavy quark jets	89
9.1	Jet response definition for the JES uncertainty evaluation	17	20.2	Calorimeter response uncertainty	89
9.2	Uncertainty in the JES calibration	18	20.3	Uncertainties due to Monte Carlo modelling	89
9.3	Uncertainty on the calorimeter response	18	20.4	Final bottom quark JES uncertainty	91
9.4	Uncertainties due to the detector simulation	20	20.5	Validation of the heavy quark energy scale using tracks	91
9.5	Uncertainties due to the event modelling in Monte Carlo generators	21	21	Study of jet punch-through	94
9.6	<i>In situ</i> intercalibration using events with dijet topologies	21	21.1	Event selection for punch-through analysis	94
9.7	Uncertainties due to multiple proton-proton collisions	24	21.2	Energy depositions in the hadronic calorimeter	94
9.8	Summary of jet energy scale systematic uncertainties	29	21.3	Dijet balance as an indication of punch-through	95
9.9	Discussion of special cases	29	21.4	Summary of the jet punch-through study	96
10	Jet energy scale uncertainties validation with <i>in situ</i> techniques for the EM+JES scheme	31	22	Summary	96
10.1	Comparison of transverse momentum balance of jets from calorimeter and tracking	31			
10.2	Photon-jet transverse momentum balance	37			
10.3	Multijet transverse momentum balance	43			
10.4	Summary of JES validation using <i>in situ</i> techniques	48			
10.5	JES uncertainty from combination of <i>in situ</i> techniques	48			
11	Jet energy calibration based on global jet properties	51			
11.1	Global sequential technique	51			
11.2	Properties derived from the internal jet structure	51			
11.3	Derivation of the global sequential correction	51			
12	Jet energy scale uncertainties for jet calibrations based on global jet properties	52			
12.1	Validation of the global sequential calibration using dijet events	52			
12.2	Sensitivity of the global sequential calibration to pile-up	58			
12.3	Summary on the JES uncertainty for the global sequential calibration	58			
13	Jet calibration schemes based on cell energy weighting	58			
13.1	Global cell energy density weighting calibration	58			
13.2	Local cluster weighting calibration	59			
13.3	Jet energy calibration for jets with calibrated constituents	61			

1 Introduction

Collimated sprays of energetic hadrons, called jets, are the dominant feature of high energy proton-proton interactions at the Large Hadron Collider (LHC) at CERN. In Quantum Chromodynamics (QCD) jets are produced via the fragmentation of quarks and gluons. They are key ingredients for many physics measurements and for searches for new phenomena.

During the year 2010 the ATLAS detector collected proton-proton collision data at a centre-of-mass energy of $\sqrt{s} = 7$ TeV corresponding to an integrated luminosity of 38 pb^{-1} . The uncertainty in the jet energy measurement is the dominant experimental uncertainty for numerous physics results, for example the cross-section measurement of inclusive jets, dijets or multi-jets [1–4], as well as of vector bosons accompanied by jets [5], and new physics searches with jets in the final state [6].

Jets are observed as groups of topologically related energy deposits in the ATLAS calorimeters. They are reconstructed with the anti- k_t algorithm [7].

Using a Monte Carlo (MC) simulation the observed jets are calibrated such that, on average, the jet energy corresponds to that of the associated stable particles in the ATLAS detector. The calibration of the jet energy scale (JES) should ensure the correct measurement of the average energy across the whole detector and needs to be independent of additional events produced in proton-proton collisions at high luminosity compounding on the event of interest.

In this document, the jet calibration strategies adopted by the ATLAS experiment are outlined and studies to evaluate the uncertainties in the jet energy measurement are presented. A first estimate of the JES uncertainty, described in Ref. [1], was based on information available before the first LHC collisions. It also exploited transverse momentum balance in events with only two jets at high transverse momenta (p_T). A reduced uncertainty with respect to Ref. [1] is presented that is based on the increased knowledge of the detector performance obtained during the analysis of the first year of ATLAS data taking.

ATLAS has developed several jet calibration schemes [8] with different levels of complexity and different sensitivity to systematic effects, which are complementary in their contribution to the jet energy measurement. Each calibration scheme starts from the measured calorimeter energy at the electromagnetic (EM) energy scale, which correctly measures the energy deposited by electromagnetic showers. In the simplest scheme (EM+JES) the jet calibration is derived as a simple correction relating the calorimeter's response to the true jet energy. More sophisticated schemes exploit the topology of the calorimeter energy depositions to correct for calorimeter non-compensation (nuclear energy losses, etc.) and other jet reconstruction effects.

For the simple EM+JES calibration scheme based only on the JES correction, the JES uncertainty can be determined from the single hadron response measurements in small data sets collected *in situ* or in test-beams. With a large data set available the JES uncertainty can also be determined using the ratio of the jet transverse momentum to the momentum of a reference object and by a comparison of the data to the Monte Carlo simulation.

Several techniques have been developed to directly determine the uncertainty on the jet energy measurement *in situ*. The

JES uncertainty can be obtained by comparing the jet energy to a well calibrated reference object. A standard technique to probe the absolute jet energy scale, used also in earlier hadron collider experiments, is to measure the p_T balance between the jet and a well-measured object: a photon or a Z boson. However, the currently limited data statistics imposes a limit on the p_T range that can be tested with this technique. The JES uncertainty on higher jet transverse momenta up to the TeV-scale can be assessed using the multijet balance technique where a recoil system of well-calibrated jets at lower p_T is balanced against a single jet at higher p_T . A complementary technique uses the total momentum of the tracks associated to the jets as reference objects. While the resolution of the jet energy measurement using tracks in jets is rather poor, the mean jet energy can be determined to the precision of a few percent.

The standard jet calibration and the corresponding uncertainty on the energy measurement are determined for isolated jets in an inclusive jet data sample. Additional uncertainties are evaluated for differences in the response of jets induced by quarks or gluons and for special topologies with close-by jets.

The outline of the paper is as follows.

First the ATLAS detector (Section 2) is described. An overview of the jet calibration procedures and the various calibration schemes is given in Section 3. The Monte Carlo simulation framework is introduced in Section 4. The data samples, data quality assessment and event selection are described in Section 5. Then, the reconstruction (Section 6), and the selection (Section 7) of jets are discussed. The jet calibration method is outlined in Section 8 which includes a prescription to correct for the extra energy due to multiple proton-proton interactions (pile-up).

Section 9 describes the sources of systematic uncertainties for the jet energy measurement and their estimation using Monte Carlo simulations and collision data. Section 10 describes several *in situ* techniques used to validate these systematic uncertainties. Section 11 presents a technique to improve the resolution of the energy measurements and to reduce the flavour response differences by exploiting the topology of the jets. The systematic uncertainties associated with this technique are described in Section 12. The jet calibration schemes based on calorimeter cell energy weighting in jets are introduced in Section 13, and the associated JES uncertainties are estimated from the *in situ* techniques as described in Section 14. Section 15 summarises the systematic uncertainties for all studied jet calibration schemes.

The jet reconstruction efficiency and its uncertainty is discussed in Section 16. The response uncertainty of non-isolated jets is investigated in Section 17, while Section 18 and Section 19 discuss response difference for jets originating from light quarks or gluons and presents a method to determine, on average, the jet flavour content in a given data sample. In Section 20 JES uncertainties for jets where a heavy quark is identified are investigated. Finally, possible effects from lack of full calorimeter containment of jets with high transverse momentum are studied in Section 21. The overall conclusion is given in Section 22.

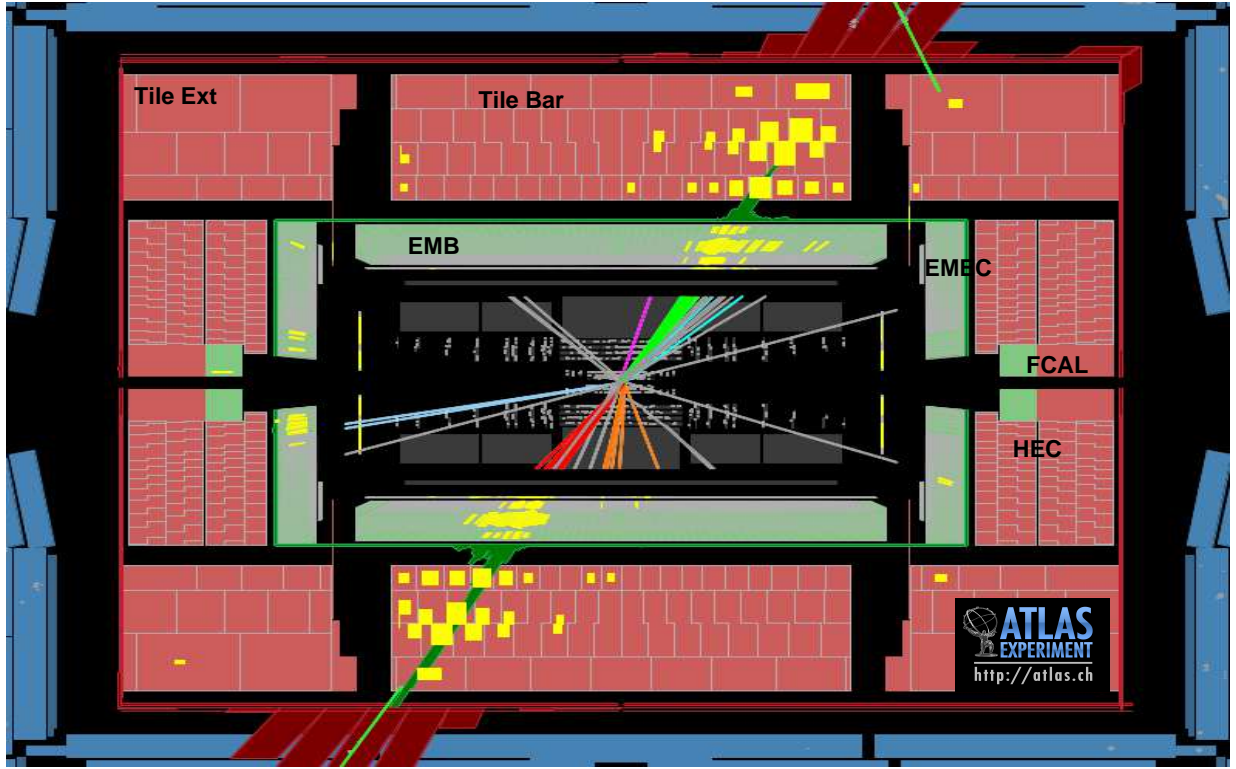


Fig. 1: Display of the central part of the ATLAS detector in the x - z view showing the highest mass central dijet event collected during the 2010 data taking period. The two leading jets have $p_T^{\text{jet}} = 1.3$ TeV with $y = -0.68$ and $p_T^{\text{jet}} = 1.2$ TeV with $y = 0.64$, respectively. The two leading jets have an invariant mass of approximately 3.1 TeV. The missing transverse energy in the event is 46 GeV. The lines in the inner detector indicate the reconstructed particle trajectories. The energy deposition in the calorimeter cells are displayed as light rectangles. The size of the rectangles is proportional to the energy deposits. The histograms attached to the LAr and the Tile calorimeter illustrate the amount of deposited energy.

2 The ATLAS detector

The ATLAS detector is a multi-purpose detector designed to observe particles produced in proton-proton and heavy ion collisions. A detailed description can be found in Ref. [9]. The detector consists of an inner detector, sampling electromagnetic and hadronic calorimeters and muon chambers. Figure 1 shows a sketch of the detector outline together with an event with two jets at high transverse momenta.

The inner detector (ID) is a tracking system immersed in a magnetic field of 2 T provided by a solenoid and covers a pseudorapidity¹ $|\eta| \lesssim 2.5$. The ID barrel region $|\eta| \lesssim 2$ consists of three layers of pixel detectors (Pixel) close to the beam-pipe, four layers of double-sided silicon micro-strip detectors (SCT)

¹ The ATLAS coordinate system is a right-handed system with the x -axis pointing to the centre of the LHC ring and the y -axis pointing upwards. The polar angle θ is measured with respect to the LHC beam-line. The azimuthal angle ϕ is measured with respect to the x -axis. The pseudorapidity η is an approximation for rapidity y in the high energy limit, and it is related to the polar angle θ as $\eta = -\ln \tan \frac{\theta}{2}$. The rapidity is defined as $y = 0.5 \times \ln[(E + p_z)/(E - p_z)]$, where E denotes the energy and p_z is the component of the momentum along the beam direction. Transverse momentum and energy are defined as $p_T = p \times \sin \theta$ and $E_T = E \times \sin \theta$, respectively.

providing eight hits per track at intermediate radii, and a transition radiation tracker (TRT) composed of straw tubes in the outer part providing 35 hits per track. At $|\eta| > 1$ the ID end-cap regions each provide three Pixel discs and nine SCT discs perpendicular to the beam direction.

The liquid argon (LAr) calorimeter is composed of sampling detectors with full azimuthal symmetry, housed in one barrel and two endcap cryostats. A highly granular electromagnetic (EM) calorimeter with accordion-shaped electrodes and lead absorbers in liquid argon covers the pseudorapidity range $|\eta| < 3.2$. It contains a barrel part (EMB, $|\eta| < 1.475$) and an endcap part (EMEC, $1.375 \leq |\eta| < 3.2$) each with three layers in depth (from innermost to outermost EMB1, EMB2, EMB3 and EMEC1, EMEC2, EMEC3). The middle layer has a 0.025×0.025 granularity in $\eta \times \phi$ space. The innermost layer (strips) consists of cells with eight times finer granularity in the η -direction and with 3-times coarser granularity in the ϕ direction.

For $|\eta| < 1.8$, a presampler (Presampler), consisting of an active LAr layer is installed directly in front of the EM calorimeters, and provides a measurement of the energy lost before the calorimeter.

A copper-liquid argon hadronic endcap calorimeter (HEC, $1.5 \leq |\eta| < 3.2$) is located behind the EMEC. A copper/tungsten-liquid argon forward calorimeter (FCAL) covers the region clos-

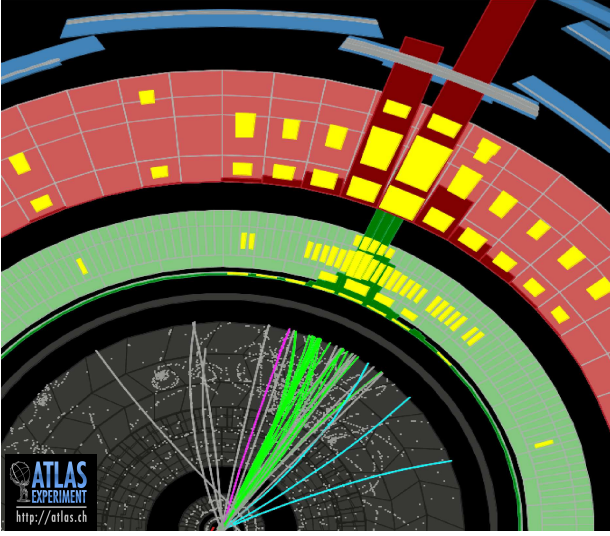


Fig. 2: Zoom of the x - y view of the ATLAS detector showing one of the high- p_T jets of the event shown in Figure 1. The energy depositions in the calorimeter cells are displayed as light rectangles. The size of the rectangles is proportional to the energy deposits. The dark histograms attached to the LAr (Tile) calorimeter illustrates the amount of deposited energy. The lines in the ID display the reconstructed tracks originating from the interaction vertex.

est to the beam at $3.1 \leq |\eta| < 4.9$. The HEC has four layers and the FCAL has three layers. From innermost to outermost these are: HEC0, HEC1, HEC2, HEC3 and FCal0, FCal1, FCal2. Altogether, the LAr calorimeters correspond to a total of 182,468 readout cells, i.e. 97.2% of the full ATLAS calorimeter readout.

The hadronic Tile calorimeter ($|\eta| < 1.7$) surrounding the LAr cryostats completes the ATLAS calorimetry. It consists of plastic scintillator tiles and steel absorbers covering $|\eta| < 0.8$ for the barrel and $0.8 \leq |\eta| < 1.7$ for the extended barrel. Radially, the hadronic Tile calorimeter is segmented into three layers, approximately 1.4, 3.9 and 1.8 interaction lengths thick at $\eta = 0$; the $\Delta\eta \times \Delta\phi$ segmentation is 0.1×0.1 (0.2×0.1 in the last radial layer). The last layer is used to catch the tails of the longitudinal shower development. The three radial layers of the Tile calorimeter will be referred to (from innermost to outermost) as Tile0, Tile1, Tile2².

Between the barrel and the extended barrels there is a gap of about 60 cm, which is needed for the ID and the LAr services. Gap scintillators (Gap) covering the region $1.0 \leq |\eta| < 1.2$ are installed on the inner radial surface of the extended barrel modules in the region between the Tile barrel and the extended barrel. Crack scintillators (Scint) are located on the front of the LAr endcap and cover the region $1.2 \leq |\eta| < 1.6$.

The muon spectrometer surrounds the ATLAS calorimeter. A system of three large air-core toroids, a barrel and two endcaps, generates a magnetic field in the pseudorapidity range of

$|\eta| < 2.7$. The muon spectrometer measures muon tracks with three layers of precision tracking chambers and is instrumented with separate trigger chambers.

The trigger system for the ATLAS detector consists of a hardware-based Level 1 (L1) and a software-based higher level trigger (HLT) [10]. Jets are first identified at L1 using a sliding window algorithm from coarse granularity calorimeter towers. This is refined using jets reconstructed from calorimeter cells in the HLT. The lowest threshold inclusive jet trigger is fully efficient for jets with $p_T \gtrsim 60$ GeV. Events with lower p_T jets are triggered by the minimum bias trigger scintillators (MBTS) mounted at each end of the detector in front of the LAr endcap calorimeter cryostats at $|z| = \pm 3.56$ m.

3 Introduction to jet energy calibration methods

Hadronic jets used for ATLAS physics analyses are reconstructed by a jet algorithm starting from the energy depositions of electromagnetic and hadronic showers in the calorimeters. An example of a jet recorded by the ATLAS detector and displayed in the plane transverse to the beam line is shown in Figure 2.

The jet Lorentz four-momentum is reconstructed from the corrected energy and angles with respect to the primary event vertex. For systematic studies and calibration purposes *track jets* are built from charged particles using their momenta measured in the inner detector. Reference jets in Monte Carlo simulations (*truth jets*) are formed from simulated stable particles using the same jet algorithm.

The jet energy calibration relates the jet energy measured with the ATLAS calorimeter to the true energy of the corresponding jet of stable particles entering the ATLAS detector.

The jet calibration corrects for the following detector effects that affect the jet energy measurement:

1. **Calorimeter non-compensation:** partial measurement of the energy deposited by hadrons.
2. **Dead material:** energy losses in inactive regions of the detector.
3. **Leakage:** energy of particles reaching outside the calorimeters.
4. **Out of calorimeter jet cone:** energy deposits of particles inside the truth jet entering the detector that are not included in the reconstructed jet.
5. **Noise thresholds and particle reconstruction efficiency:** signal losses in the calorimeter clustering and jet reconstruction.

Jets reconstructed in the calorimeter system are formed from calorimeter energy depositions reconstructed at the *electromagnetic energy scale* (EM) or from energy depositions that are corrected for the lower detector response to hadrons. The EM scale correctly reconstructs the energy deposited by particles in an electromagnetic shower in the calorimeter. This energy scale is established using test-beam measurements for electrons in the barrel [11–14] and the endcap calorimeters [15, 16]. The absolute calorimeter response to energy deposited via electromagnetic processes was validated in the hadronic calorimeters using muons, both from test-beams [14, 17] and pro-

² In the barrel, the Tile layers will be called TileBar0, TileBar1, TileBar2 and in the extended barrel TileExt0, TileExt1 and TileExt2.

duced *in situ* by cosmic rays [18]. The energy scale of the electromagnetic calorimeters is corrected using the invariant mass of Z bosons produced in proton-proton collisions ($Z \rightarrow e^+e^-$ events) [19]. The correction for the lower response to hadrons is solely based on the topology of the energy depositions observed in the calorimeter.

In the simplest case the measured jet energy is corrected, on average, using Monte Carlo simulations, as follows:

$$E_{\text{calib}}^{\text{jet}} = E_{\text{meas}}^{\text{jet}} / \mathcal{F}_{\text{calib}}(E_{\text{meas}}^{\text{jet}}), \text{ with } E_{\text{meas}}^{\text{jet}} = E_{\text{EM}}^{\text{jet}} - \mathcal{O}(N_{\text{PV}}). \quad (1)$$

The variable $E_{\text{EM}}^{\text{jet}}$ is the calorimeter energy measured at the electromagnetic scale, $E_{\text{calib}}^{\text{jet}}$ is the calibrated jet energy and $\mathcal{F}_{\text{calib}}$ is the calibration function that depends on the measured jet energy and is evaluated in small jet pseudorapidity regions. The variable $\mathcal{O}(N_{\text{PV}})$ denotes the correction for additional energy from multiple proton-proton interactions depending on the number of primary vertices (N_{PV}).

The simplest calibration scheme (called EM+JES) applies the JES corrections to jets reconstructed at the electromagnetic scale. This calibration scheme allows a simple evaluation of the systematic uncertainty from single hadron response measurements and systematic Monte Carlo variations. This can be achieved with small data sets and is therefore suitable for early physics analyses.

Other calibration schemes use additional cluster-by-cluster and/or jet-by-jet information to reduce some of the sources of fluctuations in the jet energy response, thereby improving the jet energy resolution. For these calibration schemes the same jet calibration procedure is applied as for the EM+JES calibration scheme, but the energy corrections are numerically smaller.

The global calorimeter cell weighting (GCW) calibration exploits the observation that electromagnetic showers in the calorimeter leave more compact energy depositions than hadronic showers with the same energy. Energy corrections are derived for each calorimeter cell within a jet, with the constraint that the jet energy resolution is minimised. The cell corrections account for all energy losses of a jet in the ATLAS detector. Since these corrections are only applicable to jets and not to energy depositions in general, they are called “global” corrections.

The local cluster weighting (LCW) calibration method first clusters together topologically connected calorimeter cells and classifies these clusters as either electromagnetic or hadronic. Based on this classification energy corrections are derived from single pion Monte Carlo simulations. Dedicated corrections are derived for the effects of non-compensation, signal losses due to noise threshold effects, and energy lost in non-instrumented regions. They are applied to calorimeter clusters and are defined without reference to a jet definition. They are therefore called “local” corrections. Jets are then built from these calibrated clusters using a jet algorithm.

The final jet energy calibration (see Equation 1) can be applied to EM scale jets, with the resulting calibrated jets referred to as EM+JES, or to GCW and LCW calibrated jets, with the resulting jets referred to as GCW+JES and LCW+JES jets.

A further jet calibration scheme, called global sequential (GS) calibration, starts from jets calibrated with the EM+JES

calibration and exploits the topology of the energy deposits in the calorimeter to characterise fluctuations in the jet particle content of the hadronic shower development. Correcting for such fluctuations can improve the jet energy resolution. The corrections are applied such that the mean jet energy is left unchanged. The correction uses several jet properties and each correction is applied sequentially. In particular, the longitudinal and transverse structure of the hadronic shower in the calorimeter is exploited.

The simple EM+JES jet calibration scheme does not provide the best performance, but allows in the central detector region the most direct evaluation of the systematic uncertainties from the calorimeter response to single isolated hadron measured *in situ* and in test-beams and from systematic variations of the Monte Carlo simulation. For the GS the systematic uncertainty is obtained by studying the response after applying the GS calibration with respect to the EM+JES calibration. For the GCW+JES and LCW+JES calibration schemes the JES uncertainty is determined from *in situ* techniques.

For all calibration schemes the JES uncertainty in the forward detector regions is derived from the uncertainty in the central region using the transverse momentum balance in events where only two jets are produced.

In the following, the calibrated calorimeter jet transverse momentum will be denoted as $p_{\text{T}}^{\text{jet}}$, and the jet pseudorapidity as η .

4 Monte Carlo simulation

4.1 Event generators

The energy and direction of particles produced in proton-proton collisions are simulated using various event generators. An overview of Monte Carlo event generators for LHC physics can be found in Ref. [20]. The samples using different event generators and theoretical models used are described below:

1. PYTHIA with the MC10 or AMBT1 tune: The event generator PYTHIA [21] simulates non-diffractive proton-proton collisions using a $2 \rightarrow 2$ matrix element at leading order in the strong coupling to model the hard subprocess, and uses p_{T} -ordered parton showers to model additional radiation in the leading-logarithmic approximation [22]. Multiple parton interactions [23], as well as fragmentation and hadronisation based on the Lund string model [24] are also simulated. The proton parton distribution function (PDF) set used is the modified leading-order PDF set MRST LO* [25]. The parameters used for tuning multiple parton interactions include charged particle spectra measured by ATLAS in minimum bias collisions [26], and are denoted as the ATLAS MC10 tune [27].
2. The PERUGIA2010 tune is an independent tune of PYTHIA with increased final state radiation to better reproduce the jet shapes and hadronic event shapes using LEP and TEVATRON data [28]. In addition, parameters sensitive to the production of particles with strangeness and related to jet fragmentation have been adjusted.
3. HERWIG+JIMMY uses a leading order $2 \rightarrow 2$ matrix element supplemented with angular-ordered parton showers

in the leading-logarithm approximation [29]. The cluster model is used for the hadronisation [30]. Multiple parton interactions are modelled using JIMMY [31]. The model parameters of HERWIG/JIMMY have been tuned to ATLAS data (AUET1 tune) [32]. The MRST LO* PDF set [25] is used.

4. HERWIG++ [33] is based on the event generator HERWIG, but redesigned in the C++ programming language. The generator contains a few modelling improvements. It also uses angular-ordered parton showers, but with an updated evolution variable and a better phase space treatment. Hadronisation is performed using the cluster model. The underlying event and soft inclusive interactions are described using a hard and soft multiple partonic interactions model [34]. The MRST LO* PDF set [25] is used.
5. ALPGEN is a tree level matrix-element generator for hard multi-parton processes ($2 \rightarrow n$) in hadronic collisions [35]. It is interfaced to HERWIG to produce parton showers in the leading-logarithmic approximation. Parton showers are matched to the matrix element with the MLM matching scheme [36]. For the hadronisation, HERWIG is used and soft multiple parton interactions are modelled using JIMMY [31] (with the ATLAS MC09 tune [37]). The PDF set used is CTEQ6L1 [38].

4.2 Simulation of the ATLAS detector

The GEANT4 software toolkit [39] within the ATLAS simulation framework [40] propagates the generated particles through the ATLAS detector and simulates their interactions with the detector material. The energy deposited by particles in the active detector material is converted into detector signals with the same format as the ATLAS detector read-out. The simulated detector signals are in turn reconstructed with the same reconstruction software as used for the data.

In GEANT4 the model for the interaction of hadrons with the detector material can be specified for various particle types and for various energy ranges. For the simulation of hadronic interactions in the detector, the GEANT4 set of processes called QGSP_BERT is chosen [41]. In this set of processes, the Quark Gluon String model [42] is used for the fragmentation of the nucleus, and the Bertini cascade model [43] for the description of the interactions of hadrons in the nuclear medium.

The GEANT4 simulation and in particular the hadronic interaction model for pions and protons, has been validated with test-beam measurements for the barrel [14, 44–46] and end-cap [15, 16, 47] calorimeters. Agreement within a few percent is found between simulation and data for pion momenta between 2 GeV and 350 GeV.

Further tests have been carried out *in situ* comparing the single hadron response, measured using isolated tracks and identified single particles. Agreement within a few percent is found for the inclusive measurement [48, 49] and for identified pions and protons from the decay products of kaon and lambda particles produced in proton-proton collisions at 7 TeV [50]. With this method particle momenta of pions and protons in the range from a few hundred MeV to 6 GeV can be reached. Good agreement between Monte Carlo simulation and data is found.

4.3 Nominal Monte Carlo simulation samples

The baseline (nominal) Monte Carlo sample used to derive the jet energy scale and to estimate the sources of its systematic uncertainty is a sample containing high- p_T jets produced via strong interactions. It is generated with the PYTHIA event generator with the MC10 tune (see Section 4.1), passed through the full ATLAS detector simulation and is reconstructed as the data.

The ATLAS detector geometry used in the simulation of the nominal sample reflects the geometry of the detector as best known at the time of these studies. Studies of the material of the inner detector in front of the calorimeters have been performed using secondary hadronic interactions [51]. Additional information is obtained from studying photon conversions [52] and the energy flow in minimum bias events [53].

4.4 Simulated pile-up samples

For the study of multiple proton-proton interactions, two samples have been used, one for in-time and one for out-of-time pile-up. The first simulates additional proton-proton interactions per bunch crossing, while the second one also contains pile-up arising from bunches before or after the bunch where the event of interest was triggered (for more details see Section 5 and Section 8.1). The bunch configuration of LHC (organised in bunch trains) is also simulated. The additional number of primary vertices in the in-time (bunch-train) pile-up sample is 1.7 (1.9) on average.

5 Data sample and event selection

5.1 Data taking period and LHC conditions

Proton-proton collisions at a centre-of-mass energy of $\sqrt{s} = 7$ TeV, recorded from March to October 2010 are analysed. Only data with a fully functioning calorimeter and inner detector are used. The data set corresponds to an integrated luminosity of 38 pb^{-1} . Due to different data quality requirements the integrated luminosity can differ for the various selections used in the *in situ* technique analyses.

Several distinct periods of machine configuration and detector operation were present during the 2010 data taking. As the LHC commissioning progressed, changes in the beam optics and proton bunch parameters resulted in changes in the number of pile-up interactions per bunch crossing. The spacing between the bunches was no less than 150 ns.

Figure 3 shows the evolution of the maximum of the distribution of the number of interactions (peak) derived from the online luminosity measurement and assuming an inelastic proton-proton scattering cross section of 71.5 mb [54].

The very first data were essentially devoid of multiple proton-proton interactions until the optics of the accelerator beam (specifically β^*) were changed in order to decrease the transverse size of the beam and increase the luminosity³. This change alone

³ The parameter β^* is the value of the β -function (the envelope of all trajectories of the beam particles) at the collision point and smaller values of β^* imply a smaller physical size of the beams and thus a higher instantaneous luminosity.

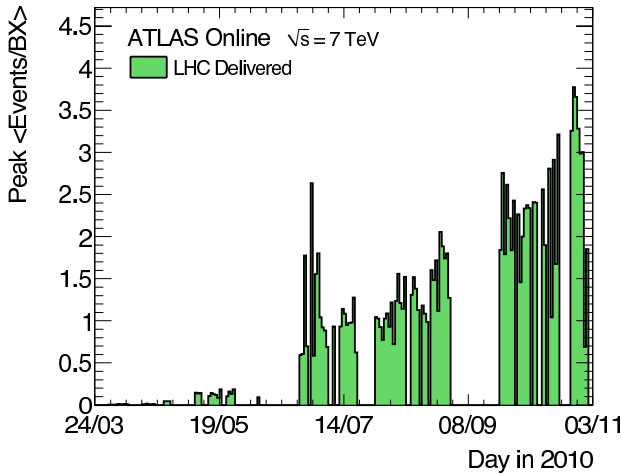


Fig. 3: The peak number of interactions per bunch crossing (“BX”) as measured online by the ATLAS luminosity detectors [54].

raised the fraction of events with at least two observed interactions from less than 2% to between 8% and 10% (May-June 2010).

A further increase in the number of interactions occurred when the number of protons per bunch (ppb) was increased from approximately $5 - 9 \cdot 10^{10}$ to $1.15 \cdot 10^{11}$ ppb. Since the number of proton-proton collisions per bunch crossing is proportional to the square of the bunch intensity, the fraction of events with pile-up increased to more than 50% for runs between June and September 2010.

Finally, further increasing the beam intensity slowly raised the average number of interactions per bunch crossing to more than three by the end of the proton-proton run in November 2010.

5.2 Event selection

Different triggers are used to select the data samples, in order to be maximally efficient over the entire jet p_T -range of interest. The dijet sample is selected using the hardware-based calorimeter jet triggers [10, 55], which are fully efficient for jets with $p_T^{\text{jet}} > 60$ GeV. For lower p_T^{jet} a trigger based on the minimum bias trigger scintillators is used.

The multijet sample uses either the inclusive jet trigger or a trigger that requires at least two, three or more jets with $p_T > 10$ GeV at the EM scale. These triggers are fully efficient for jets with $p_T^{\text{jet}} > 80$ GeV.

Each event is required to have a primary hard scattering vertex. A primary vertex is required to have at least five tracks ($N_{\text{pp}}^{\text{tracks}}$) with a transverse momentum of $p_T^{\text{track}} > 150$ MeV. The primary vertex associated to the event of interest (hard scattering vertex) is the one with the highest associated transverse track momentum squared used in the vertex fit $\Sigma(p_T^{\text{track}})^2$, where the sum runs over all tracks used in the vertex fit. This renders the contribution from fake vertices due to beam backgrounds to be negligible.

The γ -jet sample is selected using a photon trigger [10] that is fully efficient for photons passing offline selections. The higher threshold for the photon p_T is 40 GeV and this trigger was not pre-scaled; the lower threshold is 20 GeV and this trigger was pre-scaled at high luminosity.

5.3 Data quality assessment

The ATLAS data quality (DQ) selection is based upon inspection of a standard set of distributions that leads to a data quality assessment for each subdetector, usually segmented into barrel, forward and endcap regions, as well as for the trigger and for each type of reconstructed physics object (jets, electrons, muons, etc.). Each subsystem sets its own DQ flags, which are recorded in a conditions database. Each analysis applies DQ selection criteria, and defines a set of luminosity blocks (each corresponds to approximately two minutes of data taking). The good luminosity blocks used are those not flagged for having issues affecting a relevant subdetector.

Events with minimum bias and calorimeter triggers were required to belong to specific runs and run periods in which the detector, trigger and reconstructed physics objects have passed a data quality assessment and are deemed suitable for physics analysis.

The primary systems of interest for this study are the electromagnetic and hadronic calorimeters, and the inner tracking detector for studies of the properties of tracks associated with jets.

6 Jet reconstruction

In data and Monte Carlo simulation jets are reconstructed using the anti- k_t algorithm [7] with distance parameters $R = 0.4$ or $R = 0.6$ using the FASTJET software [56]. The four-momentum recombination scheme is used. Jet finding is done in y - ϕ coordinates, while jet corrections and performance studies are often done in η - ϕ coordinates. The jet p_T reconstruction threshold is $p_T^{\text{jet}} > 7$ GeV.

In the following, only anti- k_t jets with distance parameter $R = 0.6$ are discussed in detail. The results for jets with $R = 0.4$ are similar, if not stated otherwise.

6.1 Reconstructed calorimeter jets

The input to *calorimeter jets* can be topological calorimeter clusters (*topo-clusters*) [16, 57] or calorimeter towers. Only topo-clusters or towers with a positive energy are considered as input to jet finding.

6.1.1 Topological calorimeter clusters

Topological clusters are groups of calorimeter cells that are designed to follow the shower development taking advantage of the fine segmentation of the ATLAS calorimeters. The topo-cluster formation algorithm starts from a *seed* cell, whose signal-to-noise (S/N) ratio is above a threshold of $S/N = 4$. The noise

	Loose	Medium
HEC spikes	$(f_{\text{HEC}} > 0.5 \text{ and } f_{\text{HECquality}} > 0.5)$ or $ E_{\text{neg}} > 60 \text{ GeV}$	Loose or $f_{\text{HEC}} > 1 - f_{\text{HECquality}} $
Coherent EM noise	$f_{\text{EM}} > 0.95 \text{ and } f_{\text{quality}} > 0.8$ and $ \eta < 2.8$	Loose or $f_{\text{EM}} > 0.9 \text{ and } f_{\text{quality}} > 0.8 \text{ and } \eta < 2.8$
Non-collision background	$ t_{\text{jet}} > 25 \text{ ns}$ or $(f_{\text{EM}} < 0.05 \text{ and } f_{\text{ch}} < 0.05 \text{ and } \eta < 2)$ or $(f_{\text{EM}} < 0.05 \text{ and } \eta \geq 2)$ or $(f_{\text{max}} > 0.99 \text{ and } \eta < 2)$	Loose or $ t_{\text{jet}} > 10 \text{ ns}$ or $(f_{\text{EM}} < 0.05 \text{ and } f_{\text{ch}} < 0.1 \text{ and } \eta < 2)$ or $(f_{\text{EM}} > 0.95 \text{ and } f_{\text{ch}} < 0.05 \text{ and } \eta < 2)$

Table 1: Selection criteria used to reject fake jets and non-collision background.

is estimated as the absolute value of the energy deposited in the calorimeter cell divided by the RMS of the energy distribution measured in events triggered at random bunch crossings. Cells neighbouring the seed (or the cluster being formed) that have a signal-to-noise ratio of at least $S/N = 2$ are included iteratively. Finally, all calorimeter cells neighbouring the formed topo-cluster are added. The topo-cluster algorithm efficiently suppresses the calorimeter noise.

The topo-cluster algorithm also includes a splitting step in order to optimise the separation of showers from different close-by particles: All cells in a topo-cluster are searched for local maxima in terms of energy content with a threshold of 500 MeV. This means that the selected calorimeter cell has to be more energetic than any of its neighbours. The local maxima are then used as seeds for a new iteration of topological clustering, which splits the original cluster into more topo-clusters.

A topo-cluster is defined to have an energy equal to the energy sum of all the included calorimeter cells, zero mass and a reconstructed direction calculated from the weighted averages of the pseudorapidities and azimuthal angles of the constituent cells. The weight used is the absolute cell energy and the positions of the cells are relative to the nominal ATLAS coordinate system.

6.1.2 Calorimeter towers

Calorimeter towers are static, $\Delta\eta \times \Delta\phi = 0.1 \times 0.1$, grid elements built directly from calorimeter cells⁴.

ATLAS uses two types of calorimeter towers: with and without noise suppression. Calorimeter towers based on all calorimeter cells are called *non-noise-suppressed calorimeter towers* in the following. Noise-suppressed towers make use of the topo-clusters algorithm, i.e. only calorimeter cells that are included in topo-clusters are used. Therefore, for a fixed geometrical area, noise-suppressed towers have the same energy content as the topo-clusters.

Both types of calorimeter towers have an energy equal to the energy sum of all included calorimeter cells. The formed Lorentz four-momentum has zero mass.

⁴ For the few calorimeter cells that are larger than the $\Delta\eta \times \Delta\phi = 0.1 \times 0.1$ (like in the last Tile calorimeter layer and the HEC inner wheel) or have a special geometry (like in the FCAL), projective tower grid geometrical weights are defined that specify the fraction of calorimeter cell energy to be attributed to a particular calorimeter tower.

6.2 Reconstructed track jets

Jets built from charged particle tracks originating from the primary hard scattering vertex (*track jets*) are used to define jets that are insensitive to the effects of pile-up and provide a stable reference to study close-by jet effects.

Tracks with $p_{\text{T}}^{\text{track}} > 0.5 \text{ GeV}$ and $|\eta| < 2.5$ are selected. They are required to have at least one (six) hit(s) in the Pixel (SCT) detector. The transverse (d_0) and longitudinal (z_0) impact parameters of the tracks measured with respect to the primary vertex are also required to be $|d_0| < 1.5 \text{ mm}$ and $|z_0 \sin \theta| < 1.5 \text{ mm}$, respectively.

The track jets must have at least two constituent tracks and a total transverse momentum of $p_{\text{T}}^{\text{track jet}} > 3 \text{ GeV}$. Since the tracking system has a coverage up to $|\eta| = 2.5$, the performance studies of calorimeter jets is carried out in the range $|\eta| < 1.9$ for $R = 0.6$ and $|\eta| < 2.1$ for $R = 0.4$.

6.3 Monte Carlo truth jets and flavour association

Monte Carlo simulation *truth jets* are built from stable particles defined to have proper lifetimes longer than 10 ps excluding muons and neutrinos.

For certain studies, jets in the Monte Carlo simulation are additionally identified as jets initiated by light or heavy quarks or by gluons based on the generator event record. The highest energy parton that points to the truth jet⁵ determines the flavour of the jet. Using this method, only a small fraction of the jets ($< 1\%$ at low p_{T} and less at high p_{T}) could not be assigned a partonic flavour. This definition is sufficient to study the flavour dependence of the jet response. Any theoretical ambiguities of jet flavour assignment do not need to be addressed in the context of a performance study.

⁵ With $\Delta R < 0.6$ for jets with $R = 0.6$ and $\Delta R < 0.4$ for jets with $R = 0.4$, where $\Delta R = \sqrt{(\Delta\eta)^2 + (\Delta\phi)^2}$.

7 Jet quality selection

Jets at high transverse momenta produced in proton-proton collisions must be distinguished from background jets not originating from hard scattering events. The main backgrounds are the following:

1. Beam-gas events, where one proton of the beam collided with the residual gas within the beam pipe.
2. Beam-halo events, for example caused by interactions in the tertiary collimators in the beam-line far away from the ATLAS detector.
3. Cosmic ray muons overlapping in-time with collision events.
4. Large calorimeter noise.

The criteria to efficiently reject jets arising from background are only applied to data. They are discussed in the following sections.

7.1 Criteria to remove non-collision background

7.1.1 Noise in the calorimeters

Two types of calorimeter noise are addressed:

1. **Sporadic noise bursts** in the hadronic endcap calorimeter (HEC), where a single noisy calorimeter cell contributes almost all of the jet energy. Jets reconstructed from these problematic cells are characterised by a large energy fraction in the HEC calorimeter (f_{HEC}) as well as a large fraction of the energy in calorimeter cells with poor signal shape quality⁶ ($f_{\text{HECquality}}$). Due to the capacitive coupling between channels, the neighbouring calorimeter cells will have an apparent negative energy (E_{neg}).
2. **Rare coherent noise** in the electromagnetic calorimeter. Similarly, fake jets arising from this source are characterised by a large electromagnetic energy fraction (f_{EM})⁷, and a large fraction of calorimeter cells with poor signal shape quality (f_{quality}).

7.1.2 Cosmic rays or non-collision background

Cosmic rays or non-collision backgrounds can induce events where the jet candidates are not in-time with the beam collision. A cut on the jet time (t_{jet}) is applied to reject these backgrounds. The jet time is reconstructed from the energy deposition in the calorimeter by weighting the reconstructed time of calorimeter cells forming the jet with the square of the cell energy. The calorimeter time is defined with respect to the event time recorded by the trigger.

A cut on the f_{EM} is applied to make sure that the jet has some energy deposited in the calorimeter layer closest to the interaction region as expected for a jet originating from the nominal interaction point.

⁶ The signal shape quality is obtained by comparing the measured pulse from the calorimeter cell to the expected pulse shape.

⁷ The EM fraction is defined as the ratio of the energy deposited in the EM calorimeter to the total energy.

Since a real jet is expected to have tracks, the f_{EM} cut is applied together with a cut on the minimal jet charged fraction (f_{ch}), defined as the ratio of the scalar sum of the p_{T} of the tracks associated to the jet divided by the jet p_{T} , for jets within the tracking acceptance.

A cut on the maximum energy fraction in any single calorimeter layer (f_{max}) is applied to further reject non-collision background.

7.1.3 Jet quality selections

Two quality selections are provided:

1. A **loose selection** is designed with an efficiency above 99%, that can be used in most of the ATLAS physics analyses.
2. A **medium selection** is designed for analyses that select jets at high transverse momentum, such as for jet cross-section measurements [1].

A tight quality selection has been developed for the measurement of the jet quality selection efficiency described in Section 7.2, but is not used in physics analyses, since the medium jet quality selection is sufficient for removing fake jets. The quality selection criteria used to identify and reject fake jets are listed in Table 1.

7.2 Evaluation of the jet quality selection efficiency

The criteria for the jet quality selection are optimised by studying samples with good and fake jets classified by their amount of missing transverse momentum significance⁸:

1. Good jets belong to events where the two leading jets have $p_{\text{T}}^{\text{jet}} > 20$ GeV, and are back-to-back ($\Delta\phi_{j-j} > 2.6$ radian) in the plane transverse to the beam, and with a small missing transverse momentum significance $E_{\text{T}}^{\text{miss}}/\sqrt{\Sigma E_{\text{T}}} < 1$.
2. Fake jets belong to events with a high transverse momentum significance $E_{\text{T}}^{\text{miss}}/\sqrt{\Sigma E_{\text{T}}} > 3$ and with a reconstructed jet back-to-back to the missing transverse momentum direction ($\Delta\phi_{E_{\text{T}}^{\text{miss}}-j} > 2.6$ radian).

As the jet quality selection criteria are only applied to data an efficiency correction for data is determined. This efficiency is measured using a tag-and-probe method in events with two jets at high transverse momentum. The reference jet ($p_{\text{T}}^{\text{ref}}$) is required to pass the tightened version of the jet quality selections, and to be back-to-back and well-balanced with the probe jet ($p_{\text{T}}^{\text{probe}}$):

$$(|p_{\text{T}}^{\text{probe}} - p_{\text{T}}^{\text{ref}}|/p_{\text{T}}^{\text{avg}} < 0.4), \text{ with } p_{\text{T}}^{\text{avg}} = (p_{\text{T}}^{\text{probe}} + p_{\text{T}}^{\text{ref}})/2. \quad (2)$$

The jet quality selection criteria were then applied to the probe jets, measuring the fraction of jets passing as a function of η and $p_{\text{T}}^{\text{jet}}$.

The resulting efficiencies for jets with $R = 0.6$ for loose and medium selections applied to the probe jets are shown in

⁸ The missing transverse momentum ($E_{\text{T}}^{\text{miss}}$) significance is defined as $E_{\text{T}}^{\text{miss}}/\sqrt{\Sigma E_{\text{T}}}$, where ΣE_{T} is the scalar sum of the transverse energies of all energy deposits in the calorimeter.

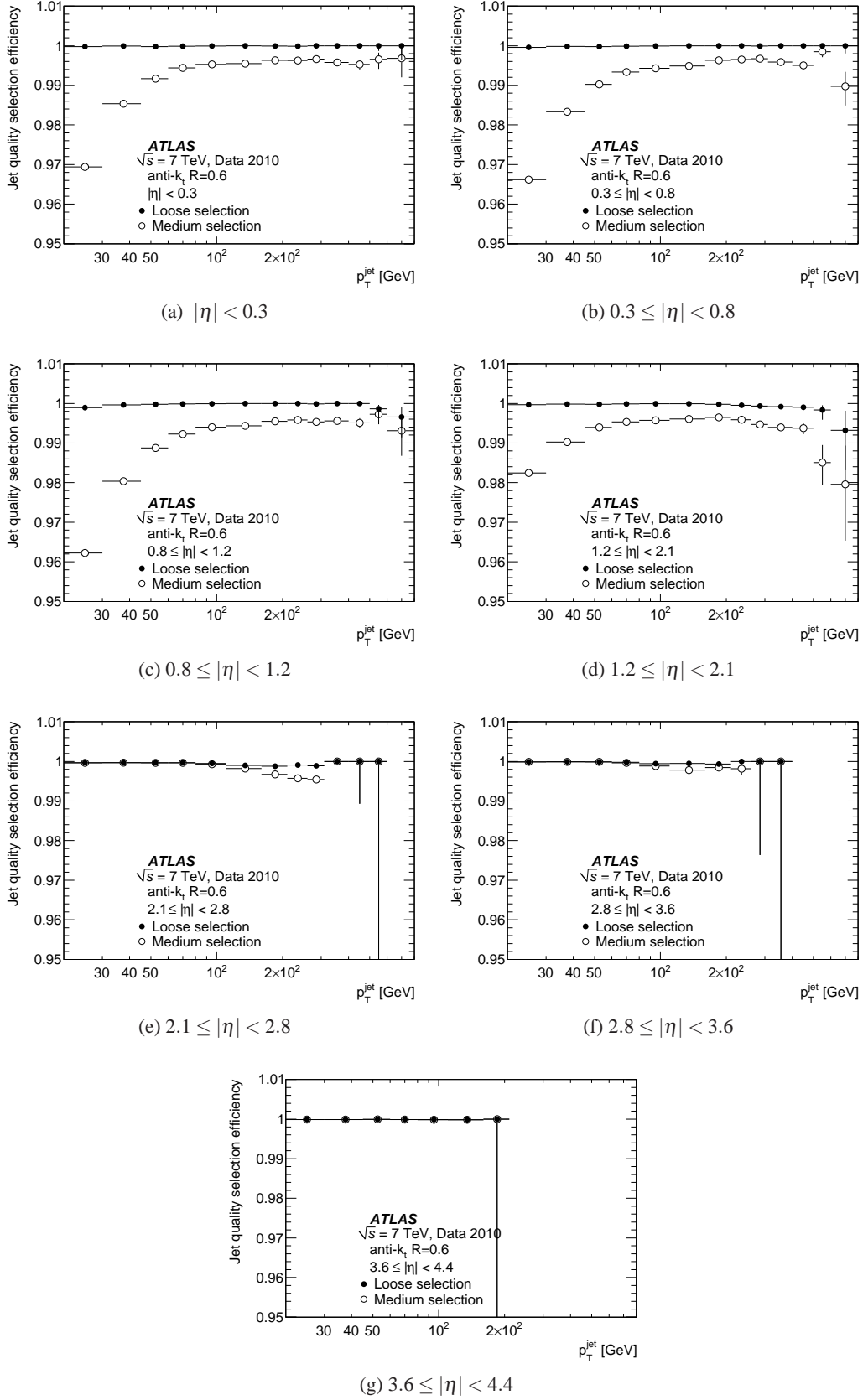


Fig. 4: Jet quality selection efficiency for anti- k_T jets with $R = 0.6$ measured with a tag-and-probe technique as a function of p_T^{jet} in bins of η , for loose and medium selection criteria (see Table 1). Only statistical uncertainties are shown. In (e), (f), (g) the loose and medium results overlap.

Figure 4. The tight selection of the reference jet was varied to study the systematic uncertainty. The loose selection criteria are close to 100% efficient. In the forward region the medium selection criteria are also close to fully efficient. In the central region they have an efficiency of 99% for $p_T^{\text{jet}} > 50$ GeV. For lower p_T jets of about 25 GeV an inefficiency of up to 3 – 4% is observed.

7.3 Summary of the jet quality selection

Quality selections used to reject fake jets with the ATLAS detector have been developed. Simple variables allow the removal of fake jets due to sporadic noise in the calorimeter or non-collision background at the analysis level, with an efficiency greater than 99% over a wide kinematic range.

8 Jet energy calibration in the EM+JES scheme

The simple EM+JES calibration scheme applies corrections as a function of the jet energy and pseudorapidity to jets reconstructed at the electromagnetic scale.

The additional energy due to multiple proton-proton collisions within the same bunch crossing (pile-up) is corrected before the hadronic energy scale is restored, such that the derivation of the jet energy scale calibration is factorised and does not depend on the number of additional interactions measured.

The EM+JES calibration scheme consists of three subsequent steps as outlined below and detailed in the following subsections:

1. **Pile-up correction:** The average additional energy due to additional proton-proton interactions is subtracted from the energy measured in the calorimeters using correction constants obtained from *in situ* measurements.
2. **Vertex correction:** The direction of the jet is corrected such that the jet originates from the primary vertex of the interaction instead of the geometrical centre of the detector.
3. **Jet energy and direction correction:** The jet energy and direction as reconstructed in the calorimeters are corrected using constants derived from the comparison of the kinematic observables of reconstructed jets and those from truth jets in Monte Carlo simulation.

8.1 Pile-up correction

8.1.1 Correction strategy

The measured energy of reconstructed jets can be affected by contributions that do not originate from the hard scattering event of interest, but are instead produced by additional proton-proton collisions within the same bunch crossing. An offset correction for pile-up is derived from minimum bias data as a function of the number of reconstructed primary vertices, N_{PV} , the jet pseudorapidity, η , and the bunch spacing.

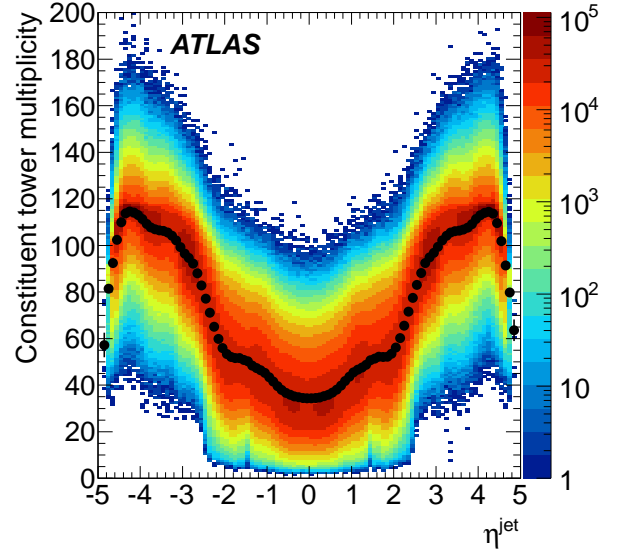


Fig. 5: Distribution of the number constituent calorimeter towers as a function of the jet pseudorapidity for anti- k_t jets with $R = 0.6$ and $p_T^{\text{jet}} > 7$ GeV. The black dots indicate the average number of tower constituents.

This offset correction applied to the jet transverse energy (E_T) at the EM scale as the first step of jet calibration can be written generically as:

$$E_T^{\text{corrected}} = E_T^{\text{uncorrected}} - \mathcal{O}(\eta, N_{\text{PV}}, \tau_{\text{bunch}}), \quad (3)$$

where $\mathcal{O}(\eta, N_{\text{PV}}, \tau_{\text{bunch}})$ corrects for the jet offset due to pile-up.

Due to the varying underlying particle spectrum and the variation in the calorimeter geometry the jet offset is derived as a function of the jet pseudorapidity. The amount of in-time pile-up is parameterised by N_{PV} . The spacing between consecutive bunches, τ_{bunch} , is considered, because it can impact the amount by which collisions in previous bunch crossings affect the jet energy measurement⁹.

The jet offset correction is proportional to the number of constituent towers in a jet as a measure of the jet area. For jets built directly from dynamically-sized topological clusters, for which no clear geometric definition is available, a model is used that describes the average area of a jet in terms of the equivalent number of constituent towers.

8.1.2 Constituent tower multiplicity of jets

The multiplicity of calorimeter towers in jets depends on the internal jet composition and on the presence of pile-up. The average tower multiplicity can be measured *in situ*.

⁹ The dependence on τ_{bunch} is explicitly allowed for due to the possibility of pile-up contributions from previous proton-proton bunch crossings for closely spaced bunches. This will be an important consideration for the 2011-2012 LHC run as the number of bunches is increased and the spacing between consecutive bunches is reduced.

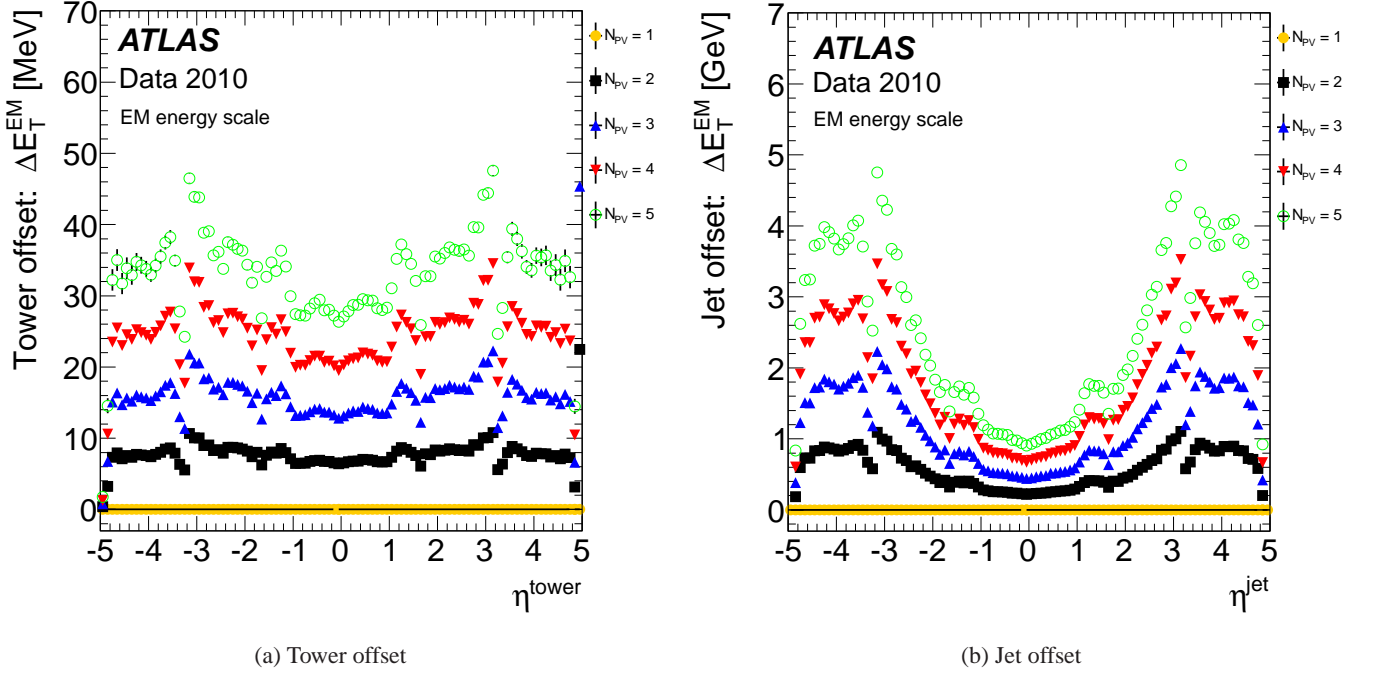


Fig. 6: Tower offset (a) and jet offset (b) at the EM scale as a function of the tower or jet pseudorapidity in bins of the number of reconstructed primary vertices. The jet offset is shown for anti- k_t jets with $R = 0.6$. Only statistical uncertainties are shown. They are typically smaller than the marker size.

Figure 5 depicts the distribution of the constituent tower multiplicity for jets based on towers with $p_T^{\text{jet}} > 7$ GeV as a function of the jet pseudorapidity. The average number of constituent towers is also indicated. This distribution is governed by the change in physical size of calorimeter towers for a constant interval in pseudorapidity, as well as by differences in the noise spectrum for the various calorimeters and sampling regions.

8.1.3 Pile-up offset for towers and jets

The calorimeter tower offset at the EM scale is derived by measuring the average tower transverse energy for all towers in events with $N_{\text{PV}} = 1, 2, \dots, N$ and comparing directly to events with $N_{\text{PV}} = N_{\text{PV}}^{\text{ref}} = 1$:

$$\mathcal{O}_{\text{tower}}(\eta, N_{\text{PV}}) = \langle E_T^{\text{tower}}(\eta, N_{\text{PV}}) \rangle - \langle E_T^{\text{tower}}(\eta, N_{\text{PV}}^{\text{ref}}) \rangle, \quad (4)$$

where the angled brackets denote a statistical average over all events. The average is computed for events at each primary vertex multiplicity. For this measurement non-noise-suppressed calorimeter towers are used (see Section 6.1.2) in order to remain sensitive to low energy depositions that may not rise above noise threshold except inside of a jet. The calorimeter tower offset is shown in Figure 6a for $1 \leq N_{\text{PV}} \leq 5$.

The tower offset can be extrapolated to an EM scale jet offset using:

$$\mathcal{O}_{\text{jet|tower}}(\eta, N_{\text{PV}}) = \mathcal{O}_{\text{tower}}(\eta, N_{\text{PV}}) \cdot A^{\text{jet}}, \quad (5)$$

where A^{jet} is the jet area that, for jets built from calorimeter towers, can be estimated from the constituent tower multiplicity, $A^{\text{jet}} = N_{\text{towers}}^{\text{jet}}$. For jets built from topo-clusters, the mean equivalent constituent tower multiplicity ($A^{\text{jet}} = \langle N_{\text{towers}}^{\text{jet}} \rangle$) is used¹⁰. The small dependencies of the constituent multiplicity on p_T^{jet} and N_{PV} are neglected in the correction, but incorporated as systematic uncertainties (see Section 9.7).

The jet offset for jets with $R = 0.6$ is shown in Figure 6b.

8.1.4 Track jet based validation and offset correction

Track jets constructed from charged particles originating from the primary hard-scattering vertex matched to the calorimeter jets provide a stable reference that can be used to measure the variation of the calorimeter E_T^{jet} as a function of N_{PV} . It is therefore possible to validate the tower-based offset correction and also to directly estimate the pile-up energy contribution to jets.

As this method is only applicable to jets within the inner detector acceptance, it serves primarily as a cross-check for the tower-based method discussed above. It can also be used, however, to derive a dedicated offset correction that can be applied to jets at energy scales other than the electromagnetic energy

¹⁰ The equivalent constituent tower multiplicity for jets based on topo-clusters is calculated from the location of the calorimeter cells of the constituent topo-clusters in the jet.

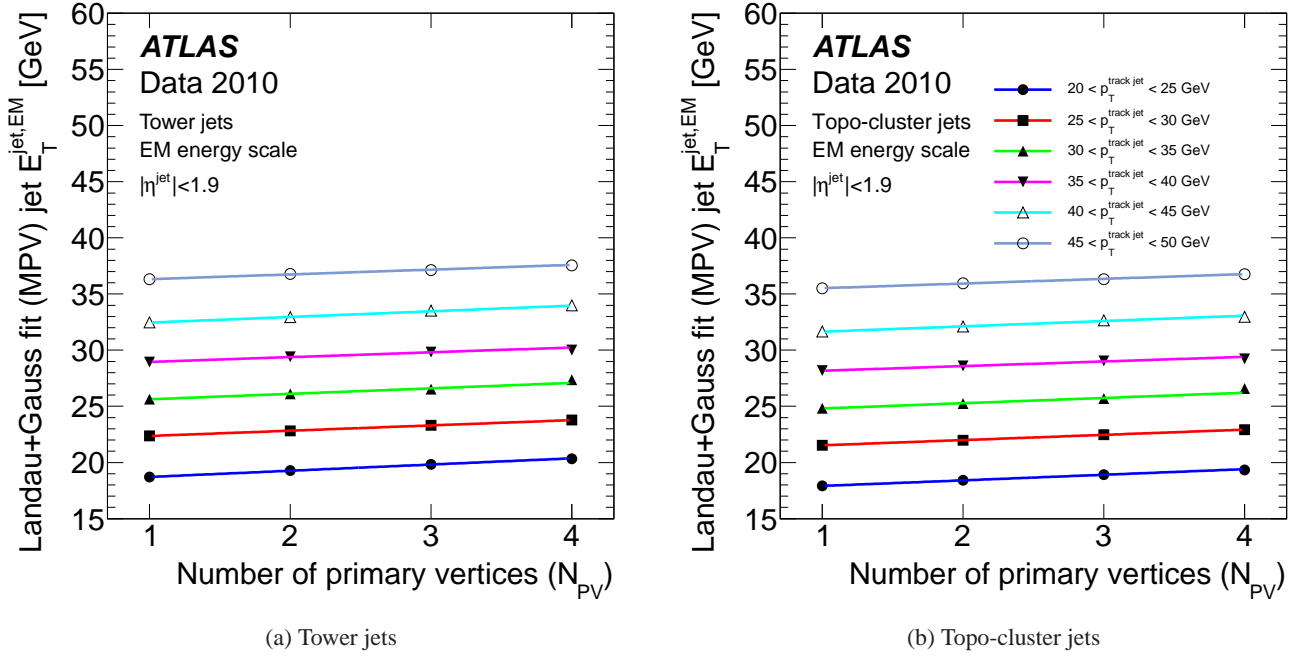


Fig. 7: Transverse jet energy E_T^{jet} for calorimeter jets associated to track jets measured at the EM scale using a Landau-Gauss fit as a function of the reconstructed vertex multiplicity, N_{PV} , in bins of $p_T^{\text{track jet}}$. Calorimeter jets are reconstructed at the EM scale with calorimeter towers (a) and topo-clusters (b) as inputs. Systematic uncertainties are not shown. The statistical uncertainties from the fit results are smaller than the marker size.

scale. Studying the variation of the offset correction as a function of $p_T^{\text{track jet}}$ can establish the systematic uncertainty of the pile-up correction.

The criterion to match a track jet to a calorimeter jet with $R = 0.6$ is

$$\Delta R(\text{jet}, \text{trackjet}) < 0.4, \quad (6)$$

where $\Delta R = \sqrt{(\Delta\eta)^2 + (\Delta\phi)^2}$. The offset is calculated by measuring the average calorimeter jet E_T^{jet} as a function of N_{PV} and the transverse momentum of the matched track jet, $p_T^{\text{track jet}}$:

$$\mathcal{O}_{\text{track jet}} = \langle E_T^{\text{jet}}(N_{\text{PV}} | p_T^{\text{track jet}}) \rangle - \langle E_T^{\text{jet}}(N_{\text{PV}}^{\text{ref}} | p_T^{\text{track jet}}) \rangle. \quad (7)$$

The reference $N_{\text{PV}}^{\text{ref}} = 1$ is used.

Figure 7 shows the jet E_T as a function of N_{PV} for several bins in $p_T^{\text{track jet}}$. Both tower and topo-cluster jets at the electromagnetic scale are used. The most probable value (MPV) of the calorimeter jet E_T is determined from a fit using a Landau distribution convolved with a Gaussian for each range of $p_T^{\text{track jet}}$. A consistent offset of nearly $\mathcal{O} = 0.5$ GeV per vertex is found for $|\eta| < 1.9$. No systematic trend of the offset as a function of $p_T^{\text{track jet}}$ is observed.

Figure 8 presents the jet-based offset correction as a function of N_{PV} derived with respect to $N_{\text{PV}}^{\text{ref}} = 1$ for tower and topo-cluster based jet using the EM and the EM+JES scale. As expected, the magnitude of the offset is higher after EM+JES

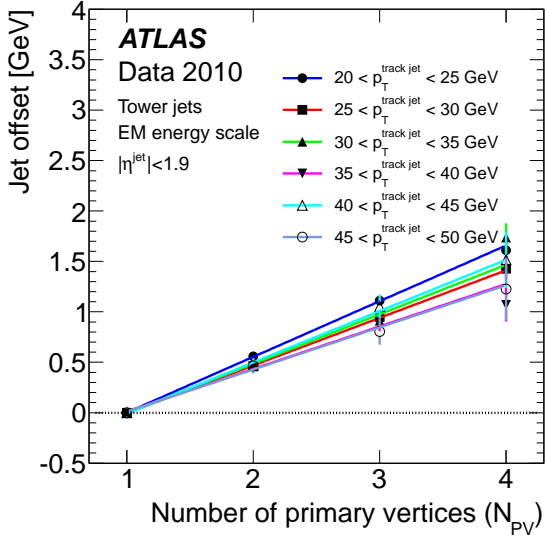
calibration (see Figure 8c and Figure 8d), and the increase corresponds to the average jet energy correction (see Section 8.3).

8.2 Jet origin correction

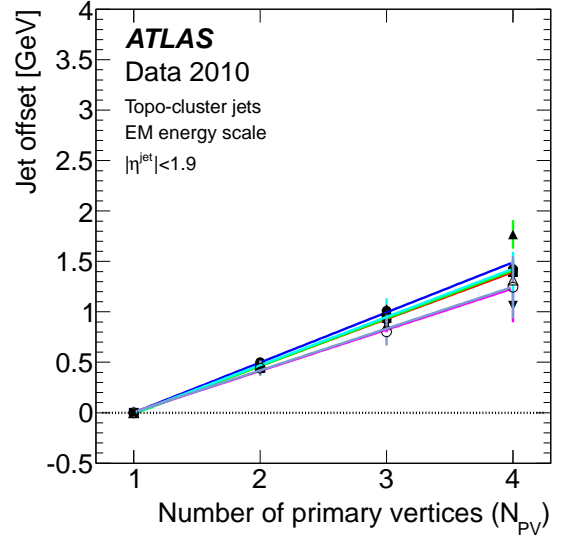
Calorimeter jets are reconstructed using the geometrical centre of the ATLAS detector as reference to calculate the direction of jets and their constituents (see Section 6). The jet four-momentum is corrected for each event such that the direction of each topo-cluster points back to the primary hard-scattering vertex. The kinematic observables of each topo-cluster are recalculated using the vector from the primary hard-scattering vertex to the topo-cluster centroid as its direction. The raw jet four-momentum is thereafter redefined as the vector sum of the topo-cluster four-momenta. The origin-corrected pseudorapidity is called η_{origin} . This correction improves the angular resolution and results in a small improvement ($< 1\%$) in the jet p_T response. The jet energy is unaffected.

8.3 Jet energy correction

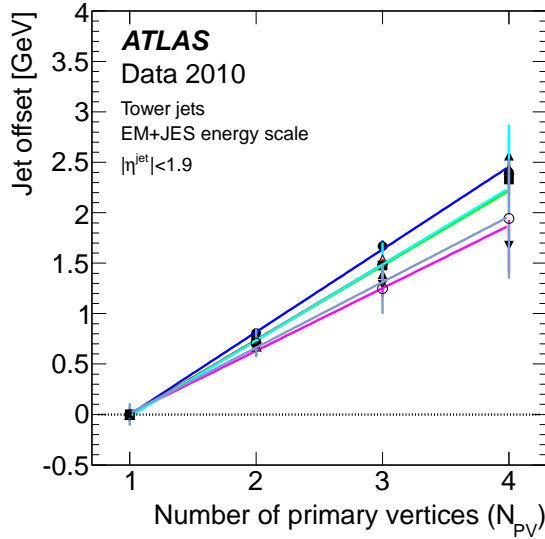
The final step of the EM+JES jet calibration restores the reconstructed jet energy to the energy of the Monte Carlo truth jet. Since pile-up effects have already been corrected for, the Monte Carlo samples used to derive the calibration do not include multiple proton-proton interactions.



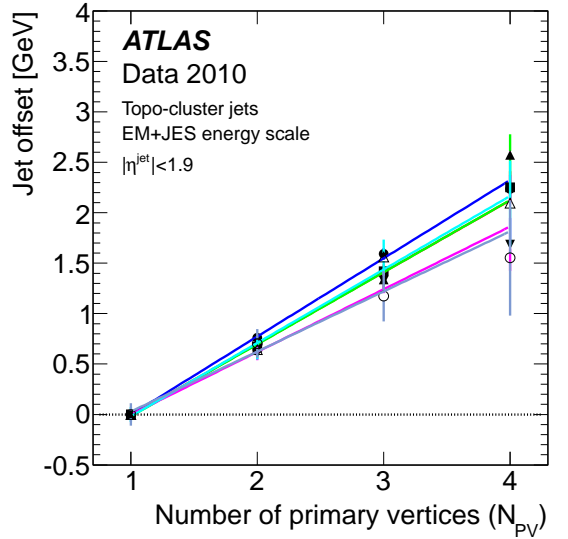
(a) Tower jet offset (EM scale)



(b) Topo-cluster jet offset (EM scale)



(c) Tower jet offset (EM+JES scale)



(d) Topo-cluster jet offset (EM+JES scale)

Fig. 8: Jet offset as a function of the number of primary vertices for several ranges of $p_T^{\text{track jet}}$ values. The track jet offset is derived for calorimeter tower jets at the EM scale (a), topo-cluster jets at the EM scale (b), calorimeter tower jets at the EM+JES scale (c), and topo-cluster jets at the EM+JES scale (d). Only statistical uncertainties from the fit results are shown.

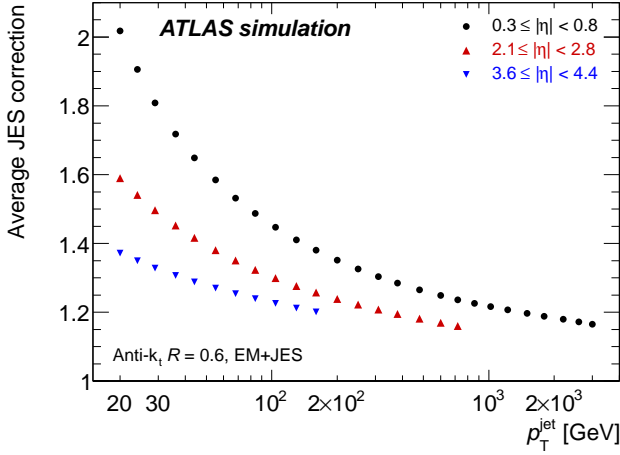


Fig. 9: Average jet energy scale correction as a function of the calibrated jet transverse momentum for three representative η -intervals obtained from the nominal Monte Carlo simulation sample. The correction is only shown over the accessible kinematic range.

The calibration is derived using all isolated calorimeter jets that have a matching isolated truth jet within $\Delta R = 0.3$. Here, an isolated jet is defined as a jet having no other jet with $p_T^{\text{jet}} > 7$ GeV within $\Delta R = 2.5R$, where R is the distance parameter of the jet algorithm. A jet is defined to be isolated, if it is isolated with respect to the same jet type, i.e. either a calorimeter or a truth jet.

The final jet energy scale calibration is first parametrised as a function of uncalibrated jet energy and η . Here the detector pseudorapidity is used rather than the origin-corrected η (used by default in physics analyses), since it more directly correspond to a region of the calorimeter. Energy is used rather than p_T , since the calorimeter responds to energy, and the response curves can be directly compared to expectation and between η bins. The method to derive this calibration is detailed below.

The EM-scale jet energy response

$$\mathcal{R}_{\text{EM}}^{\text{jet}} = E_{\text{EM}}^{\text{jet}} / E_{\text{truth}}^{\text{jet}} \quad (8)$$

for each pair of calorimeter and truth jets is measured in bins of the truth jet energy $E_{\text{truth}}^{\text{jet}}$ and the calorimeter jet detector pseudorapidity η_{det} ¹¹. For each $(E_{\text{truth}}^{\text{jet}}, \eta_{\text{det}})$ -bin, the averaged jet response $\langle \mathcal{R}_{\text{EM}}^{\text{jet}} \rangle$ is defined as the peak position of a Gaussian fit to the $E_{\text{EM}}^{\text{jet}} / E_{\text{truth}}^{\text{jet}}$ distribution. In the same $(E_{\text{truth}}^{\text{jet}}, \eta_{\text{det}})$ -bin, in addition, the average jet energy response $\langle \langle E_{\text{EM}}^{\text{jet}} \rangle \rangle$ is derived from the mean of the $E_{\text{EM}}^{\text{jet}}$ distribution. For a given η_{det} -bin k , the jet response calibration function $\mathcal{F}_{\text{calib},k}(E_{\text{EM}}^{\text{jet}})$ is obtained using a fit of the $(\langle E_{\text{EM}}^{\text{jet}} \rangle_j, \langle \mathcal{R}_{\text{EM}}^{\text{jet}} \rangle_j)$ values for each $E_{\text{truth}}^{\text{jet}}$ -bin j .

¹¹ Here, pseudorapidity refers to the original reconstructed jet before the origin correction.

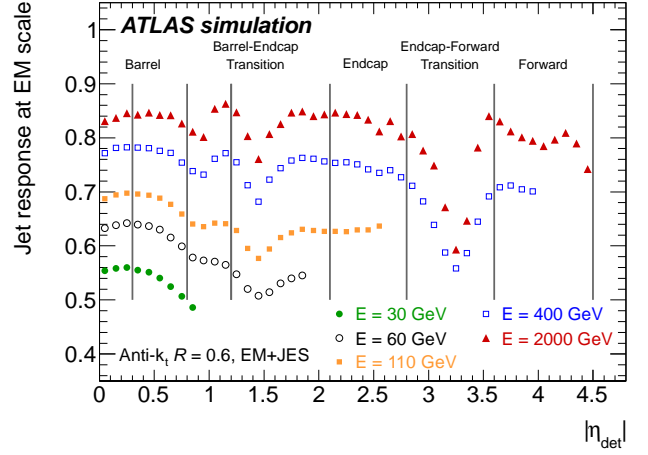


Fig. 10: Average simulated jet response ($\mathcal{R}_{\text{EM}}^{\text{jet}}$) at the electromagnetic scale in bins of EM+JES calibrated jet energy and as a function of the detector pseudorapidity η_{det} . Also shown are the η -intervals used to evaluate the JES uncertainty (see Table 2). The inverse of the response shown in each bin is equal to the average jet energy scale correction.

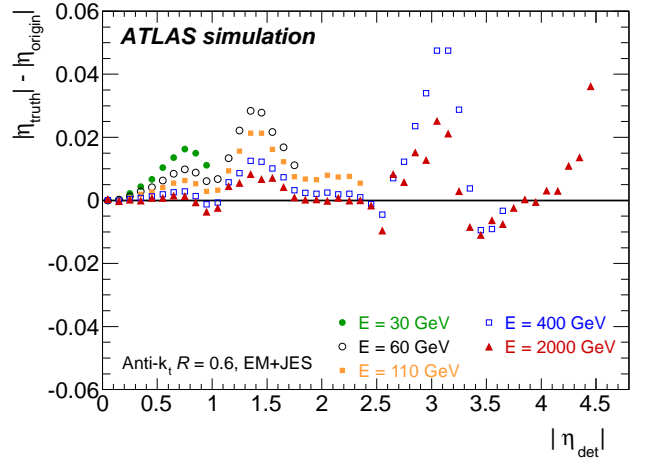


Fig. 11: Difference between the jet pseudorapidity calculated using an origin correction and the true jet pseudorapidity in bins of the calorimeter jet energy calibrated with the EM+JES scheme as a function of the detector pseudorapidity $|\eta_{\text{det}}|$.

The fitting function is parameterised as:

$$\mathcal{F}_{\text{calib},k}(E_{\text{EM}}^{\text{jet}}) = \sum_{i=0}^{N_{\text{max}}} a_i \left(\ln E_{\text{EM}}^{\text{jet}} \right)^i, \quad (9)$$

where a_i are free parameters, and N_{max} is chosen between 1 and 6 depending on the goodness of the fit.

The final jet energy scale correction that relates the measured calorimeter jet energy to the true energy is then defined as $1/\mathcal{F}_{\text{calib}}(E_{\text{EM}}^{\text{calo}})$ in the following:

$$E_{\text{EM+JES}}^{\text{jet}} = \frac{E_{\text{EM}}^{\text{jet}}}{\mathcal{F}_{\text{calib}}(E_{\text{EM}}^{\text{jet}})|_{\eta_{\text{det}}}}, \quad (10)$$

where $\mathcal{F}_{\text{calib}}(E_{\text{EM}}^{\text{jet}})|_{\eta_{\text{det}}}$ is the jet response calibration function for the relevant η_{det} -bin k .

The average jet energy scale correction $\langle 1/\mathcal{F}_{\text{calib},k}(E_{\text{calo}}^{\text{EM}}) \rangle$ is shown as a function of calibrated jet transverse momentum for three jet η -intervals in Figure 9. In this and the following figures the correction is only shown over the accessible kinematic range, i.e. values for jets above the kinematic limit are not shown.

The calorimeter jet response $\mathcal{R}_{\text{EM}}^{\text{jet}}$ is shown for various energy- and η_{det} -bins in Figure 10. The values of the jet energy correction factors range from about 2.1 at low jet energies in the central region to less than 1.2 for high energy jets in the most forward region.

8.4 Jet pseudorapidity correction

After the jet origin and energy corrections the origin-corrected jet η is further corrected for a bias due to poorly instrumented regions of the calorimeter. In these regions topo-clusters are reconstructed with a lower energy with respect to better instrumented regions (see Figure 10). This causes the jet direction to be biased towards the better instrumented calorimeter regions.

The η -correction is derived as the average difference $\Delta\eta = \eta_{\text{truth}} - \eta_{\text{origin}}$ in $(E^{\text{truth}}, \eta_{\text{det}})$ -bins, and is parameterised as a function of the calibrated jet energy $E_{\text{EM+JES}}^{\text{calo}}$ and the uncorrected η_{det} . The correction is very small ($\Delta\eta < 0.01$) for most regions of the calorimeter but larger in the transition regions. The size of the bias is illustrated as a function of the detector pseudorapidity $|\eta_{\text{det}}|$ and EM+JES calibrated jet energy in Figure 11.

9 Jet energy scale uncertainties for the EM+JES scheme

The JES systematic uncertainty is derived combining information from the single hadron response measured *in situ* and single pion test-beam measurements, uncertainties on the amount of material of the ATLAS detector, the description of the electronic noise, and the Monte Carlo modelling used in the event generation. Dedicated Monte Carlo simulation test samples are generated with different conditions with respect to the nominal Monte Carlo sample described in Section 4.3. These variations are expected to provide an estimate of the systematic effects contributing to the JES uncertainty.

The pseudorapidity bins used for the estimate of the JES uncertainty divide the ATLAS detector in the eight η -regions specified in Table 2 and Figure 10.

The JES systematic uncertainty for all jets with pseudorapidity $|\eta| > 0.8$ is determined using the JES uncertainty for the central barrel region ($0.3 \leq |\eta| < 0.8$) as a baseline, with a contribution from the relative calibration of the jets with respect to the central barrel region. This choice is motivated by the good knowledge of the detector geometry in the central region, and by the use of pion response measurements in the ATLAS combined test-beam, which used a full slice of the ATLAS barrel detector, for the estimate of the calorimeter response uncertainties. The region $0.3 \leq |\eta| < 0.8$ is the largest fully instrumented

η region	ATLAS detector regions
$ \eta < 0.3$	Central Barrel
$0.3 \leq \eta < 0.8$	
$0.8 \leq \eta < 1.2$	Barrel-Endcap Transition
$1.2 \leq \eta < 2.1$	
$2.1 \leq \eta < 2.8$	Endcap
$2.8 \leq \eta < 3.2$	
$3.2 \leq \eta < 3.6$	Endcap-Forward Transition
$3.6 \leq \eta < 4.5$	
	Forward

Table 2: Detector regions used for the JES uncertainty estimate.

$|\eta|$ region considered where combined test-beam results, used to estimate the calorimeter uncertainty, are available for the entire pseudorapidity range.

This section describes the sources of systematic uncertainties and their effect on the response of EM+JES calibrated jets. In Section 9.1, the selection of jets used to derive Monte Carlo based components of the JES systematic uncertainty is discussed. The contributions to the JES systematics due to the following effects are then described:

1. JES calibration method (Section 9.2).
2. Calorimeter response (Section 9.3).
3. Detector simulation (Section 9.4).
4. Physics model and parameters employed in the Monte Carlo event generator (Section 9.5).
5. Relative calibration for jets with $|\eta| > 0.8$ (Section 9.6).
6. Additional proton-proton collisions (pile-up) (Section 9.7).

Section 9.8 discusses how the final uncertainties are calculated. Additional uncertainties such as those for close-by jets are mentioned in Section 9.9 and discussed in more detail in Section 17.

9.1 Jet response definition for the JES uncertainty evaluation

The components of the JES uncertainty derived from Monte Carlo samples are obtained by studying the average calorimeter energy response of calibrated jets. The average energy or p_{T} response, defined as

$$\langle \mathcal{R}^{\text{jet}} \rangle = \langle E^{\text{jet}}/E^{\text{truth}} \rangle \text{ or } \langle \mathcal{R}(p_{\text{T}}^{\text{jet}}) \rangle = \langle p_{\text{T}}^{\text{jet}}/p_{\text{T}}^{\text{truth}} \rangle, \quad (11)$$

is obtained as the peak position from a Gaussian fit to the distribution of the ratio of the kinematic quantities for reconstructed and truth jets by matching isolated calorimeter jets to Monte Carlo truth jets as described in Section 8.3, but without the isolation cut for truth jets¹². This is done separately for the nominal and each of the alternative Monte Carlo samples. Only MC truth jets with $p_{\text{T}}^{\text{truth}} > 15$ GeV, and calorimeter jets with $p_{\text{T}}^{\text{jet}} > 7$ GeV after calibration, are considered. The calibrated

¹² The isolation cut for truth jets on the average jet response has a negligible impact on the average jet response given that truth jets are matched to isolated reconstructed jets.

response $\langle \mathcal{R}^{\text{jet}} \rangle$ is studied in bins of the truth jet transverse momentum p_T^{truth} . For each p_T^{truth} -bin, an associated calibrated p_T value is calculated by multiplying the bin centre with the average response.

The shifts between the Monte Carlo truth level p_T^{truth} bin centres and the reconstructed p_T^{jet} bin centres are negligible with respect to the chosen p_T bin widths. Hence the average jet response can be obtained to a good approximation as a function of p_T^{jet} .

9.2 Uncertainty in the JES calibration

After the jets in the nominal jet Monte Carlo simulation sample are calibrated (see Section 8), the jet energy and p_T response still show slight deviations from unity at low p_T (non-closure). This can be seen in Figure 12, showing the jet response for p_T and energy as a function of p_T^{jet} for the nominal Monte Carlo sample in the barrel (a) and endcap (b) and the most forward (c) regions for anti- k_t jets with $R = 0.6$.

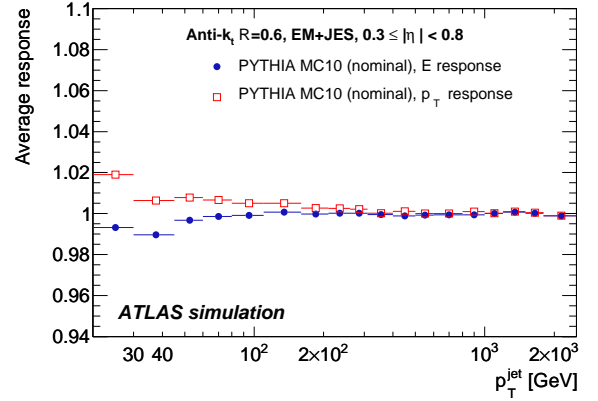
Any deviation from unity in the jet energy or p_T response after the application of the JES to the nominal Monte Carlo sample implies that the kinematic observables of the calibrated calorimeter jet are not restored to that of the corresponding truth jet (non-closure). Besides approximations made when deriving the calibration (fit quality, parametrisation of calibration curve), the non-closure is due to the application of the same correction factor for energy and transverse momentum. Closure can therefore only be achieved if the reconstructed jet mass is close to the true jet mass. If this is not the case, such as for low p_T jets, restoring only the jet energy and pseudorapidity will lead to a bias in the p_T calibration. The non-closure is also affected by jet resolution and by details how the Monte Carlo samples are produced in order to cover the large kinematic range in jet transverse momentum.

The systematic uncertainty due to the non-closure of the nominal JES calibration is taken as the larger deviation of the response in either energy or p_T from unity. In the barrel region ($0.3 \leq |\eta| < 0.8$) this contribution amounts to about 2% at low p_T^{jet} and less than 1% for $p_T^{\text{jet}} > 30$ GeV. In the endcap and forward regions, the closure is less than 1% for $p_T^{\text{jet}} > 20$ GeV, and the energy response is within 1% for jets with transverse momentum above 30 GeV. The deviation of the jet response from unity after calibration is taken as a source of systematic uncertainty.

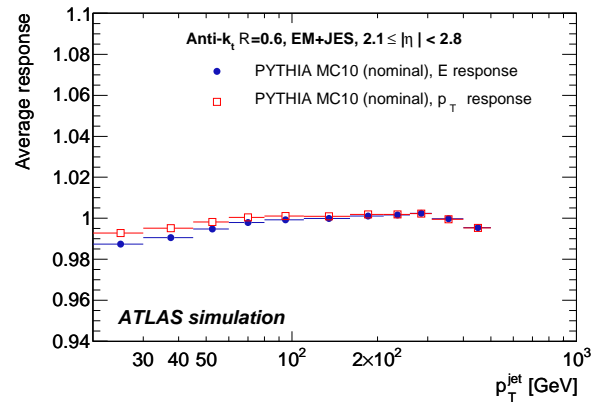
For physics analysis the non-closure uncertainty only needs to be considered when an absolute jet energy or transverse momentum is needed. For analyses where only the description of the data by the Monte Carlo simulation is important, this uncertainty does not need to be considered.

9.3 Uncertainty on the calorimeter response

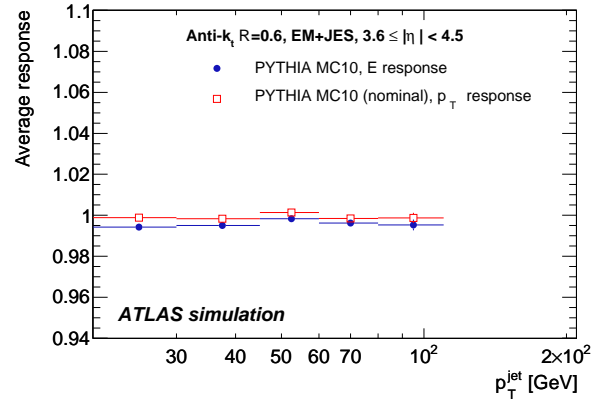
The response and corresponding uncertainties for single particles interacting in the ATLAS calorimeters can be used to derive the jet energy scale uncertainty in the central calorimeter region as detailed in Ref. [49, 58].



(a) $0.3 \leq |\eta| < 0.8$

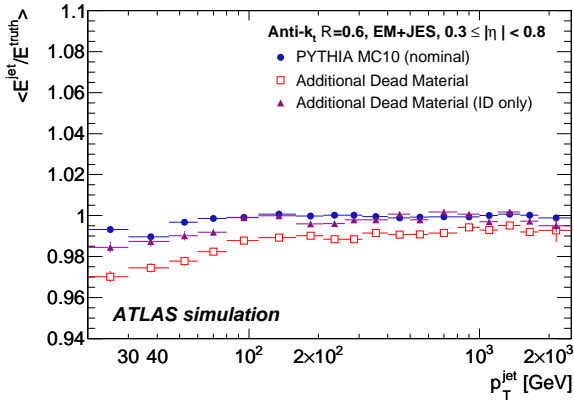


(b) $2.1 \leq |\eta| < 2.8$

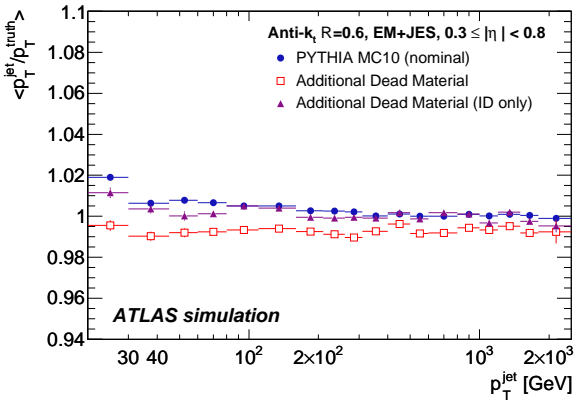


(c) $3.6 \leq |\eta| < 4.5$

Fig. 12: Average simulated jet p_T response (open squares) after the EM+JES calibration and jet energy response (full circles) as a function of p_T^{jet} for the nominal Monte Carlo sample for jets in the central (a), endcap (b) and most forward (c) calorimeter regions. Systematic uncertainties are not shown. Statistical uncertainties are smaller than the marker size.



(a) Energy response



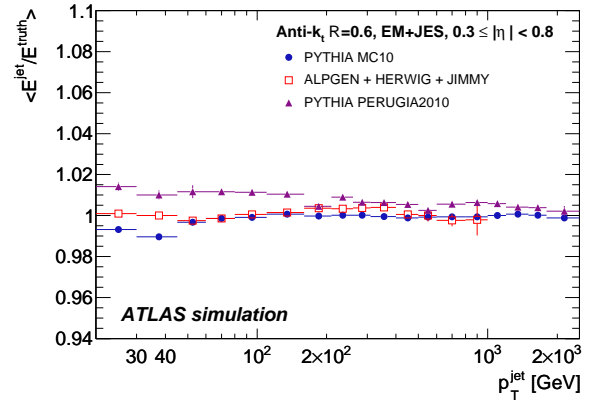
(b) Transverse momentum response

Fig. 13: Average simulated jet response in energy (a) and in p_T (b) as a function of p_T^{jet} in the central region ($0.3 \leq |\eta| < 0.8$) in the case of additional dead material in the inner detector (full triangles) and in both the inner detector and the calorimeters (open squares). The response within the nominal Monte Carlo sample is shown for comparison (full circles). Only statistical uncertainties are shown.

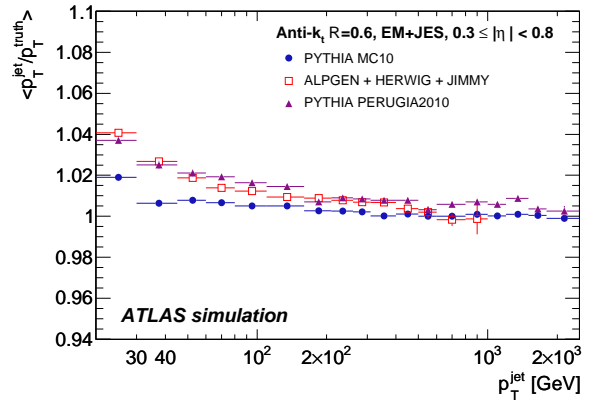
In the ATLAS simulation infrastructure the true calorimeter energy deposits in each calorimeter cell can be traced to the particles generated in the collision. The uncertainty in the calorimeter response to jets can then be obtained from the response uncertainty in the individual particles constituting the jet. The *in situ* measurement of the single particle response detailed in Ref. [49] significantly reduces the uncertainty due to the limited knowledge of the exact detector geometry, in particular that due to the presence of additional dead material, and the modelling of the exact way particles interact in the detector.

The following single particle response measurements are used:

1. The single hadron energy measured in a cone around an isolated track with respect to the track momentum (E/p) in the momentum range from $0.5 \leq p^{\text{track}} < 20$ GeV.
2. The pion response measurements performed in the 2004 combined test-beam, where a full slice of the ATLAS de-



(a) Energy response



(b) Transverse momentum response

Fig. 14: Average simulated response in energy (a) and in p_T (b) as a function of p_T^{jet} in the central region ($0.3 \leq |\eta| < 0.8$) for ALPGEN+HERWIG+JIMMY (open squares) and PYTHIA with the PERUGIA2010 tune (full triangles). The response of the nominal Monte Carlo simulation sample is shown for comparison (full circles). Only statistical uncertainties are shown.

tector was exposed to pion beams with momenta between 20 GeV and 350 GeV [45].

Uncertainties for charged hadrons are estimated from these measurements as detailed in Ref. [49]. Additional uncertainties are related to:

1. The calorimeter acceptance for low p_T particles that do not reach the calorimeter or are not reconstructed in a topo-cluster due to the noise thresholds.
2. Calorimeter response to particles with $p > 400$ GeV for which the uncertainty is conservatively estimated as 10%, to account for possible calorimeter non-linearities and longitudinal leakage.
3. The baseline absolute electromagnetic scale for the hadronic and electromagnetic calorimeters for particles in the kinematic range not measured *in situ*.
4. The calorimeter response to neutral hadrons is estimated by comparing various models in GEANT4. An uncertainty of 10% for particles with an energy $E < 3$ GeV and 5% for higher energies is obtained.

At high transverse momentum, the dominant contribution to the calorimeter response uncertainties is due to particles with momenta covered by the test-beam. In the pseudorapidity range $0 \leq |\eta| < 0.8$ the shift of the relative jet energy scale expected from the single hadron response measurements in the test-beam is up to $\approx 1\%$, and the uncertainty on the shift is from 1% to 3%. The total envelope (the shift added linearly to the uncertainty) of about 1.5 – 4%, depending on the jet transverse momentum, is taken as the relative JES calorimeter uncertainty. The calorimeter uncertainty is shown in Figure 23.

9.4 Uncertainties due to the detector simulation

9.4.1 Calorimeter cell noise thresholds

As described in Section 6.1.1, topo-clusters are constructed based on the signal-to-noise ratio of calorimeter cells, where the *noise* is defined as the RMS of the measured cell energy distribution in events with no energy depositions from collision events. Discrepancies between the simulated noise and the real noise in data can lead to differences in the cluster shapes and to the presence of fake topo-clusters. For data, the noise can change over time¹³, while the noise RMS used in the simulation is fixed at the time of the production of the simulated data sets. These effects can lead to biases in the jet reconstruction and calibration, if the electronic noise injected in the Monte Carlo simulation does not reflect that data.

The effect of the calorimeter cell noise mis-modelling on the jet response is estimated by reconstructing topo-clusters, and thereafter jets, in Monte Carlo using the noise RMS measured from data. The actual energy and noise simulated in the Monte Carlo are left unchanged, but the values of the thresholds used to include a given calorimeter cell in a topo-cluster are shifted according to the cell noise RMS measured in data. The response for jets reconstructed with the modified noise thresholds are compared with the response for jets reconstructed in exactly the same sample using the default Monte Carlo noise thresholds.

To further understand the effect of the noise thresholds on the jet response, the noise thresholds were shifted. An increase of each calorimeter cell threshold by 7% in the Monte Carlo simulation is found to give a similar shift in the jet response as using the noise RMS from data. Raising and lowering the cell thresholds by 7% shows that the effect on the jet response from varying the cell noise thresholds is symmetric. This allows the use of the calorimeter cell noise thresholds derived from data as a representative sample to determine the jet energy scale uncertainty and covers the cases when the data have either more or less noise than the simulation.

The maximal observed change in jet response is used to estimate the uncertainty on the jet energy measurement due to the calorimeter cell noise modelling. It is found to be below 3% for the whole pseudorapidity range, and negligible for jets with transverse momenta above 45 GeV. The uncertainties assigned to jets with transverse momenta below 45 GeV are:

- 1% and 2% for $20 \leq p_T^{\text{jet}} < 30$ GeV for anti- k_t jets with $R = 0.4$ and $R = 0.6$ jets, respectively,
- 1% for $30 \leq p_T^{\text{jet}} < 45$ GeV for both R values.

9.4.2 Additional detector material

The jet energy scale is affected by possible deviations in the material description as the jet energy scale calibration has been derived to restore the energy lost assuming a geometry as simulated in the nominal Monte Carlo sample. Simulated detector geometries that include systematic variations of the amount of material have been designed using test-beam measurements [12], in addition to 900 GeV and 7 TeV data [52, 53, 59]. The possible additional material amount is estimated from these *in situ* measurements and the *a priori* knowledge of the detector construction. Specific Monte Carlo simulation samples have been produced using these distorted geometries.

In the case of uncertainties derived with *in situ* techniques, such as those coming from the single hadron response measurements detailed in Section 9.3, most of the effects on the jet response due to additional dead material do not apply, because *in situ* measurements do not rely on any simulation where the material could be misrepresented. However, the quality criteria of the track selection for the single hadron response measurement effectively only allow particles that have not interacted in the Pixel and SCT layers of the inner detector to be included in the measurement.

Therefore the effect of dead material in these inner detector layers on the jet response needs to be taken into account for particles in the momentum range of the single hadron response measurement. This is achieved using a specific Monte Carlo sample where the amount of material is systematically varied by adding 5% of material to the existing inner detector services [19]. The jet response in the two cases is shown in Figure 13.

Electrons, photons, and hadrons with momenta $p > 20$ GeV are not included in the single hadron response measurements and therefore there is no estimate based on *in situ* techniques for the effect of any additional material in front of the calorimeters. This uncertainty is estimated using a dedicated Monte Carlo simulation sample where the overall detector material is systematically varied within the current uncertainties [19] on the detector geometry. The overall changes in the detector geometry include:

1. The increase in the inner detector material mentioned above.
2. An extra 0.1 radiation length (X_0) in the cryostat in front of the barrel of the electromagnetic calorimeter ($|\eta| < 1.5$).
3. An extra 0.05 X_0 between the presampler and the first layer of the electromagnetic calorimeter.
4. An extra 0.1 X_0 in the cryostat after the barrel of the electromagnetic calorimeter.
5. Extra material in the barrel-endcap transition region in the electromagnetic calorimeter ($1.37 < |\eta| < 1.52$).

The uncertainty contribution due to the overall additional detector material is estimated by comparing the EM+JES jet response in the nominal Monte Carlo simulation sample with the jet response in a Monte Carlo simulation sample with a distorted geometry (see Figure 13), and scaled by the average energy fraction of electrons, photons and high transverse momentum hadrons within a jet as a function of p_T .

¹³ Time-dependent noise changes for single cells in data are accounted for using regular measurements.

9.5 Uncertainties due to the event modelling in Monte Carlo generators

The contributions to the JES uncertainty from the modelling of the fragmentation, the underlying event and other choices in the event modelling of the Monte Carlo event generator are obtained from samples based on ALPGEN+HERWIG+JIMMY and the PYTHIA PERUGIA2010 tune discussed in Section 4.

By comparing the baseline PYTHIA Monte Carlo sample to the PYTHIA PERUGIA2010 tune, the effects of soft physics modelling are tested. The PERUGIA2010 tune provides, in particular, a better description of the internal jet structure recently measured with ATLAS [3]. The ALPGEN Monte Carlo uses different theoretical models for all steps of the event generation and therefore gives a reasonable estimate of the systematic variations. However, the possible compensation of modelling effects that shift the jet response in opposite directions cannot be excluded.

Figure 14 shows the calibrated jet kinematic response for the two Monte Carlo generators and tunes used to estimate the effect of the Monte Carlo theoretical model on the jet energy scale uncertainty. The kinematic response for the nominal sample is shown for comparison. The ratio of the nominal response to that for each of the two samples is used to estimate the systematic uncertainty to the jet energy scale, and the procedure is further detailed in Section 9.8.

9.6 *In situ* intercalibration using events with dijet topologies

The response of the ATLAS calorimeters to jets depends on the jet direction, due to the different calorimeter technology and to the varying amounts of dead material in front of the calorimeters. A calibration is therefore needed to ensure a uniform calorimeter response to jets. This can be achieved by applying correction factors derived from Monte Carlo simulations. Such corrections need to be validated *in situ* given the non-compensating nature of the calorimeters in conjunction with the complex calorimeter geometry and material distribution.

The relative jet calorimeter response and its uncertainty is studied by comparing the transverse momenta of a well-calibrated central jet and a jet in the forward region in events with only two jets at high transverse momenta (dijets). Such techniques have been applied in previous hadron collider experiments [60, 61].

9.6.1 Intercalibration method using a fixed central reference region

The traditional approach for η -intercalibration with dijet events is to use a fixed central region of the calorimeters as the reference region. The relative calorimeter response to jets in other calorimeter regions is then quantified by the p_T balance between the reference jet and the probe jet, exploiting the fact that these jets are expected to have equal p_T due to transverse momentum conservation. The p_T balance can be characterised

by the asymmetry \mathcal{A} , defined as

$$\mathcal{A} = \frac{p_T^{\text{probe}} - p_T^{\text{ref}}}{p_T^{\text{avg}}}, \quad (12)$$

with $p_T^{\text{avg}} = (p_T^{\text{probe}} + p_T^{\text{ref}})/2$. The reference region is chosen as the central region of the barrel: $|\eta| < 0.8$. If both jets fall into the reference region, each jet is used, in turn, as the reference jet. As a consequence, the average asymmetry in the reference region will be zero by construction.

The asymmetry is then used to measure an η -intercalibration factor c for the probe jet, or its response relative to the reference jet $1/c$, using the relation

$$\frac{p_T^{\text{probe}}}{p_T^{\text{ref}}} = \frac{2 + \mathcal{A}}{2 - \mathcal{A}} = 1/c. \quad (13)$$

The asymmetry distribution is calculated in bins of jet η_{det} and p_T^{avg} . The bins are labeled i for each probe jet η_{det} and k for each p_T^{avg} -bin. Intercalibration factors are calculated for each bin according to Equation (13):

$$c_{ik} = \frac{2 - \langle \mathcal{A}_{ik} \rangle}{2 + \langle \mathcal{A}_{ik} \rangle}, \quad (14)$$

where the $\langle \mathcal{A}_{ik} \rangle$ is the mean value of the asymmetry distribution in each bin. The uncertainty on $\langle \mathcal{A}_{ik} \rangle$ is taken to be the RMS/\sqrt{N} of each distribution, where N is the number of events per bin.

9.6.2 Intercalibration using the matrix method

A disadvantage with the method outlined above is that all events are required to have a jet in the central reference region. This results in a significant loss of event statistics, especially in the forward region, where the dijet cross section drops steeply as the rapidity interval between the jets increases. In order to use the full event statistics, the default method can be extended by replacing the “probe” and “reference” jets by “left” and “right” jets defined as $\eta^{\text{left}} < \eta^{\text{right}}$. Equations (12) and (13) then become:

$$\mathcal{A} = \frac{p_T^{\text{left}} - p_T^{\text{right}}}{p_T^{\text{avg}}} \quad \text{and} \quad \mathcal{R}_{lr} = \frac{p_T^{\text{left}}}{p_T^{\text{right}}} = \frac{c^{\text{right}}}{c^{\text{left}}} = \frac{2 + \mathcal{A}}{2 - \mathcal{A}}, \quad (15)$$

where the term \mathcal{R} denotes the ratio of the responses, and c^{left} and c^{right} are the η -intercalibration factors for the left and right jets, respectively.

In this approach there is a response ratio distribution, \mathcal{R}_{ijk} , whose average value $\langle \mathcal{R}_{ijk} \rangle$ is evaluated for each η^{left} -bin i , η^{right} -bin j and p_T^{avg} -bin k . The relative correction factor c_{ik} for a given jet η -bin i and for a fixed p_T^{avg} -bin k , is obtained by minimising a matrix of linear equations:

$$S(c_{1k}, \dots, c_{Nk}) = \sum_{j=1}^N \sum_{i=1}^{j-1} \left(\frac{1}{\Delta \langle \mathcal{R}_{ijk} \rangle} (c_{ik} \langle \mathcal{R}_{ijk} \rangle - c_{jk}) \right)^2 + X(c_{ik}), \quad (16)$$

where N denotes the number of η -bins, $\Delta \langle \mathcal{R}_{ijk} \rangle$ is the statistical uncertainty of $\langle \mathcal{R}_{ijk} \rangle$ and the function $X(c_{ik})$ is used to quadratically suppress deviations from unity of the average corrections¹⁴. Note that if the jet response does not vary with η , then the relative response will be unity for each $(\eta_{\text{left}}, \eta_{\text{right}})$ -bin combination (see Equation 15). A perfect minimization $S = 0$ is achieved when all correction factors equal unity.

The minimisation of Equation 16 is done separately for each $p_{\text{T}}^{\text{avg}}$ -bin k , and the resulting calibration factors c_{ik} (for each jet η -bin i) are scaled such that the average calibration factor in the reference region $|\eta| < 0.8$ equals unity.

9.6.3 Selection of dijet events

Events are retained if there were at least two jets above the jet reconstruction threshold of $p_{\text{T}}^{\text{jet}} > 7$ GeV. The event is rejected if either of the two leading jets did not satisfy the standard jet selection criteria (see Section 7).

Events are required to satisfy a specific logic using one central and one forward jet trigger, which select events based on jet activity in the central ($|\eta| < 3.2$) and forward ($|\eta| > 3.2$) trigger regions, respectively [10]. The requirements are chosen such that the trigger efficiency, for a specific region of $p_{\text{T}}^{\text{avg}}$, was greater than 99% and approximately flat as a function of the pseudorapidity of the probe jet.

To cover the region $p_{\text{T}}^{\text{avg}} < 45$ GeV, events triggered by the minimum bias trigger scintillators were used. To enhance events which have only two jets at high p_{T} , the following selection criteria are applied;

$$p_{\text{T}}^{\text{avg}} > 20 \text{ GeV}, \quad \Delta\phi(j_1, j_2) > 2.6 \text{ rad}, \quad (17)$$

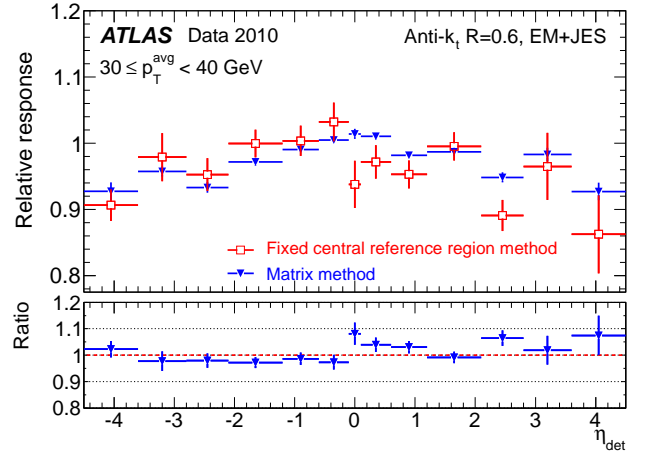
$$p_{\text{T}}(j_3) < \max(0.15 p_{\text{T}}^{\text{avg}}, 7 \text{ GeV}), \quad (18)$$

where j_i denotes the i^{th} highest p_{T} jet in the event and $\Delta\phi(j_1, j_2)$ is the azimuthal angle between the two leading jets.

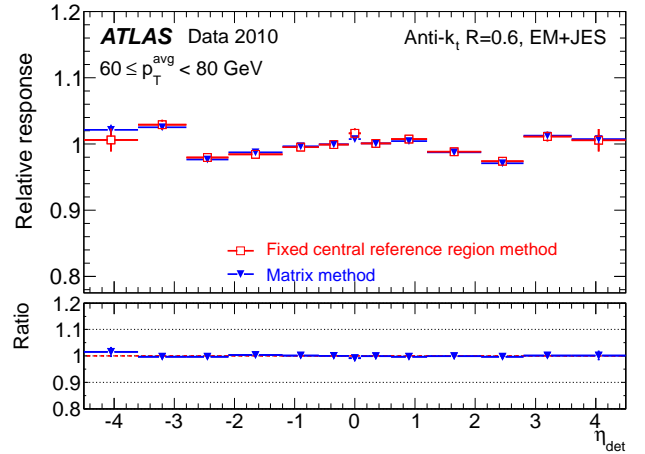
The lowest $p_{\text{T}}^{\text{avg}}$ -bins are likely to suffer from biases. At very low $p_{\text{T}}^{\text{avg}}$, it is expected that this technique may not measure accurately the relative response to jets, because the assumption of dijet balance at hadron level may start to fail. First, there are residual low- p_{T} jet effects since the selection criterion on the third jet, which is used to suppress the unbalancing effects of soft QCD radiation, is not as efficient due to the jet reconstruction threshold of 7 GeV. Second, the jet reconstruction efficiency is worse for low- p_{T} jets.

9.6.4 Comparison of intercalibration methods

The relative jet response obtained with the matrix method is compared to the relative jet response obtained using the method with a fixed reference region. Figure 15 shows the jet response relative to central jets ($1/c$) for two $p_{\text{T}}^{\text{avg}}$ -bins, $30 \leq p_{\text{T}}^{\text{avg}} < 40$



(a) $30 \leq p_{\text{T}}^{\text{avg}} < 40$ GeV



(b) $60 \leq p_{\text{T}}^{\text{avg}} < 80$ GeV

Fig. 15: Relative response of anti- k_t jets with $R = 0.6$ calibrated with the EM+JES scheme, $1/c$, as a function of the pseudorapidity measured using the matrix and fixed central reference region η -intercalibration methods. Results are presented for two bins of $p_{\text{T}}^{\text{avg}}$: $30 \leq p_{\text{T}}^{\text{avg}} < 40$ GeV measured in minimum bias data (a), and $60 \leq p_{\text{T}}^{\text{avg}} < 80$ GeV measured in data collected using jet triggers (b). The lower part of the figures shows the ratio of the two methods. The central reference region is $0.1 \leq |\eta| < 0.6$. Only statistical uncertainties are shown.

40 GeV and $60 \leq p_{\text{T}}^{\text{avg}} < 80$ GeV. These results are obtained for a reference region $0.1 \leq |\eta| < 0.6$ and therefore not directly comparable to the results discussed below where $0.1 \leq |\eta| < 0.8$ is used.

The response observed using the fixed reference region method is compatible with those obtained using the matrix method¹⁵. These results are representative of all the phase space regions studied in this analysis and the matrix method is therefore

¹⁴ $X(c_{ik}) = K \left(N_{\text{bins}}^{-1} \sum_{i=1}^{N_{\text{bins}}} c_{ik} - 1 \right)^2$ is defined with K being a constant and N_{bins} being the number of η -bins (number of indices i). This term prevents the minimisation from choosing the trivial solution: all c_{ik} equal to zero. The value of the constant K does not impact the solution as long as it is sufficiently large ($K \approx 10^6$).

¹⁵ As discussed in Section 9.6.3, even for an ideal detector the asymmetry, and hence the relative response, is not expected to be exactly flat due to the effects of soft QCD radiation and other soft particle activities.

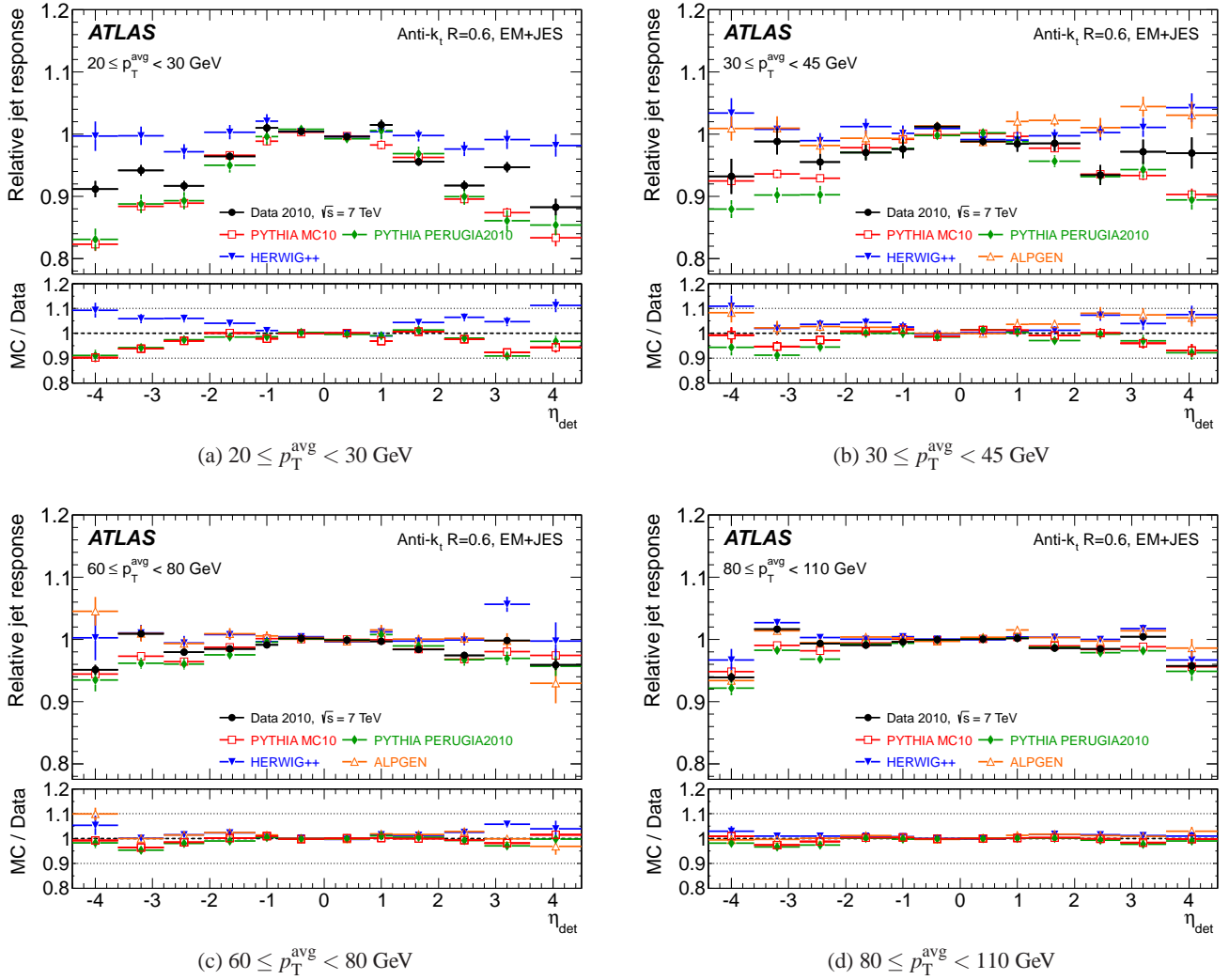


Fig. 16: Relative jet response, $1/c$, of anti- k_t jets with $R = 0.6$ as a function of the jet pseudorapidity measured using the matrix η -intercalibration method in bins of the average p_T of the two leading jets (a) $20 \leq p_T^{\text{avg}} < 30$ GeV, (b) $30 \leq p_T^{\text{avg}} < 45$ GeV, (c) $60 \leq p_T^{\text{avg}} < 80$ GeV and $80 \leq p_T^{\text{avg}} < 110$ GeV. The lower part of each figure shows the ratio of Monte Carlo simulation to data. Only statistical uncertainties are shown.

used to give the final uncertainty on the *in situ* η -intercalibration due to its higher statistical precision.

9.6.5 Comparison of data with Monte Carlo simulation

Figure 16 shows the relative response obtained with the matrix method as a function of the jet pseudorapidity for data and Monte Carlo simulations in four p_T^{avg} regions.

The response in data is reasonably well reproduced by the Monte Carlo simulations for $p_T^{\text{jet}} > 60$ GeV, with the Monte Carlo simulation and data agreeing typically better than 2% in the central region ($|\eta| < 2.8$) and 5–10% (depending on p_T^{avg}) in the forward region ($|\eta| > 2.8$). At lower values of p_T , the data do not agree as well with the Monte Carlo simulations and the Monte Carlo simulations themselves show a large spread around the data. For $20 \leq p_T^{\text{avg}} < 30$ GeV, the Monte Carlo sim-

ulation deviates from the data by about 10% for $|\eta| > 2.8$, with the different Monte Carlo simulations predicting both higher and lower relative responses than that observed in the data.

The main differences, due to residual low- p_T jet effects (see Section 9.6.3), occur between PYTHIA with the MC10 or the PERUGIA tune on one side and ALPGEN/HERWIG++ on the other. The differences therefore apparently reflect a difference in physics modelling between the event generators.

Figure 17 shows the relative response as a function of p_T^{avg} . The distributions are shown for jets in the region $1.2 \leq |\eta| < 2.1$ and also for those in the region $3.6 \leq |\eta| < 4.5$. Again, the response is reasonably well described by the Monte Carlo simulation for all calorimeter regions at high p_T and the more central region at low p_T .

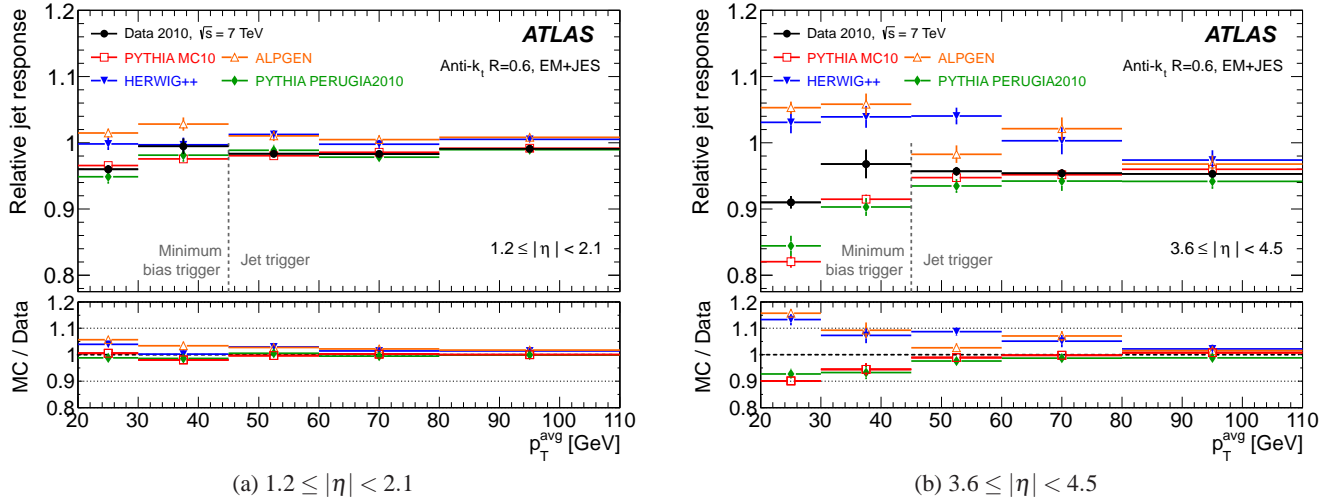


Fig. 17: Relative jet response, $1/c$, of anti- k_t jets with $R = 0.6$ as a function of p_T^{avg} found using the matrix η -intercalibration method for (a) $1.2 \leq |\eta| < 2.1$ and (b) $3.6 \leq |\eta| < 4.5$. For $p_T^{\text{avg}} < 45$ GeV, the data are collected using the minimum bias trigger stream. For $p_T^{\text{avg}} > 45$ GeV, the data are collected using the calorimeter trigger stream. The lower part of each figure shows the ratio of Monte Carlo simulation to data. Only statistical uncertainties are shown.

9.6.6 Total uncertainties in the forward region

The Monte Carlo simulation predictions for the relative jet response diverge at low values of p_T^{avg} . The data themselves lie between the different predictions. The uncertainty on the relative jet response must reflect this disagreement because there is no *a priori* reason to believe one theoretical prediction over another.

The uncertainty on the relative response is taken to be the RMS deviation of the Monte Carlo predictions from the data. At high p_T , where the spread of Monte Carlo simulation predictions is small, the uncertainty mainly reflects the true difference between the response in data and simulation. At low p_T and large $|\eta|$, the uncertainty mainly reflects the physics modelling uncertainty, although the detector-based differences between data and simulation are also accounted for. Other uncertainty sources, such as trigger selection or the QCD radiation suppression using the third jet, are either negligible, or included in the total uncertainty assigned from the spread of Monte Carlo predictions around the data.

Figure 18 shows the uncertainty in the jet response, relative to jets in the central region $|\eta| < 0.8$, as a function of the jet p_T and $|\eta|$. The JES uncertainty, determined in the central detector region using the single particle response and systematic variations of the Monte Carlo simulations, is transferred to the forward regions using the results from the dijet balance. These uncertainties are included in the final uncertainty as follows:

1. The total JES uncertainty in the central region $0.3 \leq |\eta| < 0.8$ is kept as a baseline.
2. The uncertainty from the relative intercalibration is taken as the RMS deviation of the MC predictions from the data and is added in quadrature to the baseline uncertainty.

The measurements are performed for transverse momenta in the range $20 \leq p_T^{\text{avg}} < 110$ GeV. The uncertainty for jets with

$p_T > 100$ GeV is taken as the uncertainty of the last available p_T -bin¹⁶. The uncertainties are evaluated separately for jets reconstructed with distance parameters $R = 0.4$ and $R = 0.6$, and are in general found to be slightly larger for $R = 0.4$.

Figure 19 shows the relative jet response, and the associated intercalibration uncertainty calculated as detailed above, as a function of jet $|\eta|$ for two representative p_T^{avg} -bins.

9.7 Uncertainties due to multiple proton-proton collisions

The offset to the jet transverse energy due to pile-up interactions can be measured at the EM scale from the average energy in calorimeter towers in minimum bias events. The uncertainty in the pile-up corrections can be obtained by varying certain analysis choices and by studying the jet response with respect to the transverse momentum of track jets as a function of the number of primary vertices.

9.7.1 Tower-based offset closure test using track jets

The systematic uncertainty in the jet offset correction can be evaluated using track jets. Figure 8 shows the variation of the offset among the various ranges of $p_T^{\text{track jet}}$. The result indicates a systematic uncertainty on the correction of approximately $\delta(\mathcal{O}_{\text{track jet}}^{\text{EM}}) < 100$ MeV per additional vertex at the EM scale and $\delta(\mathcal{O}_{\text{track jet}}^{\text{EM+JES}}) < 200$ MeV per additional vertex at the EM+JES scale. Since the jet pile-up offset was about 500 MeV

¹⁶ This is justified by the decrease of the intercalibration uncertainty with p_T , but cannot completely exclude the presence of calorimeter non-linearities for jet energies above those used for the intercalibration.

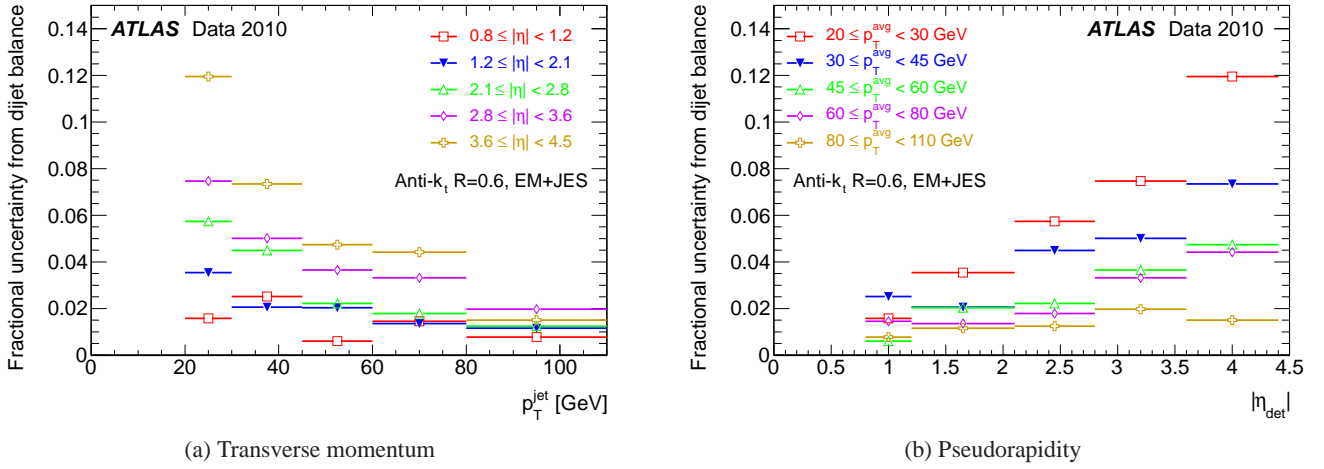


Fig. 18: Fractional response uncertainty for anti- k_t jets with $R = 0.6$ calibrated with the EM+JES scheme as obtained from the dijet balance *in situ* technique as a function of p_T^{jet} for various $|\eta|$ -regions of the calorimeter (a) and as a function of $|\eta|$ in various p_T^{jet} bins (b).

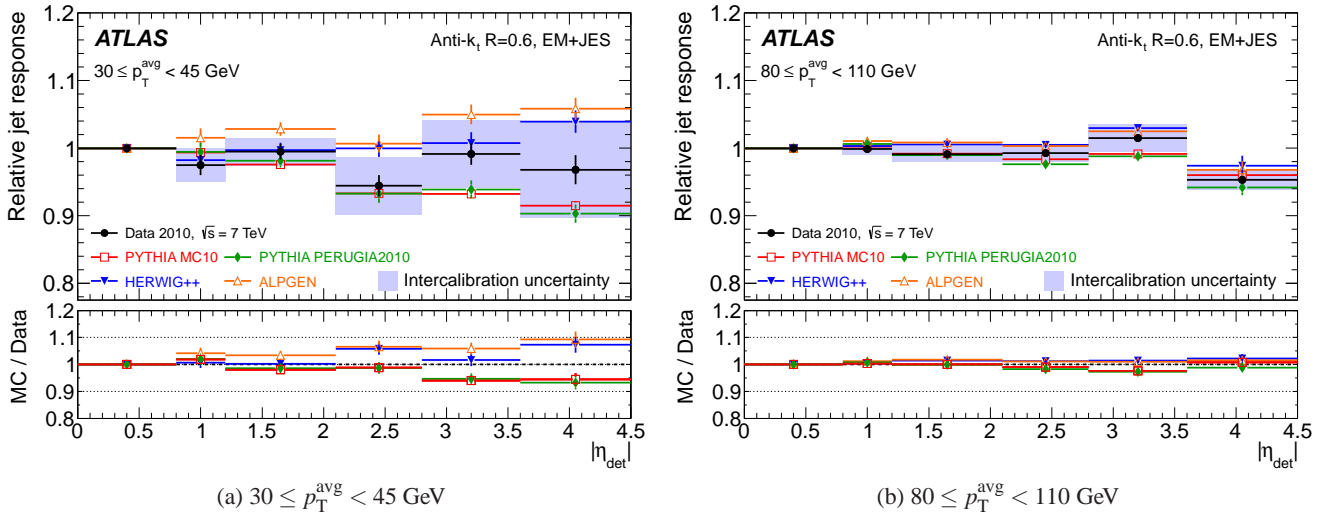


Fig. 19: Average jet response for anti- k_t jets with $R = 0.6$ calibrated with the EM+JES scheme measured relative to a central reference jet within $|\eta| < 0.8$ in data and various Monte Carlo generator samples as a function of $|\eta|$ for p_T^{avg} in the ranges 30 – 45 GeV (a) and 80 – 110 GeV (b). The resulting systematic uncertainty component is shown as a shaded band around the data points. The errors bars on the data points only show the statistical uncertainties.

Systematic	Tower-based offset	Jet-based offset	Comments
Trigger selection	16%	16%	MBTS vs Jet triggers
Tower multiplicity variation	—	20%	$\langle N_{\text{towers}}^{\text{jet}} \rangle$ vs $p_T^{\text{track jet}}$ and N_{PV}
$p_T^{\text{track jet}}$ variation	21%	22%	Variation of 100 MeV/vertex
Total (quadrature sum)	26%	34%	Assumes uncorrelated errors
Result from closure test	2%	35%	Determined from average

Table 3: Summary of systematic uncertainties associated with the offset correction for both the tower-based offset applied jet-by-jet to tower jets and the jet-level offset applied to topo-cluster jets. The uncertainty is expressed as a percentage of the average offset correction, shown in Table 4.

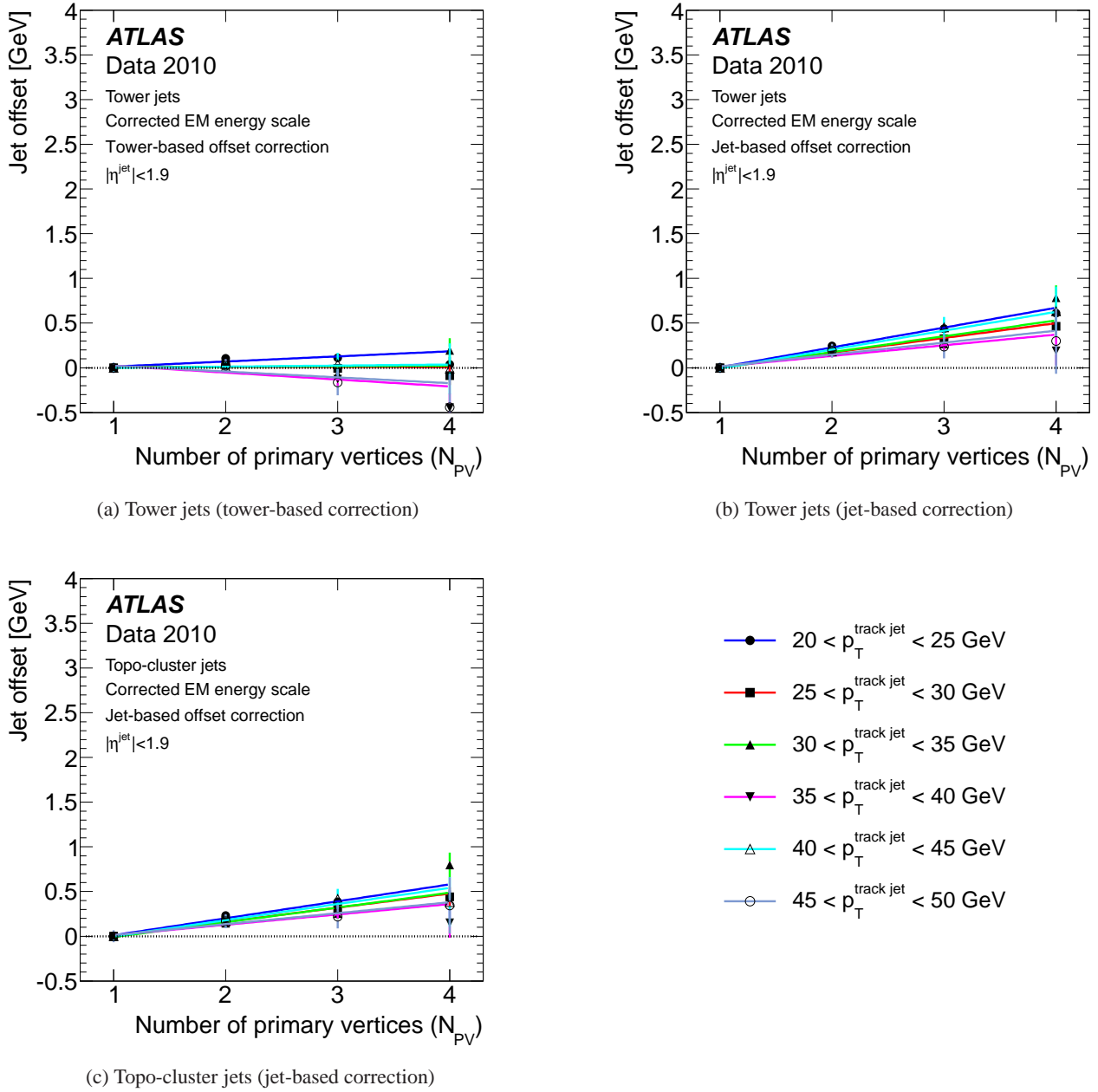


Fig. 20: Jet residual offset measured at the EM scale after pile-up correction using the most probable value E_T^{jet} obtained from a fit to a Landau+Gauss distribution for various bins in track jet transverse momentum ($p_T^{\text{track jet}}$) as a function of the primary vertex multiplicity: tower jets corrected with tower-based offset correction (using the actual number constituent towers) (a), tower jets corrected with the jet-based offset correction (using the average number of constituent towers) (b) and topo-cluster jets corrected with the jet-based offset correction (using the average number of equivalent constituent towers) (c). The axis ranges are identical to Figure 8 for ease of comparison. The jet offset is given for anti- k_t jets at the EM scale with $R = 0.6$. Only the statistical uncertainties of the fit results are shown.

Track jet p_T	Tower jets [GeV/vertex]		Topo-cluster jets [GeV/vertex]	
	Before	After	Before	After
20 - 25 GeV	0.55 ± 0.02	0.06 ± 0.02	0.50 ± 0.02	0.19 ± 0.02
25 - 30 GeV	0.47 ± 0.02	0.00 ± 0.02	0.47 ± 0.02	0.16 ± 0.02
30 - 35 GeV	0.49 ± 0.03	0.01 ± 0.03	0.47 ± 0.03	0.17 ± 0.03
35 - 40 GeV	0.42 ± 0.03	-0.08 ± 0.03	0.41 ± 0.03	0.12 ± 0.03
40 - 45 GeV	0.51 ± 0.05	0.01 ± 0.05	0.48 ± 0.05	0.18 ± 0.05
45 - 50 GeV	0.42 ± 0.06	-0.07 ± 0.06	0.41 ± 0.06	0.12 ± 0.06
Average	0.48 ± 0.02	-0.01 ± 0.02	0.46 ± 0.02	0.16 ± 0.02

Table 4: Variation of the calorimeter E_T^{jet} with pile-up for several bins in track jet p_T . Slopes are given in GeV/vertex at the electromagnetic scale for each primary vertex from additional proton-proton collisions in the event, and represent the slope of the jet offset before and after the tower-based offset correction. Tower-based corrections are applied to tower jets and jet-based corrections are applied to topo-cluster jets. The reported uncertainties are purely statistical.

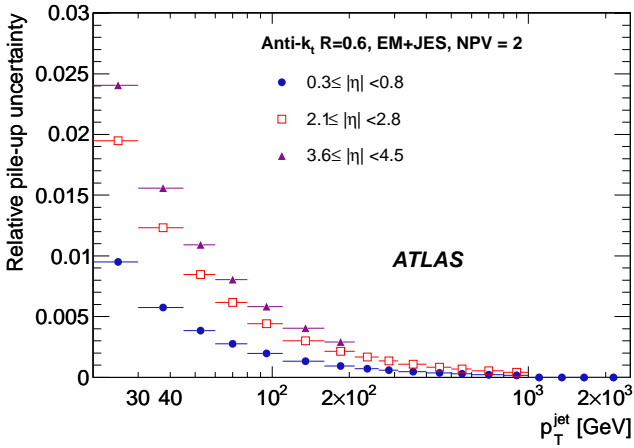


Fig. 21: Relative JES uncertainty from pile-up for anti- k_t jets with $R = 0.6$ in the case of two measured primary vertices, $N_{PV} = 2$, for central ($0.3 \leq |\eta| < 0.8$, full circles), endcap ($2.1 \leq |\eta| < 2.8$, open squares) and forward ($3.6 \leq |\eta| < 4.5$, full triangles) jets as a function of jet p_T^{jet} .

before correction, even with this conservative estimate the application of the offset correction represents an improvement of a factor of five obtained over the systematic bias associated with pile-up effects on the calorimeter jet transverse momentum.

The full offset correction shows reasonable closure when using the actual constituent tower multiplicity directly (tower-based) and a slight under-correction using the average constituent multiplicity in the jet (jet-based). Figure 20a shows the tower-based correction applied to tower jets at the EM scale as a function of the reconstructed vertex multiplicity. The tower-based correction exhibits a closure consistent with zero slope in E_T^{jet} as a function of N_{PV} . Figure 20b and Figure 20c show the jet-based correction applied to both tower jets and topo-cluster jets, respectively. The use of the jet-based offset correction slightly under-corrects for the effect of pile-up for jets constructed from *both* towers *and* topo-clusters.

The implication of this observation is two-fold:

1. There is no significant difference in the sensitivity of topo-cluster jets to pile-up as compared to tower jets.

2. There is a systematic underestimation of the average tower multiplicity in jets due to the effect of pile-up or due to differences in the jet transverse energy distribution in the derivation and the validation of the pile-up correction.

9.7.2 Jet offset correction uncertainties

The contributions to the jet offset correction uncertainty are estimated from studies that account for:

1. The effect of variations of the trigger selection on the measured non-noise-suppressed tower energy distribution that is input to the offset correction.
2. The variation with p_T^{jet} and N_{PV} of the tower multiplicity in jets based on topo-clusters¹⁷.
3. The variation of the offset correction derived from track jets as a function of the number of primary vertices for various values of track jet p_T .
4. The non-closure of the tower-based offset correction as evaluated by the dependence of the corrected calorimeter jet energy for calorimeter jets matched to track jets as a function of the number of primary vertices.

The JES uncertainty is estimated by adding all uncertainties in quadrature, including the one from the non-closure of the correction. The track jet method can be used only up to $|\eta| = 1.9$, if a full coverage of the jet area by the tracking acceptance is needed. Beyond $|\eta| = 1.9$, the dijet balance method detailed in Section 9.6 is used. This approach compares the relative jet response in events with only one reconstructed vertex with the response measured in events with several reconstructed vertices. The dijet balance method yields uncertainties similar to those intrinsic to the method also in the case of $|\eta| < 1.9$.

Each source of systematic uncertainty is summarised in Table 3 and the resulting effects expressed as a percentage of the average offset correction, shown in Table 4.

For jets based on towers the total systematic uncertainty is significantly larger than the validation of the correction using

¹⁷ This is determined from the variation in tower multiplicity for $N_{PV} = 1$ in jets matched to track jets with $25 \leq p_T < 30$ GeV as compared to $N_{PV} = 4$ in track jets with $35 \leq p_T < 40$ GeV.

track jets indicate. The larger of the two individual uncertainties (21%) is therefore adopted. This results in $\delta(\mathcal{O}^{\text{tower-based}}) = 100$ MeV per vertex¹⁸. The resulting total uncertainty is a factor of five smaller than the bias attributable to pile-up (≈ 500 MeV per vertex) even with this conservative systematic uncertainty estimation.

The offset correction for jets based on topo-clusters receives an additional uncertainty due to the average tower multiplicity approximation. This contribution is estimated to introduce a 20% uncertainty in the constituent tower multiplicity by comparing jets in events with $N_{PV} = 1 - 3$ and for the five highest $p_{T}^{\text{track jet}}$ -bins. This estimation translates directly into a 20% uncertainty on the jet-based offset. The resulting systematic uncertainty on jets corrected by the offset correction is estimated to be $\delta(\mathcal{O}^{\text{jet-based}}) \approx 160$ MeV per vertex; a factor of three smaller than the bias due to pile-up.

Figure 21 shows the relative uncertainty due to pile-up in the case of two measured primary vertices. In this case, the uncertainty due to pile-up for central jets with $p_T = 20$ GeV and pseudorapidity $|\eta| \leq 0.8$ is about 1%, while it amounts to about 2% for jets with pseudorapidity $2.1 \leq |\eta| < 2.8$ and to less than 2.5% for all jets with $|\eta| \leq 4.5$. In the case of three primary vertices, $N_{PV} = 3$, the pile-up uncertainty is approximately twice that of $N_{PV} = 2$, and with four primary vertices the uncertainty for central, endcap and forward jets is less than 3%, 6% and 8%, respectively. The relative uncertainty due to pile-up for events with up to five additional collisions becomes less than 1% for all jets with $p_T^{\text{jet}} > 200$ GeV. The pile-up uncertainty needs to be added separately to the estimate of the total jet energy scale uncertainty detailed in Section 9.8.

9.7.3 Out-of-time pile-up

The effect of additional proton-proton collisions from previous bunch crossings within trains of consecutive bunches (out-of-time pile-up) has been studied separately. The effect is found to be negligible in the 2010 data.

9.7.4 Pile-up corrections applied to jet shape measurements

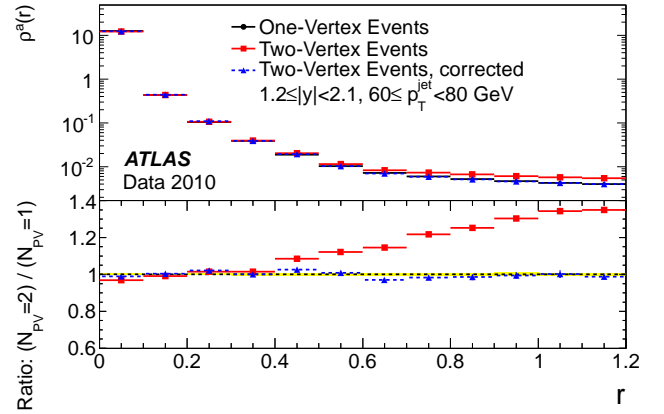
The measurement of internal jet properties like the energy flow inside jets can be made considerably more difficult in the presence of additional proton-proton collisions. The applicability of the tower-based offset presented in Section 9.7 to correct the mean jet energy can also be tested on the internal jet shape measurements.

The offset correction is applied to the measurement of the differential jet shape for $R = 0.6$ tower jets, as described in Ref. [3].

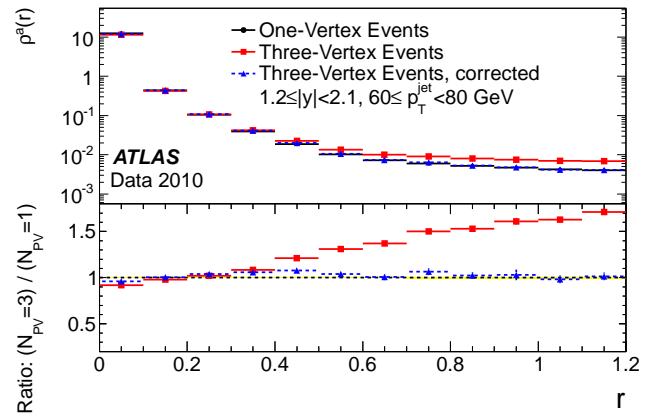
The jet shape variable used, $\rho^a(r)$, is defined as:

$$\rho^a(r) = \frac{1}{\pi \left[(r + \delta r/2)^2 - (r - \delta r/2)^2 \right]} \cdot \left\langle \frac{p_T \left(r - \frac{\delta r}{2}, r + \frac{\delta r}{2} \right)}{p_T(0, 0.7)} \right\rangle, \quad (19)$$

¹⁸ Using twice the RMS of the variation in the closure test yields a similar value.



(a) Comparison of $N_{PV} = 1$ and $N_{PV} = 2$



(b) Comparison of $N_{PV} = 1$ and $N_{PV} = 3$

Fig. 22: Measured sum p_T in annuli around the jet axis, divided by the total p_T around the jet within $\Delta R = 0.7$ of the jet axis and normalised by the area of each annulus as a function of the distance of the jet constituent to the jet axis. The shapes of jets in the rapidity range $1.2 \leq |y| < 2.1$ are compared, before and after the offset corrections, in events with one and two reconstructed vertices (a), and one and three reconstructed vertices (b). The corrected distribution is also shown (full triangles). Note that the single vertex data (full circles) are partially hidden behind the corrected multi-vertex data. Anti- k_T jets with $R = 0.6$ reconstructed from calorimeter towers are used and calibrated with the EM+JES scheme.

where $r = \sqrt{(d\eta)^2 + (d\phi)^2}$ is the distance of the jet constituents to the jet four-momentum vector and the angled brackets denote an average over all jets, $p_T(b, c)$ is the sum of the p_T of all towers with an opening angle $b \leq \Delta R < c$ with respect to the jet axis, and $\delta r = 0.1$.

This definition differs from the canonical jet shape variable $\rho(r)$ in two important ways. First, by normalising to area, the variable measures an energy density. Therefore, $\rho^a(r)$ will approach an asymptotic value far from the jet axis. The level of the asymptote is related to the energy density in the calorimeter and is measurably higher in events with pile-up. Second, all

towers are included in the definition. This allows an examination of energy outside of the jet cone, in some sense measuring “energy flow” around the jet axis.

Figure 22 depicts $\rho^a(r)$ with and without a correction of the tower constituent energy for the mean energy induced by pile-up interactions. In events with two (three) reconstructed vertices, differences in this particular jet shape variable of up to 35% (70%) just outside the jet ($r > 0.6$) and 20% (40%) near the nominal jet radius ($r = 0.6$) are observed. The bulk of the shape ($0.1 \leq r < 0.6$) is restored to that observed in events with only a single interaction, in both the core ($r < 0.1$) and the periphery ($r > 0.6$) of the jet.

The results demonstrate that the tower-based offset correction can be applied on a fine scale granularity and is valid both inside and *near* jets.

9.8 Summary of jet energy scale systematic uncertainties

The total jet energy scale uncertainty is derived by considering all the individual contributions described in the previous sections. In the central region ($|\eta| < 0.8$), the estimate proceeds as follows:

1. For each p_T^{jet} and η bin, the uncertainty due to the calibration procedure is calculated as described in Section 9.2 for both jet energy and p_T response. For each bin, the maximum deviation from unity between the energy and p_T response is taken as the final non-closure uncertainty.
2. The calorimeter response uncertainty is estimated as a function of jet η and p_T from the propagation of single particle uncertainties to the jets, as detailed in Section 9.3.
3. Sources of uncertainties estimated using Monte Carlo samples with a systematic variation are accounted as follows:
 - (a) the response in the test sample \mathcal{R}_{var} and the response in the nominal sample \mathcal{R}_{nom} is considered as a starting point for the estimate of the JES uncertainty. The deviation of this ratio from unity is defined as:

$$\Delta_{\text{JES}}(p_T^{\text{jet}}, \eta) = \left| 1 - \frac{\mathcal{R}_{\text{var}}(p_T^{\text{jet}}, \eta)}{\mathcal{R}_{\text{nom}}(p_T^{\text{jet}}, \eta)} \right|. \quad (20)$$

This deviation is calculated from both the energy and p_T response, leading to $\Delta_{\text{JES}}^E(p_T^{\text{jet}}, \eta)$ for the deviation in the energy response, and to $\Delta_{\text{JES}}^{p_T}(p_T^{\text{jet}}, \eta)$ for the deviation in the transverse momentum response.

- (b) The larger Δ_{JES} in each bin derived from the jet energy or transverse momentum response is considered as the contribution to the final JES systematic uncertainty due to the specific systematic effect:

$$\Delta_{\text{JES}}(p_T^{\text{jet}}, |\eta|) = \max(\Delta_{\text{JES}}^E(p_T^{\text{jet}}, \eta), \Delta_{\text{JES}}^{p_T}(p_T^{\text{jet}}, \eta)). \quad (21)$$

4. The estimate of the uncertainty contributions due to additional material in the inner detector and overall additional dead material are estimated as described in the previous step. These uncertainties are then scaled by the average fraction of particles forming the jet that have $p < 20$ GeV

(for the inner detector distorted geometry) and by the average fraction of particles outside the kinematic range of the single hadron response *in situ* measurements (for the overall distorted geometry).

For each (p_T^{jet}, η) -bin, the uncertainty contributions from the calorimeter, the jet calibration non-closure, and systematic Monte Carlo simulation variations are added in quadrature.

For pseudorapidities beyond $|\eta| > 0.8$, the η -intercalibration contribution is estimated for each pseudorapidity bin in the endcap region as detailed in Section 9.6.6. The pseudorapidity intercalibration contribution is added in quadrature to the total JES uncertainty determined in the $0.3 \leq |\eta| < 0.8$ region to estimate the JES uncertainty for jets with $|\eta| > 0.8$, with the exception of the non-closure term that is taken from the specific η -region. For low p_T^{jet} , this choice leads to partially double counting the contribution from the dead material uncertainty, but it leads to a conservative estimate in a region where it is difficult to estimate the accuracy of the material description.

The contribution to the uncertainty due to additional proton-proton interactions described in Section 9.7 is added separately, depending on the number of primary vertices in the event. In the remainder of the section only the uncertainty for a single proton-proton interaction is shown in detail.

Figure 23 shows the final fractional jet energy scale systematic uncertainty and its individual contributions as a function of p_T^{jet} for three selected η regions. The fractional JES uncertainty in the central region amounts to 2% to 4% for $p_T^{\text{jet}} < 60$ GeV, and it is between 2% and 2.5% for $60 \leq p_T^{\text{jet}} < 800$ GeV. For jets with $p_T^{\text{jet}} > 800$ GeV, the uncertainty ranges from 2.5% to 4%. The uncertainty amounts to up to 7% and 3%, respectively, for $p_T^{\text{jet}} < 60$ GeV and $p_T^{\text{jet}} > 60$ GeV in the endcap region, where the central uncertainty is taken as a baseline and the uncertainty due to the intercalibration is added. In the forward region, a 13% uncertainty is assigned for $p_T^{\text{jet}} = 20$ GeV. The increase in the uncertainty is dominated by the modelling of the soft physics in the forward region that is accounted for in the η -intercalibration contribution. This uncertainty contribution is estimated conservatively.

Table 5 presents a summary of the maximum uncertainties in the different η regions for anti- k_t jets with $R = 0.6$ and with p_T^{jet} of 20 GeV, 200 GeV and 1.5 TeV as examples.

The same study has been repeated for anti- k_t jets with distance parameter $R = 0.4$, and the estimate of the JES uncertainty is comparable to that obtained for anti- k_t jets with $R = 0.6$. The JES uncertainty for anti- k_t jets with $R = 0.4$ is between $\approx 4\%$ (8%, 14%) at low p_T^{jet} and $\approx 2.5\% - 3\%$ (2.5% – 3.5%, 5%) for jets with $p_T > 60$ GeV in the central (endcap, forward) region, and is summarised in Table 6.

9.9 Discussion of special cases

The jet energy scale is derived using the simulated sample of inclusive jets described in Section 4.3, with a particular mixture of quark and gluon initiated jets and with a particular selection of isolated jets. The differences in fragmentation between quark and gluon initiated jets and the effect of close-by jets give

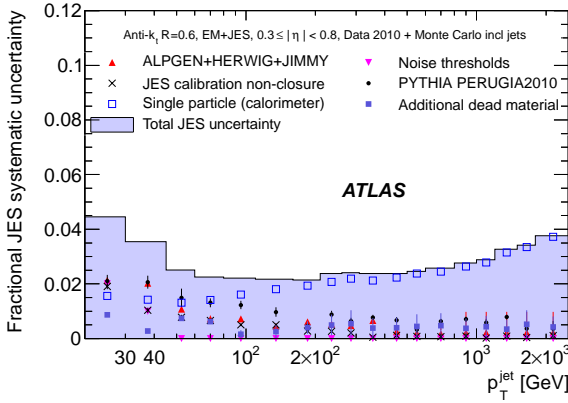
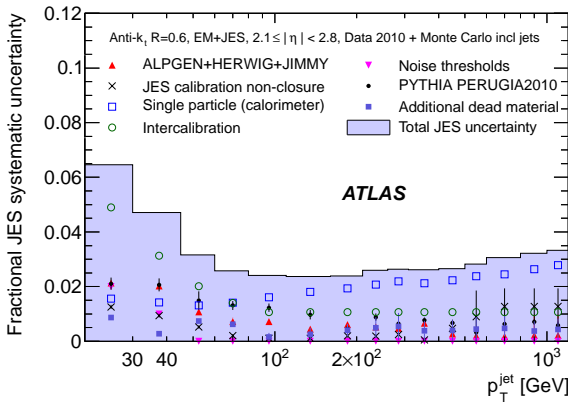
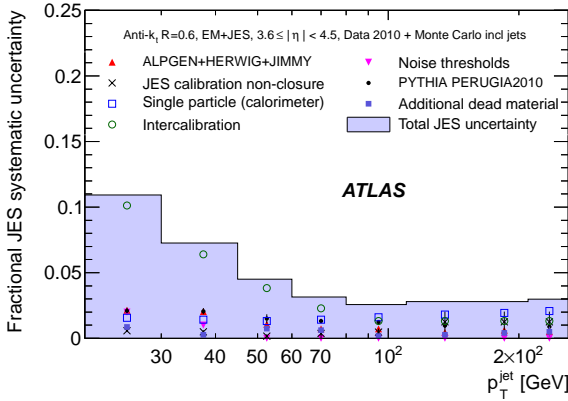
(a) $0.3 \leq |\eta| < 0.8$ (b) $2.1 \leq |\eta| < 2.8$ (c) $3.6 \leq |\eta| < 4.5$

Fig. 23: Fractional jet energy scale systematic uncertainty as a function of p_T^{jet} for jets in the pseudorapidity region $0.3 \leq |\eta| < 0.8$ in the calorimeter barrel (a), $2.1 \leq |\eta| < 2.8$ in the calorimeter endcap (b), and in the forward pseudorapidity region $3.6 \leq |\eta| < 4.5$. The total uncertainty is shown as the solid light shaded area. The individual sources are also shown together with uncertainties from the fitting procedure if applicable.

η region	Maximum fractional JES Uncertainty		
	$p_T^{\text{jet}} = 20$ GeV	200 GeV	1.5 TeV
$0 \leq \eta < 0.3$	4.6%	2.3%	3.1%
$0.3 \leq \eta < 0.8$	4.5%	2.2%	3.3%
$0.8 \leq \eta < 1.2$	4.4%	2.3%	3.3%
$1.2 \leq \eta < 2.1$	5.4%	2.4%	3.4%
$2.1 \leq \eta < 2.8$	6.5%	2.5%	
$2.8 \leq \eta < 3.2$	7.9%	3.0%	
$3.2 \leq \eta < 3.6$	8.1%	3.0%	
$3.6 \leq \eta < 4.5$	10.9%	2.9%	

Table 5: Summary of the maximum EM+JES jet energy scale systematic uncertainties for different p_T^{jet} and η regions from Monte Carlo simulation based study for anti- k_t jets with $R = 0.6$.

η region	Maximum fractional JES Uncertainty		
	$p_T^{\text{jet}} = 20$ GeV	200 GeV	1.5 TeV
$0 \leq \eta < 0.3$	4.1%	2.3%	3.1%
$0.3 \leq \eta < 0.8$	4.3%	2.4%	3.3%
$0.8 \leq \eta < 1.2$	4.4%	2.5%	3.4%
$1.2 \leq \eta < 2.1$	5.3%	2.6%	3.5%
$2.1 \leq \eta < 2.8$	7.4%	2.7%	
$2.8 \leq \eta < 3.2$	9.0%	3.3%	
$3.2 \leq \eta < 3.6$	9.3%	3.5%	
$3.6 \leq \eta < 4.5$	13.4%	4.9%	

Table 6: Summary of the maximum EM+JES jet energy scale systematic uncertainties for different p_T^{jet} and η regions from Monte Carlo simulation based study for anti- k_t jets with $R = 0.4$.

rise to a topology and flavour dependence of the energy scale. Since the event topology and flavour composition (quark and gluon fractions) may be different in final states other than the considered inclusive jet sample, the dependence of the jet energy response on jet flavour and topology has to be accounted for in physics analyses. The flavour dependence is discussed in more detail in Section 18 and an additional uncertainty specific to jets with heavy quark components is discussed in Section 20.

The JES systematic uncertainty is derived for isolated jets¹⁹. The response of jets as a function of the distance to the closest reconstructed jet needs to be studied and corrected for separately if the measurement relies on the absolute jet energy scale. The contribution to the JES uncertainty from close-by jets also needs to be estimated separately, since the jet response depends on the angular distance to the closest jet. This additional uncertainty can be estimated from the Monte Carlo simulation to data comparison of the p_T -ratio between calorimeter jets and matched track jets in inclusive jet events as a function of the isolation radius. This is discussed in more detail in Section 17.

¹⁹ This choice is motivated by the minor differences observed in the average kinematic jet response of isolated and non-isolated jets in the nominal inclusive jet Monte Carlo sample and by the need to factorise the topology dependence of the close-by jet energy scale uncertainty for final states other than the inclusive jets considered.

10 Jet energy scale uncertainties validation with *in situ* techniques for the EM+JES scheme

The jet energy calibration can be tested *in situ* using a well-calibrated object as reference and comparing data to the nominal PYTHIA Monte Carlo simulation. The following *in situ* techniques have been used by ATLAS:

1. **Comparison to the momentum carried by tracks associated to a jet:** The mean transverse momentum sum of tracks that are within a cone with size R provides an independent test of the calorimeter energy scale over the entire measured p_T^{jet} range within the tracking acceptance. The comparison is done in the jet η range $0 \leq |\eta| < 2.1$.
2. **Direct p_T balance between a photon and a jet:** Events with a photon and one jet at high transverse momentum are used to compare the transverse momentum of the jet to that of the photon. To account for effects like soft QCD radiation and energy migrating out of the jet area the data are compared to the Monte Carlo simulation. The comparison is done in the jet η range $|\eta| < 1.2$ and for photon transverse momenta $25 \leq p_T^\gamma < 250$ GeV.
3. **Photon p_T balance to hadronic recoil:** The photon transverse momentum is balanced against the full hadronic recoil using the projection of the missing transverse momentum onto the photon direction (MPF). This method does not explicitly involve a jet algorithm. The comparison is done in the same kinematic region as the direct photon balance method.
4. **Balance between a high- p_T jet and low- p_T jet system:** If jets at low transverse momentum are well-calibrated, jets at high transverse momentum can be balanced against a recoil system of low transverse momentum jets. This method can probe the jet energy scale up to the TeV-regime. The η range used for the comparison is $|\eta| < 2.8$.

All methods are applied to data and Monte Carlo simulation.

The *in situ* techniques usually rely on assumptions that are only approximately fulfilled. An example is the assumption that the jet to be calibrated and the reference object are balanced in transverse momentum. This balance can be altered by the presence of additional high- p_T particles. For the determination of the JES uncertainties the modelling of physics effects has to be disentangled from detector effects. This can be studied by systematically varying the event selection criteria. The ability of the Monte Carlo simulation to describe extreme variations of the selection criteria determines the systematic uncertainty in the *in situ* methods, since physics effects can be suppressed or amplified by these variations.

So far the *in situ* techniques are used to validate the systematic uncertainty in the jet energy measurement. However, they can also be used to obtain jet energy corrections. This is an interesting possibility when the statistical and systematic uncertainties in the samples studied become smaller than the standard JES uncertainty from the single hadron response. The results of the *in situ* techniques are discussed in the following sections.

10.1 Comparison of transverse momentum balance of jets from calorimeter and tracking

The transverse momentum of each jet can be compared with the total transverse momentum of tracks associated with the jet by means of a geometrical selection and the charged-to-total-momentum ratio:

$$r_{\text{trk}} = \frac{\sum p_T^{\text{track}}}{p_T^{\text{jet}}} \quad (22)$$

can be used to test the jet calibration. If all produced particles were pions, the symmetry of QCD under isospin transformation would require that this ratio be $2/3$ once the energy is high enough so that the total particle multiplicity is large and the initial isospin of the proton-proton system can be ignored. Production of other particles such as kaons, η mesons, and baryons gives different fractions, but their contributions can be calculated using a properly tuned event generator.

Since the tracking system provides a measurement that is independent of the calorimeter, the ratio r_{trk} can be used to determine the calorimeter jet energy scale. The r_{trk} distribution is broad but a meaningful calibration does not require very many events, since the statistical uncertainty on the mean scales as $1/\sqrt{N}$. This calibration can be used for jets confined within the tracking detector coverage. Dominant systematic uncertainties result from the knowledge of the tracking efficiency, variations in the predicted value of r_{trk} for various generator tunes and loss of tracking efficiency in the dense core of high- p_T jets.

To test the p_T^{jet} dependence of the jet energy measurement, the double ratio of charged-to-total momentum observed in data to that obtained in Monte Carlo simulation is studied:

$$R_{r_{\text{trk}}} \equiv \frac{[\langle r_{\text{trk}} \rangle]_{\text{Data}}}{[\langle r_{\text{trk}} \rangle]_{\text{MC}}} \quad (23)$$

10.1.1 Jet and track selection

To ensure that the majority of tracks associated with the jets found in the calorimeter are within the inner detector fiducial volume, jets are required to have $|\eta| < 2.1$ ²⁰ and $p_T^{\text{jet}} > 20$ GeV. To reduce the influence of nearby jets on the measurement, if two jets are separated by a distance $\Delta R < 2R$ then the softer of these two jets is rejected from the analysis.

Tracks with $p_T^{\text{track}} > 1$ GeV are selected using the criteria detailed in Section 6.2. The $p_T^{\text{track}} > 1$ GeV requirement is intended to select mainly tracks from fragmentation rather than those arising from soft and diffuse interactions.

Tracks are associated with jets using a geometric algorithm. If the distance $\Delta R_{\text{track,jet}}$ between the track and the jet is less than the distance parameter used in the jet reconstruction ($R = 0.4$ or $R = 0.6$), the track is associated to the jet. Track parameters are evaluated at the distance of closest approach to the

²⁰ Section 9.7 discusses “track jets” obtained by running the anti- k_t jet algorithm using tracks as input. Those studies are restricted to $|\eta| < 1.9$ to avoid bias in the position of the centre of the jet due to tracking inefficiencies. Since the jets in this section are found using calorimeter information, no such bias is present and it is therefore possible to extend the pseudorapidity coverage to $|\eta| < 2.1$.

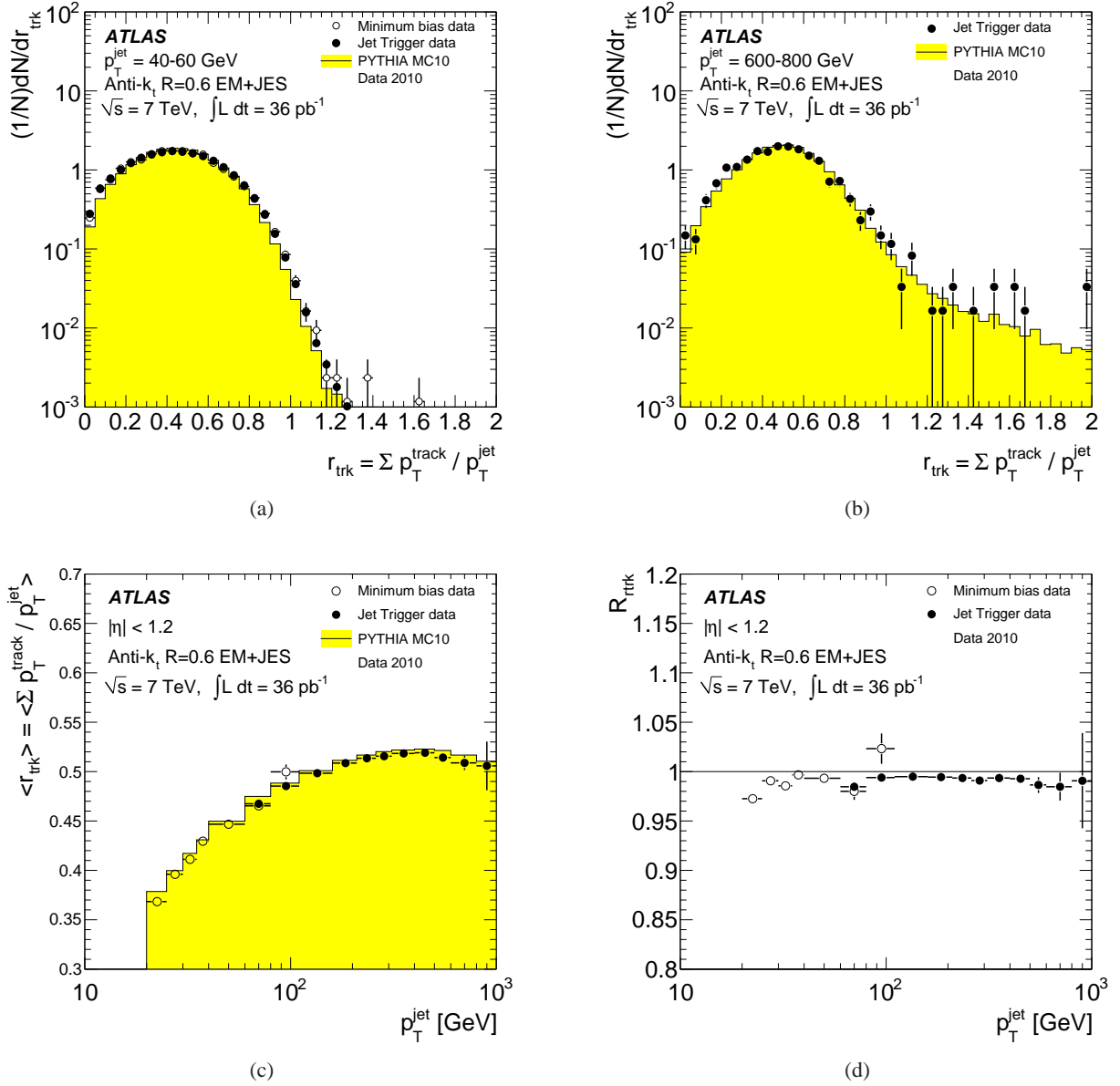


Fig. 24: The distribution of the charged-to-total momentum ratio r_{trk} for $40 \leq p_{\text{T}}^{\text{jet}} < 60$ GeV (a) and for $600 \leq p_{\text{T}}^{\text{jet}} < 800$ GeV (b), the average charged-to-total momentum ratio $\langle r_{\text{trk}} \rangle$ for data and Monte Carlo simulation as a function of $p_{\text{T}}^{\text{jet}}$ (c) and the ratio of $\langle r_{\text{trk}} \rangle$ for data and Monte Carlo simulation ($R_{r_{\text{trk}}}$) as a function of $p_{\text{T}}^{\text{jet}}$ for the pseudorapidity range $|\eta| < 1.2$ (d) for anti- k_t jets with $R = 0.6$ calibrated using the EM+JES scheme. The data measured with the jet (minimum bias) trigger are shown as closed (open) circles. Only statistical uncertainties are shown.

primary hard-scattering vertex and are *not* extrapolated to the calorimeter. This simple association algorithm facilitates comparison with charged particles from truth jets whose parameters correspond to those measured at the origin.

10.1.2 Comparison of data and Monte Carlo simulation

The jet response validation using the total momentum measured in tracks depends on a comparison of the mean value of r_{trk} observed in the data to that predicted in the Monte Carlo simulation. It is therefore important to demonstrate that the baseline Monte Carlo generator and simulation provide a reasonable description of the data.

ATLAS has measured the charged particle fragmentation function for jets with $25 \leq p_T^{\text{jet}} < 500$ GeV and $|\eta| < 1.2$ and has compared the measurement with the predictions of several Monte Carlo generators and generator tunes [62].

The jet fragmentation function and the transverse jet profile are compared to various Monte Carlo event generators and tunes. The jet fragmentation function is measured using charged particles with momentum fraction z with respect to the jet momentum $F(z, p_T^{\text{jet}}) = 1/N_{\text{jet}} dN_{\text{ch}}/dz$.

The growth of the mean charged particle multiplicity with p_T^{jet} is well modelled by the Monte Carlo simulation. The measured jet fragmentation function agrees well with the PYTHIA MC10 and the PERUGIA2010 tunes within the measurement uncertainties. The jet fragmentation function is described by the PYTHIA tunes. The HERWIG++ Monte Carlo generator is not consistent with the data.

For observables related to jet properties in the direction transverse to the jet axis the Monte Carlo generators (HERWIG and the various PYTHIA tunes) show reasonable agreement with data, but none of the generators agrees within the experimental uncertainties over the full kinematic range. For instance, the PYTHIA MC10 tune shows an excess of about 10% in the transverse charged particle distributions close to the jet axis.

These measurements indicate that the PYTHIA MC10 and PERUGIA2010 tunes span the range of fragmentation functions that are consistent with the data. The studies presented here use the MC10 tune to obtain the central values of the Monte Carlo predictions. Systematic uncertainties are assessed from the difference between the MC10 and PERUGIA2010 PYTHIA tunes.

The r_{trk} distributions used to validate the JES are shown for data and simulation for two typical bins of jet p_T in Figure 24a and Figure 24b. Agreement between data and simulation is good, although the data distribution is somewhat wider than the Monte Carlo simulation. Figure 24c and Figure 24d show $\langle r_{\text{trk}} \rangle$ for data and simulation and the average double ratio $R_{r_{\text{trk}}}$, respectively, as a function of p_T^{jet} . Figure 24d demonstrates that the measured JES calibration agrees with that predicted by the Monte Carlo simulation to better than 2% for $p_T^{\text{jet}} > 25$ GeV. Measurements using the minimum bias and jet triggers are consistent for those p_T^{jet} bins where both triggers are accessible.

10.1.3 Systematic uncertainties

The systematic uncertainties associated with the method using the total track momentum to test the JES are discussed below.

Generator model dependence While basic isospin arguments constrain the mean fraction of the jet momentum observed in charged tracks, the prediction for r_{trk} does depend on details of the physics model used in the Monte Carlo generator. Systematic uncertainties arise from:

1. The parametrisation of the fragmentation function and of the underlying event (which mainly affect the fraction of the momentum carried by particles below the $p_T = 1$ GeV cut used for this analysis).
2. The model of colour reconnection (which can change the distribution of particles with low momenta).
3. The probability of producing strange quarks and baryons (which are iso-doublets rather than iso-triplets like the pion) and of producing iso-scalars such as the η .

The size of these uncertainties has been estimated by studying a wide range of PYTHIA tunes²¹. A list of the PYTHIA tunes studied is given in Table 7.

These studies have been done at the generator level and have been cross-checked using simulated samples when the appropriate tunes were available with full simulation.

The data have also been compared to default tunes of HERWIG++ and HERWIG+JIMMY. PYTHIA tune 117, and the default HERWIG++ and HERWIG+JIMMY tunes are not consistent with the measured $f(z)$ distributions. Since these generators do not described the fragmentation functions measured by ATLAS [62] they are excluded from consideration when determining the systematic uncertainty on the JES measurement.

At low p_T^{jet} , the variations between tunes arise mainly from differences in the hardness of the jet fragmentation, which affects the fraction of charged particles falling below the 1 GeV cut on p_T^{track} . In general, PYTHIA tunes that include the “colour annealing” model of colour reconnection exhibit harder fragmentation than similar tunes without colour annealing. At high p_T^{jet} , differences among tunes are primarily associated with the strangeness and baryon content of the truth jets. Versions of PYTHIA tuned to LEP data (including flavour-dependent fragmentation measurements) using the tuning software PROFESSOR [63] in general show a charged fraction about 1% higher than the other tunes considered here. Using a conservative approach, the value of systematic uncertainty has been symmetrised around the baseline tune using the absolute value of the largest deviation of the tunes considered from the baseline.

Inner detector material description The dominant systematic uncertainty on the reconstruction efficiency for isolated tracks is derived from the uncertainty on the simulation’s description of material in the inner detector. The systematic uncertainty on the efficiency is independent of p_T^{track} for tracks with $p_T^{\text{track}} > 500$ MeV but is η -dependent, ranging from 2%

²¹ Additional information about the PYTHIA tunes can be found in Ref. [28].

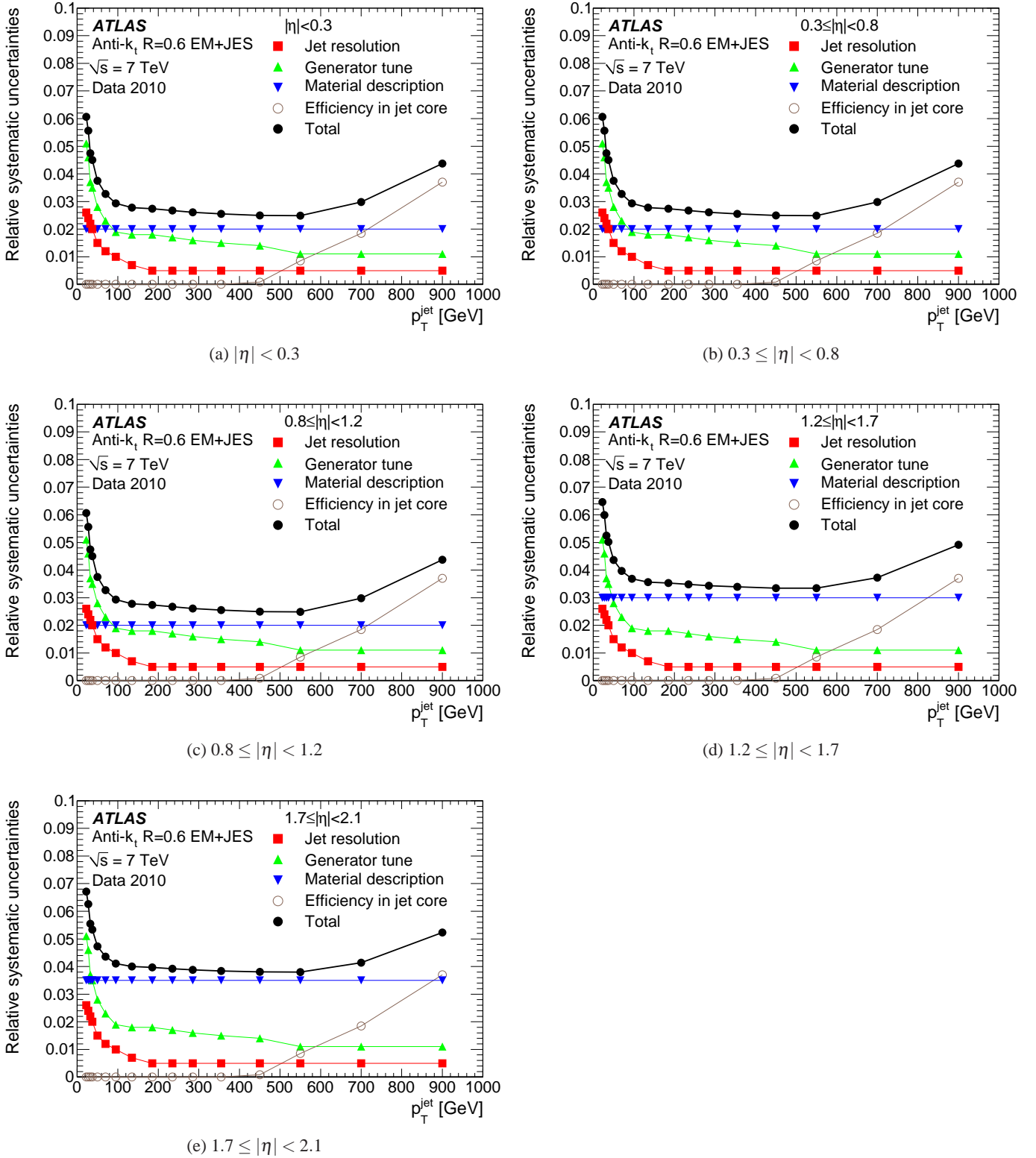


Fig. 25: Relative systematic uncertainty on the JES obtained by comparing the total momentum of tracks associated to jets to the calorimeter measurements for different η regions for anti- k_t jets with $R = 0.6$ calibrated with the EM+JES scheme as a function of p_T^{jet} . The total and the individual systematic uncertainties, as evaluated from the inclusive jet Monte Carlo simulation, are shown.

Tune Name	PYTUNE Value	Comments
MC10	–	ATLAS default (p_T ordered showering)
MC09	–	ATLAS default for Summer 2010 (p_T ordered showering)
RFTA	100	Rick Field Tune A Q^2 ordered showering
	107	Tune A with “colour annealing” colour reconnection
	110	Tune A with LEP tune from Professor
	117	Tune 110 with “colour annealing” colour reconnection
	129	Tune of Q^2 ordered showering and UE with Professor
	320	PERUGIA0 (p_T ordered showering)
PERUGIA2010	327	PERUGIA0 with updated fragmentation and more parton radiation

Table 7: PYTHIA generator tunes used to study the systematic uncertainty on the prediction for r_{trk} . Tunes specified by number (e.g. 100) refer to the value of the PYTUNE parameter [28]. A dash in the table indicates that the particular tune has no PYTUNE value.

for $|\eta^{\text{track}}| < 1.3$ to 7% for $2.3 \leq |\eta^{\text{track}}| < 2.5$ [64]. Convoluting these uncertainties with the appropriate η^{track} distributions results in systematic uncertainties on r_{trk} that range from 2% for jet pseudorapidities $|\eta| < 1.2$ to 3.5% for pseudorapidities $1.7 \leq |\eta| < 2.1$.

Uncertainties in the material distributions also affect the probability that photon conversions produce charged particles that can be included in the r_{trk} measurement. The track selection used here requires at least one Pixel hit and most of the material in the ID is at a larger radius than the Pixel detector, resulting in a small systematic uncertainties associated with rate of conversions.

Tracking efficiency in the jet core There are several effects that change the tracking efficiency and resolution inside a jet compared to those for isolated tracks:

1. When two tracks are close together, their hits may overlap. While the pattern recognition software allows tracks to share hits, the resolution is degraded since the calculated position of the hit is affected by the presence of the other track. The probability of not assigning hits to tracks increases.
2. When the hit density becomes high in the core of the jet, failures in the pattern recognition may result in the creation of tracks by combining hits that in fact came from several particles. Such tracks are called *fake tracks*.
3. When two high- p_T tracks are close together in space, they will share hits over many layers. In this case, one of the two tracks may be lost. This effect, referred to as *loss of efficiency*, becomes more important as the p_T^{jet} increases.

The reliability of the simulation to predict the size of these effects depends on whether the software properly models merging of ID hits. Detailed comparisons of the data and Monte Carlo simulation indicate that the simulation accurately reproduces the degradation of response in the jet core and models the degradation in resolution well. Comparison of the fraction of tracks with $z > 1$ in data and Monte Carlo simulation constrains the size of the non-Gaussian tails in the track resolution. Any residual difference in resolution between data and simulation is absorbed in the quoted uncertainty due to ID alignment.

Fake tracks and loss of efficiency are studied in the simulation using a hit-based matching algorithm using truth jets.

These studies indicate that the rate for reconstructing fake tracks remains at 0.1% for the full p_T^{jet} range considered here, but that there is loss of tracking efficiency near the core of high- p_T jets. This effect has a negligible effect on r_{trk} for jets with $p_T^{\text{jet}} < 500$ GeV, but increases with p_T^{jet} such that on average $\sim 7.5\%$ of the charged track momentum is lost for jets in the range $800 \leq p_T^{\text{jet}} < 1000$ GeV. A relative uncertainty of 50% is assigned to the value of the inefficiency that is caused by merged hits. While this effect gives the largest systematic uncertainty on the JES for $p_T^{\text{jet}} \gtrsim 600$ GeV (1.9% for $600 \leq p_T^{\text{jet}} < 800$ GeV and 3.7% for $800 \leq p_T^{\text{jet}} < 1000$ GeV), it is still smaller than the present statistical uncertainty at these values of p_T^{jet} .

Inner detector alignment For high p_T tracks, the momentum resolution achieved in the ID is worse than that of the simulation. This degradation in resolution is attributed to an imperfect alignment of the ID. The systematic uncertainty on r_{trk} is obtained by degrading the tracking resolution in the simulation. The size of this additional resolution smearing is determined by studying the width of the measured mass distribution for Z -decays $Z \rightarrow \mu^+ \mu^-$. This procedure results in a systematic uncertainty of less than 0.2% for all p_T^{jet} and η .

Calorimeter jet p_T resolution The systematic uncertainty due to jet transverse momentum resolution [65] is determined by smearing the jet four-momentum (without changing η or ϕ) in Monte Carlo simulation. The relative uncertainty on the p_T^{jet} resolution is 5% for $0 \leq |\eta| < 0.8$ and 10% for $0.8 \leq |\eta| < 2.1$. The effect of this variation is largest for low values of p_T^{jet} and high values of η ; for $p_T^{\text{jet}} < 40$ GeV and $0.8 < |\eta| < 2.1$ the uncertainty on $R_{r_{\text{trk}}}$ is $\sim 2\%$.

Combined systematic uncertainty The above uncertainties are assumed to be uncorrelated and are combined in quadrature. The resulting total uncertainties are shown in Figure 25 as a function of p_T^{jet} for several regions of η .

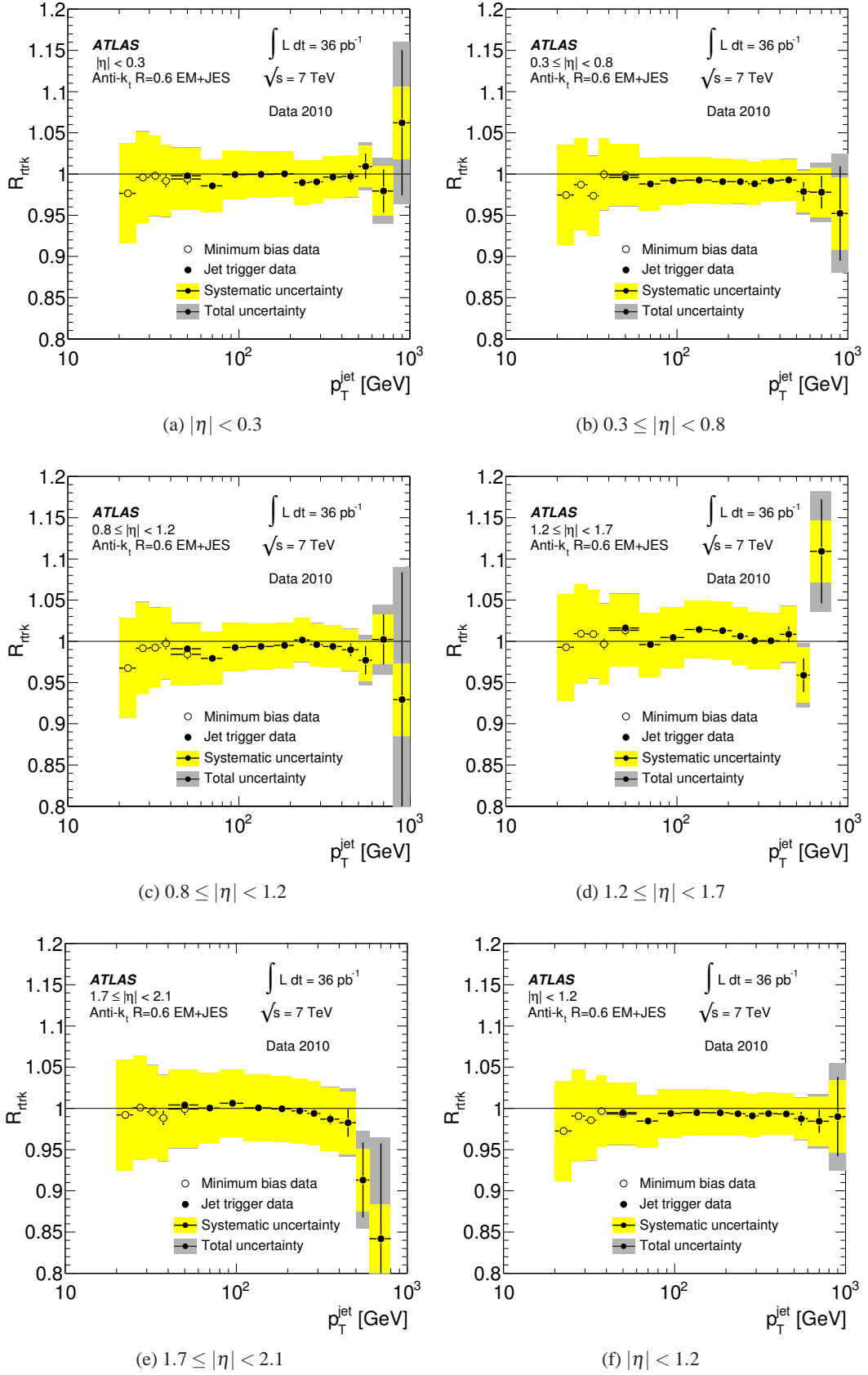


Fig. 26: Double ratio of the mean track to calorimeter response ratio in data and Monte Carlo simulation $R_{\text{trk}} = [r_{\text{trk}}]_{\text{Data}}/[r_{\text{trk}}]_{\text{MC}}$ for anti- k_t jets with $R = 0.6$ calibrated with the EM+JES scheme as a function of p_T^{jet} for various η bins. Systematic (total) uncertainties are shown as a light (dark) band.

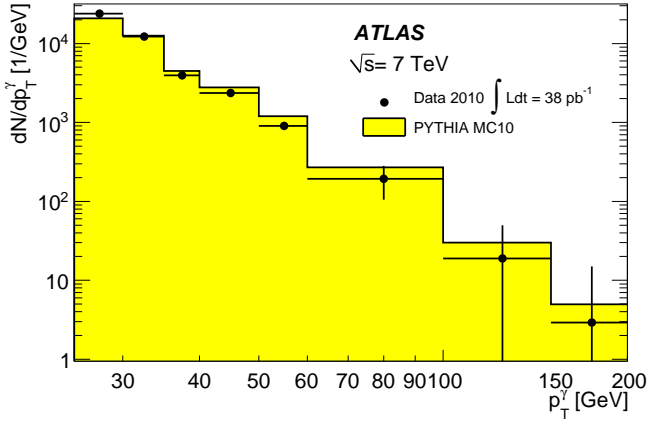


Fig. 27: Distribution of the photon transverse momentum for events passing the photon selection criteria described in Section 10.2.4. A correction is made in the first p_T^γ bin for the pre-scale applied to the trigger in this p_T^γ range. The Monte Carlo simulation is normalised to the observed number of events observed in data and corrected for the trigger pre-scale. Uncertainties are statistical only.

10.1.4 Summary of JES uncertainty from tracks

Final results for anti- k_t jets with $R = 0.6$ and EM+JES corrections are shown in Figure 26 for five bins in η with the derived systematic uncertainties. To facilitate comparisons at high p_T^{jet} , where the statistical uncertainties are large, the combined data from the three bins with $|\eta| < 1.2$ are also displayed. Averaging all data with $p_T^{\text{jet}} > 25$ GeV and $|\eta| < 1.2$ yields a value of r_{trk} that agrees with the simulation to better than 1%. This small discrepancy is well within the quoted systematic uncertainty, which is highly correlated between bins in p_T^{jet} . No significant variation of R_{trk} with p_T^{jet} is observed. For $|\eta| > 1.2$, the statistical uncertainties are large for $p_T^{\text{jet}} > 500$ GeV. For $p_T^{\text{jet}} < 500$ GeV, the level of agreement between data and simulation is similar to that obtained at low η .

In summary, r_{trk} , the ratio of track to calorimeter transverse momentum, is used to validate the JES for anti- k_t jets with $R = 0.4$ and $R = 0.6$ calibrated with the EM+JES calibration scheme. Systematic uncertainties associated with jet modelling and track reconstruction are assessed and the method is shown to provide a JES uncertainty evaluation independent of the modelling of the calorimeter response. Systematic uncertainties are below 3% for $0 \leq |\eta| < 0.8$ and rise to $\sim 4\%$ for $1.7 \leq |\eta| < 2.1$ for $40 \leq p_T^{\text{jet}} < 800$ GeV. The results agree within systematic uncertainties with those predicted using the ATLAS calorimeter simulation and provide an independent estimate of the overall jet energy scale and its uncertainty.

10.2 Photon-jet transverse momentum balance

In γ -jet events, a jet recoils against a photon at high transverse momentum. The photon energy, being accurately measured in

the electromagnetic calorimeter, is used as a reference. Such a topology can be used to validate the jet energy measurement. Any discrepancy between data and simulation may be taken as an uncertainty on the jet energy calibration.

Two methods of balancing the photon and the recoiling jet transverse momentum with different sensitivities and systematic uncertainties are used: the direct p_T balance technique and the missing transverse momentum projection fraction technique.

10.2.1 Direct transverse jet momentum balance technique

The direct p_T balance technique exploits the approximate transverse momentum balance in events with only one photon and one jet with high p_T . The ratio of the jet p_T to the photon p_T ($p_T^{\text{jet}}/p_T^\gamma$) is used to estimate the jet response. Since the photon p_T is well-measured and well-described by the simulation, the quality of the jet p_T calibration can be assessed by comparing data and Monte Carlo simulation using the ratio $p_T^{\text{jet}}/p_T^\gamma$. This technique was used at the CDF experiment [61].

10.2.2 Missing transverse momentum projection fraction technique

The missing transverse momentum (E_T^{miss}) projection fraction (MPF) technique exploits the momentum balance, in the transverse plane, of the photon and the hadronic recoil to derive the detector response to jets. This technique has been used in the past for the D0 experiment [60].

The missing transverse momentum vector (E_T^{miss}) is defined as the opposite of the vector sum of the transverse projections of calorimeter energy deposits. The missing transverse momentum is calculated from the energy deposits in the calorimeter cells that are included in topo-clusters. The calorimeter cell energy is computed using the same calibration as the one used in the jet calibration scheme to be tested. The missing transverse momentum is corrected for the photon four-momentum. The reconstructed jet four-momentum is not directly used in the missing transverse momentum calculation.

The MPF technique is based on the assumption that the only missing transverse momentum in a γ -jet event arises from calorimeter non-compensation, signal losses due to noise suppression and energy losses in the non-active regions of the detector by the hadronic jet. The transverse momentum balance can be written as:

$$p_T^\gamma + p_T^{\text{jet}} = 0, \quad (24)$$

where p_T^γ and p_T^{jet} is the photon and jet transverse momentum vector. The particles produced by the hard scatter and their interaction in the calorimeter can be expressed in terms of the observables:

$$\mathcal{R}^\gamma p_T^\gamma + \mathcal{R}^{\text{jet}} p_T^{\text{jet}} = -E_T^{\text{miss}}, \quad (25)$$

where \mathcal{R}^γ is the calorimeter response to photons. Since the calorimeter is well calibrated for photons, $\mathcal{R}^\gamma = 1$. The variable \mathcal{R}^{jet} denotes the calorimeter response to jets. By using the

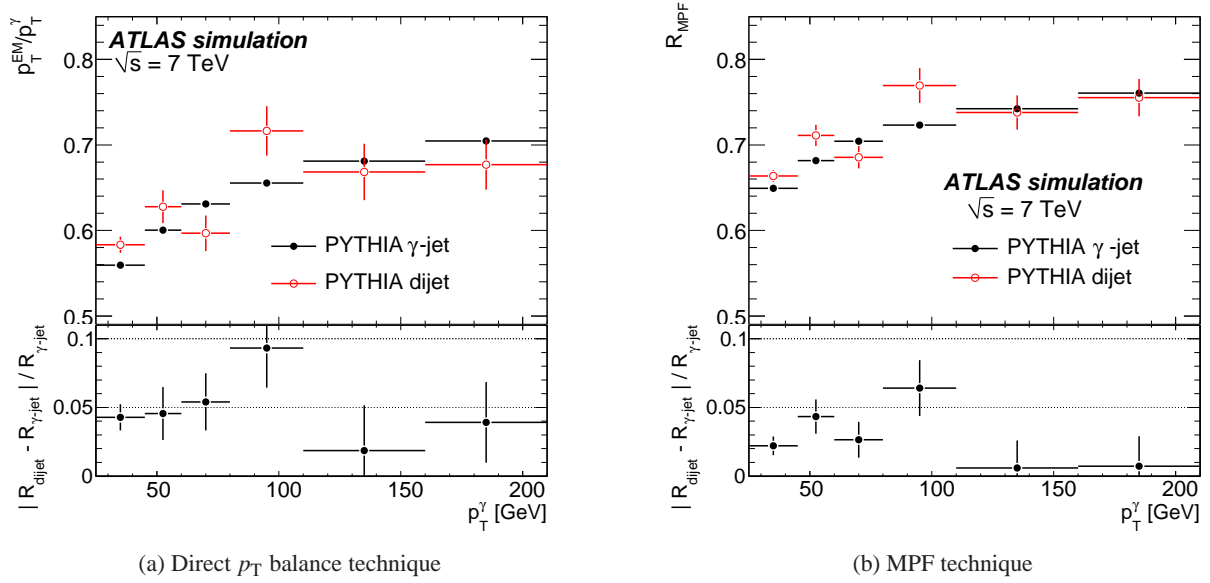


Fig. 28: Average jet response measured at the EM scale as a function of p_T^γ as determined by the direct p_T balance technique for anti- k_t jets with $R = 0.6$ (a) and by the MPF technique (b) for γ -jet events and dijet events where one jet has been reconstructed as a photon, as derived in the Monte Carlo simulation. The lower part of the figures shows the absolute response difference between the dijet and γ -jet events with respect to the response of γ -jet events. Only statistical uncertainties are shown.

Variable	Threshold
$ \eta $	< 1.2
p_T^γ	> 25 GeV
$ \eta^\gamma $	< 1.37
$E_T^{\gamma\text{isolation}}$	< 3 GeV
$\Delta\phi_{\text{jet}-\gamma}$	$> \pi - 0.2$ rad
$p_T^{\text{jet}2}/p_T^\gamma$	$< 10\%$

Table 8: Criteria used to select events with a photon and a jet with high transverse momentum.

above two equations and projecting the E_T^{miss} in the direction of the photon the response can be written as:

$$\mathcal{R}_{\text{MPF}} = 1 + \frac{p_T^\gamma \cdot E_T^{\text{miss}}}{|p_T^\gamma|^2}, \quad (26)$$

which is defined as the MPF response.

Note that the MPF technique measures the calorimeter response by relying only on the photon and E_T^{miss} quantities and does not use the jet energy directly. Therefore the MPF response is independent of the jet algorithm.

10.2.3 Photon-jet Monte Carlo simulation sample

The γ -jet sample is simulated with the event generator PYTHIA using the ATLAS MC10 tune [27].

The systematic uncertainty from jets which are identified as photons (fakes) are studied with an inclusive PYTHIA jet

sample using the MC09 tune [37]²². To efficiently produce this sample a generated event is only fully simulated if it contains at least one generated particle jet with $p_T > 17$ GeV. These jets are computed from the sum of the four-momenta of all stable generated particles within a 0.18×0.18 region in $\eta \times \phi$. Events in the dijet sample with prompt photons, e.g. that are produced by radiation are removed.

10.2.4 Selection of the photon-jet data sample

The leading photon in each event must have $p_T^\gamma > 25$ GeV and lie in the pseudorapidity range $|\eta^\gamma| < 1.37$. In this range the photon is fully contained within the electromagnetic barrel calorimeter. Furthermore, events in which the leading photon is in a calorimeter region where an accurate energy measurement is not possible are rejected. In each event only the leading photon is considered.

The leading photon candidate must also satisfy strict photon identification criteria [66], meaning that the pattern of energy deposition in the calorimeter is consistent with the expected photon showering behaviour. The photon candidate must be isolated from other activity in the calorimeter ($E_T^{\gamma\text{isolation}}$) with an isolation cone of size $R = 0.4$. If the leading photon does not meet all of these criteria, the event is rejected.

Only events are retained that fired an online trigger requiring a photon candidate with $p_T^\gamma > 20$ GeV or $p_T^\gamma > 40$ GeV. At the trigger level the photon identification requirements are less strict than those of the off-line selection.

²² Since a large event statistics is needed for this sample, only a sample with an older tune was available.

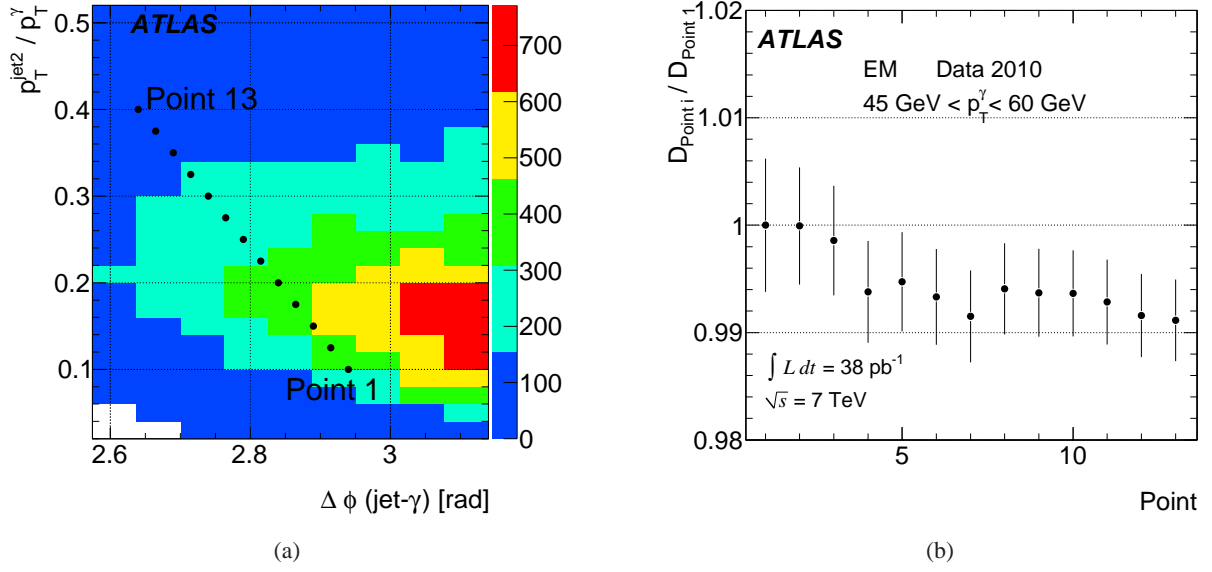


Fig. 29: The values of radiation-suppressing cut thresholds (points) used to probe the soft QCD radiation systematic uncertainty, as a function of $\Delta\phi_{\text{jet-}\gamma}$ and $p_T^{\text{jet2}}/p_T^\gamma$ overlaid with the number of events observed in data (a). The nominal selection is the bottom-rightmost point labelled “Point 1”. Relative change in the MPF response between data and Monte Carlo simulation (b), defined as $D = [\mathcal{R}_{\text{MPF}}]_{\text{Data}} / [\mathcal{R}_{\text{MPF}}]_{\text{MC}}$ from the point given on the x -axis to point 1, when relaxing the soft QCD radiation suppression as indicated in (a). Only statistical uncertainties are shown.

The p_T distribution of photons in events selected with the above criteria is shown in Figure 27. The small discrepancies between the p_T^γ spectrum in data and Monte Carlo simulation do not affect the comparison of the jet response in data and Monte Carlo simulation.

The leading jet must be in the fiducial region $|\eta| < 1.2$. Soft QCD radiation can affect the p_T balance between the jet and photon. The following two selection cuts are applied to suppress this effect. To select events in which the photon and the leading jet are back-to-back, $\Delta\phi_{\text{jet-}\gamma} > \pi - 0.2$ radians is required. The presence of sub-leading jets is suppressed by requiring that the sub-leading jet has p_T less than 10% of the p_T of the leading photon²³. A summary of the event selection criteria can be found in Table 8.

10.2.5 Systematic uncertainties of the photon-jet *in situ* validation technique

Uncertainties due to background from jets identified as photons (fakes), soft QCD radiation, in-time pile-up, non-functional calorimeter read-out regions and the photon energy scale are studied.

Background in the photon-jet sample The systematic uncertainty from jets which are identified as photons (fakes)

²³ This cut is not applied, if it would be below the jet p_T reconstruction threshold of $p_T^{\text{jet}} = 7$ GeV. If in this case a sub-leading jet with $p_T^{\text{jet}} \geq 7$ GeV is present, the event is rejected.

	Direct p_T balance [%]		MPF [%]	
p_T^γ range [GeV]	45 – 60	110 – 160	45 – 60	110 – 160
Background	± 1.0	± 0.4	± 0.6	± 0.1
Soft QCD radiation	± 0.8	± 0.9	± 0.7	± 0.4
In-time pile-up	± 0.8	± 0.8	± 0	± 0
Photon scale	$+0.5$ -0.3	$+0.5$ -0.3	$+0.2$ -0.5	$+0.3$ -0.5
Total systematics	$+1.6$ -1.5	$+1.4$ -1.3	$+0.9$ -1.0	$+0.5$ -0.6

Table 9: Individual systematic uncertainties in the jet energy scale from both the direct p_T balance and the MPF techniques at two values of p_T^γ .

are studied with the inclusive jet Monte Carlo simulation sample described in Section 10.2.3. Dijet events in which one of the jets is misidentified as a photon contribute to the data sample but not to Monte Carlo simulation signal sample. The rate of dijet events faking photons is sensitive to the detailed modelling of the jet fragmentation and the detector simulation, and is therefore subject to large uncertainties.

The systematic uncertainty from this background is determined in two steps. First the difference in the detector response between the γ -jet ($\mathcal{R}_{\gamma\text{-jet}}$) and the filtered dijet sample ($\mathcal{R}_{\text{dijet}}$) is determined in the Monte Carlo simulation as seen in Figure 28. Also shown is the absolute response difference $|\mathcal{R}_{\text{dijet}} - \mathcal{R}_{\gamma\text{-jet}}|$ relative to the response of the γ -jet sample-. A response difference of maximally 3 – 5% is estimated.

To estimate the contribution from background in the signal region the distribution of photon candidates observed in the sidebands of a two-dimensional distribution is used. The

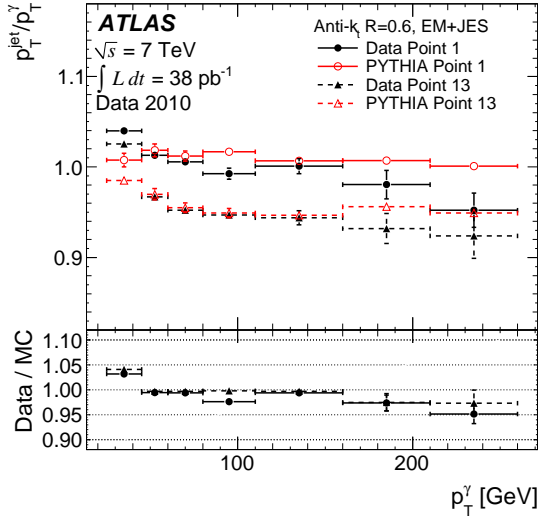


Fig. 30: Average jet response as determined by the direct p_T balance technique with the nominal selection (Point 1) and with a set of relaxed radiation suppression cuts (Point 13), for anti- k_t jets with $R = 0.6$ calibrated with the EM+JES scheme as a function of the photon transverse momentum for data and Monte Carlo simulation. Only statistical uncertainties are shown.

transverse isolation energy, $E_T^{\gamma\text{isolation}}$, and the photon identification of the photon candidate are used for this estimate. On the isolation axis, the signal region contains photon candidates with $E_T^{\gamma\text{isolation}} < 3$ GeV, while the sideband contains photon candidates with $E_T^{\gamma\text{isolation}} > 5$ GeV. On the other axis, photon candidates passing the identification criteria belong to the signal region, while those that fail the tight identification criteria but pass a background-enriching selection belong to the photon identification sideband. Further details are found in Ref. [66].

The purity P measured in the signal sample is about 0.6 at $p_T = 25$ GeV and rises to about 0.95 at higher p_T ²⁴. The systematic uncertainty is then calculated as

$$\varepsilon = \left(\frac{\mathcal{R}_{\text{dijet}} - \mathcal{R}_{\gamma\text{-jet}}}{\mathcal{R}_{\gamma\text{-jet}}} \right) \cdot (1 - P). \quad (27)$$

The systematic uncertainty is below 1% for the direct balance technique and below 0.6% for the MPF technique. The effect of background contamination in the γ -jet sample has been further validated by relaxing the photon identification criteria. Both data and Monte Carlo simulation show a 3% variation in response for the direct p_T balance technique, mostly at low p_T . This is consistent with the systematic uncertainty computed with the purity method using Equation 27, e.g. for the lowest p_T bin 40% of the events are expected to be dijet background giving a response that is 5% higher than the response of γ -jet events.

²⁴ This is similar to the purity measured in Ref. [66] and small differences are due to the different data samples.

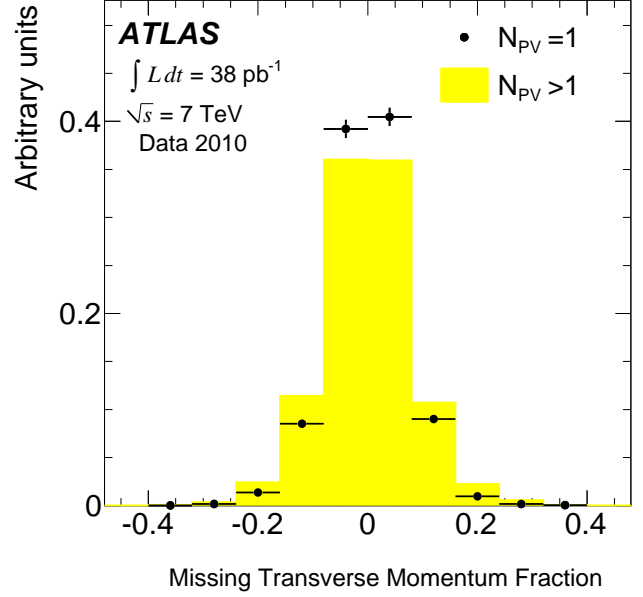


Fig. 31: The missing transverse momentum fraction (MTF) distribution for data with exactly one reconstructed primary vertex N_{PV} , and with more than one reconstructed primary vertex. Only statistical uncertainties are shown.

Soft QCD radiation suppression cuts The stability of the jet response ratio of the data to the Monte Carlo simulation is explored by varying the radiation suppression cuts. Figure 29a shows the thresholds for the $p_T^{\text{jet}2}/p_T^{\gamma}$ and $\Delta\phi_{\text{jet}-\gamma}$ cuts for 13 sets of cuts. Figure 29b illustrates the change in the ratio of the data to the Monte Carlo simulation of the MPF response for each of these 13 sets of cuts, for one typical p_T^{γ} bin. The result demonstrates that the ratio of the data response to the Monte Carlo response is not sensitive to the exact values of the radiation cuts, within the 1% level. The systematic uncertainty is taken as the difference in the data to Monte Carlo ratio between the nominal cuts defining the signal sample, and the loosest cuts in all p_T -bins, labelled as “Point 13” in Figure 29a.

The MPF-determined response changes slightly between the data and the Monte Carlo simulation, the systematic uncertainty is 0.7% at $p_T^{\gamma} = 50$ GeV and falls to 0.4% at $p_T^{\gamma} = 135$ GeV. The quoted values are determined from linear fits to the points analogous to those shown in Figure 29b.

The stability of the ratio of the data to the Monte Carlo simulation for the response measured with the direct p_T balance technique is shown in Figure 30. The response measured in either data or in Monte Carlo simulation varies by up to 10% due to differing radiation suppression cuts. However, the data to Monte Carlo ratio with and without the radiation suppression cuts is stable within $\sim 1\%$.

In-time pile-up The average number of proton-proton collisions in each bunch crossing grew significantly during the data-taking period. Thus, there is a non-negligible fraction of events containing in-time pile-up (see Section 8.1). The additional collisions produce extra particles which can overlap with

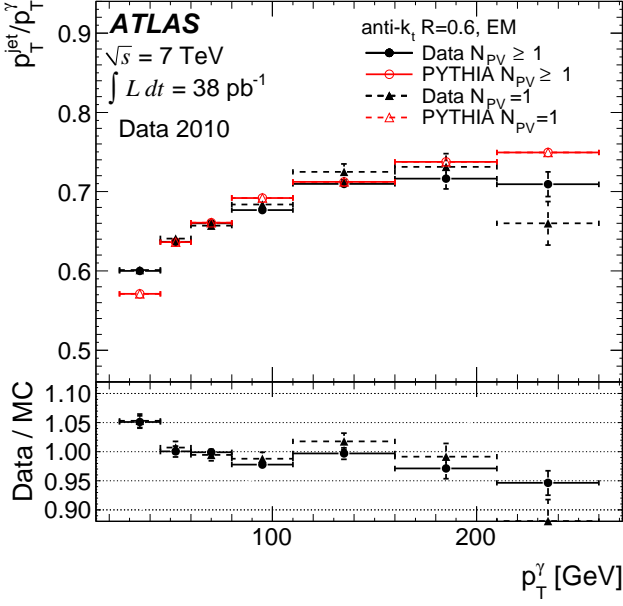


Fig. 32: Average jet response for anti- k_t jets with $R = 0.6$ at the EM scale as determined by the direct p_T balance technique in events with any number of reconstructed primary vertices and in events with exactly one reconstructed vertex as a function of the photon transverse momentum for both data and Monte Carlo simulation. The lower part of the figure shows the data to Monte Carlo simulation ratio. Only statistical uncertainties are shown.

the hard interaction of interest in the ATLAS detector. The increased energy is about 0.5 GeV per additional reconstructed primary vertex (see Section 8.1.4).

The MPF technique is expected to be insensitive to in-time pile-up events. Because in-time pile-up is random and symmetric in ϕ , the mean of the quantity $p_T^\gamma \times E_T^{\text{miss}}$ should be robust against in-time pile-up. The missing transverse fraction (MTF) is defined as:

$$\text{MTF} = \frac{(p_T^\gamma \times E_T^{\text{miss}})_z}{|p_T^\gamma|^2} = \frac{|E_T^{\text{miss}}|}{|p_T^\gamma|} \sin(\phi_{E_T^{\text{miss}}} - \phi_{p_T^\gamma}), \quad (28)$$

where $(p_T^\gamma \times E_T^{\text{miss}})_z$ is the z -component of the vector resulting from the cross product. The MTF measures the activity in the plane perpendicular to the photon p_T . The mean of the MTF is zero, if there is no bias due to in-time pile-up.

Figure 31 shows the MTF distribution for data with and without in-time pile-up. For both these distributions the means are compatible with zero.

From the study of the MTF distribution and other checks, such as the dependence of the MPF on N_{PV} , it can be justified that in-time pile-up can be neglected and no systematic uncertainty is attributed to the MPF method. In the case of the direct p_T balance technique the impact of in-time pile-up is explored by comparing the p_T balance between events with exactly one identified primary vertex and events with any number of vertices. As seen in Figure 32 the ratio of the response in data to the response in Monte Carlo simulation for events with exactly

one vertex and for events with more than one vertex is consistent with a variation of 0.8%. This is taken as a systematic uncertainty.

No effect due to the offset correction for in-time pile-up is seen (see Section 8.1), and no systematic uncertainty is attributed to the offset correction for in-time pile-up.

Impact of missing calorimeter read-out regions For a small subset of the calorimeter channels the calorimeter read-out is not functioning properly. The energy of these calorimeter cells is evaluated using the trigger tower information, which has larger granularity and less accurate resolution. While photons reconstructed in or near such a region are not considered in the analysis, there is no such rejection applied to jets. A sub-sample of events with no jet containing such a cell has been used to evaluate a possible systematic uncertainty between data and simulation. Within the statistical uncertainty, no bias is observed for the MPF γ -jet technique or the direct p_T balance technique, therefore no systematic uncertainty is assigned.

Photon energy scale Both the direct p_T balance and the MPF techniques are sensitive to the photon energy scale. The absolute electron energy scale has been measured *in situ* using the invariant mass constraint in $Z \rightarrow e^+e^-$ for electrons. The uncertainty on the photon energy scale results in a systematic uncertainty smaller than 1%, depending on p_T^{jet} and η .

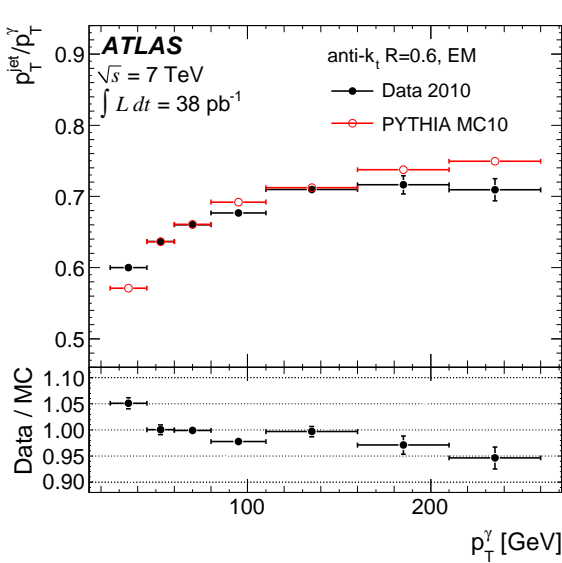
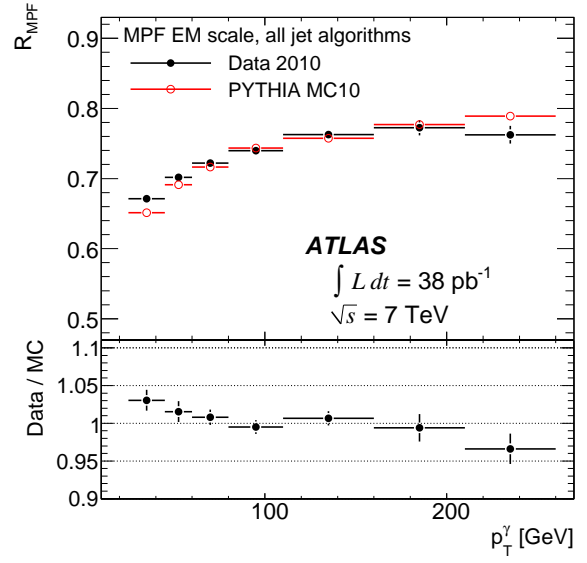
The direct p_T balance technique and the MPF technique find a systematic uncertainty which is approximately opposite in sign. This sign difference is caused by the upwards shift in photon energy leading to an equivalent downwards shift in E_T^{miss} , and vice versa.

The response measured with both the MPF and the direct p_T balance techniques has been studied for converted and non-converted photons. The results of both samples agree within the statistical uncertainties. No additional systematic uncertainty has been considered for this effect, which is already accounted for in the photon energy scale and the photon background systematic uncertainty.

Total systematic uncertainty Table 9 shows a summary of the systematic uncertainties studied for the direct p_T balance and MPF techniques. The total systematic uncertainties for each method are similar, although each method is sensitive to different effects. Total systematic uncertainties are found on the data to Monte Carlo simulation jet response ratio of smaller than 1% for the MPF method and of smaller than 1.6% for direct balance method.

10.2.6 Results from the photon-jet balance

The direct p_T balance and MPF techniques are used to validate the jet response *in situ* by comparing data and Monte Carlo simulation. The response in data and Monte Carlo simulation for the EM scale energy is shown in Figure 33. The jet response in data and Monte Carlo simulation agrees within uncertainties in the range $p_T^\gamma > 45$ GeV. In the range $25 \leq p_T^\gamma < 45$ GeV there

(a) Direct p_T balance technique

(b) MPF technique

Fig. 33: Average jet response as determined by the direct p_T balance for anti- k_t jets with $R = 0.6$ (a) and the MPF technique (b) using the EM scale for both data and Monte Carlo simulation as a function of the photon transverse momentum. The lower part of the figure shows the data to Monte Carlo simulation ratio. Only statistical uncertainties are shown.

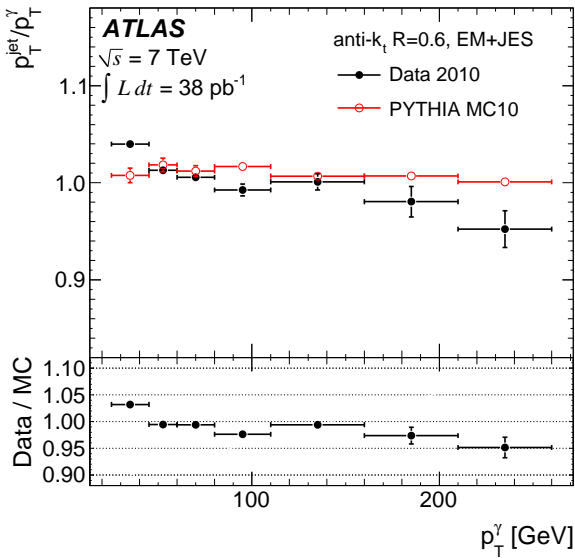


Fig. 34: Average jet response as determined by the direct p_T balance technique for anti- k_t jets with $R = 0.6$ calibrated with the EM+JES scheme as a function of the photon transverse momentum for both data and Monte Carlo simulation. The lower part of the figure shows the data to Monte Carlo simulation ratio. Only statistical uncertainties are shown.

Since the EM+JES calibration depends only on the p_T and η of the jet, it is possible to validate the EM+JES calibration scheme by using the EM scale as a function of p_T^{γ} and η . Figure 34 shows the jet response measured in both data and Monte Carlo simulation using the direct p_T balance technique with the anti- k_t jet algorithm with $R = 0.6$ for the EM+JES calibration scheme. The data to Monte Carlo simulation agreement is within $\pm 5\%$.

Figure 35 shows the ratio of $p_T^{\text{jet}}/p_T^{\gamma}$ between data and Monte Carlo simulation together with the total uncertainty on the determination of the data to Monte Carlo simulation ratio, for anti- k_t jets with $R = 0.6$. Similarly, Figure 36 shows the response ratio of data to Monte Carlo simulation, as determined using the MPF technique together with the total uncertainty on the determination of the data to Monte Carlo simulation ratio.

For $p_T^{\gamma} > 45 \text{ GeV}$, the response in data and Monte Carlo simulation agree to within 3% for both MPF and direct balance techniques up to about 210 GeV. In the range $25 \leq p_T^{\gamma} < 45 \text{ GeV}$ there is an observed shift of 5% for the direct p_T balance technique and 3% for the MPF technique. The lower response at the highest p_T^{γ} is further discussed in Section 10.5.2.

The size of these shifts is consistent with the systematic uncertainty on the EM+JES jet energy calibration (see Section 9). At high p_T^{γ} the dominant uncertainty is statistical while the systematic uncertainty dominates at low p_T^{γ} .

10.2.7 Summary of the photon-jet balance

The validation of the EM+JES calibration scheme for jets with the anti- k_t jet algorithm reconstructed from topo-clusters using *in situ* methods is presented. Agreement between the response

is a shift in the data to Monte Carlo ratio of 5% for the direct p_T balance technique and 3% for the MPF technique.

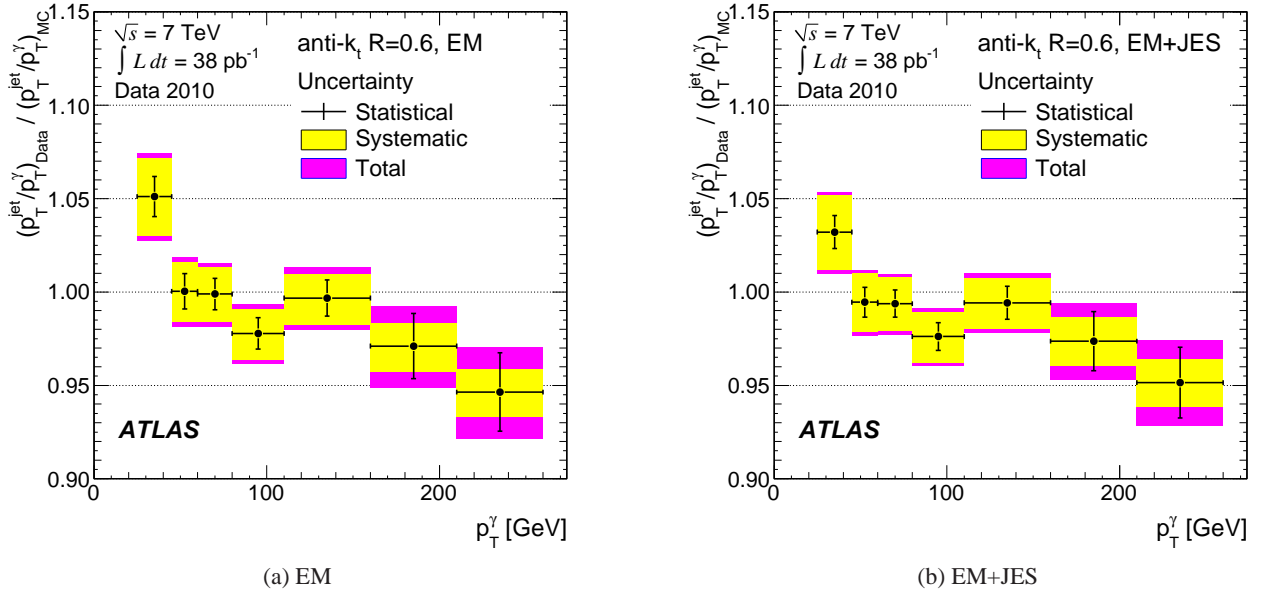


Fig. 35: Average jet response ratio of data to Monte Carlo simulation using the direct p_T balance technique for each input energy scale, EM (a) and EM+JES (b), as a function of the photon transverse momentum. Statistical and systematic uncertainties (light band) are included with the total uncertainty shown as the dark band.

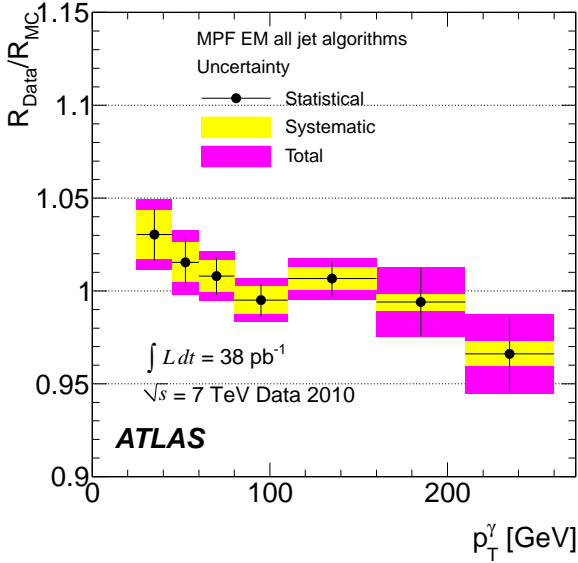


Fig. 36: Average jet response ratio of data to Monte Carlo simulation using the MPF method at the EM scale as a function of the photon transverse momentum. Statistical and systematic uncertainties (light band) are included. The total uncertainty is shown as the dark band.

in data and Monte Carlo simulation is found to be within statistical uncertainties for $45 \leq p_T^\gamma < 210$ GeV. Both techniques observe a shift in the data to Monte Carlo simulation ratio for $25 \leq p_T^\gamma < 45$ GeV. The total systematic uncertainties of the

γ -jet *in situ* technique is estimated to be less than 1.6% for $45 \leq p_T^\gamma < 240$ GeV.

10.3 Multijet transverse momentum balance

The p_T reach in the γ -jet transverse momentum balance technique is limited by the available event statistics. The multijet balance technique where a recoil system of low- p_T jets balances several jets at lower p_T^{jet} can be used to assess the jet calibration at higher p_T . Jet transverse momenta up to the TeV region can be probed. The same method can also be used to obtain correction factors for possible non-linearities at very high p_T^{jet} . Here, the method is only used to assess the JES uncertainty.

10.3.1 The multijet balance technique

The method exploits the p_T balance in events where the highest p_T jet (leading jet) is produced back-to-back in ϕ to a multijet system. The leading jet is required to have significantly larger transverse momentum than other jets in the event. In this way the leading jet is at a higher p_T^{jet} scale compared to other reconstructed jets, called non-leading jets. The ensemble of the non-leading jets passing the selection cuts is referred to as the recoil system.

The event topology used in this analysis is sketched in Figure 37. The vectorial sum of the transverse momenta of all non-leading jets defines the transverse momentum of the recoil system (p_T^{Recoil}), which is expected to approximately balance the transverse momentum of the leading jet (p_T^{Leading}). Thus a correlation between the momentum scale of the leading jet and the

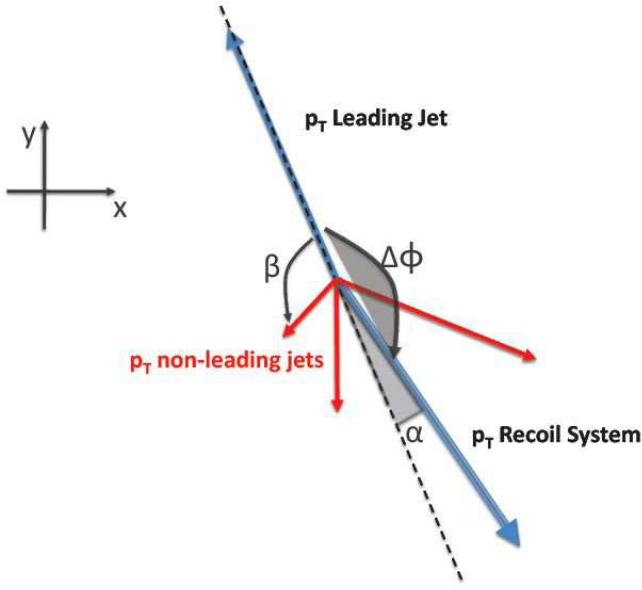


Fig. 37: Sketch of the event topology used for the multijet balance technique in the $x - y$ -plane.

scale of the non-leading jets can be established. If the absolute JES is well-known for all non-leading jets, the JES of the leading jet can be verified by studying the multijet balance (MJB) that is defined as the ratio:

$$\text{MJB} = \frac{|p_T^{\text{Leading}}|}{|p_T^{\text{Recoil}}|}. \quad (29)$$

Moreover, the p_T^{Recoil} is a good estimator of the true leading jet p_T , and it is therefore interesting to study MJB as a function of p_T^{Recoil} . In the ideal case MJB should be equal to one; however, various effects such as the presence of close-by jets, soft gluon emission, pile-up or the selection criteria themselves may introduce a bias.

The comparison between the balance measured in the simulation ($[\text{MJB}]_{\text{MC}}$) and the data ($[\text{MJB}]_{\text{Data}}$) can be interpreted as a source of systematic uncertainty and therefore the ratio

$$r = [\text{MJB}]_{\text{Data}} / [\text{MJB}]_{\text{MC}} \quad (30)$$

can be used to assess the high p_T JES uncertainty.

The jets belonging to the recoil system must be confined to a lower jet energy scale with respect to the leading jet in order to ensure that the multijet balance is testing the absolute high p_T scale and not only the intercalibration between jets. There are various analysis methods to constrain the leading jet to a higher p_T scale with respect to the jets in the recoil system. In this analysis it is done by setting an upper limit on the ratio between the transverse momentum of the second highest p_T jet (p_T^{Jet2}) and the p_T^{Recoil} . This cut is very efficient in selecting multijet events while minimising the bias on the transverse momentum of the leading jet.

Variable	Cut value
Jet p_T	$> 20 \text{ GeV}$
Jet rapidity	$ y < 2.8$
Number of good jets	≥ 3
p_T^{Recoil}	$> 80 \text{ GeV}$
α	$< 0.3 \text{ radian}$
β	$> 1 \text{ radian}$
$p_T^{\text{Jet2}}/p_T^{\text{Recoil}}$	< 0.6

Table 10: Selection criteria to define the event sample for the multijet balance analysis.

10.3.2 Selection of multijet events

Two jet trigger selections have been used to cover a wide p_T range with large enough statistics. The first trigger selection requires at least one jet with $p_T > 15 \text{ GeV}$ at the EM scale in the level-1 calorimeter trigger. The data collected with this trigger are used to cover the region of $p_T^{\text{Recoil}} < 260 \text{ GeV}$. The second trigger selection, which requires at least one jet with $p_T > 95 \text{ GeV}$ for the level-1 trigger, is used to populate the region of $p_T^{\text{jet}} \geq 260 \text{ GeV}$. The two trigger thresholds are fully efficient for jets with $p_T^{\text{Recoil}} > 80 \text{ GeV}$ and $p_T^{\text{jet}} > 250 \text{ GeV}$. To avoid a trigger bias, the multijet balance is studied in events containing a recoil system with transverse momentum larger than 80 GeV .

In order to select events with one jet being produced against a well-defined recoil system, a selection is applied using two angular variables (α and β as depicted in Figure 37):

1. $\alpha = |\Delta\phi - \pi|$, where $\Delta\phi$ is the azimuthal opening angle between the highest p_T jet and the recoil system.
2. β is the azimuthal opening angle of the non-leading jet that is closest to the leading jet in ϕ , measured with respect to the leading jet.

Events are selected by requiring:

1. $\alpha = |\Delta\phi - \pi| < 0.3 \text{ radian}$.
2. $\beta > 1 \text{ radian}$, i.e. no jets within $|\Delta\phi| = 1 \text{ radian}$ around the leading jet.

The cuts applied to α and β retain the bulk of the events.

A further selection is applied to ensure that the leading jet is at a higher scale with respect to the jets composing the recoil system. This is done by requiring that the asymmetry ratio A of p_T^{Jet2} to the transverse momentum of the recoil system satisfies the following inequality:

$$A = \frac{p_T^{\text{Jet2}}}{p_T^{\text{Recoil}}} < 0.6. \quad (31)$$

This cut enables the efficient suppression of events with topologies very close to those of dijet events. This can be seen from the distributions of the ratio of the p_T^{Jet2} to the leading jet p_T shown in Figure 38 before and after the cut is applied. Events are weighted according to the pre-scale values applied at the trigger level.

This selection therefore ensures that the leading jet is at a higher scale with respect to the jets forming the recoil system.

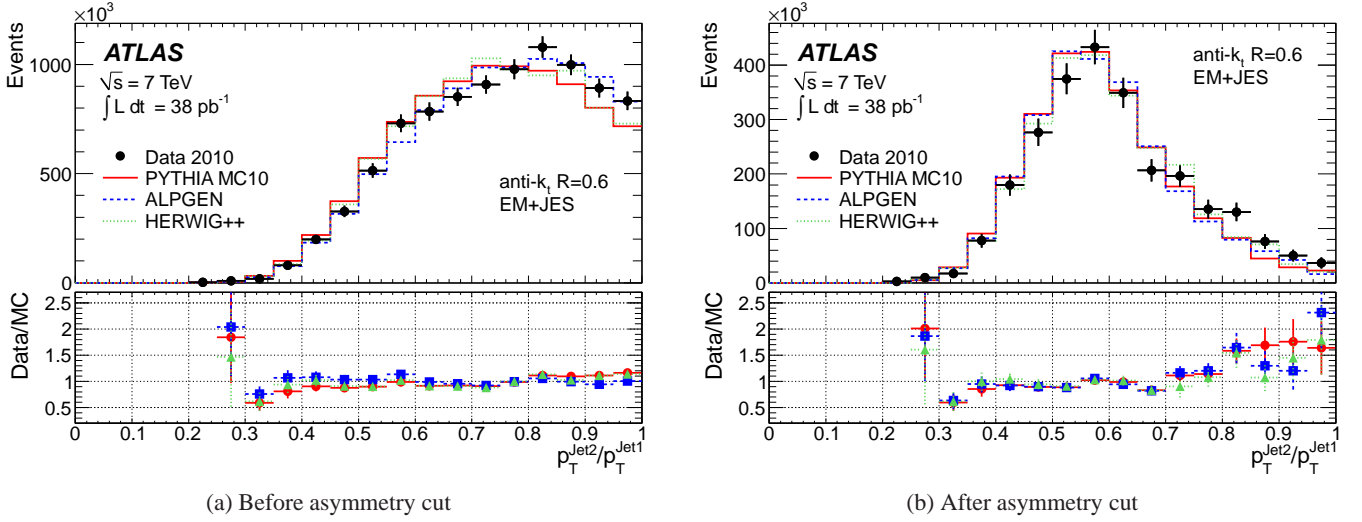


Fig. 38: Distribution of the ratio of the sub-leading to the leading jet p_T for anti- k_t jets with $R = 0.6$ before (a) and after (b) the asymmetry cut, see Equation 31, has been applied for data (full circles) and for simulation (lines). All the distributions in the simulation are normalised to the number of data events. Events selected by pre-scaled triggers have entered the histogram weighted by the pre-scale value. Only statistical uncertainties are shown.

At the same time this cut does not bias either the leading jet p_T or the recoil system p_T . This has been confirmed using Monte Carlo simulation by checking that the average response of the leading jet and recoil system p_T is not significantly shifted from one after the asymmetry cut is applied. A summary of the selection criteria used in the analysis is given in Table 10.

10.3.3 Measurement of the multijet balance

The multijet balance is studied as a function of the transverse momentum of the recoil system, p_T^{Recoil} , which is a good estimator of the true leading jet p_T as shown in Figure 39 for various Monte Carlo simulations. The ratio of reconstructed p_T^{Recoil} to the true leading jet p_T as a function of the true leading jet p_T is, on average, consistent with unity to better than 1%.

The multijet balance obtained from the selected events for the anti- k_t jet algorithm with $R = 0.6$ is shown in Figure 40 for data and Monte Carlo simulation. The transverse momentum of the recoil system ranges from 80 GeV up to 1.0 TeV for the anti- k_t jets with $R = 0.6$.

The multijet balance at low p_T^{Recoil} values shows a bias towards values lower than one. This is a due to effects which broaden the leading jet and the p_T^{Recoil} , and is a direct consequence of binning in p_T^{Recoil} . This effect is observed already for truth jets and is, after reconstruction, correctly reproduced by the Monte Carlo simulation.

The data to Monte Carlo simulation ratio obtained from the multijet balance distributions are shown in the lower part of Figure 40. The average value of the data to Monte Carlo simulation ratio is within 3% for transverse jet momenta up to the TeV-region. The data to Monte Carlo simulation ratio provides an estimate of the uncertainty on the leading jet p_T scale.

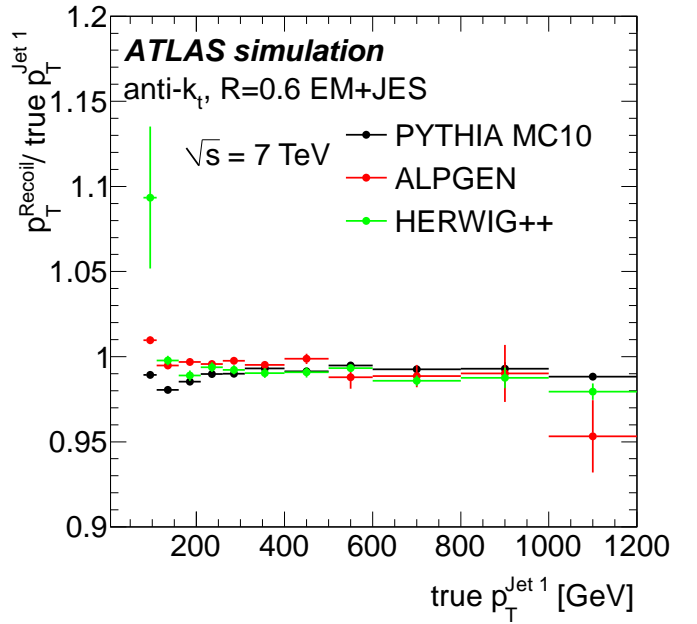


Fig. 39: Ratio of the reconstructed recoil system p_T to the true leading jet p_T for anti- k_t jets with $R = 0.6$ as a function of the true leading jet p_T for three samples of Monte Carlo simulations. Only statistical uncertainties are shown.

10.3.4 Estimate of the systematic uncertainty on the multijet balance

Two main categories of systematic uncertainty have been considered:

1. The reference p_T^{jet} of the recoil system.

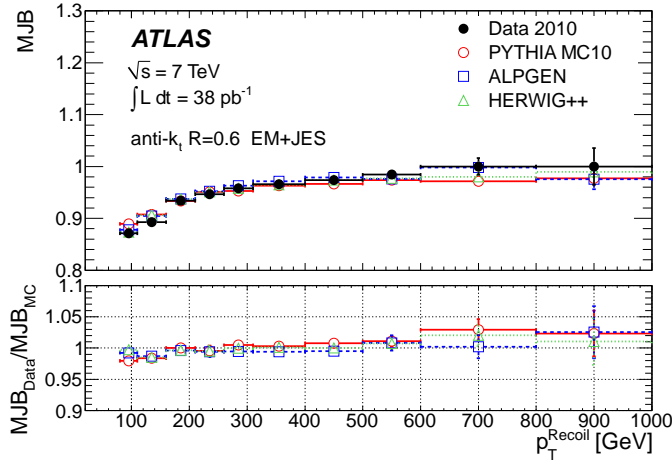


Fig. 40: Multijet balance MJB as a function of the recoil system p_T for data and Monte Carlo simulation for anti- k_t jets with $R = 0.6$. Only statistical uncertainties are shown.

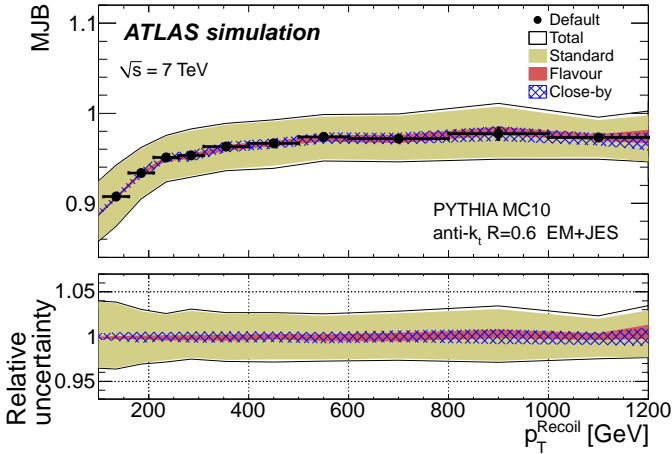


Fig. 41: The multijet balance MJB as a function of p_T^{Recoil} (full dots) with statistical uncertainties for anti- k_t jets with $R = 0.6$. The three bands are defined by the maximum shift of MJB when the jets that compose the recoil system are shifted up and down by the standard JES uncertainty, close-by jet and flavour uncertainties. The black lines show the total uncertainty obtained by adding in quadrature the individual uncertainties. The lower part of the figure shows the relative uncertainty due to the scale uncertainty of the jets that compose the recoil system, defined as the maximum relative shift with respect to the nominal value, as a function of p_T^{Recoil} .

2. The MJB used to probe the leading jet p_T , due to selection criteria or an imperfect Monte Carlo simulation modelling of the event.

The standard JES uncertainty has been obtained for isolated jets. In the case of multijet events the additional uncertainty due to close-by jets (see Section 17) and the different flavour composition (see Section 18) should be taken into account.

The systematic uncertainty on the recoil system has been calculated taking into account the following effects:

1. **JES uncertainty:** The JES uncertainty described in Section 9 is applied to each jet composing the recoil system.
2. **Close-by jet:** Jets belonging to the recoil system are often produced with another jet nearby in the multijet environment, and the jet response is dependent on the angular distance to the closest jet. The close-by jet uncertainty has been estimated by studying the p_T ratio between the calorimeter jets and matched track jets as a function of the jet transverse momentum for different jet isolation cuts. This uncertainty is discussed in more detail in Section 17.
3. **Flavour composition of the recoil system:** The JES uncertainty is estimated for the average jet composition of the inclusive jet sample. A discrepancy in the specific flavour composition between data and Monte Carlo simulation may result in an additional JES uncertainty. The procedure described in Section 18 is used to estimate this uncertainty. It requires as input the average jet response and the flavour composition uncertainty as a function of the jet p_T . In the samples used, the uncertainty on the jet p_T due to flavour composition is about 1%.

The systematic uncertainty on MJB due to the uncertainty on p_T^{Recoil} is estimated by calculating the multijet balance after shifting the p_T of all jets in the recoil system up and down by the systematic uncertainties. The total systematic uncertainty is obtained by summing in quadrature the contribution of each source and is shown in Figure 41 for anti- k_t jets with $R = 0.6$. The contributions of each single source are also shown separately. The standard JES uncertainty is the dominant source of uncertainty over the entire p_T^{jet} range.

The second category of systematic uncertainties includes sources that affect MJB used to probe the jet energy scale at high p_T^{jet} . These are discussed below.

Variable	Nominal	Range
Jet p_T	20 GeV	15-35 GeV
α	0.3 radian	0.1-0.4 radian
β	1.0 radian	0.5-1.5 radian
$p_T^{\text{Jet2}}/p_T^{\text{Recoil}}$	0.6	0.4-0.7

Table 11: Nominal cut values and the range of variation used to evaluate the systematic uncertainty on the selection criteria for the multijet balance technique. Events below the values are rejected.

In the following the various sources considered are discussed:

1. **Selection criteria:** The imperfect description given by the Monte Carlo simulation for the variables used to select the events might induce a systematic uncertainty on the multijet balance. In order to evaluate this systematic uncertainty, all relevant selection criteria are varied in a range where the corresponding kinematic variables are not strongly biased and can be examined with small enough statistical fluctua-

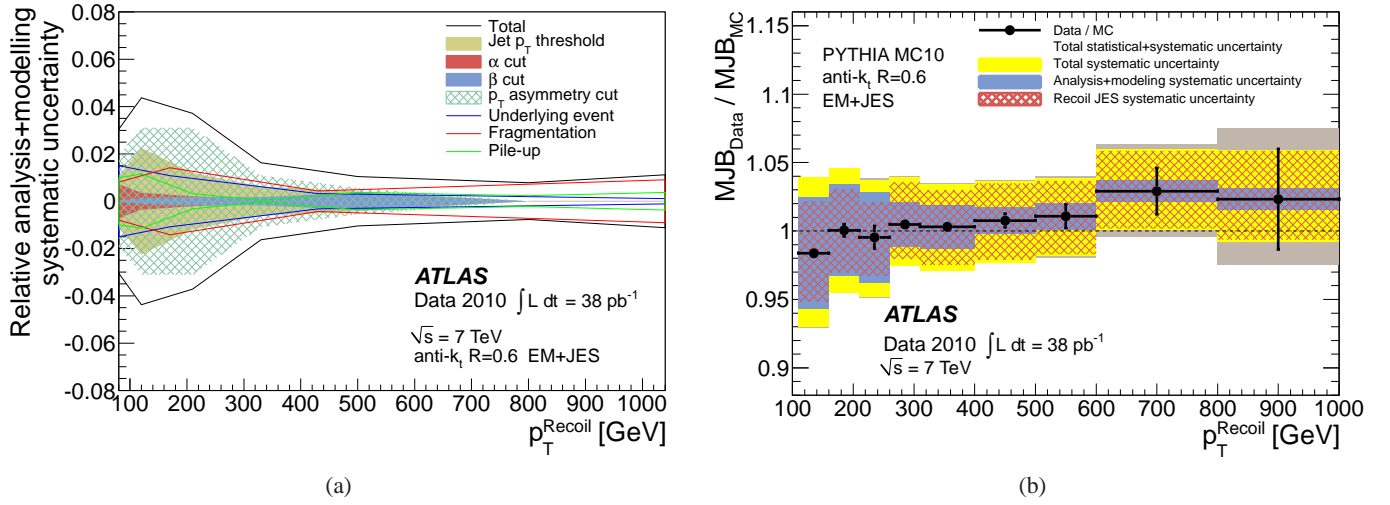


Fig. 42: a) Single contributions as a function of p_T^{Recoil} to the relative uncertainty on MJB due to the sources considered in the selection criteria and event modelling for anti- k_t jets with $R = 0.6$ (various lines) and the total uncertainty (full line) obtained as the squared sum of all uncertainties. b) Ratio of data to Monte Carlo simulation for the multijet balance (MJB) as a function of the recoil system p_T for anti- k_t jets with $R = 0.6$. The various shaded regions show the total uncertainty (dark band) obtained as the squared sum of all total systematic uncertainties (light band) and of the statistical uncertainty (error bars). Also displayed are the contributions to the systematic uncertainty due to multijet analysis cuts and event modelling (darkest band) and to the jet energy scale for jets in the recoil system (hatched band).

Source	uncertainty
Jet energy scale of the recoil system	4%
Flavour composition	$\simeq 1\%$
Close-by jets	2%
Jet p_T threshold	$< 2\%$
α cut	$< 1\%$
β cut	$< 1\%$
$p_T^{\text{Jet2}}/p_T^{\text{Recoil}}$ cut	3%
Underlying event modelling	2%
Fragmentation modelling	1.5%
Pile-up	$< 1\%$

Table 12: Maximum values of the systematic uncertainties in the whole p_T^{Recoil} range for anti- k_t jets with $R = 0.4$ or $R = 0.6$, for all effects considered in the multijet balance analysis.

tions. The nominal values and the range of variations of the selection criteria are listed in Table 11.

The systematic uncertainty on MJB originating from these sources is evaluated by calculating the multijet balance after varying the cut for each variable in the range mentioned above. For each value of the selection criteria the ratio (r) between the MJB values calculated from data and Monte Carlo simulation is evaluated as a function of the recoil system p_T . The maximum deviation of the r with varied cuts (r_{varied}) with respect to the nominal ratio (r_{nominal}), being expressed in the double ratio

$$r_{\text{varied}}/r_{\text{nominal}} \quad (32)$$

is assumed to represent the systematic uncertainty for the source. A quadratic sum of the systematic uncertainties for all sources is taken as the total systematic uncertainty.

2. **Jet rapidity acceptance:** The analysis uses only jets with $|y| < 2.8$ to have a smaller jet energy scale uncertainty on the recoil system. This selection, however, could cause an additional systematic uncertainty, if the fraction of jets produced outside the rapidity range differs in the data and Monte Carlo simulation. This effect is evaluated by studying MJB (calculated as usual from only jets with $|y| < 2.8$) for events with $p_T^{\text{Recoil}} > 80$ GeV, as a function of the total transverse energy ($\sum E_T$) summed over all jets with $|y| < 4.5$, in the data and Monte Carlo simulation. The agreement between the data and Monte Carlo simulation is satisfactory, and MJB is stable over the entire $\sum E_T$ range with the largest deviations up to 3% with the largest deviations at relatively high $\sum E_T$. Since the majority of events have a very small $\sum E_T$, this effect is considered to be negligible.
3. **Soft physics modelling:** Imperfect modelling of multiple parton interactions, of fragmentation and of parton shower radiation may affect the multijet balance in two ways. Firstly the selection criteria may act differently on samples with different modelling of the event topology. Secondly MJB itself can be directly affected, since the modelling variation acts differently on the leading jet and the recoil system. The systematic uncertainty for each of these sources is estimated by evaluating the ratio between the MJB measured using the nominal Monte Carlo simulation and an alternative Monte Carlo simulation sample where the particular

source of uncertainty is varied. As alternative Monte Carlo simulation samples HERWIG++ and PYTHIA with the PE-RUGIA tune are used.

In addition, the parameter controlling the centre-of-mass energy dependence of the cut-off parameter determining whether an event is produced via a matrix element or by the underlying event model (PARP(90)) is lowered from PYTHIA PARP(90)= 0.25 to PYTHIA PARP(90)= 0.16. This change increases the energy in the forward region. The systematic uncertainty introduced by these variations is at most 2%.

4. **Pile-up:** Imperfect description of the pile-up may introduce a systematic uncertainty. This effect is estimated by evaluating the ratio

$$\text{MJB}^{\text{pile-up}} / \text{MJB}^{\text{nominal}}, \quad (33)$$

where the nominal sample is simulated without pile-up collisions. The systematic uncertainty due to pile-up is smaller than 1% for the whole p_T^{jet} range considered.

All systematic uncertainties due to the selection criteria, event modelling and pile-up, and the total uncertainty obtained by summing them in quadrature are shown as a function of p_T^{Recoil} in Figure 42 for anti- k_t jets with $R = 0.6$.

The final systematic uncertainty resulting from the uncertainties of the recoil reference system and from the multijet balance variable added in quadrature is presented in Figure 42b for anti- k_t jets with $R = 0.6$. The total systematic uncertainty amounts to about 4% for jets of $p_T^{\text{jet}} = 1$ TeV. At high transverse momentum the main contribution to the systematic uncertainty is due to the standard JES uncertainty of the EM+JES scheme. The maximum values of the uncertainties in the p_T^{jet} range considered for each source are summarised in Table 12.

10.3.5 Summary of the multijet balance results

The data sample collected in 2010 allows the validation of the high- p_T jet energy scale to within 5% up to 1 TeV for anti- k_t jets with $R = 0.6$ and up to 800 GeV for jets with $R = 0.4$ calibrated with the EM+JES scheme. In this range the statistical uncertainty is roughly equivalent to, or smaller than, the systematic uncertainty.

10.4 Summary of JES validation using *in situ* techniques

The jet energy calibration can be tested *in situ* using a well-calibrated object as reference and comparing data to the PYTHIA Monte Carlo simulation tuned to ATLAS data [26]. The *in situ* techniques have been discussed in the previous sections, i.e. the comparison of jet calorimeter energy to the momentum carried by tracks associated to a jet (Section 10.1), the direct transverse momentum balance between a jet and a photon and the photon balance using the missing transverse momentum projection technique (Section 10.2) as well as p_T balance between a high- p_T jet recoiling against a system of lower p_T jets (Section 10.3)

The comparison of data to Monte Carlo simulation for all *in situ* techniques for the pseudorapidity range $|\eta| < 1.2$ is shown in Figure 43 together with the JES uncertainty region as estimated from the single hadron response measurements and systematic variations of the Monte Carlo simulations. The results of the *in situ* techniques support the estimate of the JES uncertainty obtained using the independent method described in Section 9.

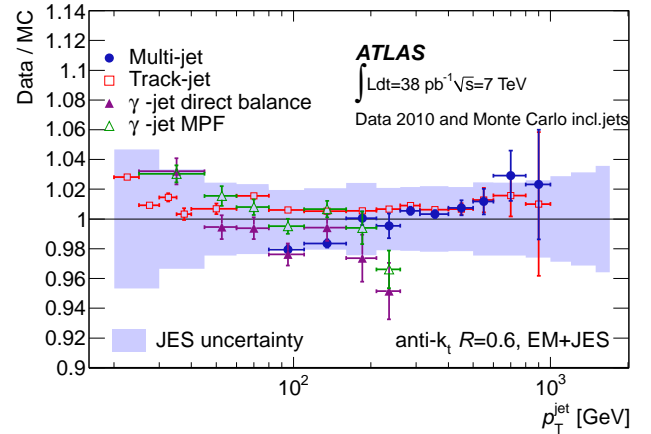


Fig. 43: Ratio of p_T^{jet} over reference p_T in data and Monte Carlo simulation for several *in situ* techniques for $|\eta| < 1.2$. Only statistical uncertainties are shown. Superimposed is the jet energy scale uncertainty obtained from single hadron response measurements and systematic Monte Carlo simulation variations as a function of p_T^{jet} (light band) for $|\eta| < 0.3$.

10.5 JES uncertainty from combination of *in situ* techniques

The JES uncertainty can also be obtained by combining the results of the *in situ* techniques described in the previous sections. In this combination the ability of the Monte Carlo simulation to describe the data, the individual uncertainties of the *in situ* techniques and their compatibility are considered.

10.5.1 Combination technique

The requirements for combining the uncertainties from the individual *in situ* techniques are:

1. Propagate all uncertainties of the individual *in situ* techniques to the final uncertainty.
2. Minimise biases on the shapes of the measured distributions, i.e. on the p_T dependence of the data to Monte Carlo simulation ratio.
3. Optimise the uncertainties on the average while respecting the two previous requirements. This is equivalent to minimise the χ^2 between the average and the individual measurements.

The combination proceeds in the following steps:

1. **Toy Monte Carlo method:** Monte Carlo pseudo-experiments are created that represent the ensemble of measurements and contain the full data treatment chain including interpolation and averaging (as described in the following steps). These pseudo-experiments are used to consistently propagate all uncertainties into the evaluation of the average. The pseudo-experiments represent the full list of available measurements and take into account all known correlations.
2. **Interpolation method:** A linear interpolation is used to obtain the nominal values²⁵. The final interpolation function per measurement, within the p_T range, is discretised into small (1 GeV) bins for the purpose of averaging.
3. **Averaging:** The data are averaged taking into account all known correlations to minimise the spread in the average measured from the Monte Carlo pseudo-experiments.

The combination of the *in situ* calibration data is performed using the software package HVPTools [67]. The systematic uncertainties are introduced in HVPTools for each component as an algebraic function of p_T or as a numerical value for each data point. The systematic uncertainties belonging to the same source are taken to be fully correlated throughout all measurements affected.

The HVPTools package transforms the *in situ* data and associated statistical and systematic covariance matrices into fine-grained p_T bins, taking into account the best knowledge of the correlations between the points within each *in situ* measurement. Statistical and systematic correlations between the measurements could also be included, but as the different measurements use independent events, these correlations are neglected²⁶. The covariance matrices are obtained by assuming systematic uncertainties corresponding to the same source are fully correlated. Statistical uncertainties, taken as independent between the data points, are added in quadrature to these matrices.

The interpolated measurements from different *in situ* methods contributing to a given momentum bin are averaged taking correlations between measurement points into account. The measurements are performed at different p_T^{jet} values and use different binning (point densities)²⁷.

To derive proper *averaging weights* for each *in situ* method, wider *averaging regions*²⁸ are defined. These regions are constructed such that all *in situ* method covering the corresponding

p_T range have at least one measurement inside. The averaging regions are used to compute weights for the *in situ* methods, which are later applied in the bin-wise average in fine 1 GeV bins.

The averaging weights for each *in situ* method are computed as follows:

1. The generation of pseudo-experiments fluctuates the data points around the original measurements taking into account all known correlations. The polynomial interpolation is redone for each pseudo-experiment for each *in situ* method.
2. For each *in situ* measurement and each Monte Carlo pseudo-experiment the new bin content for each wider region is calculated from the integral of the interpolating polynomials.
3. The contents of the wide bins are treated as new measurements and are again interpolated with polynomials. The interpolation function is used to obtain new measurements in small (1 GeV) bins for each *in situ* method in the p_T^{jet} range covered by it.
4. In each small bin a covariance matrix (diagonal here) between the measurements of each *in situ* method is computed. Using this matrix the averaging weights are obtained by χ^2 minimisation.

For the averaging weights the procedure using the large averaging regions as an intermediate step is important in order to perform a meaningful comparison of the precision of the different *in situ* methods. The average is computed avoiding shape biases which would come from the use of large bins. Therefore at this next step the fine 1 GeV bins are obtained directly from the interpolation of the original bins.

The bin-wise average between measurements is computed as follows:

1. The generation of Monte Carlo pseudo-experiments fluctuates the data points around the original measurements taking into account all known correlations. The polynomial interpolation is redone for each generated Monte Carlo pseudo-experiment for each *in situ* method.
2. For each generated pseudo-experiment, small (1 GeV) bins are filled for each measurement in the momentum intervals covered by that *in situ* method, using the polynomial interpolation.
3. The average and its uncertainty are computed in each small bin using the weights previously obtained. This will be displayed as a band with the central value given by the average while the total uncertainty on the average is represented by the band width.
4. The covariance matrix among the measurements is computed in each small bin.
5. χ^2 rescaling corrections are computed for each bin as follows: if the χ^2 value of a bin-wise average exceeds the number of degrees of freedom (n_{dof}), the uncertainty on the average is rescaled by $\sqrt{\chi^2/n_{\text{dof}}}$ to account for inconsistencies²⁹.

points of the other measurement would be statistically merged before computing the averaging weights.

²⁹ Such (small) inconsistencies are seen in the comparison of the γ -jet and track jet results in one p_T^{jet} bin.

²⁵ A second order polynomial interpolation provides in principle a better shape description. However, due to the smooth variations in the results of each *in situ* measurement, the differences between the results obtained with the two interpolation procedures are found to be negligible.

²⁶ Care was taken to avoid an overlap of the multijet balance and γ -jet result. Allowing for an overlap would have required taking into account the (strong) correlations, without a potential gain in precision.

²⁷ The method avoids replacing missing information in case of a lower point density (wider binning) by extrapolating information from the polynomial interpolation.

²⁸ For example, when averaging two measurements with unequal point spacing, a useful averaging region would be defined by the measurement of the *in situ* method with the larger point spacing, and the

The final systematic uncertainty for a given jet momentum is (conservatively) estimated by the maximum deviation between the average band and unity. The central value (measured bias) and the uncertainty on the average measurement are hence taken into account. If a correction for the measured bias were performed, only the relative uncertainty on the average would affect the final JES calibration.

A smoothing procedure, using a variable-size sliding interval with a Gaussian kernel, is applied to the systematic uncertainty. It removes spikes due to statistical fluctuations in the measurements, as well as discontinuities at the first and/or last point in a given measurement.

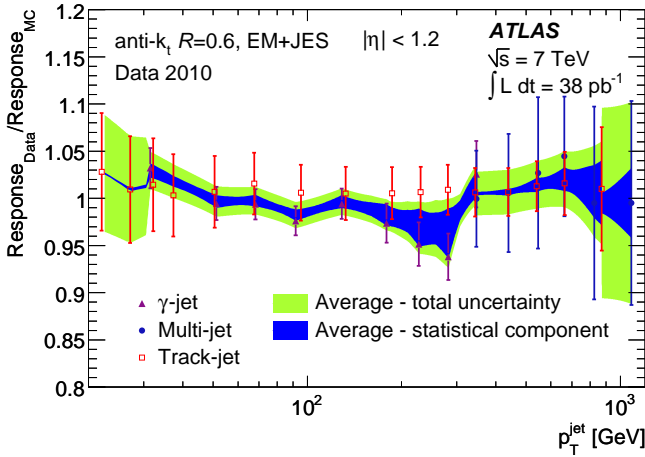


Fig. 44: Average jet response ratio of the data to the Monte Carlo simulation for jets with $|\eta| < 1.2$ as a function of the transverse jet momentum p_T for three *in situ* techniques. The error displays the statistical and systematic uncertainties added in quadrature. Shown are the results for anti- k_t jets with $R = 0.6$ calibrated with the EM+JES scheme. The light band indicates the total uncertainty from the combination of the *in situ* techniques. The inner dark band indicates the statistical component.

10.5.2 Combination results

Following the method described in the previous section the JES uncertainty for jets with $|\eta| < 1.2$ can be obtained. The multijet balance analysis is repeated for jets with $|\eta| < 1.2$, and the uncertainty for low- p_T jets is taken from the γ -jet analysis. The resulting uncertainty is larger than the one in Section 10.3.

Figure 44 shows the ratio of the jet response in data and Monte Carlo simulation as a function of the transverse jet momentum for the three *in situ* techniques using as reference objects photons (γ -jet), a system of low-energetic jets (multijet) or the transverse momentum of all tracks associated to jets (track jet). The errors shown for each *in situ* technique are the statistical and systematic uncertainties added in quadrature.

The results from the track jets cover the widest p_T^{jet} range from the lowest to the highest p_T^{jet} values. Compared to the γ -jet

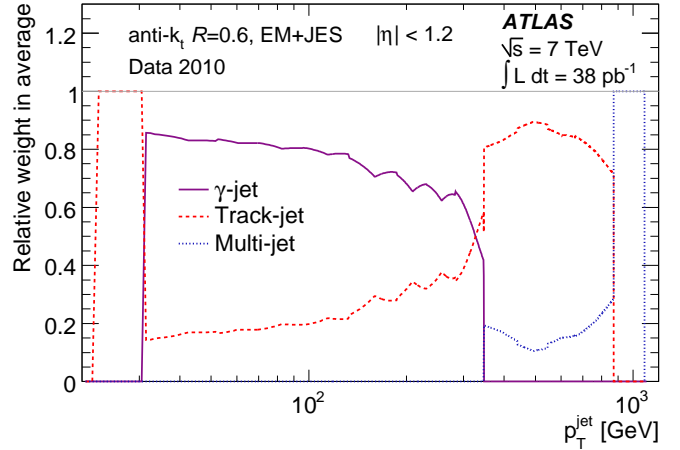


Fig. 45: Weight carried by each *in situ* technique in the combination to derive the jet energy scale uncertainty as a function of the jet transverse momentum p_T^{jet} for anti- k_t jets with $R = 0.6$ calibrated with the EM+JES scheme.

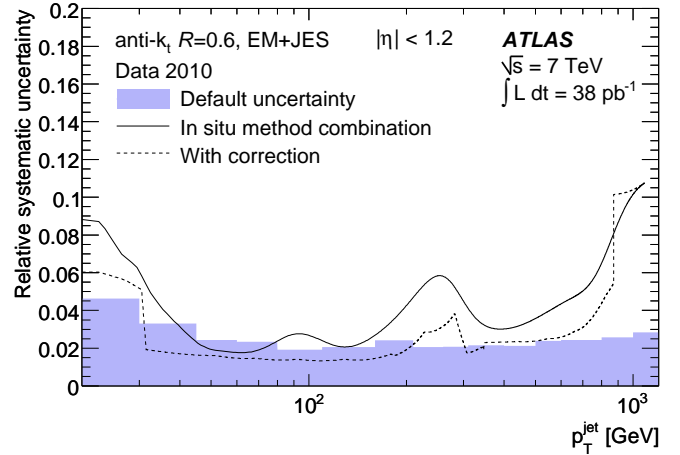


Fig. 46: Jet energy scale uncertainty from the combination of *in situ* techniques (solid line) as a function of the jet transverse momentum p_T for anti- k_t jets with $R = 0.6$ calibrated with the EM+JES scheme for $|\eta| < 1.2$. The dashed line shows the JES uncertainty that could have been achieved, if *in situ* techniques had been used to recalibrate the jets. For comparison, the shaded band indicates the JES uncertainties as derived from the single hadron response measurements and systematic Monte Carlo variations for $|\eta| < 0.3$.

results they have a relatively large systematic uncertainty. The γ -jet results cover a p_T^{jet} range up to about 300 GeV. From this point onwards the multijet balance method helps to constrain the JES uncertainty.

Figure 45 shows the contribution of each *in situ* technique to the total JES uncertainty in form of their weight. In the region $30 \lesssim p_T^{\text{jet}} \lesssim 300$ GeV the γ -jet results make the highest contribution to the overall JES uncertainty determination. The contribution is about 80% at $p_T^{\text{jet}} = 30$ GeV and decreases to

about 60% at $p_T^{\text{jet}} = 300$ GeV. At the lowest p_T^{jet} the method based on tracks determines the JES uncertainty. At about $p_T^{\text{jet}} = 300$ GeV the γ -jet results and the ones based on tracks have an about equal contribution. Above $p_T^{\text{jet}} = 300$ GeV the results based on tracks have the highest contribution to the JES uncertainty. In this region the multijet balance contributes to the JES uncertainty to about 20%. For the highest p_T^{jet} only the multijet balance is used to determine the JES uncertainty.

The final JES uncertainty obtained from the combination of the *in situ* techniques is shown in Figure 46. The JES uncertainty is about 9% at $p_T^{\text{jet}} = 20$ GeV and decreases to about 2 – 3% for $50 \leq p_T^{\text{jet}} < 200$ GeV. At the lowest p_T^{jet} the systematic uncertainty is determined by the *in situ* method based on tracks, for which the data have a higher central value than the Monte Carlo simulation. At 250 GeV, the uncertainty increases because the γ -jet results are 5% below unity and therefore pull the central value of the average down as shown in Figure 44. Moreover, the γ -jet and the track methods give different results. While for all other p_T^{jet} values the χ^2/n_{dof} is within $0.2 \leq \chi^2/n_{\text{dof}} < 0.8$, it rises to $\chi^2/n_{\text{dof}} = 2$ at 250 GeV.

For $p_T^{\text{jet}} > 350$ GeV the multijet balance contributes to the uncertainty and the resulting uncertainty is about 4 – 5% up to 700 GeV. At the highest reachable p_T^{jet} the JES uncertainty increases to 10%.

Figure 46 also compares the JES uncertainty obtained from a combination of *in situ* techniques to the one derived from the single hadron response measurements and the systematic Monte Carlo simulation variations (see Section 9). The *in situ* JES uncertainty is larger than the standard JES uncertainty in most p_T^{jet} regions. It is similar in the region $30 \lesssim p_T^{\text{jet}} \lesssim 150$ GeV. Figure 46 also shows the JES uncertainty, that could have been achieved, if the *in situ* techniques had been used to correct the jet energy scale. In this case the JES uncertainty obtained from a combination of *in situ* techniques would be slightly smaller than the standard JES uncertainty over a wide p_T^{jet} range of 30 – 700 GeV.

11 Jet energy calibration based on global jet properties

11.1 Global sequential technique

The global sequential calibration (GS) technique is a multivariate extension of the EM+JES calibration. Any variable x that is correlated with the detector response to the jet can be used. A multiplicative correction to the jet energy measurement is derived by inverting the calibrated jet response \mathcal{R} as a function of this variable:

$$C(x) = \mathcal{R}^{-1}(x) / \langle \mathcal{R}^{-1}(x) \rangle, \quad (34)$$

where $\langle \mathcal{R}^{-1}(x) \rangle$ denotes the average inverse jet response. After this correction, the remaining dependence of the response on the variable x is removed without changing the average energy, resulting in a reduction of the spread of the reconstructed jet energy and, thus, an improvement in resolution.

Several variables can be used sequentially to achieve the optimal resolution. This procedure requires that the correction for a given variable x_i (C^i) is calculated using jets to which the correction for the previous variable x_{i-1} (C^{i-1}) has already been applied. The jet transverse momentum after correction number i is given by :

$$p_T^i = C^i(x_i) \times p_T^{i-1} = C^i(x_i) \times C^{i-1}(x_{i-1}) \times p_T^{i-2} = \dots \quad (35)$$

11.2 Properties derived from the internal jet structure

The jet properties used in the GS calibration characterise the longitudinal and transverse topology of the energy deposited by the jet. A large energy deposit in the hadronic layers indicates, for example, a larger hadronic component of the jet implying an on average lower detector response in the non-compensating ATLAS calorimeter. Close to a crack region, the transverse extent of the jet is correlated to how many particles of the jet hit the poorly instrumented transition region.

Each of these jet properties may be sensitive to several effects: energy deposited in the dead material, non-compensation of the calorimeter, or unmeasured energy due to the noise suppression. In the GS calibration, no attempt is made to separate these effects. The jet properties help to significantly improve the jet energy resolution, and implicitly correct on average for these effects.

The longitudinal structure of the jet³⁰ is characterised by the fractional energy deposited in the different layers of the calorimeters before any jet calibration is applied (“layer fractions”) :

$$f_{\text{layer}} = \frac{E_{\text{EM}}^{\text{layer}}}{E_{\text{EM}}^{\text{jet}}}, \quad (36)$$

where $E_{\text{EM}}^{\text{jet}}$ is the jet energy at the EM scale and $E_{\text{EM}}^{\text{layer}}$ the energy deposited in the layer of interest, also defined at the EM scale. The transverse jet structure can be characterised by the jet width defined as:

$$\text{width} = \frac{\sum_i p_T^i \Delta R_{i,\text{jet}}}{\sum_i p_T^i}, \quad (37)$$

where the sums are over the jet constituents (i) and p_T is the transverse constituent momentum. $\Delta R_{i,\text{jet}}$ is the distance in $\eta \times \phi$ -space between the jet constituents and the jet axis. In the following study topo-clusters are used as jet constituents.

11.3 Derivation of the global sequential correction

The GS corrections are determined in jet $|\eta|$ bins of width 0.1 from $|\eta| = 0$ to $|\eta| = 4.5$. In each bin, the jet properties that provide the largest improvement in jet energy resolution have been selected in an empirical way. The chosen jet properties and the order in which they are applied are summarised in Table 13. The improvement in resolution obtained is found to be

$ \eta $ region	Corr 1	Corr 2	Corr 3	Corr 4
$ \eta < 1.2$	$f_{\text{Til}e0}$	$f_{\text{LAr}3}$	f_{ps}	width
$1.2 \leq \eta < 1.4$	$f_{\text{Til}e0}$			width
$1.4 \leq \eta < 1.7$	$f_{\text{Til}e0}$	$f_{\text{HEC}0}$		width
$1.7 \leq \eta < 3.0$		$f_{\text{HEC}0}$		width
$3.0 \leq \eta < 3.2$		$f_{\text{LAr}3}$		width
$3.2 \leq \eta < 3.4$		$f_{\text{LAr}3}$		
$3.4 \leq \eta < 3.5$		$f_{\text{LAr}3}$		width
$3.5 \leq \eta < 3.8$	$f_{\text{FCal}1}$			width
$3.8 \leq \eta < 4.5$	$f_{\text{FCal}1}$			

Table 13: Sequence of corrections in the GS calibration scheme in each $|\eta|$ region.

independent of which property is used first to derive a correction.

In the following section, “GSL” refers to the calibration applied up to the third correction (containing only the calorimeter layer fraction corrections) and “GS” to the calibration applied up to the last correction (including the width correction).

12 Jet energy scale uncertainties for jet calibrations based on global jet properties

The JES uncertainties in the global sequential jet calibration scheme are evaluated using the transverse momentum balance in events with only two jets at high transverse momentum.

By construction the GS calibration scheme preserves the energy scale of the EM+JES calibration scheme for the event sample from which the corrections have been derived. Possible changes of the JES in event samples with different topologies or jet flavours are studied in Section 19.

12.1 Validation of the global sequential calibration using dijet events

12.1.1 Dijet balance method

The GS corrections can be derived from dijet events using the dijet balance method. This method is a tag-and-probe technique exploiting the p_T imbalance between two back-to-back jets. In contrast to the method presented in Section 9.6, a correction for a truth jet imbalance is applied.

Dijet events are selected by requiring that the two highest p_T jets are back-to-back ($\Delta\phi > 2.8$ radian). The two jets are required to be in the same pseudorapidity region.

The jet whose response dependence on the layer fractions or width is studied, is referred to as the probe jet, while the other is referred to as the reference jet. The average transverse momentum of the probe and the reference jet is defined as

$$p_T^{\text{avg}} = (p_T^{\text{probe}} + p_T^{\text{ref}})/2. \quad (38)$$

Since the choice of the reference jet and the probe jet is arbitrary, events are always used twice, inverting the roles of reference and probe.

³⁰ Here, longitudinal refers to the direction along the jet axis.

The GS corrections are measured through the asymmetry variable defined as:

$$A(x) = \frac{p_T^{\text{probe}}(x) - p_T^{\text{ref}}}{p_T^{\text{avg}}(x)}, \quad (39)$$

where x is any of the properties used in the GS calibration (see Table 13). Both p_T^{probe} and p_T^{ref} depend on x , but the dependence is explicitly written only for the probe jet, because the jet property used to build the correction belongs to the probe jet.

The probe and the reference jet transverse momenta are defined with the same calibration. When computing correction factor i , they are both corrected up to the $(i-1)^{\text{th}}$ correction (see Section 11.1). The mean response as a function of x is given by:

$$\langle R(x) \rangle = \frac{1 + \langle A(x) \rangle / 2}{1 - \langle A(x) \rangle / 2}. \quad (40)$$

The measurement of the response through the asymmetry defined in Equation 39 assumes that the asymmetry is zero. This is true on average, but not when computed in bins of x . The measured asymmetry $A(x)$ is therefore a mixture of detector effects and imbalance at the level of the generated particles. In order to remove the effect of imbalance at the level of generated particles, a new asymmetry is defined:

$$A'(x) = A(x) - A_{\text{true}}(x), \quad (41)$$

where $A(x)$ is given by Equation 39 and $A_{\text{true}}(x)$ is:

$$A_{\text{true}}(x) = \frac{p_{T,\text{true}}^{\text{probe}}(x) - p_{T,\text{true}}^{\text{ref}}}{p_{T,\text{true}}^{\text{avg}}(x)}, \quad (42)$$

where $p_{T,\text{true}}^{\text{avg}}(x) = (p_{T,\text{true}}^{\text{probe}}(x) + p_{T,\text{true}}^{\text{ref}})/2$. The variable A_{true} denotes the asymmetry for truth jets (or true asymmetry) and is calculated by matching reconstructed jets to truth jets. The asymmetry A_{true} is determined in the Monte Carlo simulation. When using $A'(x)$ instead of $A(x)$ in Equation 40, the effects of imbalance at the level of generated particles are removed and the resulting response depends only on detector effects. Accounting for the truth jet imbalance is particularly important for the corrections that depend on the energy in the presampler and the jet width.

12.1.2 Validation of the dijet balance method in the Monte Carlo simulation

The dijet balance method can be checked in two different ways.

The first uses the default PYTHIA event sample with the MC10 tune and compares the response calculated using Equation 40 to the response calculated using the truth jets. Figure 47 shows this comparison for jets after the EM+JES calibration for $80 \leq p_T^{\text{jet}} < 110$ GeV and $|\eta| < 0.6$. The results obtained using the asymmetry defined as in Equation 39 and when incorporating the true asymmetry are shown. If the true asymmetry were ignored, the calculated response would be different from the true jet response by up to 4% for high values of the jet width and the presampler fraction in this particular p_T^{jet} bin. This difference increases with decreasing p_T^{jet} reaching 8% for jets of

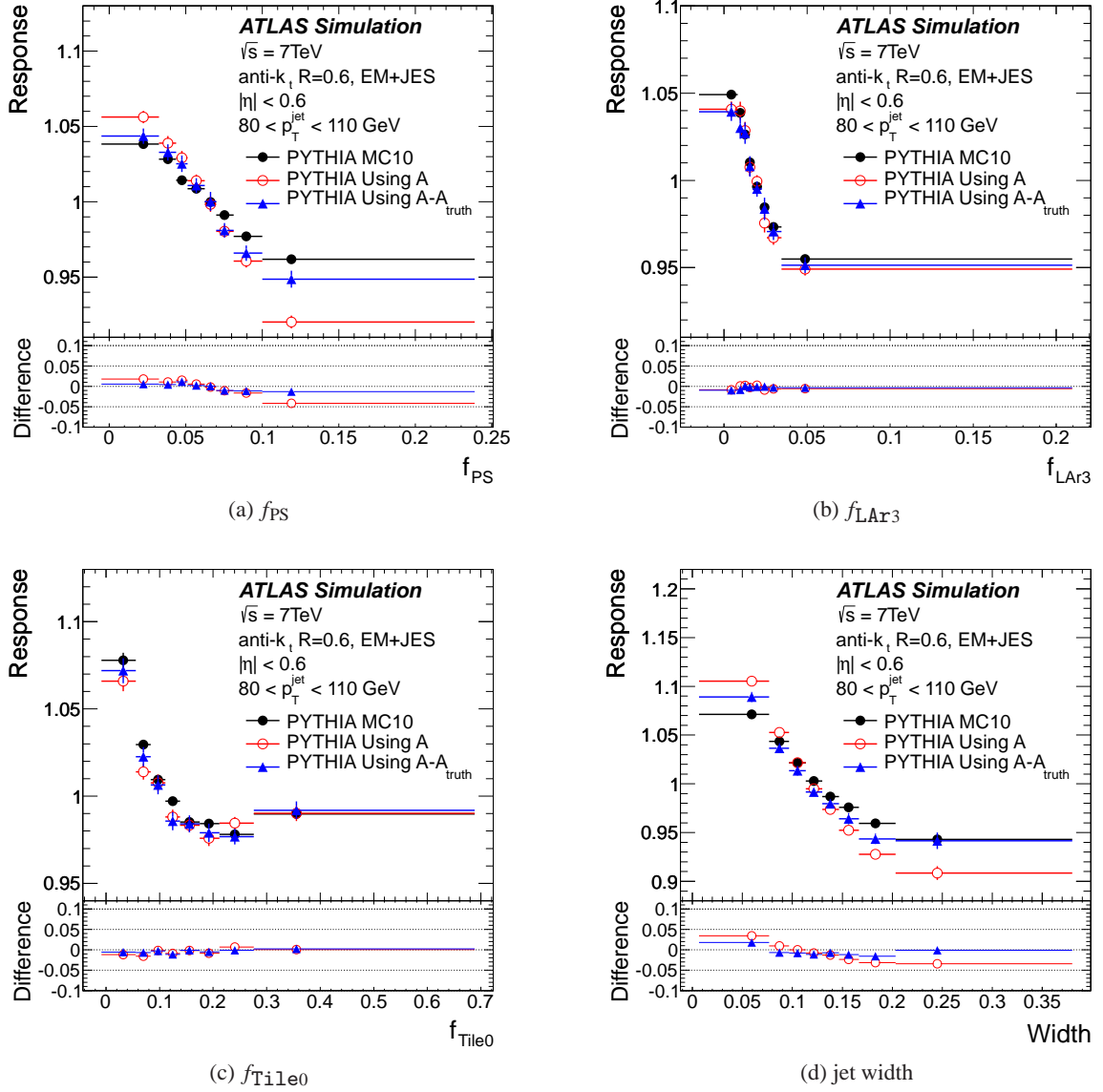


Fig. 47: Average jet response calculated using truth jets (full circles), using the reconstructed asymmetry A (open circles), and using $A - A_{\text{true}}$ (triangles) as a function of the calorimeter layer energy fraction f_{PS} (a), f_{LAr3} (b), f_{Tile0} (c) and the lateral jet width (d) in the PYTHIA MC10 sample. The lower part of each figure shows the differences between the response calculated using the truth jet and the one calculated with the dijet balance method without A_{true} (full triangles) and with A_{true} (open circles). Anti- k_t jets with $R = 0.6$ calibrated with the EM+JES scheme are used and have $80 \leq p_T^{\text{jet}} < 110\text{ GeV}$ and $|\eta| < 0.6$.

$p_T^{\text{jet}} \approx 20\text{ GeV}$. These differences are reduced to less than 2% when a correction for A_{true} is used. Similar results are found in the other p_T^{jet} and $|\eta|$ bins.

The second test compares the true asymmetry between different simulated samples. Figure 48 shows the true asymmetry as a function of f_{PS} , f_{LAr3} , f_{Tile0} and the jet width in the central region for $40 \leq p_T^{\text{jet}} < 60\text{ GeV}$ for various event samples: the reference PYTHIA sample with the MC10 tune, the PYTHIA sample with the PERUGIA2010 tune and the HERWIG++ sample. The last two samples test the sensitivity to the description of soft physics or the specifics of the hadronisation process that could cause differences in the truth jet imbalance. The true

asymmetry differs by no more than 5% in this particular p_T^{jet} and η bin. For $p_T^{\text{jet}} > 60\text{ GeV}$ and other $|\eta|$ bins, the true asymmetries differ by less than 2%. At low p_T^{jet} (below 40 GeV in the barrel), the $\Delta\phi$ cut, in particular combined with the small PERUGIA2010 and HERWIG++ samples yield statistical uncertainties of the order of 5%.

In summary, the dijet balance method allows the determination of the response as a function of the layer fractions and the jet width over the entire transverse jet momentum and pseudorapidity ranges. This method can therefore be applied to data to validate the corrections derived in the Monte Carlo simulation.

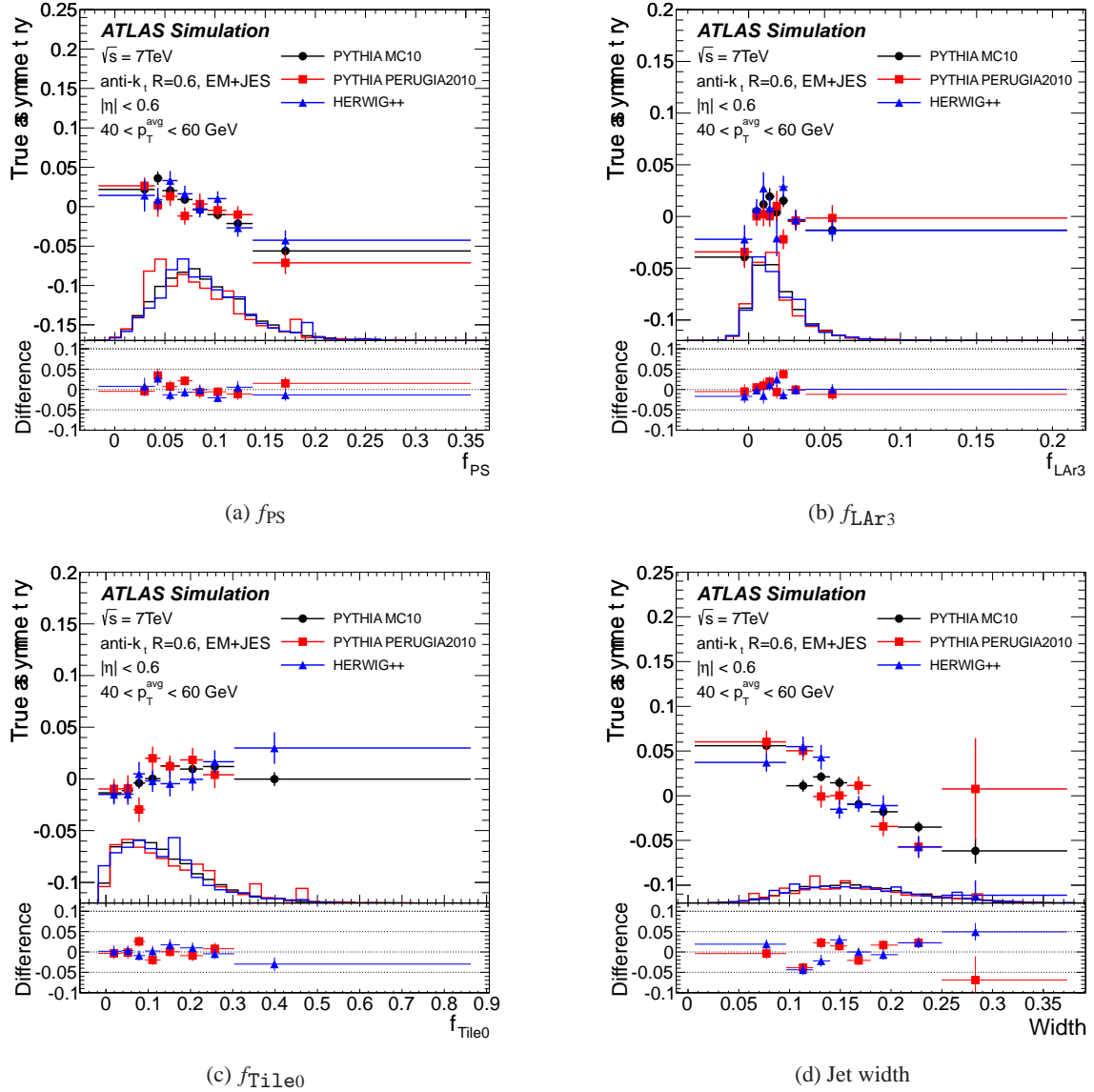


Fig. 48: Average asymmetry for truth jets obtained from various Monte Carlo event generators and tunes (PYTHIA with the MC10 and the PERUGIA2010 tune and HERWIG++) as a function of the calorimeter layer fraction f_{PS} (a), f_{LAr3} (b), f_{Tile0} (c) and the lateral jet width (d) of the probe jet. Anti- k_t jets with $R = 0.6$ calibrated with the EM+JES scheme are used and have $40 \leq p_T^{\text{avg}} < 60\text{ GeV}$ and $|\eta| < 0.6$. The distributions of the jet properties are superimposed on each figure. The lower part of each figure shows the differences between PYTHIA MC10 and the other Monte Carlo generators.

12.1.3 Differences between data based and Monte Carlo based corrections

Figure 49 shows the difference between the reconstructed asymmetry and the true asymmetry for the PYTHIA MC10 sample as a function of f_{PS} , f_{LAr3} , f_{Tile0} and width for jets with $80 \leq p_T^{\text{jet}} < 110\text{ GeV}$ and $|\eta| < 0.6$. The reconstructed asymmetries in data and the PYTHIA MC10 sample are compatible within statistical uncertainties. Similar agreement is found in the other η and p_T^{jet} regions.

The asymmetries as shown in Figure 49 are used to derive data based corrections. The difference between data and Monte

Carlo simulation provides a quantitative measure of the additional jet energy scale uncertainty introduced by the GS calibration. After the first two corrections in Table 13 the response changes by less than 1% for data based and Monte Carlo based corrections. The response changes by an additional 1% to 2% after the third (Presampler) and the fourth (width) corrections are applied in the barrel. The agreement in the endcap is within 2% (4%) for $p_T^{\text{truth}} > 60\text{ GeV}$ ($< 60\text{ GeV}$).

Data based corrections are also derived with true asymmetries coming from the PERUGIA2010 and HERWIG++ samples. These corrections are then applied to the reference PYTHIA MC10 sample and the response yielded is compared to the re-

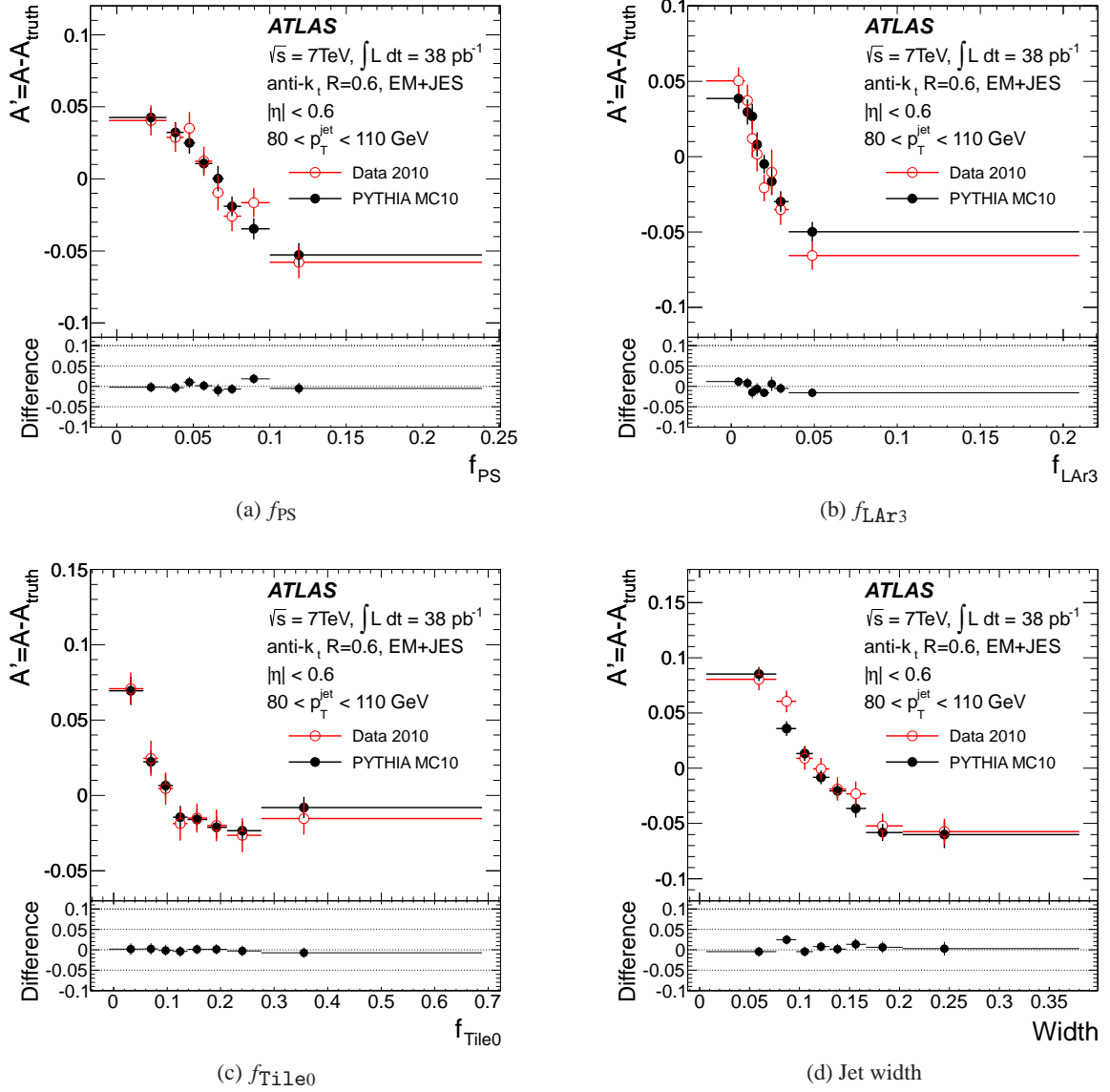


Fig. 49: Difference between the average reconstructed asymmetry and the average true asymmetry in data (open circles) and in the reference PYTHIA MC10 sample (full circles) as a function of the calorimeter layer fractions f_{PS} (a), f_{LAr3} (b), f_{Tile0} (c) and the lateral jet width (d). The lower part of each figure shows the differences between data and Monte Carlo simulation. Anti- k_t jets with $R = 0.6$ calibrated with the EM+JES scheme are used and have $80 \leq p_T^{\text{jet}} < 110 \text{ GeV}$ and $|\eta| < 0.6$.

sponse obtained after applying the reference data based corrections using the true asymmetry from the reference PYTHIA MC10 sample. The difference in response is found to be lower than 0.5% in all the p_T^{jet} and $|\eta|$ bins where the statistical uncertainty is small enough.

As a further cross-check the same GS corrections (here the Monte Carlo based ones) are applied to both data and Monte Carlo simulation samples. The difference between data and simulation reflects differences in the jet properties used as input to the GS calibration in the inclusive samples.

Figure 50 shows the mean value of f_{PS} , f_{LAr3} , f_{Tile0} and width as a function of p_T^{jet} in the barrel for data and various Monte Carlo simulation samples: the nominal PYTHIA MC10,

PYTHIA PERUGIA2010 and HERWIG++. The agreement for f_{Tile0} and f_{PS} between data and PYTHIA with the MC10 tune is within 5% over the entire p_T^{jet} range. For f_{LAr3} , this agreement is also within 5% except for $20 \leq p_T^{\text{jet}} < 30 \text{ GeV}$ where a disagreement of 7.5% is observed. A larger disagreement is found for the jet width. Jets are 5% (10%) wider in data than in Monte Carlo simulation at 200 GeV (600 GeV).

The standard deviations of the f_{LAr3} and the f_{PS} distributions show also agreement within 5% between data and PYTHIA MC10 simulation for f_{LAr3} and f_{PS} over the entire p_T^{jet} range. For f_{Tile0} and width, disagreements of 10% are observed in some p_T^{jet} bins. Similar results are found in the other

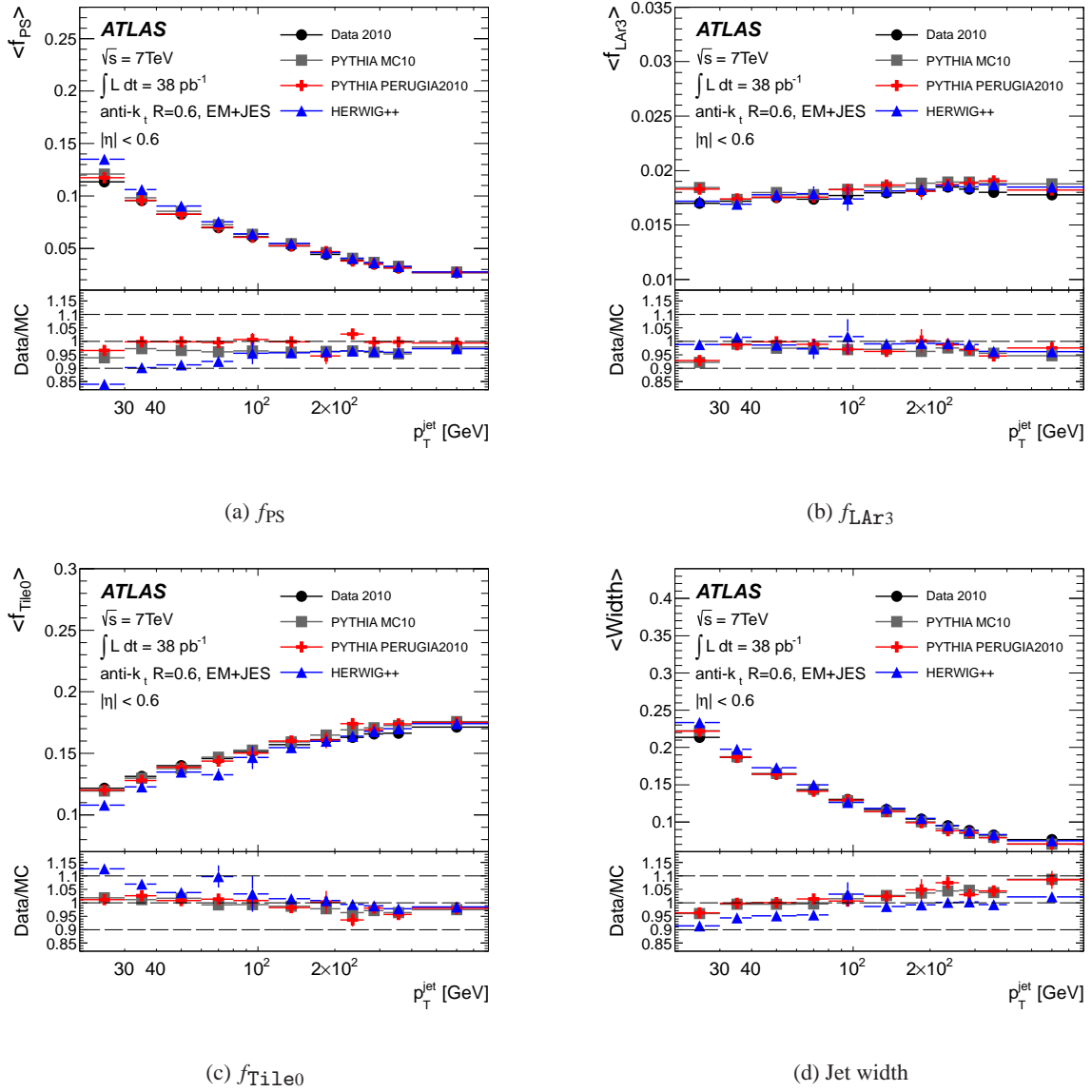


Fig. 50: Mean value of the jet calorimeter layer fractions f_{PS} (a), f_{LAr3} (b), f_{Tile0} (c) and the jet width (d) as a function of p_T^{jet} for $|\eta| < 0.6$ for data and various Monte Carlo simulations. Anti- k_t jets with $R = 0.6$ calibrated with the EM+JES scheme are used. The ratio of data to Monte Carlo simulation is shown in the lower part of each figure.

$|\eta|$ bins for the calorimeter layer fractions and the jet width, except for $2.1 \leq |\eta| < 2.8$, where the agreement for the width is slightly worse than in the other eta ranges.

Figure 50 shows that PYTHIA with the MC10 and the PYTHIA PERUGIA2010 tunes agree to within a few per cent. The agreement of the HERWIG sample with data is as good as for the other samples for f_{LAr3} and f_{Tile0} , except for $20 \leq p_T^{\text{jet}} < 30$ GeV. For f_{PS} and the width, disagreements of 5 – 10% are observed between HERWIG++ and the other samples for $p_T^{\text{jet}} < 60$ GeV. For $p_T^{\text{jet}} > 160$ GeV, HERWIG++ is found to describe the width observed in data better than the other samples.

The systematic uncertainty can be quantitatively estimated by comparing how the correction coefficients $E_{GS}^{\text{jet}}/E_{EM+JES}^{\text{jet}}$

differ between data and Monte Carlo simulation. The correction coefficient as a function of p_T^{jet} in the barrel calorimeter in data and in the PYTHIA MC10 sample after GSL and GS corrections are shown in Figure 51a and Figure 51b. The ratios of data to Monte Carlo simulation are shown in the lower part of each figure. Figure 51c and Figure 51d show the same quantity, but as a function of η for $80 \leq p_T^{\text{jet}} < 110$ GeV.

Deviations from unity in the ratios between data and Monte Carlo simulation as shown in Figure 51 represent the systematic uncertainty associated to the GS corrections. This uncertainty is added in quadrature to the EM+JES uncertainty. The results for all the p_T^{jet} and η ranges are the following:

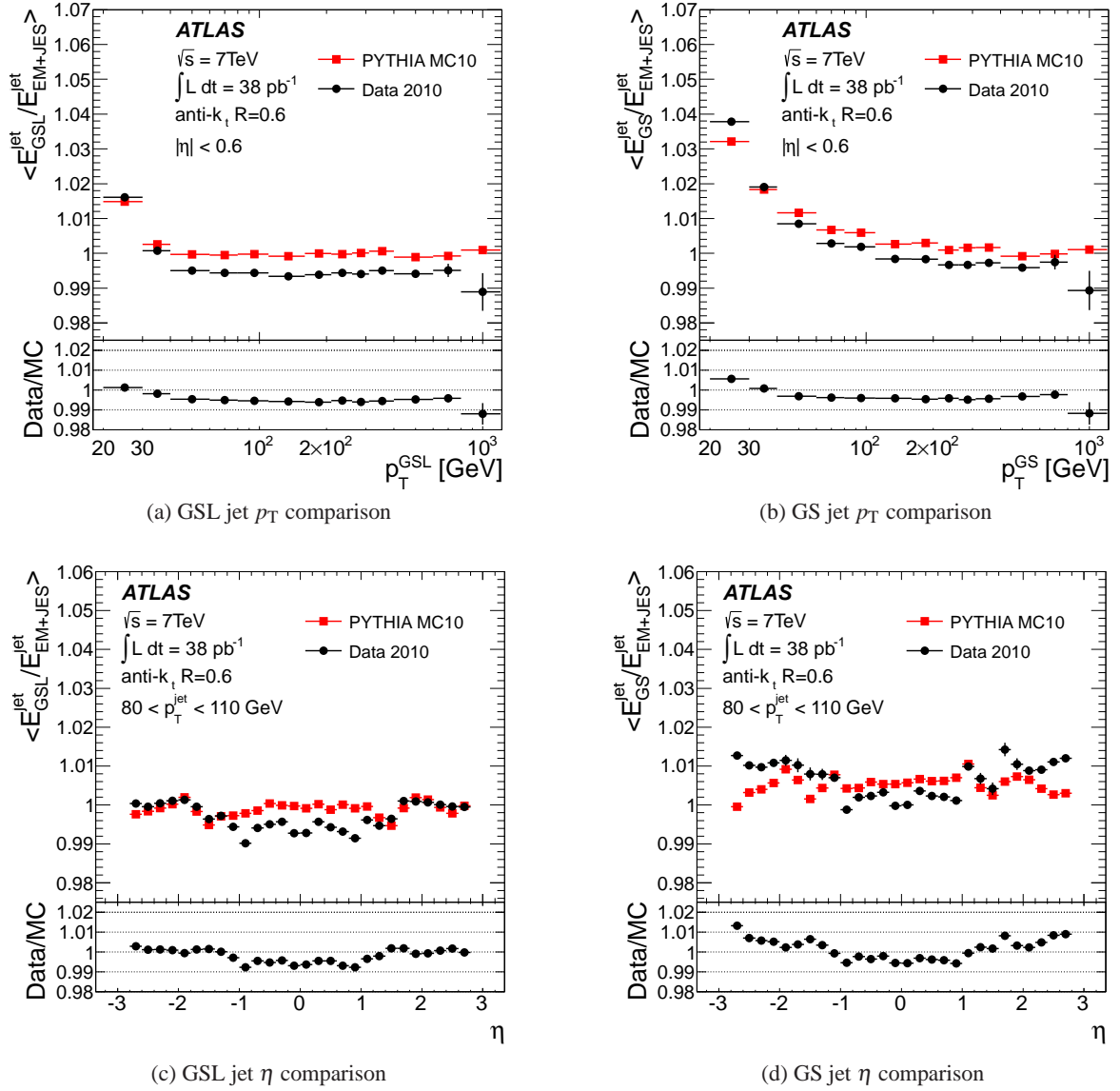


Fig. 51: Average jet energy after GSL (a,c) and GS (b,d) corrections divided by the average jet energy after the EM+JES calibration as a function of p_T^{jet} (a,b) in the calorimeter barrel and as a function of η for $80 \leq p_T^{\text{jet}} < 100$ GeV in data and the Monte Carlo simulation. Anti- k_t jets with $R = 0.6$ are used. The double ratio $[E_{\text{GS(GSL)}}/E_{\text{EM+JES}}]_{\text{Data}}/[E_{\text{GS(GSL)}}/E_{\text{EM+JES}}]_{\text{MC}}$ is shown in the lower part of each figure.

For $20 \leq p_T^{\text{jet}} < 30$ GeV and $0 \leq |\eta| < 2.1$, the data to Monte Carlo ratio varies from 0.5% to 0.7% depending on the $|\eta|$ region. For $p_T^{\text{jet}} > 30$ GeV and $0 \leq |\eta| < 2.1$, the uncertainty is lower than 0.5%. For $2.1 \leq |\eta| < 2.8$, the data to Monte Carlo ratio varies from 0.4% to 1% depending on the p_T^{jet} bin. For a given p_T^{jet} , the uncertainty is higher for $2.1 \leq |\eta| < 2.8$ than for $0 \leq |\eta| < 2.1$, because of the poorer description of the jet width. For $2.1 \leq |\eta| < 2.8$ the GSL scheme shows slightly larger difference than the GS scheme. In general, the uncertainty on the data to Monte Carlo ratio is lower than 1% for $20 \leq p_T^{\text{jet}} < 800$ GeV and $0 \leq |\eta| < 2.8$.

The uncertainty coming from the imperfect description of the jet properties and the differences between data based and Monte Carlo simulation based corrections presented in Section 12.1 are not independent. The average jet response after the GS calibration in each p_T^{jet} and η bin, which depends on both the distribution of the properties and the GS corrections, is close to the response after the EM+JES calibration.

A change in the distribution of a jet property therefore translates into a change in the GS correction as a function of this property such that the average jet response stays the same in the sample used to derive the correction. The differences described in Section 12.1 are therefore partly caused by differences in the jet properties.

12.2 Sensitivity of the global sequential calibration to pile-up

An important feature of the GS calibration is its robustness when applied in the presence of pile-up interactions, which translates into small variations in the size of each of the corrections and the distributions of the jet properties. The corrections derived in the sample without pile-up are directly applicable to the sample with pile-up with only a small additional effect on the jet energy scale.

The difference between the response after each GS correction and the response after the EM+JES calibration in the Monte Carlo simulation samples, after the offset correction as described in Section 8.1 is applied, changed by less than 1% for $p_T^{\text{truth}} > 30$ GeV after each of the GS corrections, and by 2% for lower p_T^{truth} , when samples with and without pile-up are compared. These variations are smaller than the uncertainty on the jet energy in the absence of pile-up over the entire p_T range, thus demonstrating the robustness of the additional corrections with respect to pile-up.

12.3 Summary on the JES uncertainty for the global sequential calibration

The systematic uncertainty on the global sequential calibration in the inclusive jet sample has been evaluated. It is found to be lower than 1% for $0 \leq |\eta| < 2.8$ and $20 \leq p_T^{\text{jet}} < 800$ GeV. This uncertainty is added in quadrature to the JES based on the EM+JES calibration scheme.

13 Jet calibration schemes based on cell energy weighting

Besides the simple EM+JES calibration scheme, ATLAS has developed several calibration schemes [8] with different levels of complexity and different sensitivity to systematic effects. The EM+JES calibration facilitates the evaluation of systematic uncertainties for the early analyses, but the energy resolution is rather poor and it exhibits a rather high sensitivity of the jet response to the flavour of the parton inducing the jet. These aspects can be improved using more sophisticated calibrations.

The ATLAS calorimeters are non-compensating and give a lower response to hadrons than to electrons or photons. Furthermore reconstruction inefficiencies and energy deposits outside the calorimeters lower the response to both electromagnetic and hadronic particles, but in different ways. The main motivation for calibration schemes based on cell energy density is to improve the jet energy resolution by weighting differently energy deposits from electromagnetic and hadronic showers. The calorimeter cell energy density is a good indicator, since the radiation length X_0 is much smaller than the hadronic interaction length λ_I .

Two calibration schemes implementing this idea have been developed:

1. For the global calorimeter cell energy density calibration (GCW) the weights depend on the cell energy density and are obtained from Monte Carlo simulation by optimising

Calorimeter Layer	Nb. E/V bins	Poly. Degree on E/V
PresamplerB	1	1
PresamplerE	1	1
EMB1	1	1
EME1	1	1
EMB2 and EMB3 with $ \eta < 0.8$	16	4
EMB2 and EMB3 with $ \eta \geq 0.8$	16	4
EME2 and EME3 with $ \eta < 2.5$	16	4
EME2 and EME3 with $ \eta \geq 2.5$	16	4
TileBar0, TileBar1 and TileBar2	16	4
TileExt0, TileExt1 and TileExt2	16	4
HECO-3 with $ \eta < 2.5$	16	4
HECO-3 with $ \eta \geq 2.5$	16	4
FCAL0	16	3
FCAL1 and FCAL2	16	3
Cryo term	1	1
Gap	1	1
Scint	1	1

Table 14: Number of energy density bins per calorimeter layer used in the GCW jet calibration scheme and the degree of the polynomial function used in the weight parametrisation.

the reconstructed jet energy resolution with respect to the true jet energy. This calibration is called “global” because the jet is calibrated as a whole and, furthermore, the weights that depend on the calorimeter cell energy density are derived such that fluctuations in the measurement of the jet energy are minimised and this minimisation corrects for all effects at once.

2. For the local cluster calibration (LCW) multiple variables at the calorimeter cell and the topo-cluster levels are considered in a modular approach treating the various effects of non-compensation, dead material deposits and out-of-cluster deposits independently. The corrections are obtained from simulations of charged and neutral particles. The topo-clusters in the calorimeter are calibrated “locally”, without considering the jet context, and jets are then reconstructed directly from calibrated topo-clusters.

Final jet energy scale corrections also need to be applied to the GCW and LCW calibrated jets, but they are numerically smaller than the ones for the EM+JES calibration scheme. These corrections are derived with the same procedure as described in Section 8. The resulting jets are referred to as calibrated with GCW+JES and LCW+JES schemes.

13.1 Global cell energy density weighting calibration

This calibration scheme (GCW) attempts to assign a larger cell-level weight to hadronic energy depositions in order to compensate for the different calorimeter response to hadronic and electromagnetic energy depositions. The weights also compensate for energy losses in the dead material.

In this scheme, jets are first found from topo-clusters or calorimeter towers at the EM scale. Secondly the energies of the calorimeter cells forming jets are weighted according to their energy density. Finally, a JES correction is derived from

the sum of the weighted energy in the calorimeter cells associated to the jet as a function of the jet p_T and pseudorapidity.

The weights are derived using Monte Carlo simulation information. A reconstructed jet is first matched to the nearest truth jet requiring $R_{\min} < 0.3$. No second truth jet should be within a distance of $\Delta R = 1$. The nearest truth jet should have a transverse energy $E_T > 20$ GeV. The transverse energy of the reconstructed jet should be $E_T^{\text{EM}} > 5$ GeV, where E_T^{EM} is the transverse energy of the reconstructed jet measured at the electromagnetic scale.

For each jet, calorimeter cells are identified with an integer number i denoting a calorimeter layer or a group of layers in the ATLAS calorimeters. Afterwards, each cell is classified according to its energy density which is defined as the calorimeter cell energy measured at the electromagnetic scale divided by the geometrical cell volume (E/V).

A weight w_{ij} is introduced for each calorimeter cell within a layer i at a certain energy density bin j . The cells are classified in up to 16 E/V bins according to the following formula:

$$j = \frac{\ln \frac{E/\text{GeV}}{V/\text{mm}^3}}{\ln 2} + 26, \quad (43)$$

where j is an integer number between 0 and 15. Calorimeter cells in the presampler, the first layer of the electromagnetic calorimeter, the gap and crack scintillators (Gap, Scint) are excluded from this classification. A constant weight is applied to these cells independent of their E/V . The cryostat (Cryo) term is computed as the geometrical average of the energy deposited in the last layer of the electromagnetic barrel LAr calorimeter and the first layer of the Tile calorimeter. This gives a good estimate of the energy loss in the material between the LAr and the Tile calorimeters.

In the case of the seven layers without energy density segmentation the weights are denoted by v_i . Table 14 shows the number of energy density bins for each calorimeter layer.

The jet energy is then calculated as:

$$E_{\text{GCW}}^{\text{jet}} = \sum_{i=1}^{10} \sum_{j=1}^{16} w_{ij} E_{ij} + \sum_{i=1}^7 v_i E_i, \quad (44)$$

where w_{ij} (v_i) are the GCW calibration constants. In order to reduce the number of degrees of freedom, for a given layer i , the energy density dependence of each element w_{ij} is parameterised by a common polynomial function of third and fourth degree depending on the layer (see Table 14). In this way the number of free parameters used to calibrate any jet is reduced from 167 to 45.

The weights are computed by minimising the following function:

$$\chi^2 = \frac{1}{N_{\text{jet}}} \sum_{\text{jet}=1}^{N_{\text{jet}}} \left(\frac{E_{\text{GCW}}^{\text{jet}}}{E_{\text{truth}}^{\text{jet}}} - 1 \right)^2, \quad (45)$$

where N_{jet} is the total number of jets in the Monte Carlo sample used. This procedure provides weights that minimise the jet energy resolution. The mathematical bias on the mean jet energy that is introduced in particular at low jet energies (see Ref. [68]) is corrected by an additional jet energy calibration following the method described in Section 8 and discussed in Section 13.3.

13.2 Local cluster weighting calibration

This calibration scheme [16, 69] corrects locally the topo-clusters in the calorimeters independent of any jet context. The calibration starts by classifying topo-clusters as mainly electromagnetic or hadronic depending on cluster shape variables [57]. The cluster shape variables characterise the topology of the energy deposits of electromagnetic or hadronic showers and are defined as observables derived from calorimeter cells with positive energy in the cluster and the cluster energy. All weights depend on this classification and both hadronic and electromagnetic weights are applied to each cluster.

13.2.1 Barycentre of the longitudinal cluster depth

The barycentre of the longitudinal depth of the topo-cluster (λ_{centre}) is defined as the distance along the shower axis from the front of the calorimeter to the shower centre. The shower centre has coordinates:

$$\langle i \rangle = \frac{\sum_{k|E_k>0} E_k i_k}{\sum_{k|E_k>0} E_k}, \quad (46)$$

with i taking values of the spatial coordinates x, y, z and E_k denoting the energy in the calorimeter cell k . Only calorimeter cells with positive energy are used.

The shower axis is determined from the spatial correlation matrix of all cells in the topo-cluster with positive energies:

$$C_{ij} = \frac{\sum_{k|E_k>0} E_k^2 (i_k - \langle i \rangle)(j_k - \langle j \rangle)}{\sum_{k|E_k>0} E_k^2}, \quad (47)$$

with $i, j = x, y, z$. The shower axis is the eigenvector of this matrix closest to the direction joining the interaction point and the shower centre.

13.2.2 Cluster isolation

The cluster isolation is defined as the ratio of the number of unclustered calorimeter cells³¹ that are neighbours of a given topo-cluster to the number of all neighbouring cells. The neighbourhood relation is defined in two dimensions, i.e. within the individual calorimeter layer³².

After calculating the cluster isolation for each individual calorimeter layer, the final cluster isolation variable is obtained by weighting the individual layer cell ratios by the energy fractions of the topo-cluster in these layers. This assures that the isolation is evaluated where the topo-cluster has most of its energy.

The cluster isolation is zero for topo-clusters where all neighbouring calorimeter cells in each layer are inside other topo-clusters and one for topo-clusters with no neighbouring cell inside any other topo-cluster.

³¹ Unclustered calorimeter cells that are not contained in any topo-cluster.

³² In general, topo-clusters are formed in a three dimensional space defined by η , ϕ and the calorimeter depth.

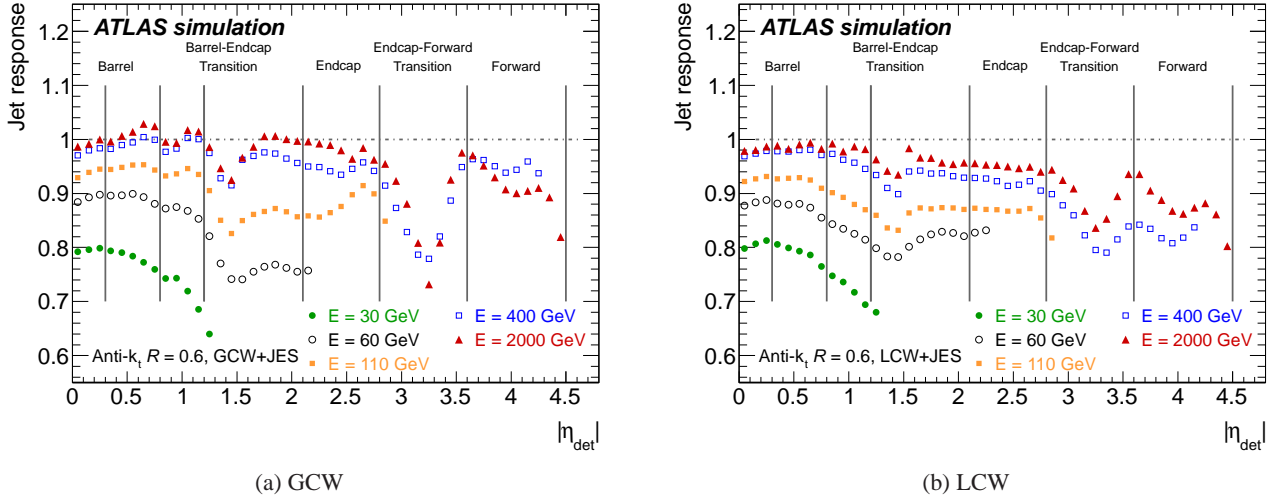


Fig. 52: Average simulated jet energy response at the GCW (a) and the LCW (b) scale in bins of the GCW+JES and LCW+JES calibrated jet energy and as a function of the detector pseudorapidity $|\eta_{\text{det}}|$.

13.2.3 Cluster energy correction

All corrections are derived from the Monte Carlo simulations for single charged and neutral pions. The hadronic shower simulation model used is QGSP_BERT. The detector geometry and topo-cluster reconstruction is the same as in the nominal Monte Carlo simulation sample. A flat distribution in the logarithm of pion energies from 200 MeV to 2 TeV is used.

The corrections are derived with respect to the true deposited energy in the active and inactive detector region (“calibration hits”).

True energy depositions are classified in three types by the ATLAS software:

1. The **visible energy**, like the energy deposited by ionisation.
2. The **invisible energy**, like energy absorbed in nuclear reactions.
3. The **escaped energy**, like the energy carried away by neutrinos³³.

The local cluster calibration proceeds in the following steps:

1. **Cluster classification:** The expected population in logarithmic bins of the topo-cluster energy, the cluster depth in the calorimeter, and the average cell energy density are used to calculate classification weights. The weights are calculated for small $|\eta|$ regions by mixing neutral and charged pions with a ratio of 1 : 2. This assumes that 2/3 of the pions should be charged. Clusters are classified as mostly electromagnetic or mostly hadronic. The calculated weight denotes the probability p for a cluster to stem from a hadronic interaction.
2. **Hadronic weighting:** Topo-clusters receive calorimeter cell correction weights derived from detailed Monte Carlo simulations of charged pions. Calorimeter cells in topo-clusters are weighted according to the topo-cluster energy and

the calorimeter cell energy density. The hadronic energy correction weights are calculated from the true energy deposits as given by the Monte Carlo simulation (w_{HAD}) multiplied by a weight to take into account the different nature of hadronic and electromagnetic showers.

The applied weight is

$$w_{\text{HAD}} \cdot p + w_{\text{EM}} \cdot (1 - p), \quad (48)$$

where $w_{\text{EM}} = 1$ and p is the probability of the topo-cluster to be hadronic as determined by the classification step. Dedicated correction weight tables for each calorimeter layer in 0.2-wide $|\eta|$ -bins are used. The correction weight tables are binned logarithmically in topo-cluster energy and cell energy density (E/V).

3. **Out-of-cluster (OOC) corrections:** A correction for isolated energy deposits inside the calorimeter, but outside topo-clusters is applied. These are energy depositions not passing the noise thresholds applied during the clustering. These corrections depend on $|\eta|$, the energy measured around the topo-cluster and the cluster barycentre λ_{centre} . There are two sets of constants for hadronic and electromagnetic showers and both are used for each cluster with the respective weights of p and $1 - p$. The OOC correction is finally multiplied with the cluster isolation value discussed in Section 13.2.2 in order to avoid double counting.
4. **Dead material (DM) corrections:** Energy deposits in materials outside the calorimeters are corrected. For energy deposits in upstream material like the inner wall of the cryostat, the presampler signals are highly correlated to the lost energy. The corrections are derived from the sum of true energy depositions in the material in front and behind the calorimeter and from the presampler signal.

The correction for energy deposited in the outer cryostat wall between the electromagnetic and the hadronic barrel calorimeters is based on the geometrical mean of the energies in the layers just before and just beyond the cryostat

³³ The escaped energy is recorded at the place where the particle that escapes the detector volume (“world volume” in GEANT4 terminology) is produced.

wall. Corrections for other energy deposits without clear correlations to topo-cluster observables are obtained from look-up tables binned in topo-cluster energy, the pseudorapidity $|\eta|$, and the shower depth. Two sets of DM weights for hadronic and electromagnetic showers are used. The weights are applied according to the classification probability p defined above.

All corrections are defined with respect to the electromagnetic scale energy of the topo-cluster. Since only calorimetric information is used, the LCW calibration does not account for low-energy particles which do not create a topo-cluster in the calorimeter. This is, for instance, the case when the energy is absorbed entirely in inactive detector material or particles are bent outside of the calorimeter acceptance.

13.3 Jet energy calibration for jets with calibrated constituents

The simulated response to jets at the GCW and LCW energy scales, i.e. after applying weights to the calorimeter cells in jets or after the energy corrections to the topo-clusters, are shown in Figure 52 as a function of η_{det} for various jet energy bins. The inverse of the response shown in each bin is equal to the average jet energy scale correction. The final jet energy correction needed to restore the reconstructed jet energy to the true jet energy is much smaller than in the case of the EM+JES calibration shown in Figure 10.

14 Jet energy scale uncertainties for jet calibrations based on cell weighting

The jet energy scale uncertainty for jets based on cell weighting is obtained using the same *in situ* techniques as described in Section 10. The results for each *in situ* technique together with the combination of all *in situ* techniques are discussed in Section 14.3.

In order to build up confidence in the Monte Carlo simulation the description of the variables used as inputs to the cell weighting by the Monte Carlo simulation is discussed in Section 14.1 for the global cell weighting scheme and in Section 14.2 for the local cluster weighting scheme.

14.1 Energy density as input to the global cell weighting calibration

The global cell energy density weighting calibration scheme (see Section 13.1) applies weights to the energy deposited in each calorimeter cell according to the calorimeter cell energy density (E/V , where V is the calorimeter cell volume defined before). This attempts to compensate for the different calorimeter response to hadronic and electromagnetic showers, but it also compensates for energy losses in the dead material. The description of the calorimeter cell energy density in the Monte Carlo simulation is therefore studied to validate this calibration scheme.

Only calorimeter cells inside jets with $p_{\text{T}}^{\text{jet}} > 20$ GeV and $|y| < 2.8$ built of topo-clusters and with a cell energy of at least two standard deviations above the noise thresholds are considered for this comparison. Similar results have been obtained using cells inside jets built from calorimeter towers. The Monte Carlo simulation reproduces the generic features of the data over many orders of magnitude. However, the following paragraphs discuss those differences, all of which are on the order of a few percent.

Figure 53 shows the calorimeter cell energy density distributions in data and Monte Carlo simulation for cells in representative longitudinal segments of the barrel and forward calorimeters. Fewer cells with high energy density are observed in data than predicted by Monte Carlo simulation in the barrel presampler (a) and in the second layer of the barrel electromagnetic calorimeter (b). This behaviour is observed for other segments of the barrel electromagnetic calorimeter, but not for the second layer of the Tile barrel calorimeter (c). Here, a good agreement between data and Monte Carlo simulation is found over the full energy density spectrum. Only for the lowest energy densities are slight differences found. Good agreement is also present in the first layer of the Tile extended barrel calorimeter, while the energy density is on average smaller for the second and third layer in the data than in the Monte Carlo simulation. Such a deficit of high energy density cells in data is also observed for the second and third layer of the scintillators placed in the gap between the Tile barrel and extended barrel modules. Better agreement is found between data and Monte Carlo simulation for the first layer of the scintillators.

The second layer of the endcap electromagnetic calorimeter (d) shows a similar behaviour to that observed in the barrel: fewer cells are found at high energy density in the data than in the Monte Carlo simulation. This effect is present in all three layers of the endcap electromagnetic calorimeter, yet it becomes more pronounced with increasing calorimeter depth. A similar effect, but of even larger magnitude has been observed for cells belonging to the endcap presampler. The first layer of the endcap hadronic calorimeter (e) shows a better agreement between data and Monte Carlo simulation. This agreement is also present for other layers of the HEC. In the first layer of the forward calorimeter more cells with energy densities in the middle part of the spectrum are found in data than in Monte Carlo simulation (f). This effect has been observed in other FCAL layers, and it becomes slightly more pronounced with increasing FCAL depth.

14.2 Cluster properties inside jets as input to the local cluster weighting calibration

The LCW weights are defined with respect to the electromagnetic scale energy of the topo-clusters and can therefore be applied in any arbitrary order. This allows systematic checks of the order in which the corrections are applied. There are four cluster properties used in the LCW calibration scheme:

1. The energy density in cells in topo-clusters.
2. The cluster energy fraction deposited in different calorimeter layers.
3. The isolation variable characterising the energy around the cluster.

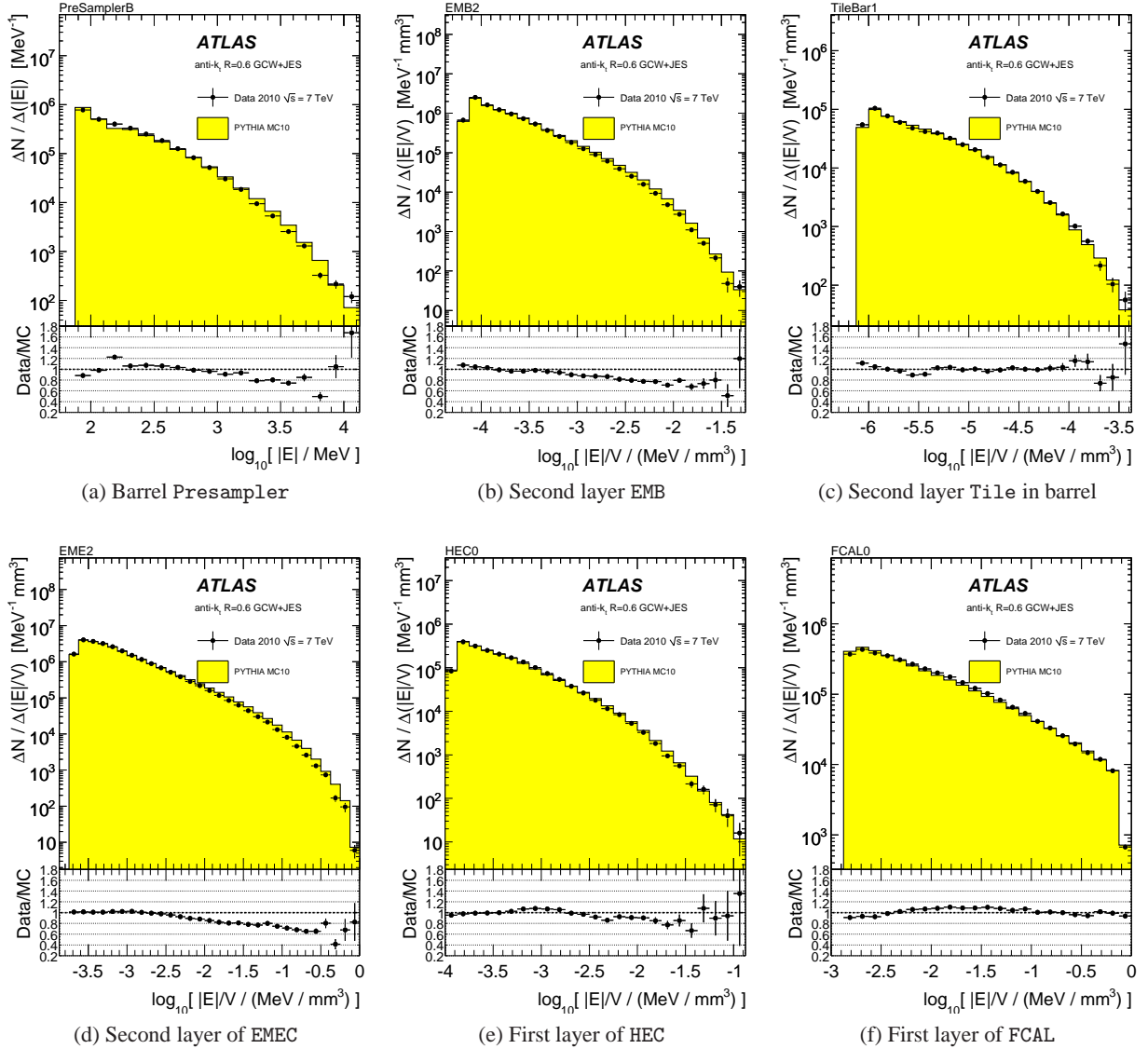


Fig. 53: Calorimeter cell energy density distributions used in the GCW jet calibration scheme in data (points) and Monte Carlo simulation (shaded area) for calorimeter cells in the barrel presampler (a), the second layer of the barrel electromagnetic calorimeter (b), the second layer of the barrel hadronic Tile calorimeter (c), the second layer of the endcap electromagnetic calorimeter (d), the first layer of the endcap hadronic calorimeter (e) and the first layer of the forward calorimeter (f). Anti- k_t jets with $R = 0.6$ requiring $p_T^{\text{jet}} > 20$ GeV and $y < 2.8$ calibrated with the GCW+JES scheme are used. Monte Carlo simulation distributions are normalised to the number of cells in data distributions. The ratio of data to Monte Carlo simulation is shown in the lower part of each figure. Only statistical uncertainties are shown.

4. The depth of the cluster barycentre in the calorimeter.

In addition, the cluster energy after each correction step and the cluster location can be compared in data and Monte Carlo simulation.

14.2.1 Cluster isolation

Figure 54 shows the distributions of the cluster isolation variable for all topo-clusters in calibrated jets with $p_T^{\text{jet}} > 20$ GeV

and $|y| < 2.8$ for topo-clusters classified as electromagnetic (a) and hadronic (b).

The cluster isolation variable is bounded between 0 and 1, with higher values corresponding to higher isolation (see Section 13.2.2). Most of the topo-clusters in lower energetic jets have a high degree of isolation. The peaks at 0.25, 0.5 and 0.75 are due to the topo-clusters in boundary regions which are geometrically difficult to model or regions with a small number of calorimeter cells. Such topo-clusters contain predominantly gap scintillator cells or are located at the boundary of the HEC and the FCAL calorimeters.

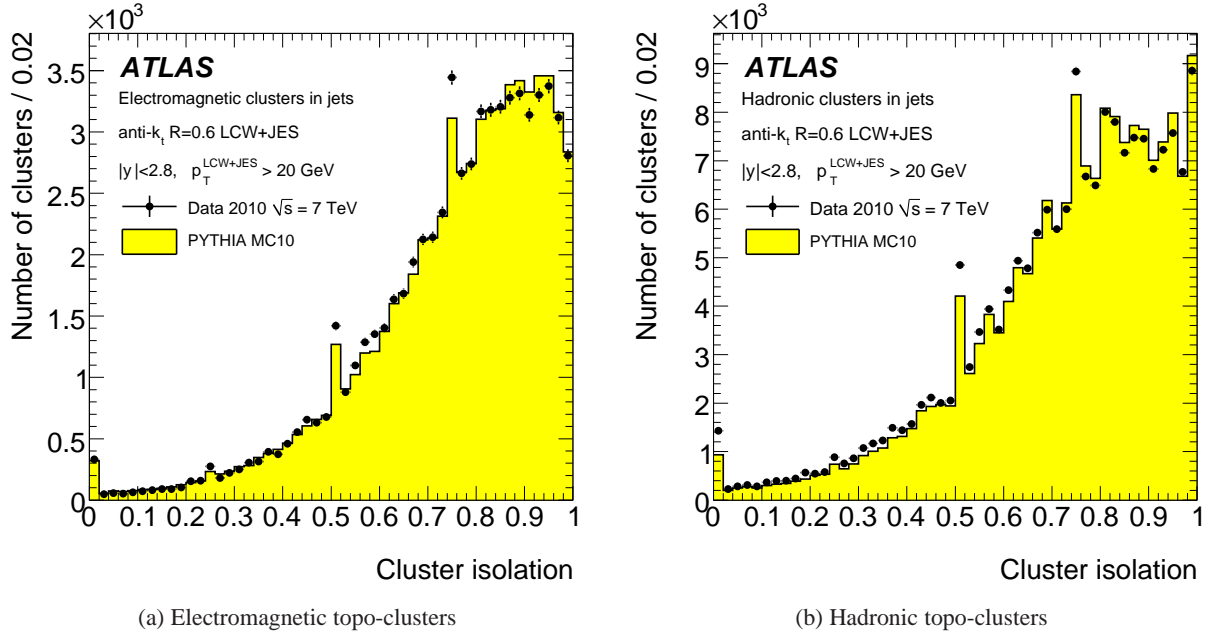


Fig. 54: Distributions of the isolation variable for topo-clusters classified as electromagnetic (a) and as hadronic (b) in data (points) and Monte Carlo simulation (shaded area). Topo-clusters associated to anti- k_t jets with $R = 0.6$ with $p_T^{\text{jet}} > 20$ GeV and $|y| < 2.8$ calibrated with the LCW+JES scheme are used.

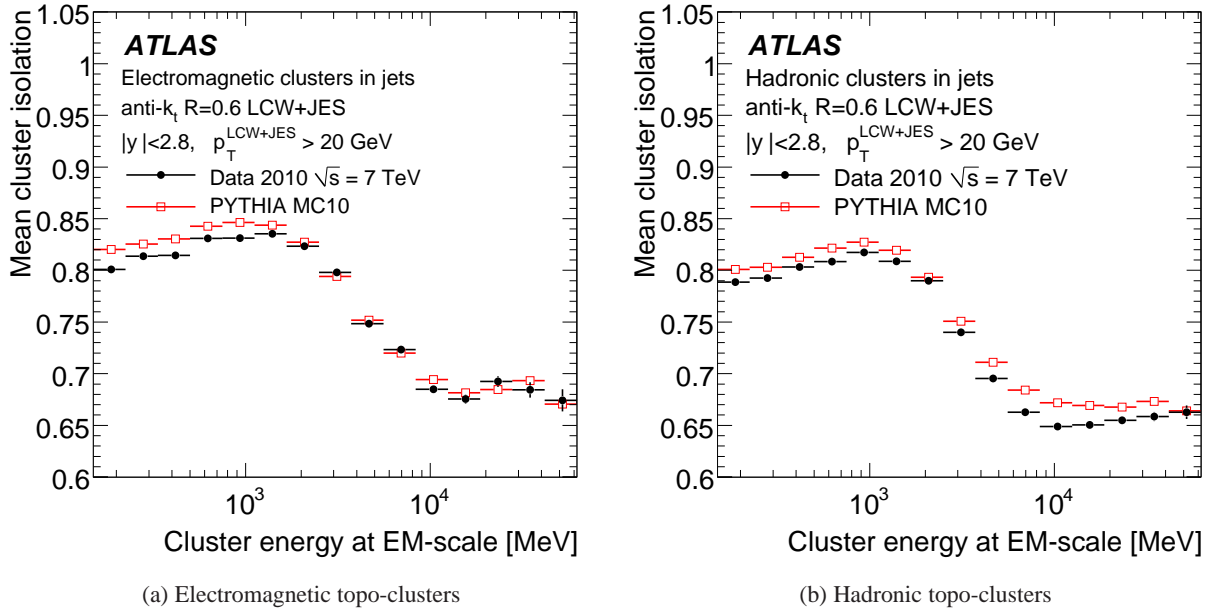


Fig. 55: Mean value of the cluster isolation variable for topo-clusters classified as electromagnetic (a) and as hadronic (b) as a function of the topo-cluster energy measured at the EM scale, in data (closed circles) and Monte Carlo simulation (open squares). Topo-clusters associated to anti- k_t jets with $R = 0.6$ with $p_T^{\text{jet}} > 20$ GeV and $|y| < 2.8$ calibrated with the LCW+JES scheme are used.

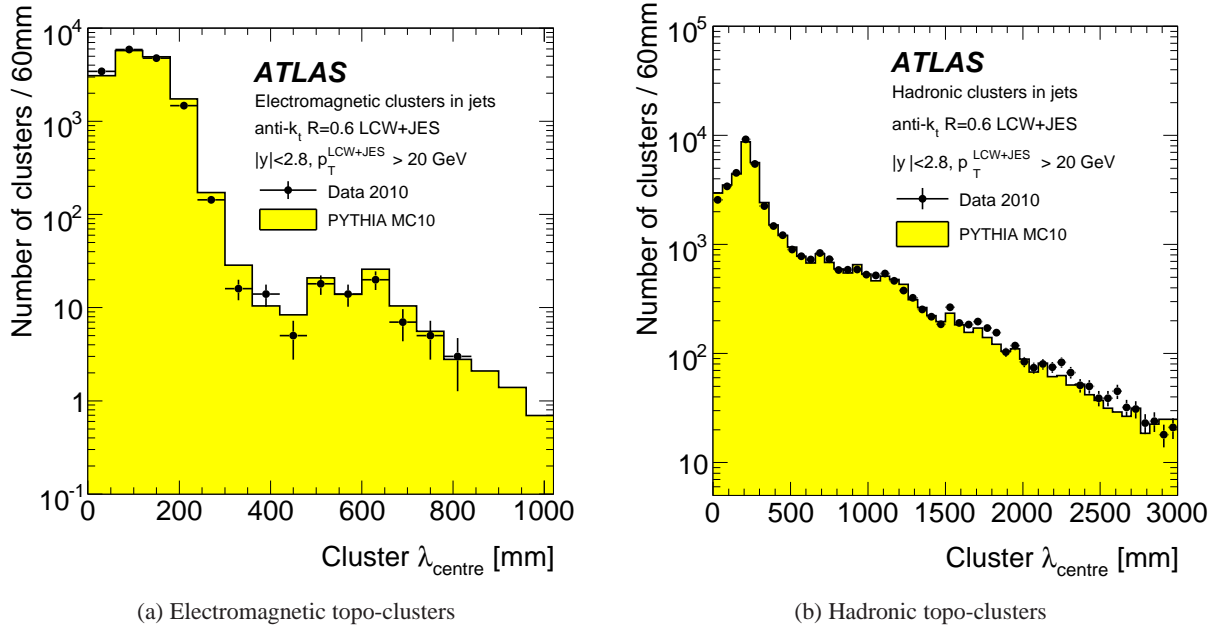


Fig. 56: Distributions of the longitudinal cluster barycentre λ_{centre} for topo-clusters classified as electromagnetic (a) and as hadronic (b) in data (points) and Monte Carlo simulation (shaded area). Topo-clusters associated to anti- k_t jets with $R = 0.6$ with $p_T^{\text{jet}} > 20$ GeV and $|y| < 2.8$ calibrated with the LCW+JES scheme are used.

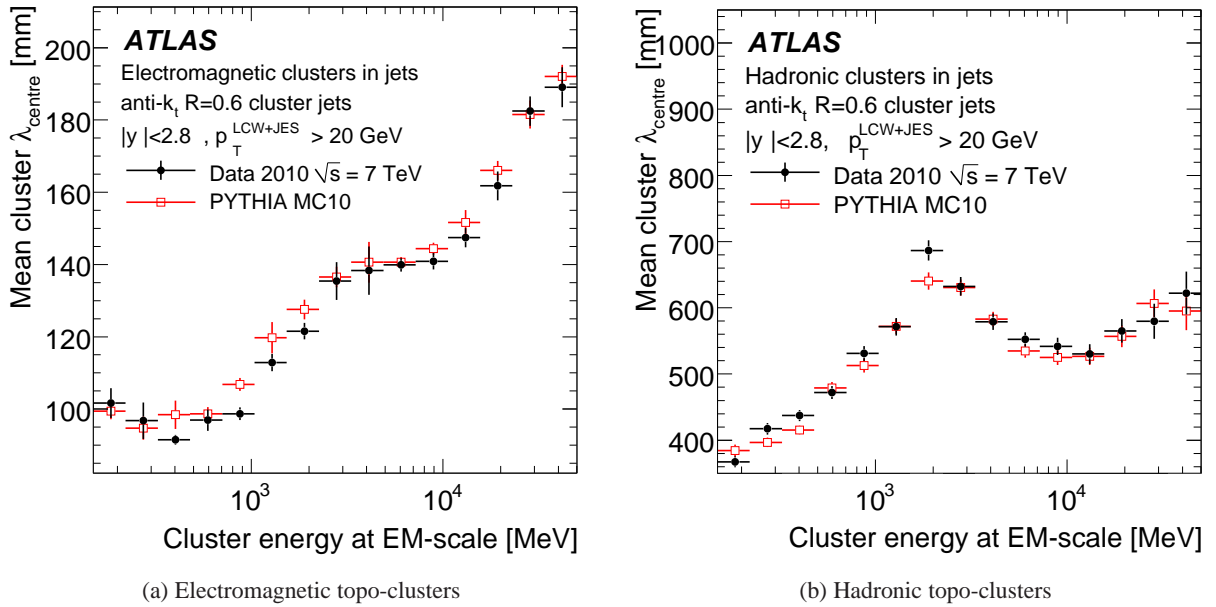
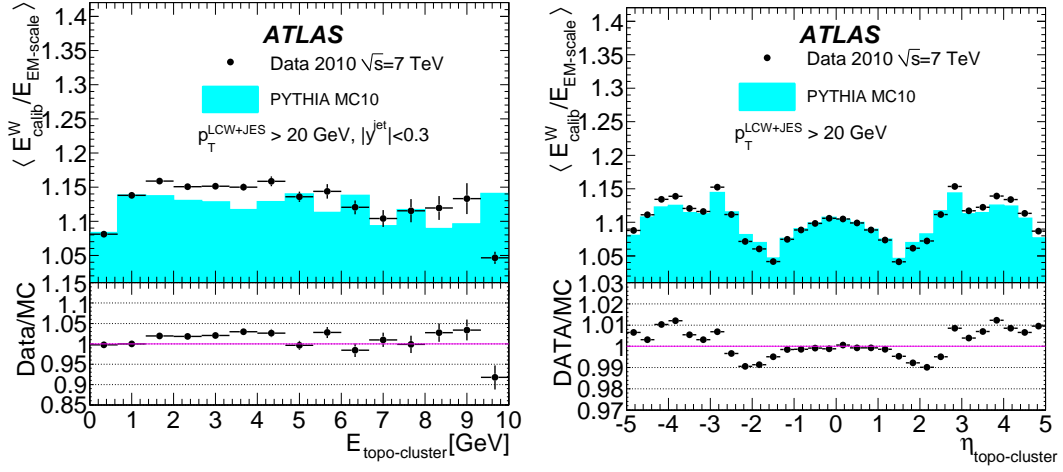
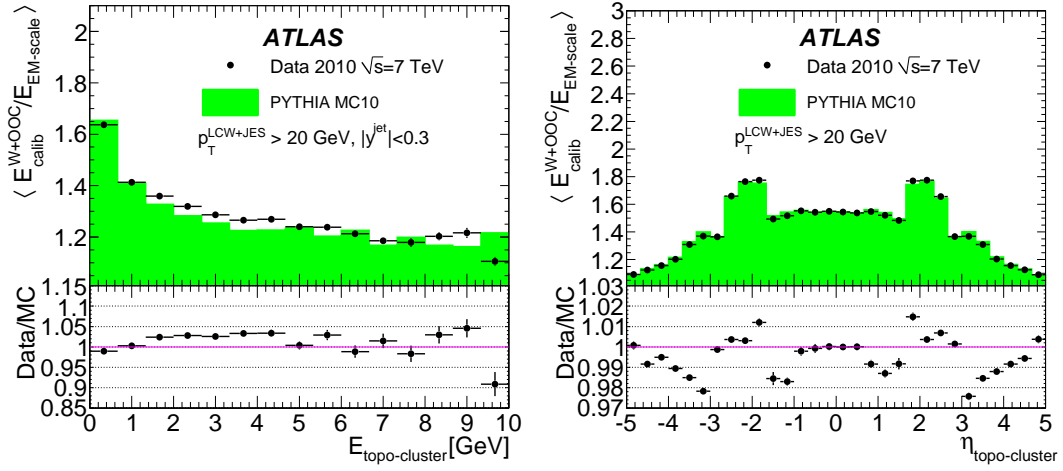


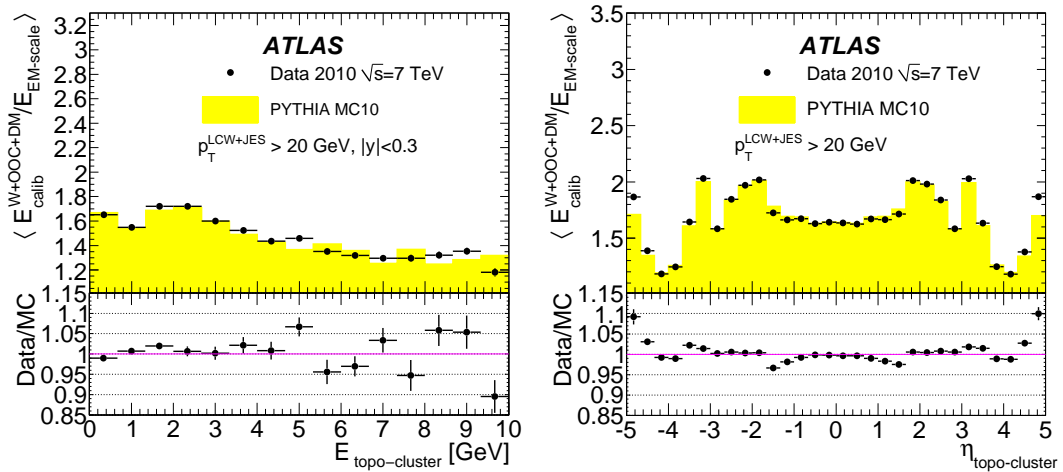
Fig. 57: Mean value of the longitudinal cluster barycentre λ_{centre} as a function of the topo-cluster energy measured at the EM scale for topo-clusters classified as electromagnetic (a) and as hadronic in data (b) in data (closed circles) and Monte Carlo simulation (open squares). Topo-clusters associated to anti- k_t jets with $R = 0.6$ with $p_T^{\text{jet}} > 20$ GeV and $|y| < 2.8$ calibrated with the LCW+JES scheme are used.



(a) Hadronic response weights



(b) Hadronic response and out-of-cluster weights



(c) Hadronic response, out-of-cluster and dead material weights

Fig. 58: Mean calibrated topo-cluster energy divided by the uncalibrated topo-cluster energy in data (points) and Monte Carlo simulation (shaded area) as a function of the uncalibrated topo-cluster energy (left) and pseudorapidity (right) after hadronic response weighting (a), adding out-of-cluster corrections (b), and adding dead material corrections (c) applied to topo-clusters in jets. The corrections are sequentially applied. Anti- k_t jets with $R = 0.6$ in the LCW+JES scheme are required to have $p_T^{\text{jet}} > 20$ GeV. In addition, for the results as a function of the topo-cluster energy (left) the jets have been restricted to $|y| < 0.3$.

The features observed are similar for topo-clusters classified as mostly electromagnetic and those classified as mostly hadronic. A reasonable agreement between data and Monte Carlo simulation (see Fig. 54) is found. The agreement in the peaks corresponding to the transition region between calorimeters is not as good as in the rest of the distribution.

Figure 55 shows the mean value of the topo-cluster isolation variable as a function of the topo-cluster energy for all topo-clusters in jets with $p_T^{\text{jet}} > 20$ GeV and $|\eta| < 2.8$ for topo-clusters classified as electromagnetic (a) or as hadronic (b). The Monte Carlo simulation consistently predicts more isolated topo-clusters than observed in the data, particularly at topo-cluster energies $E < 2$ GeV and for both hadronic and electromagnetic cluster classifications. This feature is present in all rapidity regions, except for very low energy topo-clusters classified as mostly electromagnetic in very central jets.

14.2.2 Longitudinal cluster barycentre

Figure 56 shows the cluster barycentre λ_{centre} distributions for all topo-clusters in LCW calibrated jets with $p_T^{\text{jet}} > 20$ GeV and $|\eta| < 2.8$ and for both cluster classifications. Most topo-clusters classified as electromagnetic have their centre in the electromagnetic calorimeter, as expected. Those topo-clusters classified as mostly hadronic are very often in the electromagnetic calorimeter, since these low p_T jets do not penetrate far into the hadronic calorimeter. However, a structure is observed, related to the position of the different longitudinal layers in the hadronic calorimeter. This structure is more prominent when looking at individual rapidity regions, being smeared where the geometry is not changing in this inclusive distribution. Good agreement is observed between data and Monte Carlo simulation.

Figure 57 shows the mean value of distributions of λ_{centre} as a function of the cluster energy for all topo-clusters in jets with $p_T^{\text{jet}} > 20$ GeV and $|\eta| < 2.8$, again for both types of topo-clusters. In this case, topo-clusters classified as mostly electromagnetic have their barycentre deeper in the calorimeter on average as the cluster energy increases. A different behaviour is observed for clusters tagged as hadronic, for which the mean depth in the calorimeter increases until approximately 2 GeV, at which point the mean depth decreases again. The shape of the mean depth as a function of energy is different for different jet rapidities due to the changing calorimeter geometry. However, the qualitative features are similar, with a monotonic increase up to some topo-cluster energy, and a decrease thereafter. This is likely due to an increased probability of a hadronic shower to be split into two or more clusters with increased cluster energy. A good agreement is observed between data and Monte Carlo simulation.

14.2.3 Cluster energy after LCW corrections

In this section the size of each of the three corrections of the topo-cluster calibration is studied in data and Monte Carlo simulation. This provides a good measure of how the differences between data and Monte Carlo simulation observed in previous sections impact the size of the corrections applied.

Figure 58 shows the mean value of the ratio of the calibrated topo-cluster energy to the uncalibrated topo-cluster energy after each calibration step as a function of the topo-cluster energy and pseudorapidity. Only topo-clusters in LCW calibrated jets with $p_T^{\text{jet}} > 20$ GeV are considered. For the results shown as a function of topo-cluster energy the pseudorapidity of the jets is, in addition, restricted to $|\eta| < 0.3$.

The agreement between data and Monte Carlo simulation is within 5% for the full pseudorapidity range and is generally better for lower topo-cluster energies where the correction for the out-of-cluster energy dominates. As the topo-cluster energy increases the largest corrections become the hadronic response and the dead material corrections.

An agreement to about 1% is observed in a wide region in most of the barrel region after each correction. The agreement between data and Monte Carlo simulation is within 2% for all topo-cluster pseudorapidities after the hadronic and the out-of-cluster corrections. Larger differences are observed between data and Monte Carlo simulation in the transition region between the barrel and the endcap and in the forward region once the dead material correction is applied.

14.3 Jet energy scale uncertainty from *in situ* techniques for jets based on cell weighting

For the jet calibration schemes based on cell weighting the JES uncertainty is evaluated using *in situ* techniques. The same techniques as described in Section 10 are employed. The final JES uncertainty is obtained from a combination of all *in situ* techniques following the prescription in Section 10.5.

14.3.1 Comparison of transverse momentum balance from calorimeter and tracking

The result of the JES validation using the total transverse momentum of the tracks associated to jets (see Section 10.1) is shown in Figure 59 for jets calibrated with the GCW+JES scheme and in Figure 60 for jets calibrated with the LCW+JES scheme in various jet pseudorapidity regions within $|\eta| < 2.1$. The bin $|\eta| < 1.2$ is obtained by combining the $|\eta| < 0.3$, $0.3 \leq |\eta| < 0.8$ and $0.8 \leq |\eta| < 1.2$ bins.

Similar results as for the EM+JES scheme are obtained. In both cases, the agreement between data and simulation is excellent and within the uncertainties of the *in situ* method. The calibration schemes agree to within a few per cent, except for the bins with very low numbers of events.

14.3.2 Photon-jet transverse momentum balance

The response measured by the direct p_T balance technique (see Section 10.2.1) for the GCW+JES and LCW+JES calibrations is shown in Figure 61. The agreement of the Monte Carlo simulation with data is similar for both calibration schemes. The data to Monte Carlo agreement is 3 to 5%.

Figure 62 shows the comparison of the response determined by the MPF technique (see Section 10.2.2), measured in data and Monte Carlo simulation at the GCW and LCW jet energy

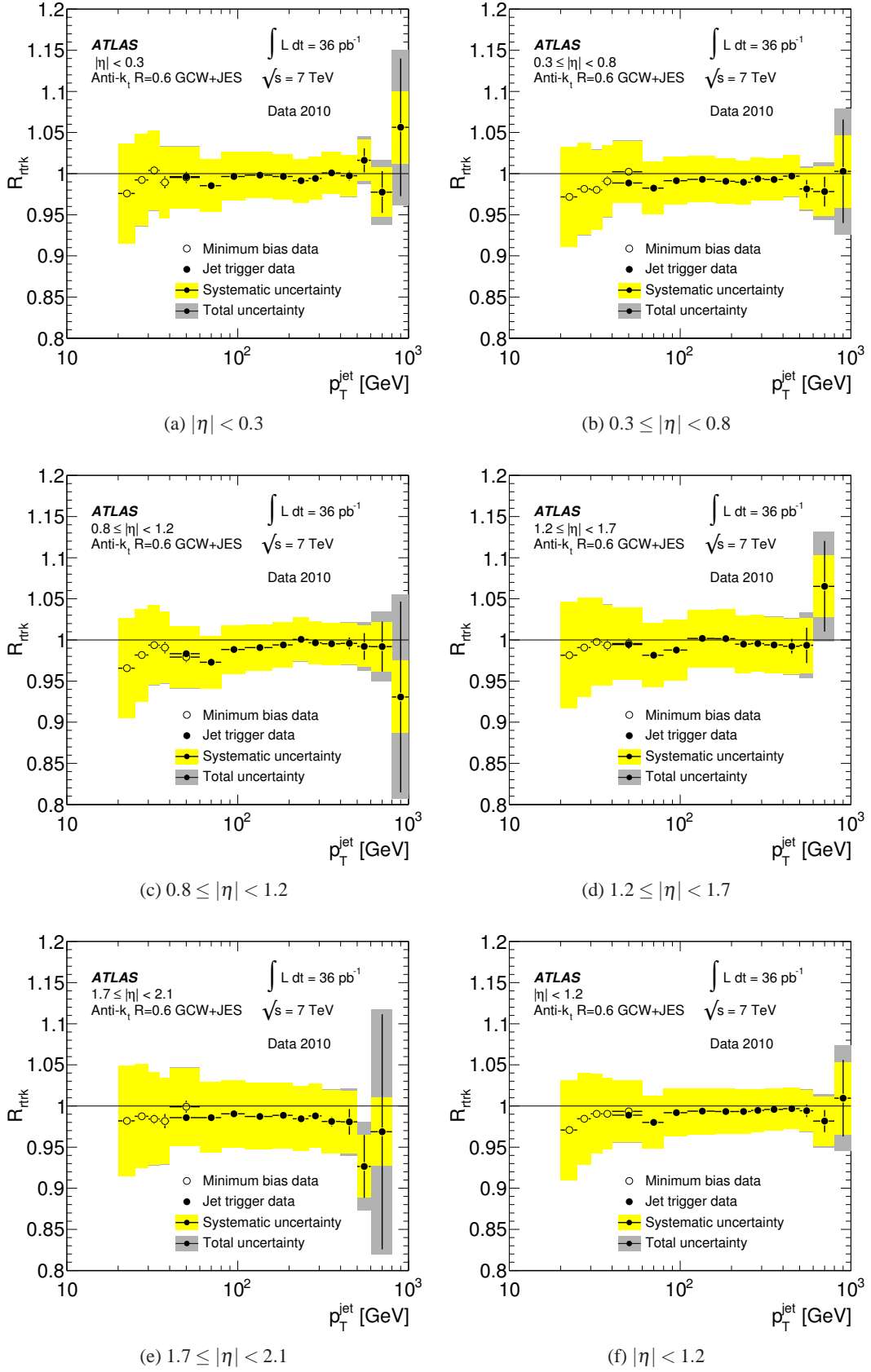


Fig. 59: Double ratio of the track to calorimeter response comparison in data and Monte Carlo simulation, $R_{\text{trk}} = [\langle r_{\text{trk}} \rangle]_{\text{Data}} / [\langle r_{\text{trk}} \rangle]_{\text{MC}}$, for anti- k_t jets with $R = 0.6$ using the GCW+JES calibration scheme as a function of p_T^{jet} for various η bins. Systematic (total) uncertainties are shown as a light (dark) band.

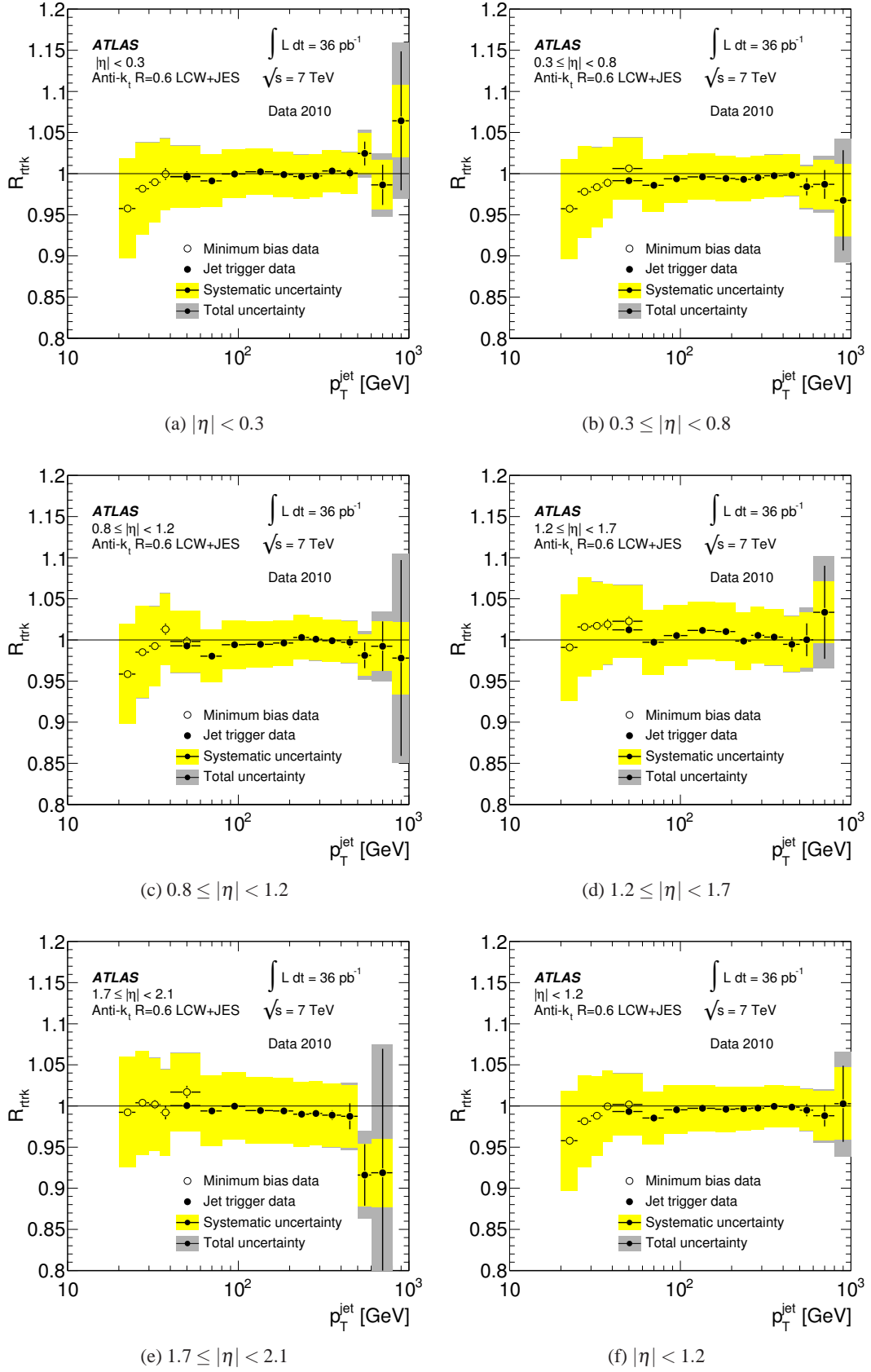


Fig. 60: Double ratio of the track to calorimeter response comparison in data and Monte Carlo simulation, $R_{\text{trk}} = [\langle r_{\text{trk}} \rangle]_{\text{Data}} / [\langle r_{\text{trk}} \rangle]_{\text{MC}}$, for anti- k_t jets with $R = 0.6$ using the LCW+JES calibration scheme as a function of p_T^{jet} for various η bins. Systematic (total) uncertainties are shown as a light (dark) band.

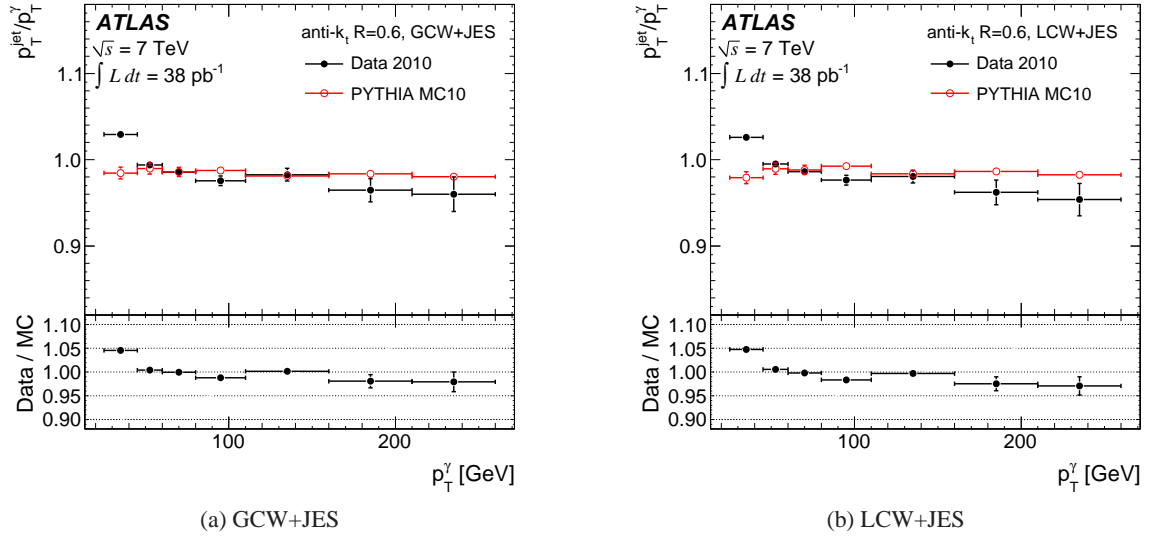


Fig. 61: Average jet response as determined by the direct p_T balance technique for anti- k_t jets with $R = 0.6$ calibrated with the GCW+JES (a) and LCW+JES (b) scheme as a function of photon transverse momentum for both data and Monte Carlo simulation. The lower part of each figure shows the data to Monte Carlo simulation ratio. Only statistical uncertainties are shown.

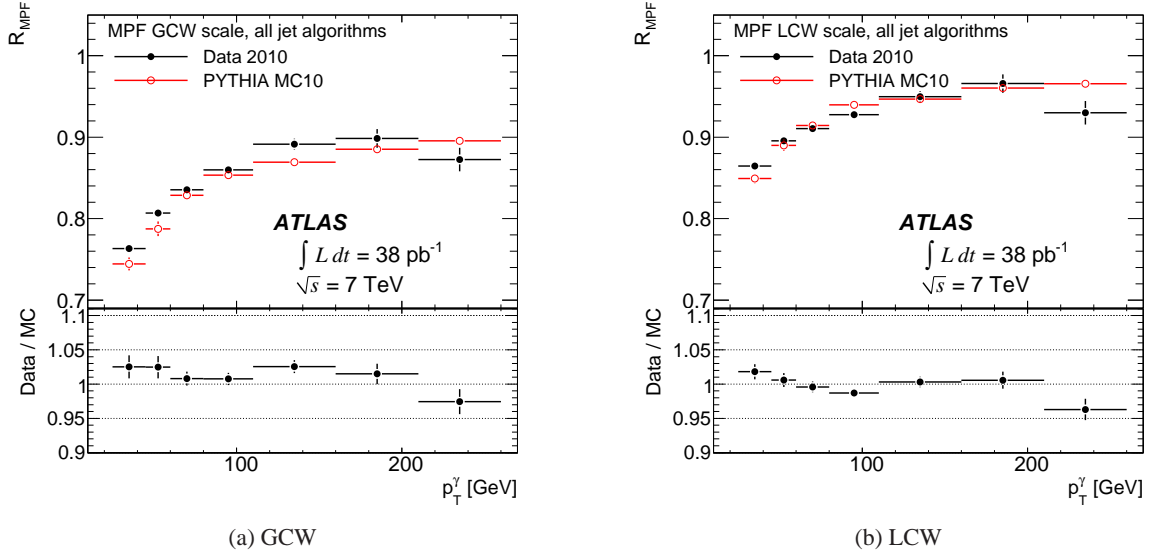


Fig. 62: Average calorimeter response as determined by the MPF technique for the GCW (a) and LCW (b) calibration scheme as a function of photon transverse momentum for both data and Monte Carlo simulation. The lower part of each figure shows the data to Monte Carlo simulation ratio. Only statistical uncertainties are shown.

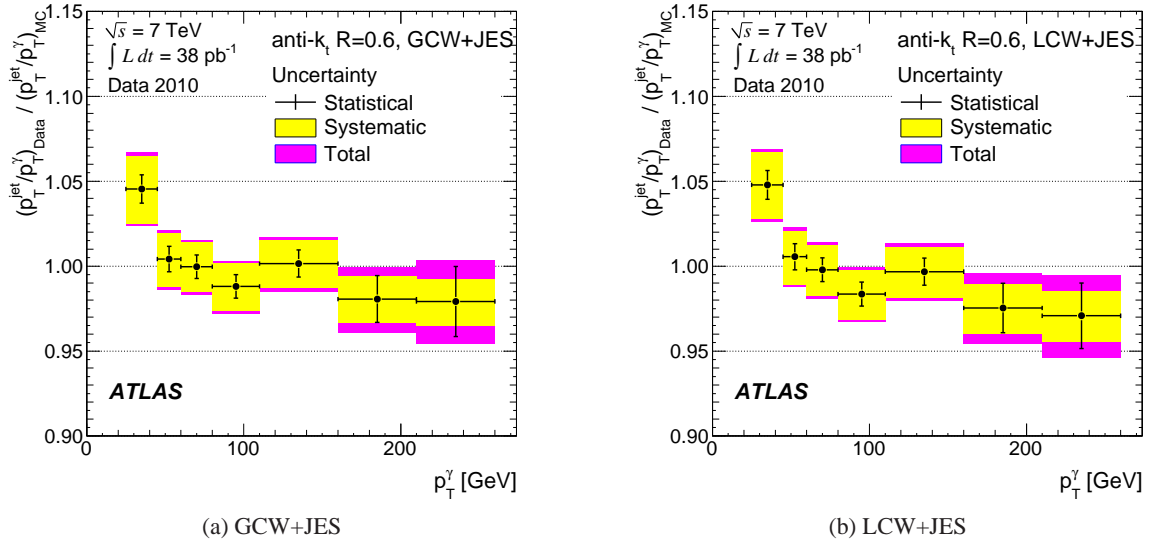


Fig. 63: Average jet response in data to the response in Monte Carlo simulation using the direct p_T balance technique of anti- k_t jets with $R = 0.6$ calibrated with the GCW+JES (a) and LCW+JES (b) scheme as a function of photon transverse momentum. Statistical and systematic uncertainties (light band) are included with the total uncertainty shown as the dark band.

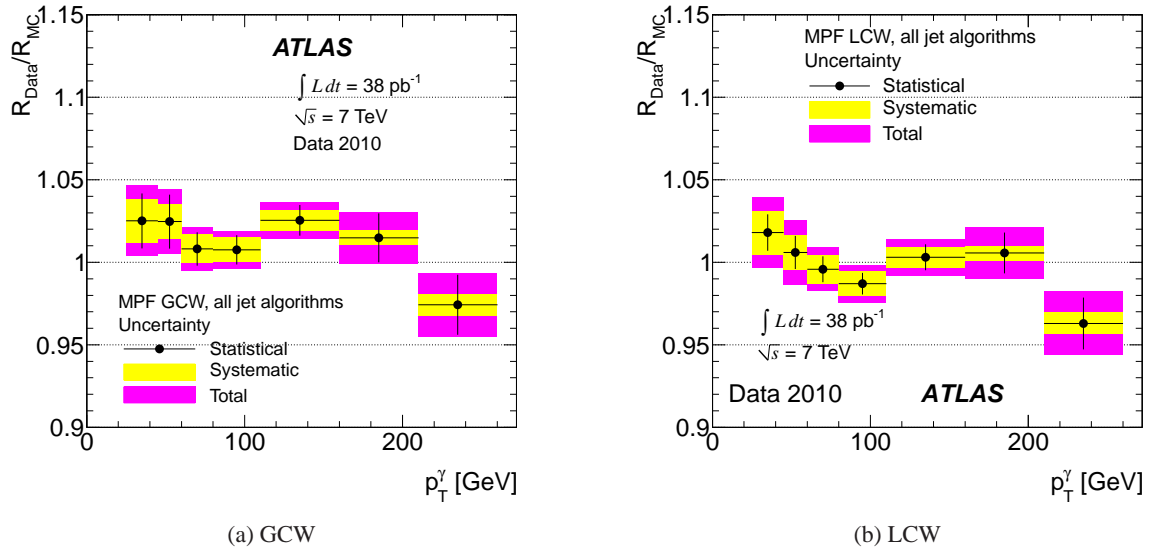


Fig. 64: The ratios of the MPF calorimeter response in data to the response in Monte Carlo simulation using the MPF method for each input energy scale GCW (a), and LCW (b) as a function of the photon transverse momentum. Statistical and systematic uncertainties (light band) are included. The total uncertainty is shown as the dark band.

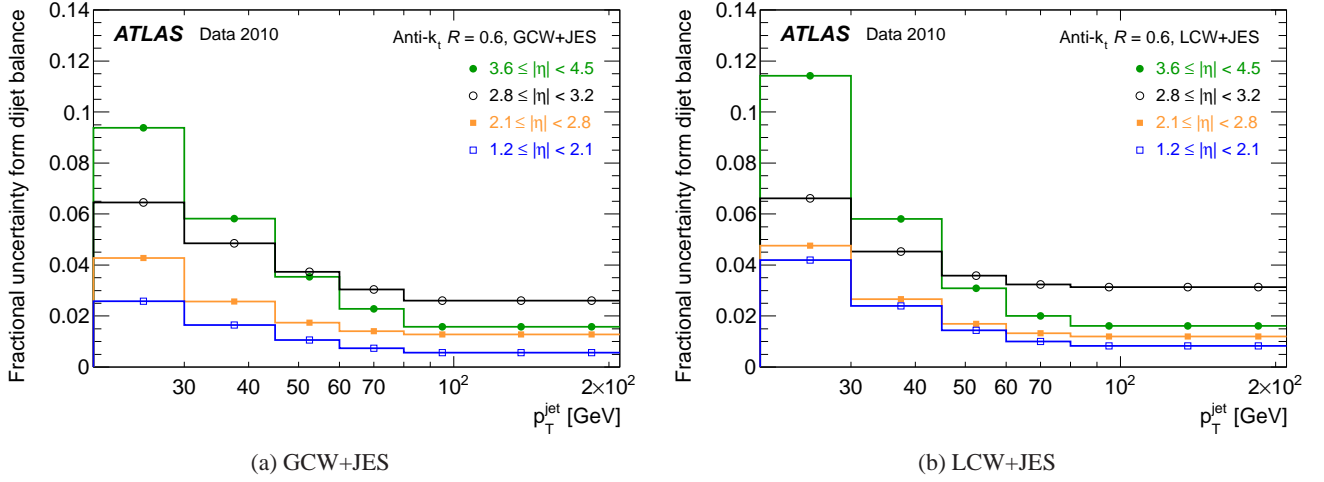


Fig. 65: Uncertainty in the jet response obtained from the dijet η -intercalibration technique for anti- k_t jets with $R = 0.6$ as a function of the jet p_T for various $|\eta|$ -regions of the calorimeter. The jets are calibrated with the GCW+JES (a) and the LCW+JES (b) calibration schemes. Only statistical uncertainties are shown.

scales. To calculate the response using the MPF technique at these energy scales the E_T^{miss} is calculated using GCW or LCW calibrated topo-clusters as an input³⁴. All the JES calibrations are found to be consistent between data and Monte Carlo simulation to within 3 to 4%.

The ratios of jet response in data to the response in Monte Carlo simulation using the direct p_T balance technique for the GCW+JES and LCW+JES jet calibration schemes as a function of the photon transverse momentum are shown in Figure 63. The agreement of data and Monte Carlo simulation is within 5% and is compatible with unity within the statistical and systematic uncertainties. A similar result for the MPF technique is shown in Figure 64. Good agreement between data and Monte Carlo simulation is found.

14.3.3 Intercalibration of forward jets using events with dijet topologies

The transverse momentum balance in events with only two jets at high transverse energy can be used to determine the JES uncertainty for jets in the forward detector region. The matrix method, described in Section 9.6, is used in order to test the performance of the GCW+JES and LCW+JES calibrations for jets with $|\eta| > 1.2$ and to determine the JES uncertainty in the forward region based on the well calibrated jet in the central reference region.

The same selection and method as for the test of the EM+JES calibration is applied, with two exceptions: the reference region is defined by $|\eta_{\text{det}}| < 1.2$ instead of $|\eta_{\text{det}}| < 0.8$, and a fit is applied to smooth out statistical fluctuations. The JES uncertainty in the reference regions is obtained from the γ -jet results

³⁴ For the GCW calibration scheme the cell energies in the topo-clusters are multiplied by the cell energy weights described in Section 13.1.

(see Section 14.3.2) and using the sum of track momenta (Section 14.3.1).

Figure 65 shows the resulting uncertainties as a function of p_T^{jet} for various η -bins. The uncertainty is taken as the RMS spread of the relative response from the Monte Carlo predictions around the relative response measured in data (see Section 9.6.6). The JES uncertainty introduced by the dijet balance is largest at lower p_T^{jet} and smallest at higher p_T^{jet} . For $p_T^{\text{jet}} > 100$ GeV the JES uncertainty for the GCW+JES scheme is less than 1% for $1.2 \leq |\eta| < 2.1$ and about 2.5% for $2.8 \leq |\eta| < 3.2$. For $p_T^{\text{jet}} = 20$ GeV the JES uncertainty is about 2% for $1.2 \leq |\eta| < 2.1$ and about 9.5% for $3.6 \leq |\eta| < 4.5$.

The JES uncertainties for the LCW+JES calibration scheme are slightly larger than those for GCW+JES scheme.

14.3.4 Multijet transverse momentum balance

The multijet balance (MJB) technique, described in Section 10.3, is used to evaluate the JES uncertainty in the high transverse momentum region for the GCW+JES and LCW+JES calibration schemes. The method and selection cuts used are the same as those for the EM+JES calibrated jets.

Figure 66 shows the MJB for anti- k_t jets with $R = 0.6$ obtained using the GCW+JES and LCW+JES calibrations in the data and Monte Carlo simulation as a function of the recoil p_T . The agreement between the data and MC simulations, evaluated as the data to Monte Carlo simulation ratio, are very similar to those for the EM+JES calibration.

The systematic uncertainties on the MJB for these cell energy weighting calibration schemes are evaluated in the same way as the EM+JES calibration, described in Section 10.3.4, except for the component of the standard JES uncertainty on the recoil system. The JES uncertainty for jets in the recoil system is obtained from the *in situ* γ -jet balance discussed in Section 14.3.2. In this case, the systematic uncertainty on the

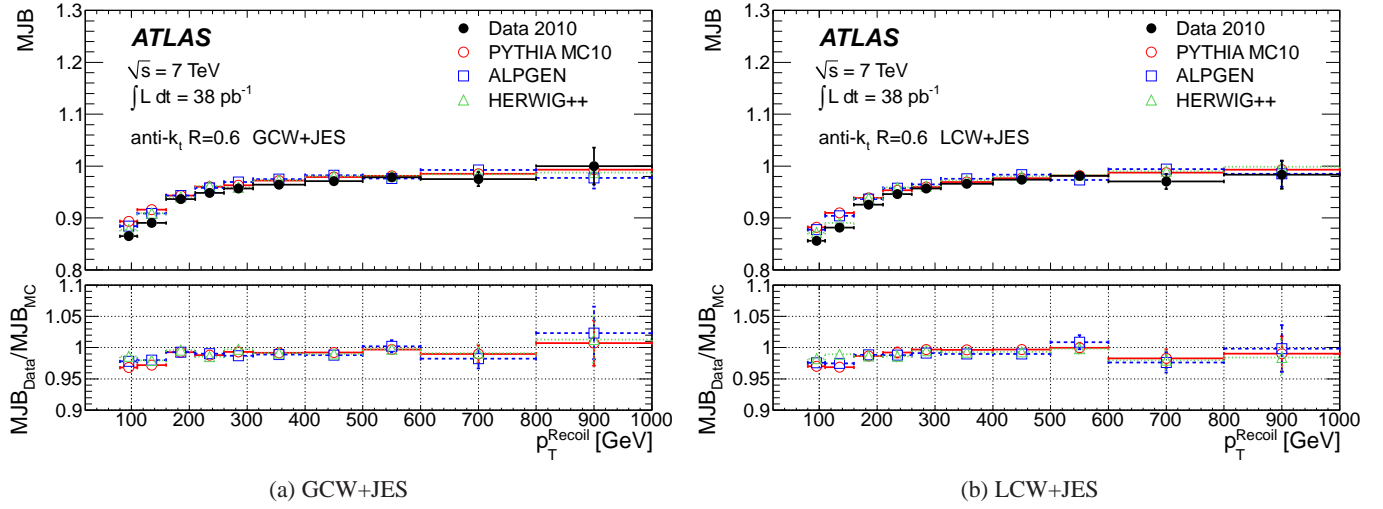


Fig. 66: Multijet balance MJB as a function of the recoil system p_T for data and Monte Carlo simulation for the anti- k_t algorithm with $R = 0.6$ using the GCW+JES (a) and LCW+JES (b) calibration scheme. Only statistical uncertainties are shown.

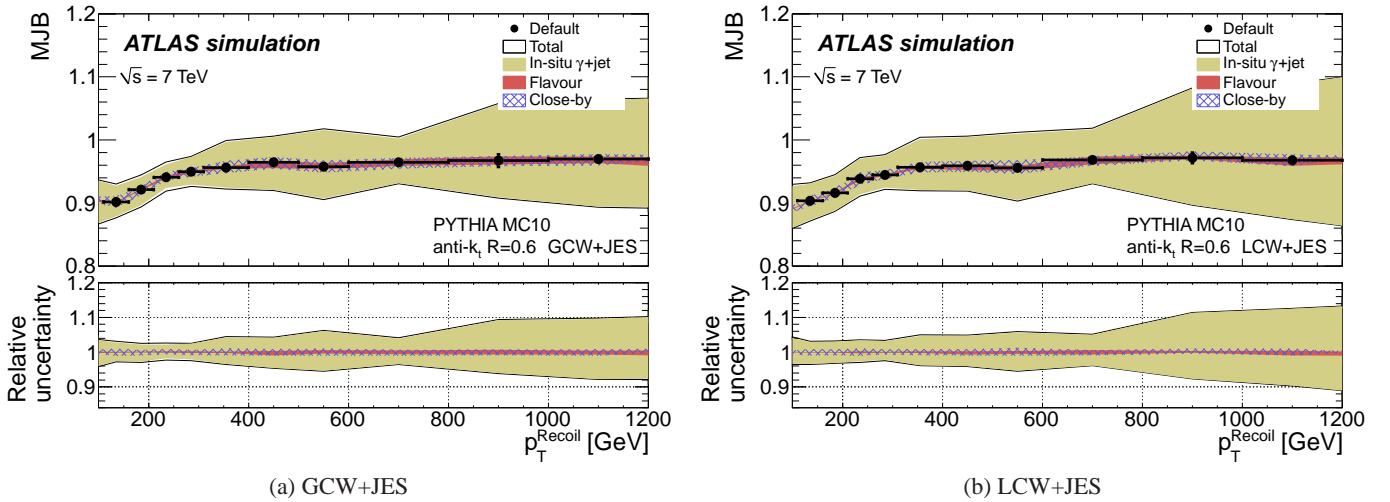


Fig. 67: The multijet balance MJB_{MC} as a function of the recoil system p_T (full dots) for anti- k_t jets with $R = 0.6$ using the GCW+JES (a) and LCW+JES (b) calibration schemes. The three bands are defined by the maximum shift of MJB when the jets that compose the recoil system are shifted up and down by the JES uncertainty determined from the γ -jet balance, close-by jet and flavour uncertainties. The black lines show the total uncertainty obtained by adding in quadrature the individual uncertainties. The lower part of the figure shows the relative uncertainty due to the scale uncertainty of the jets that compose the recoil system, defined as the maximum relative shift with respect to the nominal value, as a function of p_T^{Recoil} .

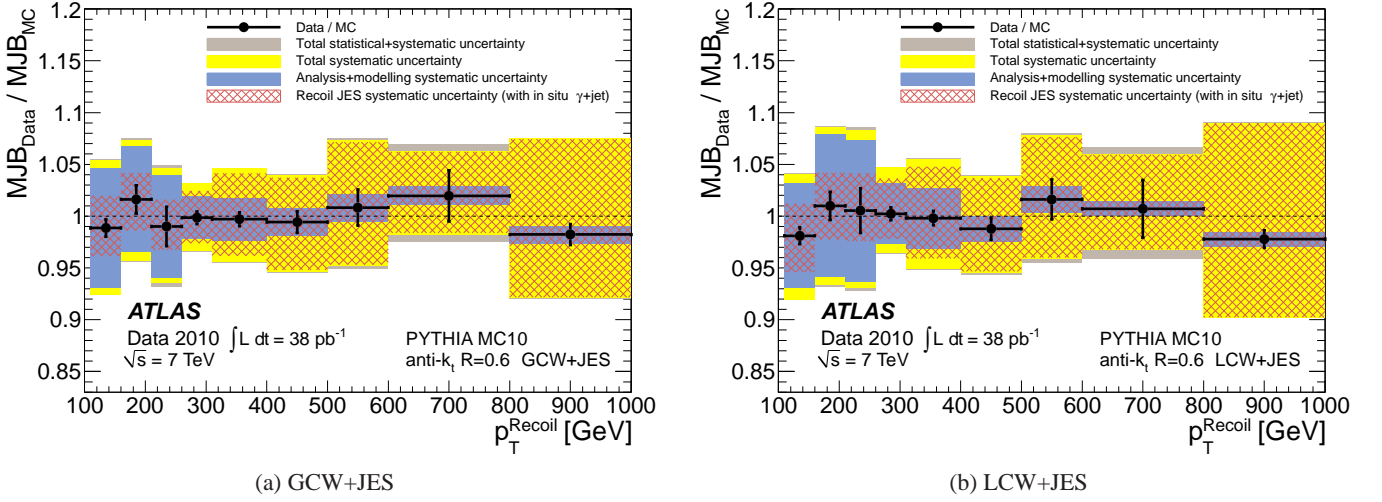


Fig. 68: Ratio of the data to MC for the multijet balance as a function of the recoil system p_T for anti- k_t jets with $R = 0.6$ using the GCW+JES (a) and LCW+JES (b) calibration schemes. The various shaded regions show the total uncertainty (dark band) obtained as the squared sum of the total systematic uncertainty (light band) and of the statistical uncertainty (error bars). Also displayed are the contributions to the systematic uncertainty due to analysis cuts and event modelling (darkest band) and to the jet energy scale for jets in the recoil system (hatched band).

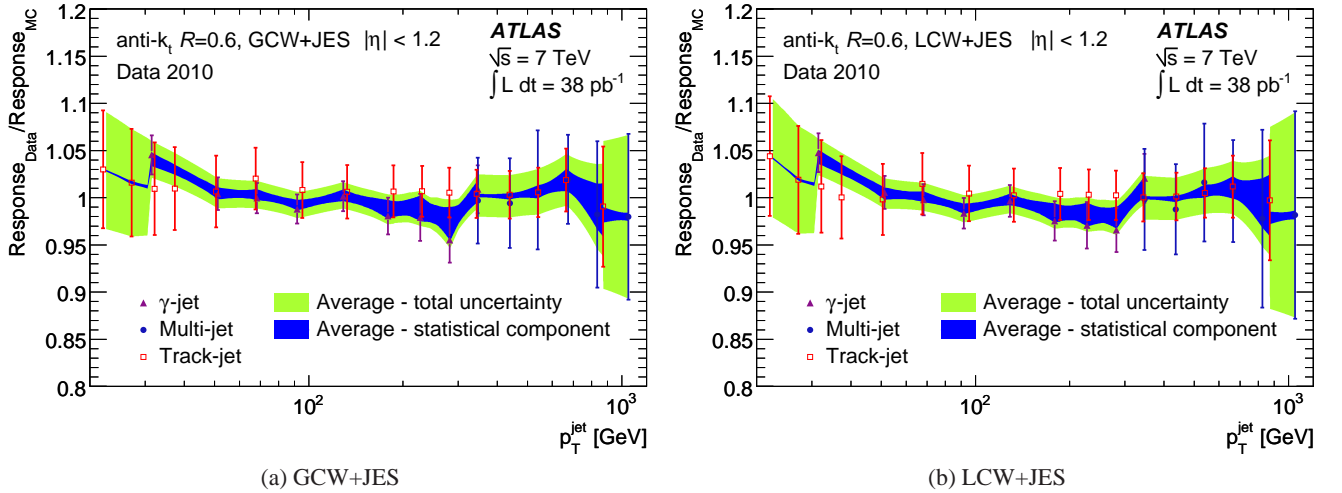


Fig. 69: Jet response ratio of the data to the Monte Carlo simulation as a function of p_T^{jet} for three *in situ* techniques using as reference objects: photons (γ -jet), a system of low energetic jets (multijet) or the transverse momentum of all tracks associated to jets (tracks in jets). The error bar displays the statistical and systematic uncertainties added in quadrature. Shown are the results for anti- k_t jets with $R = 0.6$ calibrated with the GCW+JES (a) and LCW+JES (b) calibration schemes. The light band indicates the combination of the *in situ* techniques. The inner dark band shows the fraction due to the statistical uncertainty.

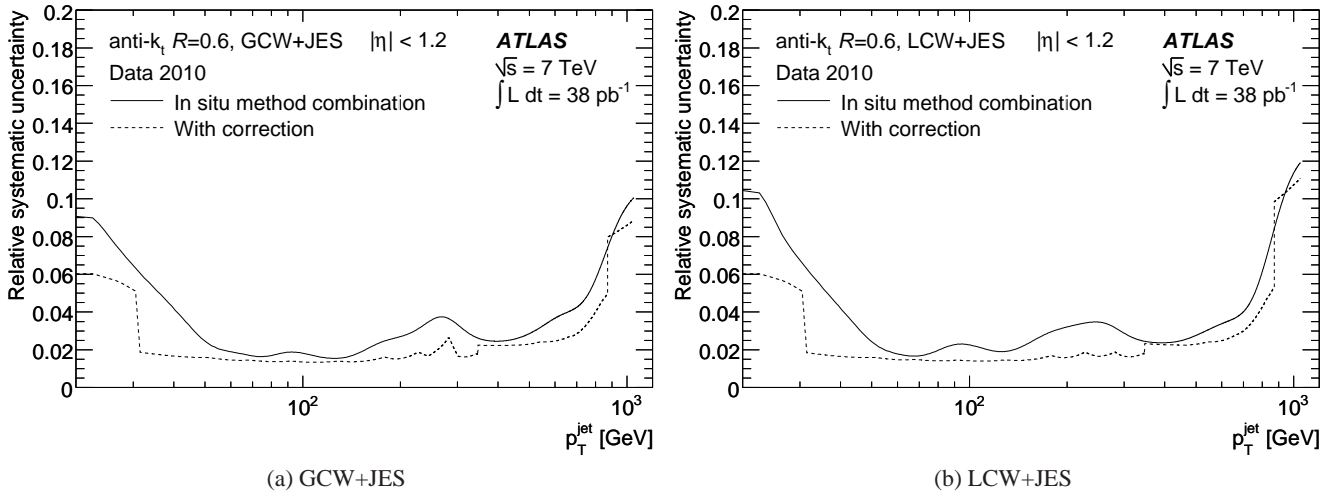


Fig. 70: Jet energy scale uncertainty (solid line) as a function of p_T^{jet} for anti- k_t jets with $R = 0.6$ for $|\eta| < 1.2$ calibrated with the GCW+JES (a) and the LCW+JES (b) calibration scheme. The dashed line shows the JES uncertainty that could have been achieved, if *in situ* techniques had been used to recalibrate the jets.

MJB due to the recoil system JES uncertainty is then calculated by shifting the p_T of recoil jets up and down by the γ -jet JES uncertainty. In order to apply the γ -jet JES uncertainty to the recoil system, the MJB analysis is performed with jets selected within the range $|\eta| < 1.2$, where the JES uncertainty based on γ -jet events has been derived. The close-by jet and flavour composition systematic uncertainties are also re-evaluated for the GCW+JES and LCW+JES jets using the same method (see Section 17).

Figure 67 shows the total and individual JES systematic uncertainties on the recoil system for anti- k_t jets with $R = 0.6$ calibrated by the GCW+JES and LCW+JES schemes. The increase of the JES uncertainty at high p_T^{jet} above 800 GeV is caused by a large JES systematic uncertainty due to limited γ -jet event statistics at high p_T .

The systematic uncertainties associated with the analysis method and event modelling are re-evaluated in the same way as for the EM+JES calibration scheme and then added to the recoil system JES systematic uncertainties. The summary of all systematic uncertainties and the total uncertainty obtained by adding the statistical and systematic uncertainties in quadrature is shown in Figure 68 for anti- k_t jets with $R = 0.6$.

14.3.5 Cell weighting JES uncertainty from combination of *in situ* techniques

Figure 69 shows the jet response ratio of data to Monte Carlo simulation for the various *in situ* techniques as a function of the jet transverse momentum for the GCW+JES (a) and the LCW+JES (b) calibration schemes. Statistical and systematic uncertainties are displayed. The average from the combination of all *in situ* techniques is overlaid.

The weight of each *in situ* technique contributing to the average is similar to the one for the EM+JES calibration scheme

shown in Figure 45. The contributions are also similar for the LCW+JES and the GCW+JES calibration schemes.

Figure 70 shows the final JES uncertainty for the GCW+JES (a) and the LCW+JES (b) calibration schemes for $|\eta| < 1.2$. At the lowest p_T the JES uncertainty is about 9% to 10% and decreases for increasing p_T^{jet} . For $p_T^{\text{jet}} > 50$ GeV it is about 2% and at $p_T^{\text{jet}} = 250$ GeV it is about 3 to 4%. For jets in the TeV-regime the JES uncertainty is 10 to 12%.

Figure 70 also shows the JES uncertainty attainable, if the *in situ* techniques had been used to correct the jet energy. Using the *in situ* techniques for jet calibration would have resulted in an improved JES uncertainty for both jet calibration schemes based on cell energy weighting.

The JES uncertainty obtained in the central reference region ($|\eta| < 1.2$) is used to derive the JES uncertainty in the forward region using the dijet balance technique. The central region JES uncertainty is combined with the uncertainties from the dijet balance shown in Figure 65.

15 Summary of jet energy scale uncertainties of various calibration schemes

The EM+JES uncertainties are derived from single hadron response measurements and from systematic variations of the Monte Carlo simulation (see Section 9).

The JES uncertainty for the GS jet calibration scheme is given by the sum in quadrature of the EM+JES uncertainty and the uncertainty associated to the GS corrections. The latter, derived in Section 12, is conservatively taken to be 0.5% for $30 < p_T < 800$ GeV and $|\eta| < 2.1$ and 1% for $p_T < 30$ GeV and $2.1 < |\eta| < 2.8$. These uncertainties are also supported by *in situ* techniques.

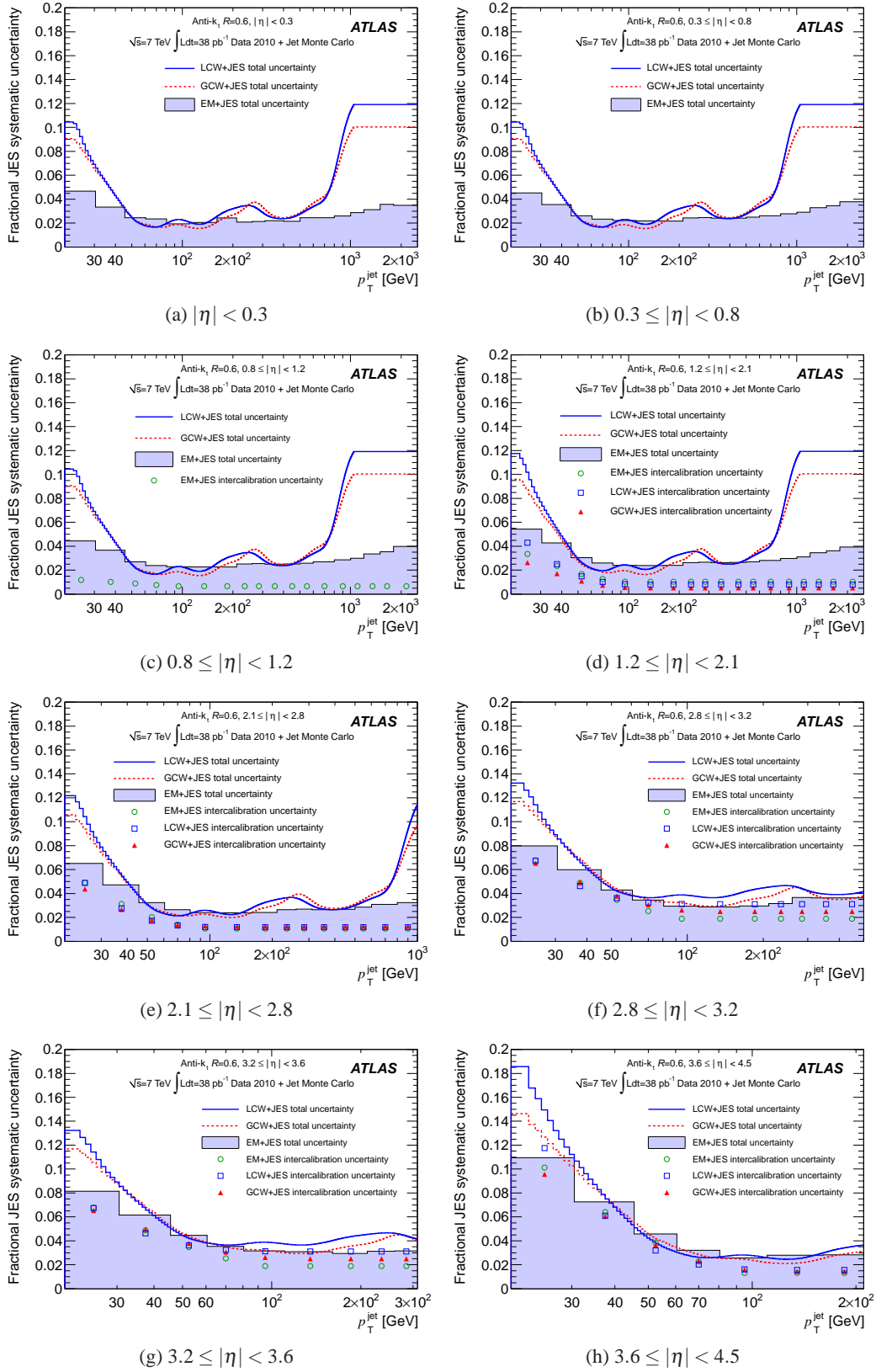


Fig. 71: Fractional JES uncertainties as a function of p_T^{jet} for anti- k_t jets with $R = 0.6$ for the various η regions for the LCW+JES (full line) and the GCW+JES (dashed line) schemes. These are derived from a combination of the *in situ* techniques which are limited in the number of available events at large p_T^{jet} . The fractional JES uncertainty for EM+JES derived from single hadron response measurements and systematic Monte Carlo simulation variations is overlaid as shaded area for comparison. The η -intercalibration uncertainty is shown as open symbols for $|\eta| > 0.8$ for the EM+JES and for $|\eta| > 1.2$ for the LCW+JES and GCW+JES schemes.

The JES uncertainties in the LCW+JES and GCW+JES jet calibration schemes are derived from a combination of several *in situ* techniques.

Figure 71 shows a comparison of the JES uncertainties for the EM+JES, the LCW+JES and the GCW+JES jet calibration schemes for various η -regions. The uncertainties in the LCW+JES and GCW+JES schemes derived in Section 14 are similar, but the uncertainty for the GCW+JES calibration scheme is a bit smaller for very low and very large p_T^{jet} .

Over a wide kinematic range, $40 \lesssim p_T^{\text{jet}} \lesssim 600$ GeV, all calibration schemes show a similar JES uncertainty. At $p_T^{\text{jet}} \approx 250$ GeV the uncertainties based on the *in situ* techniques are about 2% larger compared to the uncertainty results from the EM+JES calibration scheme.

For $p_T^{\text{jet}} < 40$ GeV and $p_T^{\text{jet}} > 600$ GeV the EM+JES calibration scheme has a considerably smaller uncertainty. For the high p_T regions the JES calibration based on *in situ* suffers from the limited number of events in the data samples. At low p_T the systematic uncertainty on the *in situ* methods leads to a larger JES uncertainty.

16 Jet reconstruction efficiency

A tag-and-probe method is implemented to measure *in situ* the jet reconstruction efficiency relative to track jets. Because track jets (see Section 6.2) and calorimeter jets (see Section 6.1) are reconstructed by independent ATLAS sub-detectors, a good agreement between data and Monte Carlo simulation for this matching efficiency means that the absolute jet reconstruction efficiency can be determined from the simulation.

16.1 Efficiency in the Monte Carlo simulation

The jet reconstruction efficiency is determined in the Monte Carlo simulation by counting in how many cases a calorimeter jet can be matched to a truth jet. Reconstructed jets are matched to truth jets, if their jet axes are within $\Delta R < 0.4$.

Figure 72a shows the jet reconstruction efficiency for anti- k_t jets with $R = 0.6$ calibrated with the EM+JES, GCW+JES, and LCW+JES calibration schemes as a function of the transverse momentum of the truth jet. The efficiency reaches its maximum value for a truth jet transverse momentum of 20 GeV. The lower part of the figure shows the ratio of the efficiency in the GCW+JES and LCW+JES calibration schemes to that obtained from the EM+JES scheme. Similar performance is found for all calibration schemes.

The small differences at low p_T^{jet} might be caused by the slightly better jet energy resolution obtained with the GCW+JES and the LCW+JES calibration schemes. Moreover, jets based on the LCW+JES scheme are built from calibrated topo-clusters while the jets calibrated with the EM+JES and the GCW+JES calibration schemes use topo-clusters at the electromagnetic scale.

16.2 Efficiency *in situ* validation

The ability of the Monte Carlo simulation to correctly reproduce the jet reconstruction in the data is tested using track jets that provide an independent reference.

A tag-and-probe technique is used as described in the following steps:

1. Only track jets with $p_T > 5$ GeV and $|\eta| < 1.9$ are considered.
2. The track jet with the highest p_T in the event is defined as the reference object.
3. The reference object is required to have $p_T > 15$ GeV³⁵.
4. The reference track jet is matched to a calorimeter jet with $p_T^{\text{jet}} > 7$ GeV, if $\Delta R(\text{tag, calojet}) < 0.6$ ³⁶.
5. The probe track jet must be back-to-back to the reference jet in ϕ with $|\Delta\phi| \geq 2.8$ radian.
6. Events with additional track jets within $|\Delta\phi| \geq 2.8$ radian are rejected.
7. The calorimeter reconstruction efficiency with respect to track jets is then defined as the fraction of probe jets matched to a calorimeter jet using $\Delta R(\text{probe, calojet}) < R$ (with $R = 0.4$ or $R = 0.6$) with respect to all probe jets.

The jet reconstruction efficiency is measured in a sample of minimum bias events and is compared to a minimum bias Monte Carlo simulation. Due to the restriction of $|\eta| < 1.9$ on track jets, the measurement is only valid for calorimeter jets with $|\eta| < 1.9 + R$, where $R = 0.4$ or $R = 0.6$.

Figures 72b-d show the measured calorimeter reconstruction efficiency with respect to track jets as a function of the calorimeter jet transverse momentum for anti- k_t jets with $R = 0.6$ calibrated with the EM+JES, GCW+JES, and LCW+JES calibration schemes³⁷. The reconstruction efficiency reaches a plateau close to 100% at a jet transverse calorimeter momentum of about 25 GeV. The matching efficiency in data (ϵ_{Data}) and in Monte Carlo simulation (ϵ_{MC}) shows a good overall agreement except at low p_T^{jet} where the efficiency in data is slightly lower than in the Monte Carlo simulation. Similar performance is found for all calibration schemes.

The systematic uncertainties on the jet reconstruction efficiency measured *in situ* are obtained by varying the following event selection requirements for both data and Monte Carlo simulation: the opening angle $|\Delta\phi|$ between the reference and

³⁵ Reference track jets with $p_T < 15$ GeV are not used, since they would result in a sample of biased probe track jets. In this case, mostly events where the probe track jet has fluctuated up in energy (such that it passes the 5 GeV threshold) would be kept. The 15 GeV cut has been determined by measuring the jet reconstruction efficiency relative to track jets as a function of the reference track jet p_T . The measured efficiency for low probe track jet p_T was found to be dependent on the reference track jet p_T when the latter is smaller than 15 GeV. The jet reconstruction efficiency is stable for a reference track jet p_T greater than 15 GeV.

³⁶ The less restrictive matching criterion with respect to previous sections is motivated by the lower p_T .

³⁷ Technically, the efficiency is first measured as a function of the track jet p_T . Using the known relation between the average track jet and the average calorimeter jet p_T , the track jet p_T is then converted to the calorimeter jet p_T^{jet} .

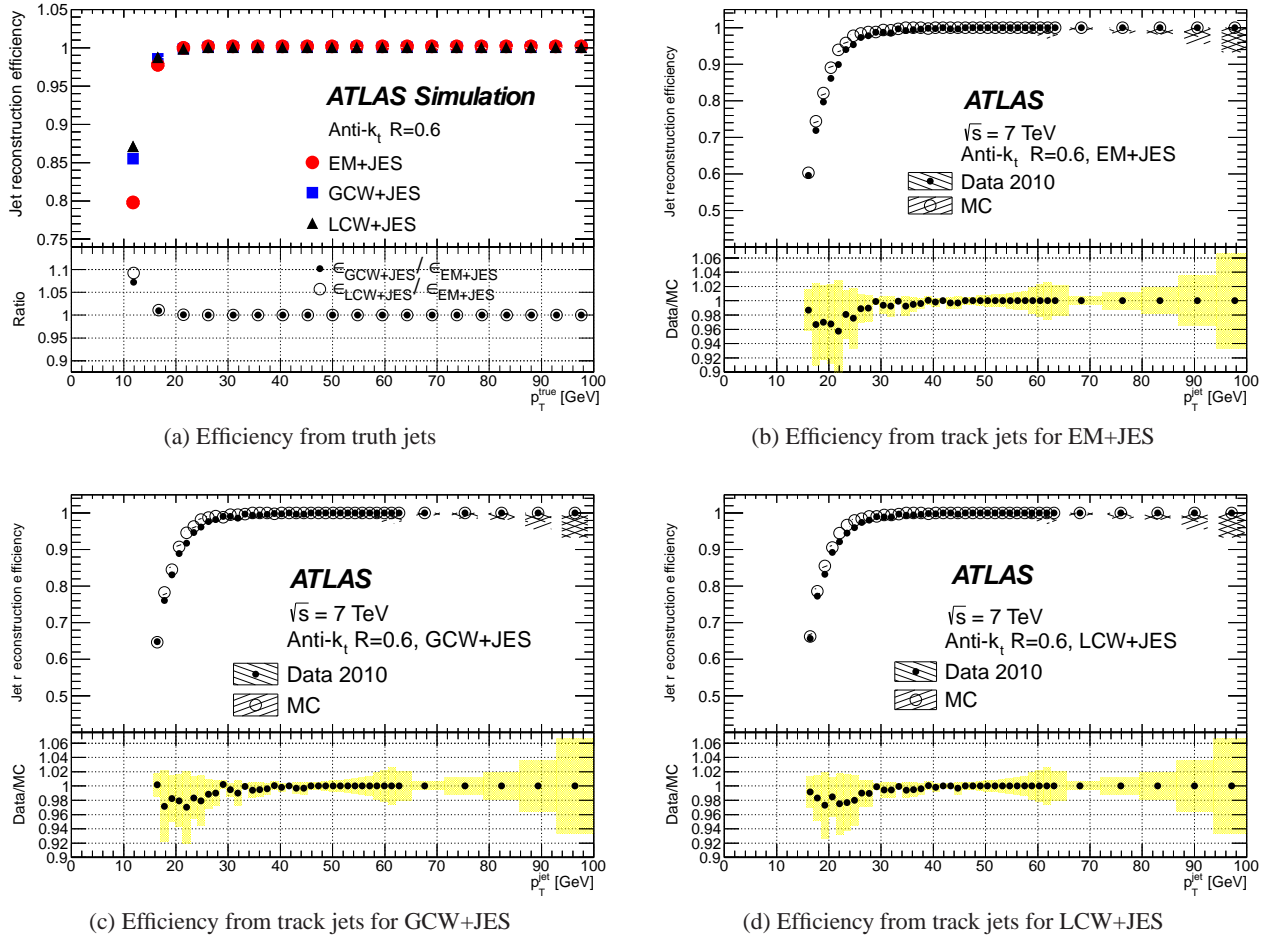


Fig. 72: Calorimeter jet reconstruction efficiency with respect to truth jets (a) and track jets (b,c,d) as a function of the truth jet (a) or the calorimeter jet (b,c,d) p_T for the three calibration schemes: EM+JES (b), GCW+JES (c) and LCW+JES (d). The lower part of the figure (a) shows ratio of the efficiency of the LCW+JES and the GCW+JES calibration schemes to that of the EM+JES calibration scheme. The ratio of data to Monte Carlo simulation is also shown in the lower part of the figure for (b), (c) and (d). The hatched area correspond to the systematic uncertainty obtained by variations in the *in situ* method.

the probe track jets, the ΔR requirement between the tag track jet and the calorimeter jet and the probe track jet and the calorimeter jet.

The sensitivity in both data and Monte Carlo simulation to the azimuthal opening angle as well as to the $\Delta R(\text{tag, calojet})$ variation is small. However, the efficiency shows a sensitivity with respect to the $\Delta R(\text{probe jet, calo jet})$. The variation of $\epsilon_{\text{Data}}/\epsilon_{\text{MC}}$ for these different parameters is shown in Figure 72. At high p_T^{jet} the statistical uncertainties after the cut variations lead to an enlarged uncertainty band.

The systematic uncertainty of the *in situ* determination is larger than the observed shift between data and Monte Carlo simulation. For $p_T^{\text{jet}} < 30$ GeV a systematic uncertainty of 2% for jets is assigned.

16.3 Summary of jet reconstruction efficiency

The jet reconstruction efficiency is derived using the nominal inclusive jet Monte Carlo simulation sample. The systematic uncertainty is evaluated using a tag-and-probe technique using track jets in both data and Monte Carlo simulation.

The jet reconstruction efficiency is well described by the Monte Carlo simulation and is within the systematic uncertainty of the *in situ* method. A systematic uncertainty of 2% for jets with $p_T^{\text{jet}} < 30$ GeV is assigned and negligible for higher p_T^{jet} .

17 Response uncertainty of non-isolated jets

The standard ATLAS jet calibration and associated JES uncertainty is obtained using only isolated jets (see Section 8.3).

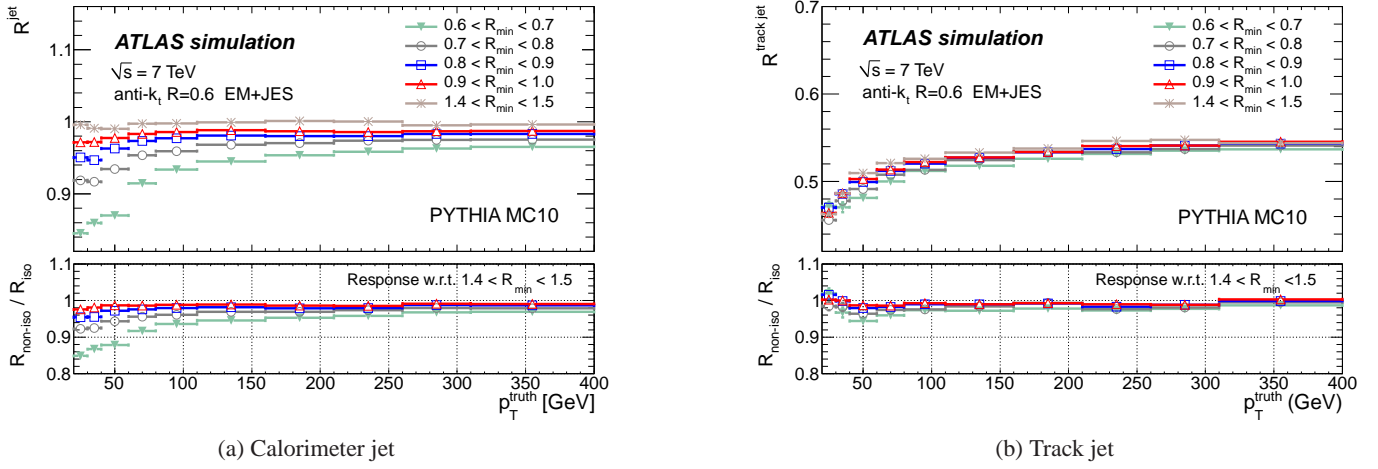


Fig. 73: Average ratio of calorimeter jet (a) and the track jet (b) p_T to the matched truth jet p_T as a function of truth jet p_T for anti- k_t jets with $R = 0.6$, for different R_{min} values. The bottom part of the figure shows the relative response of non-isolated jets with respect to that of isolated jets, obtained as the calorimeter or track jet response for $R_{\text{min}} < 1.0$ divided by the jet response for $1.4 \leq R_{\text{min}} < 1.5$.

Jets are, however, often produced with nearby jets in a busy environment such as found in multijet topologies or in events where top-quark pairs are produced. Therefore a separate study is needed to determine the additional JES uncertainty for jets with nearby jet activity.

Jets with $p_T^{\text{jet}} > 20$ GeV and $|y| < 2.8$ calibrated with the EM+JES scheme are used. The close-by JES uncertainty is evaluated within $|y| < 2.0$.

17.1 Evaluation of close-by jet effects

The effect due to close-by jets is evaluated in the Monte Carlo simulation by using truth jets as a reference. Similarly, track jets are used as a reference in both data and Monte Carlo simulation (see Sections 6.2 and 6.3 for comparison). The calorimeter jet response relative to these reference jets is examined for different values of R_{min} , the distance from the calorimeter jet to the closest jet in η - ϕ space.

The relative calorimeter jet response to the truth jets provides an absolute p_T scale for the calorimeter jets, while the relative response to the track jets allows *in situ* validation of the calorimeter jet response and the evaluation of the systematic uncertainty. For this purpose, the track jet response in data needs to be established for the non-isolated case and the associated systematic uncertainty has to be understood.

In the relative response measurement in the Monte Carlo simulation, the truth jet is matched to the calorimeter jet or track jet in η - ϕ space by requiring $\Delta R < 0.3$. Similarly, the track jet is matched to the calorimeter jet within $\Delta R < 0.3$ when the relative response to the track jet is examined. If two or more jets are matched within the ΔR range, the closest matched jet is taken.

The calorimeter response to the matched track jet is defined as the ratio of the calorimeter jet p_T^{jet} to the track jet transverse

momentum ($p_T^{\text{track jet}}$)

$$r^{\text{calo/track jet}} = p_T^{\text{jet}} / p_T^{\text{track jet}}. \quad (49)$$

This response is examined as a function of the jet transverse momentum p_T^{jet} and for different R_{min} values measured relative to the closest calorimeter jet with $p_T > 7$ GeV at the EM energy scale³⁸. The ratio of the calorimeter jet response for non-isolated (i.e. small R_{min}) to the response of isolated (large R_{min}) jets, is given by

$$r_{\text{non-iso/iso}}^{\text{calo/track jet}} = r_{\text{non-iso}}^{\text{calo/track jet}} / r_{\text{iso}}^{\text{calo/track jet}}. \quad (50)$$

This ratio is compared between data and Monte Carlo simulations.

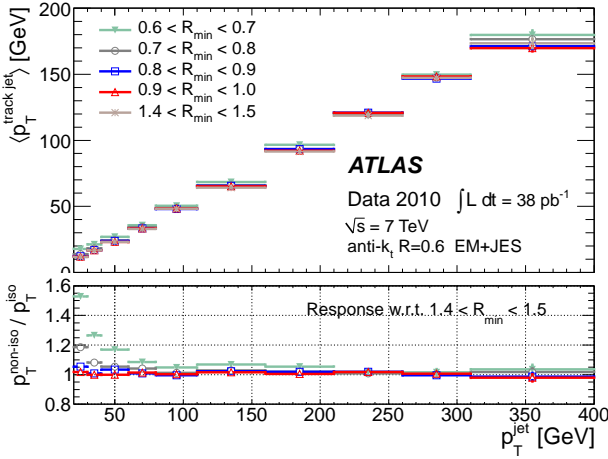
$$A_{\text{close-by}} = \left[r_{\text{non-iso/iso}}^{\text{calo/track jet}} \right]_{\text{Data}} / \left[r_{\text{non-iso/iso}}^{\text{calo/track jet}} \right]_{\text{MC}}. \quad (51)$$

The deviation of $A_{\text{close-by}}$ is assumed to represent the component of calorimeter JES uncertainty due to close-by jets. This uncertainty, convolved with the systematic uncertainty in the track jet response due to a nearby jet, provides the total JES systematic uncertainty due to the close-by jet effect.

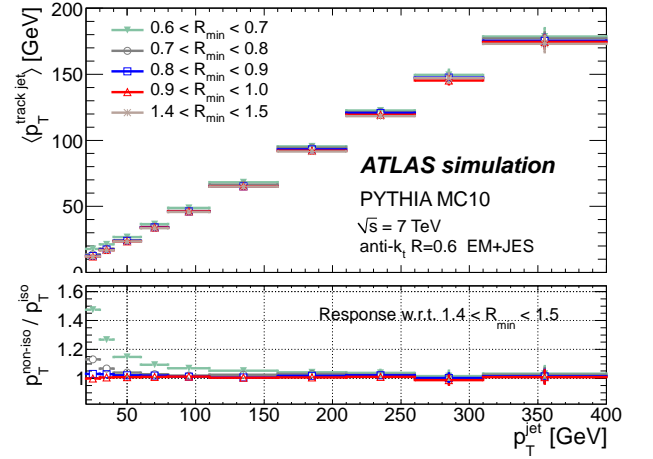
17.2 Non-isolated jet response

Events that contain at least two jets with $p_T^{\text{jet}} > 20$ GeV and absolute rapidity $|y| < 2.8$ are selected. The response of non-isolated jets is studied in the Monte Carlo simulation using the calorimeter jet response $\mathcal{R}^{\text{jet}} = p_T^{\text{jet}} / p_T^{\text{truth}}$.

³⁸ Unless otherwise stated, calorimeter jets (selected as listed below) and nearby jets (selected with $p_T > 7$ GeV at the EM scale) are both used in the jet response measurement, if a matched track jet is found.



(a) Data



(b) MC

Fig. 74: Average track jet p_T as a function of calorimeter jet p_T for anti- k_t jets with $R = 0.6$ in data (a) and MC simulations (b) for different R_{\min} values. The lower part shows the relative response of non-isolated jets with respect to that of isolated jets, obtained as the track jet p_T for $R_{\min} < 1.0$ divided by that for $1.4 \leq R_{\min} < 1.5$.

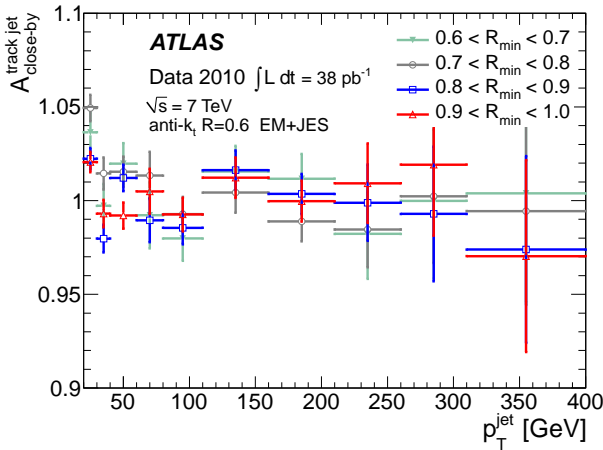


Fig. 75: Ratio of data to Monte Carlo simulation of the track jet $p_T^{\text{close-by}}$ for non-isolated jets divided by the track jet $p_T^{\text{track jet}}$ for isolated jets as a function of the jet p_T^{jet} . Only statistical uncertainties are shown.

Figure 73a shows the calorimeter jet response as a function of p_T^{truth} for anti- k_t jets with $R = 0.6$. The jet response was measured for nearby jets in bins of R_{\min} values. The lower part of the figure shows the ratio of the non-isolated jet response for $R_{\min} < 1.0$ to the isolated response $1.4 \leq R_{\min} < 1.5$,

$$\mathcal{R}_{\text{non-iso}}^{\text{jet}} / \mathcal{R}_{\text{iso}}^{\text{jet}}. \quad (52)$$

The observed behaviour at small R_{\min} values indicates that the non-isolated jet response is lower by up to 15% relative to the isolated jet response for $p_T^{\text{jet}} > 20$ GeV, if the two jets are within $R_{\min} < R + 0.3$. The magnitude of this effect depends on p_T^{jet} and is largest at low p_T^{jet} .

	$R = 0.6$		$R = 0.4$	
p_T^{jet} [GeV]	20 – 30	> 30	20 – 30	> 30
$0.4 \leq R_{\min} < 0.5$	-	-	2.7%	2.8%
$0.5 \leq R_{\min} < 0.6$	-	-	1.7%	2.3%
$0.6 \leq R_{\min} < 0.7$	3.9%	1.9%	2.5%	2.7%
$0.7 \leq R_{\min} < 0.8$	5.1%	1.6%	-	-
$0.8 \leq R_{\min} < 0.9$	2.5%	1.9%	-	-

Table 15: Summary of jet energy scale systematic uncertainty assigned for non-isolated jets accompanied by a close-by jet within the denoted R_{\min} ranges. The second row in the table indicates the p_T range of the non-isolated jets. Anti- k_t jets with $R = 0.6$ and $R = 0.4$ are used.

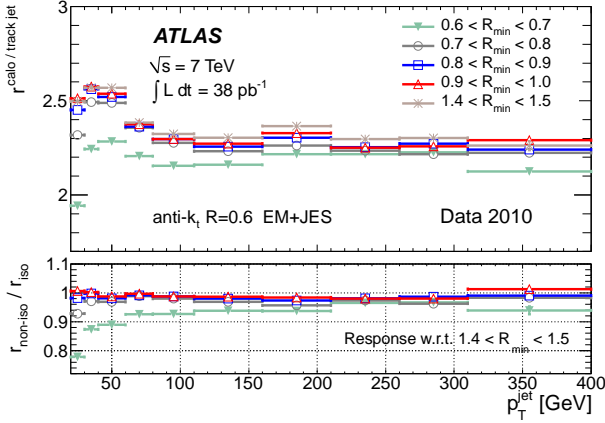
The track jet response relative to the matched truth jet is defined as

$$\mathcal{R}^{\text{track jet}} = p_T^{\text{track jet}} / p_T^{\text{truth}}. \quad (53)$$

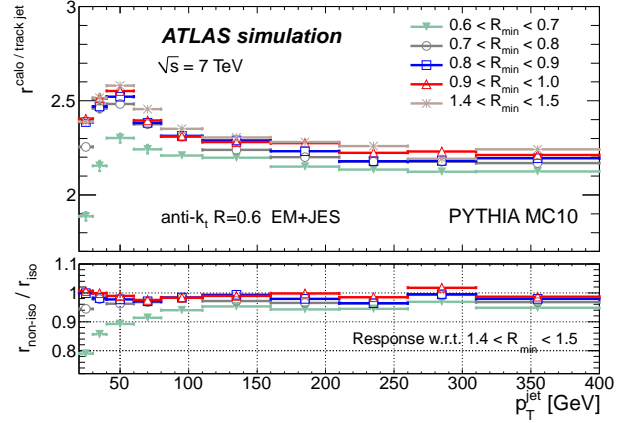
Figure 73b shows $\mathcal{R}^{\text{track jet}}$ as a function of p_T^{truth} for anti- k_t jets with $R = 0.6$. The track jet response is more stable against the presence of close-by jets and has a much weaker R_{\min} dependence than the calorimeter jet response. This results from the smaller ambiguity in the matching between the truth and track jets that are both measured from the primary interaction point. Moreover, track jets are less influenced by magnetic field effects than calorimeter jets.

17.3 Non-isolated jet energy scale uncertainty

Figure 74 shows the average track jet transverse momentum as a function of p_T^{jet} for anti- k_t jets with $R = 0.6$ in both data and Monte Carlo simulations for various R_{\min} values. The lower part of the figure shows the p_T ratio of non-isolated to isolated



(a) Data



(b) Monte Carlo simulation

Fig. 76: Ratio of calorimeter jet p_T^{jet} to the matched track jet p_T^{jet} as a function of calorimeter jet p_T^{jet} for anti- k_t jets with $R = 0.6$ in data (a) and Monte Carlo simulations (b) for different R_{\min} values. The lower part shows the relative response of non-isolated jets with respect to that of isolated jets, obtained as the jet response for $R_{\min} < 1.0$ divided by the jet response for $1.4 \leq R_{\min} < 1.5$.

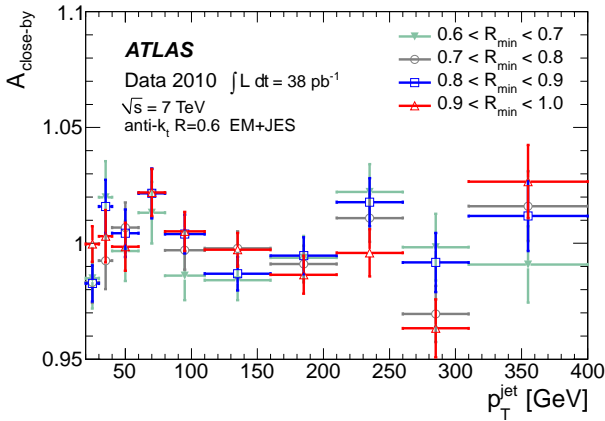


Fig. 77: Data to Monte Carlo simulation ratio of the relative response of non-isolated jets with respect to that of isolated jets for anti- k_t jets with $R = 0.6$ calibrated with the EM+JES scheme. Only statistical uncertainties are shown.

track jets defined as

$$r_{\text{non-iso/iso}}^{\text{track jet}} = p_{T,\text{non-iso}}^{\text{track jet}} / p_{T,\text{iso}}^{\text{track jet}}. \quad (54)$$

The data to MC ratio defined as

$$A_{\text{close-by}}^{\text{track jet}} = \left[r_{\text{non-iso/iso}}^{\text{track jet}} \right]_{\text{Data}} / \left[r_{\text{non-iso/iso}}^{\text{track jet}} \right]_{\text{MC}} \quad (55)$$

is compared between data and Monte Carlo simulations in Figure 75. This ratio can be used to assess the potential of track jets to test close-by effects in the small R_{\min} range. The agreement between data and Monte Carlo simulation is quite satisfactory: within 2 to 3% for $p_T^{\text{jet}} > 30$ GeV and slightly worse for $20 \leq p_T^{\text{jet}} < 30$ GeV.

Therefore, the track jet response systematic uncertainty is assigned separately for the two p_T^{jet} regions: $|1 - A_{\text{close-by}}^{\text{track jet}}|$ is

used as the uncertainty for $20 \leq p_T^{\text{jet}} < 30$ GeV, while for $p_T^{\text{jet}} > 30$ GeV a standard deviation of the $A_{\text{close-by}}^{\text{track jet}}$ is calculated and assigned as the uncertainty. These uncertainties are typically 1.5% (2.0%) for anti- k_t jets with $R = 0.6$ (0.4).

The calorimeter jet p_T^{jet} relative to the matched track jet $p_T^{\text{track jet}}$ ($r_{\text{calo/track jet}}$) is shown in Figure 76 as a function of p_T^{jet} for anti- k_t jets with $R = 0.6$ in data and Monte Carlo simulations. The non-isolated jet response relative to the isolated jet response, $r_{\text{non-iso/iso}}^{\text{calo/track jet}}$, shown in the bottom part of Figure 76 reproduces within a few per cent the behaviour in the ratio $\mathcal{R}_{\text{non-iso}}^{\text{jet}} / \mathcal{R}_{\text{iso}}^{\text{jet}}$ for the Monte Carlo simulation response of calorimeter to truth jet p_T in Figure 73.

The $r_{\text{calo/track jet}}^{\text{non-iso/iso}}$ data to Monte Carlo ratio $A_{\text{close-by}}$ (see Equation 51) is shown in Figure 77. The R_{\min} dependence of the non-isolated jet response in the data is well described by the Monte Carlo simulation.

Within the statistical uncertainty, $A_{\text{close-by}}$ differs from unity by at most $\sim 3\%$ depending on the R_{\min} value in the range of $R \leq R_{\min} < R + 0.3$. No significant p_T^{jet} dependence is found over the measured p_T range of $20 \leq p_T^{\text{jet}} < 400$ GeV.

The overall JES uncertainty due to nearby jets is taken as the track jet response systematic uncertainty added in quadrature with the deviation from one of the weighted average of $A_{\text{close-by}}$ over the entire p_T range, but added separately for each R_{\min} range. The final uncertainties are summarised in Table 15 for the two jet distance parameters.

The $A_{\text{close-by}}$ ratio has been examined for each of the two close-by jets either with the lower or the higher p_T^{jet} , and no apparent difference is observed with respect to the inclusive case shown in Figure 77. Therefore, both calorimeter jets which are close to each other are subject to this uncertainty.

17.4 Summary of close-by jet uncertainty

The uncertainty is estimated by comparing in data and Monte Carlo simulation the track jet response. They are both examined as function of the distance R_{\min} between the jet and the closest jet in the calorimeter.

The close-by jet systematic uncertainty on the jet energy scale is $2.5 - 5.1\%$ ($1.7 - 2.7\%$) and $1.6 - 1.9\%$ ($2.3 - 2.8\%$) for $R = 0.6$ ($R = 0.4$) jets with $20 \leq p_T^{\text{jet}} < 30$ GeV and $p_T^{\text{jet}} > 30$ GeV, respectively, in the range of $R \leq R_{\min} < R + 0.3$ and jet rapidity $|\eta| < 2.0$. When the two jets are separated in distance by $R + 0.3$ or more, the jet response becomes similar to that for the isolated jets and hence no additional systematic uncertainty is required. No significant jet p_T dependence is observed at $p_T^{\text{jet}} > 30$ GeV for the close-by jet systematic uncertainty.

18 Light quark and gluon jet response and sample characterisation

In the previous sections the JES uncertainty for inclusive jets was determined. However, details of the jet fragmentation and showering properties can influence the jet response measurement. In this section the JES uncertainties due to jet fragmentation which is correlated to the flavour of the parton initiating that jet (e.g. see Ref. [70]) are investigated. An additional term in the JES uncertainty is derived for event samples that have a different flavour content than the nominal Monte Carlo simulation sample.

The jet energy scale systematic uncertainty due to the difference in response between gluon and light quark initiated jets (henceforth gluon jets and light quark jets) can be reduced by measuring the flavour composition of a sample of jets using template fits to certain jet properties that are sensitive to changes in fragmentation. Although these jet properties may not have sufficient discrimination power to determine the partonic origin of a specific jet, it is possible to determine the average flavour composition of a sufficiently large sample of jets. The average flavour compositions can be determined using jet property templates built in the Monte Carlo simulation for pure samples.

Templates are constructed in dijet events, which are expected to comprise mostly gluon jets at low transverse momentum and central rapidities. They are then applied to events with a high- p_T photon balancing a high- p_T jet (γ -jet events), which are expected to comprise mostly light quark jets balancing the photon. The application of this technique is further demonstrated with a sample of multijet events, wherein the jets are initiated mostly by gluons from radiation.

18.1 Data samples for flavour dependence studies

Two data samples in addition to the inclusive jet sample discussed before are used for the studies of the flavour dependence of the jet response.

1. **γ -jet sample** Photons with $p_T > 45$ GeV are selected in the barrel calorimeter (with pseudorapidity $|\eta| < 1.37$) and a jet back-to-back ($\Delta\phi > \pi - 0.2$ radians) to the photon is

required. The second-leading jet in the event is required to have a p_T^{jet} below 10% of the p_T^{jet} of the leading jet. Anti- k_t jets with $R = 0.6$ are used. Anti- k_t jets with $R = 0.6$ are used.

2. **Multijet sample** Jets with $p_T^{\text{jet}} > 60$ GeV and $|\eta| < 2.8$ are selected and the number of selected jets defines the sample of at least two, three or four jets.

18.2 Flavour dependence of the calorimeter response

Jets identified in the Monte Carlo simulation as light quark jets have significantly different response from those identified as gluon jets (see Section 6.3).

The flavour-dependence of the jet response is in part a result of the differences in particle level properties of the two types of jets. For a given jet p_T jets identified as gluon jets tend to have more particles, and those particles tend to be softer than in the case of light quark jets. Additionally, the gluon jets tend to be wider (i.e. with lower energy density in the core of the jet) before interacting with the detector. The magnetic field in the inner detector amplifies the broadness of gluon jets, since their low- p_T charged particles tend to bend more than the higher p_T particles in light quark jets. The harder particles in light quark jets additionally tend to penetrate further into the calorimeter.

The difference in calorimeter response between gluon jets and light quark jets in the Monte Carlo simulation is shown in Figure 78. Jets in the barrel ($|\eta| < 0.8$) and in the endcap ($2.1 \leq |\eta| < 2.8$) calorimeters are shown separately. For jets calibrated with the EM+JES scheme light quark jets have a 5 – 6% higher response than gluon jets at low p_T^{jet} . This difference decreases to about 2% at high p_T^{jet} .

Since response differences are correlated with differences in the jet properties, more complex jet calibration schemes that are able to account for jet shower properties variations can partially compensate for the flavour dependence. At low p_T^{jet} the difference in response between light quark jets and gluon jets is reduced to 4 – 5% for the LCW+JES and GCW+JES schemes and about 3% for the GS scheme. For $p_T^{\text{jet}} > 300$ GeV the flavour dependence of the jet response is below 1% for the LCW+JES and GCW+JES and the GS schemes.

The closer two jets are to one another, the more ambiguous the flavour assignment becomes. The flavour assignment can become particularly problematic when one truth jet is matched to two reconstructed calorimeter jets (“splitting”) or two truth jets are matched to one reconstructed calorimeter jet (“merging”). Several different classes of close-by jets are examined for changes in the flavour dependence of the jet response. No significant deviation from the one of isolated jets is found. Therefore, the cases can be treated separately. The jet energy scale uncertainty specific to close-by jets is examined further in Section 17.

18.3 Systematic uncertainties due to flavour dependence

Each jet energy calibration schemes restore the average jet energy to better than 2% with small uncertainties in a sample of

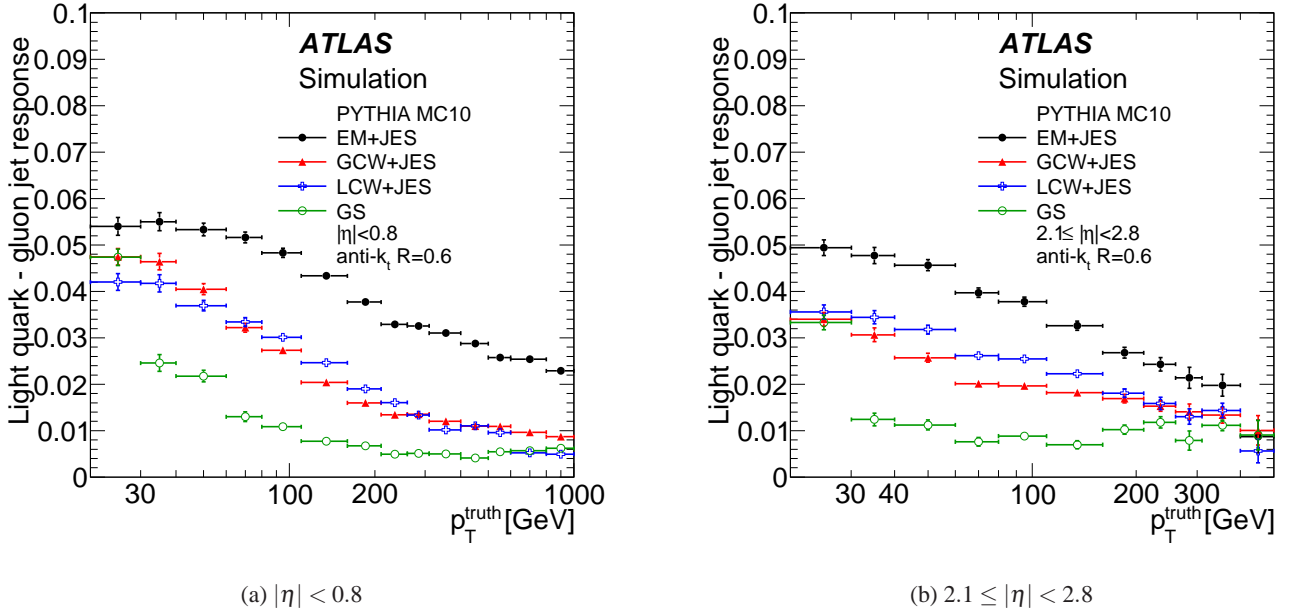


Fig. 78: Difference in average response of gluon and light quark jets as a function of the truth jet p_T for anti- k_t jets with $R = 0.6$ in the barrel (a) and the endcap (b) calorimeters as determined in Monte Carlo simulation. Various calibration schemes are shown. The data sample used contains at least two jets with $p_T^{\text{jet}} > 60$ GeV and $|\eta| < 2.8$. Only statistical uncertainties are shown.

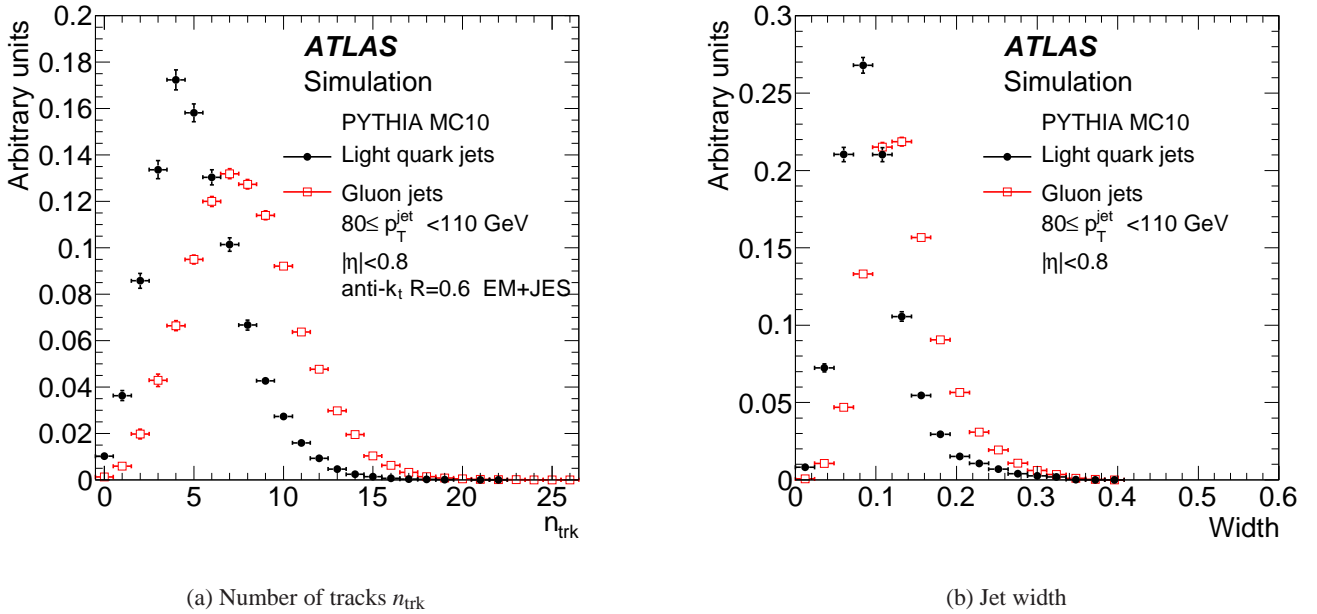
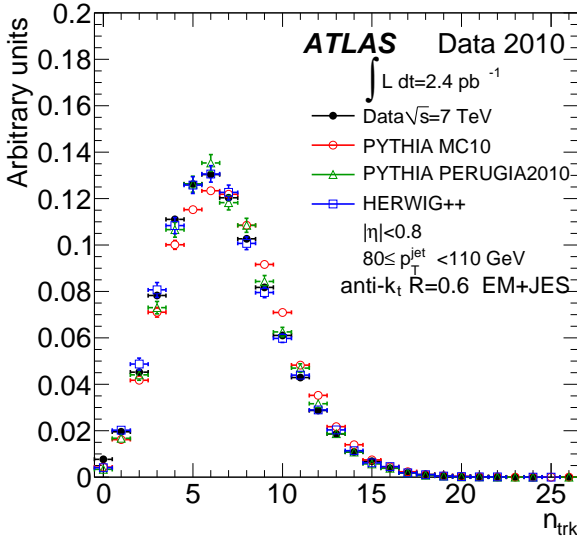
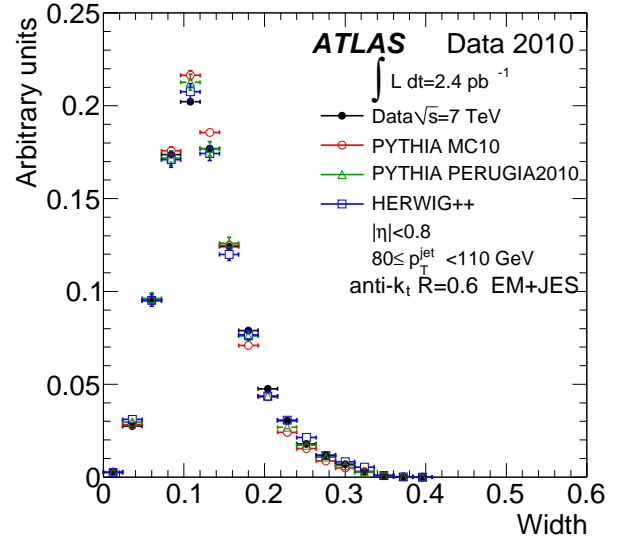
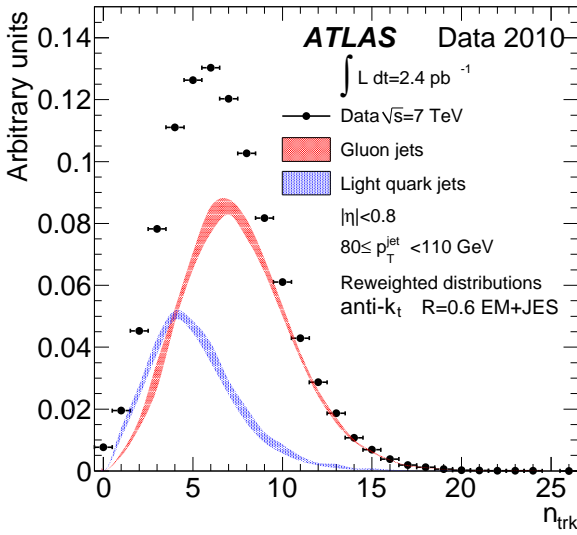
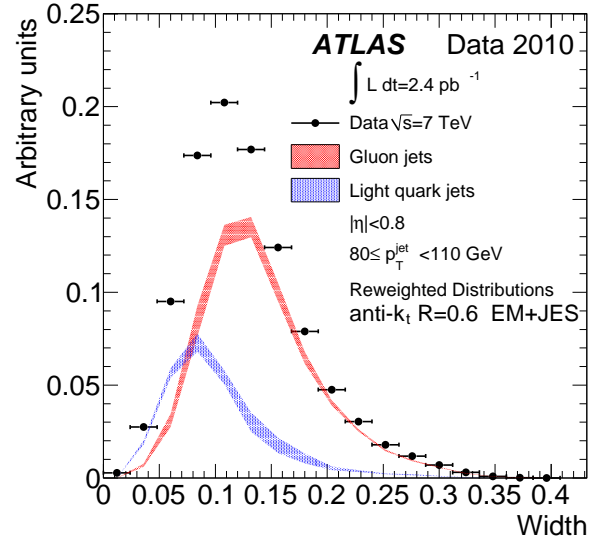


Fig. 79: Distribution of the number of tracks associated to the jet n_{trk} (a) and the jet width (b) for isolated anti- k_t jets with $R = 0.6$ classified as light quark jets (solid circles) and gluon jets (open squares) in the Monte Carlo simulation. Jets with $|\eta| < 0.8$ and $80 \leq p_T^{\text{jet}} < 110$ GeV are shown. The distributions are normalised to unit area. Uncertainties are statistical only.

(a) Number of tracks n_{trk} 

(b) Jet width

Fig. 80: Distribution of the number of tracks associated to the jet, n_{trk} (a) and the jet width (b) for isolated anti- k_t jets with $R = 0.6$ in data (solid circles) and Monte Carlo simulation. The PYTHIA MC10 tune (open circles) and PERUGIA2010 tune (open triangles), and HERWIG++ (open squares) distributions are shown for jets with $|\eta| < 0.8$ and $80 \leq p_T^{\text{jet}} < 110$ GeV. The distributions are all normalised to unity. Uncertainties are statistical only.

(a) Number of tracks n_{trk} 

(b) Jet width

Fig. 81: Distribution of the number of tracks associated to the jet, n_{trk} (a) and the jet width (b) for isolated anti- k_t jets with $R = 0.6$ in data (closed circles) and Monte Carlo simulation (bands). Light quark jets are shown as a dark band, gluon jets are shown as a light band. The width of the band represents the maximum variation among the PYTHIA MC10 and PERUGIA2010 tunes and the HERWIG++ Monte Carlo simulation samples. Jets with $|\eta| < 0.8$ and $80 \leq p_T^{\text{jet}} < 110$ GeV are included. The inclusive distributions are all normalised to unity. The inclusive Monte Carlo distributions, including the heavy quark jet contributions (not shown), are reweighted to match the inclusive distribution of the data. Uncertainties are statistical only.

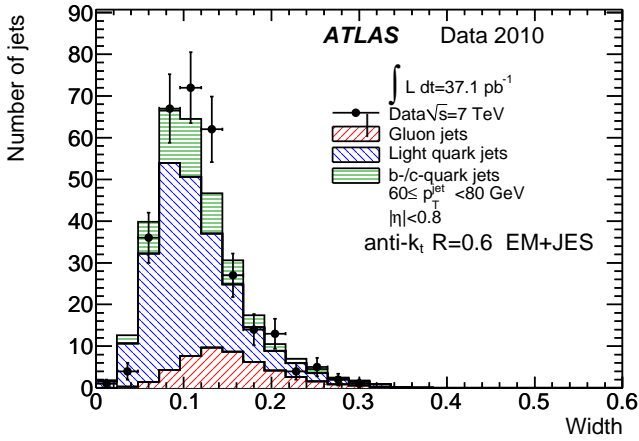


Fig. 82: The jet width template fit in a γ -jet data sample using templates derived from the inclusive jet Monte Carlo simulation sample created using the PYTHIA MC10 tune. Jets with $|\eta| < 0.8$ and $60 \leq p_T^{\text{jet}} < 80$ GeV are shown. The fraction of heavy quark jets is taken directly from the MC simulation.

inclusive jets. However, subsamples of jets are not perfectly calibrated, as in the case of light quark jets and gluon jets. The divergence from unity is flavour dependent and may be different in Monte Carlo simulation and data, particularly if the flavour content in the data sample is not well-described by the Monte Carlo simulation. This results in an additional term in the systematic uncertainty for any study using an event or jet selection different from that of the sample in which the jet energy scale was derived.

18.3.1 Systematic uncertainty from MC variations

In order to test the response uncertainties of exclusive samples of either gluon or light quark jets, a large number of systematic variations in the Monte Carlo simulation are investigated (see Ref. [1] for details on the variations). The response difference of quark and gluon jets to that of the inclusive jets is found to be very similar for each of the systematic Monte Carlo variations. Therefore the additional uncertainty on the response of gluon jets is neglected.

These conclusions are in good agreement with the studies which derive the calorimeter jet response using the single hadron response in Refs. [49, 58], where the uncertainties of the quark and gluon response are similar within 0.5%.

The results are found to be stable under variations of the Monte Carlo simulation samples including soft physics effects like colour reconnections. With more data, a variety of final states may be tested to investigate more details of the light quark and gluon jet response.

18.3.2 Systematic uncertainty from average flavour content

The flavour dependent uncertainty term depends on both the average flavour content of the sample and on how well the flavour content is known, e.g. the uncertainty for a generic new physics search with an unknown jet flavour composition is different from the uncertainty on a new physics model in which only light quark jets are produced. The response for any sample of jets, \mathcal{R}_s , can be written as³⁹:

$$\begin{aligned} \mathcal{R}_s &= f_g \times \mathcal{R}_g + f_q \times \mathcal{R}_q + f_b \times \mathcal{R}_b + f_c \times \mathcal{R}_c = \\ &= 1 + f_g \times (\mathcal{R}_g - 1) + f_q \times (\mathcal{R}_q - 1) \\ &\quad + f_b \times (\mathcal{R}_b - 1) + f_c \times (\mathcal{R}_c - 1), \end{aligned} \quad (56)$$

where R_x is the detector response to jets and f_x is the fraction of jets for $x = g$ (gluon jets), q (light quark jets), b (b -quark jets), and c (c -quark jets) and $f_g + f_q + f_b + f_c = 1$. For simplicity, the fraction of heavy quark jets is taken to be known. This approximation will be dealt with in the systematic uncertainty analysis for heavy quarks in Section 18.4.

Since variations in the flavour fractions and the jet flavour response translate into variations of the jet response for a given sample, the uncertainty on the jet response can be approximately expressed as:

$$\begin{aligned} \Delta \mathcal{R}_s &= \Delta f_g \times (\mathcal{R}_g - 1) + \Delta f_q \times (\mathcal{R}_q - 1) + \\ &+ f_g \times \Delta \mathcal{R}_g + f_q \times \Delta \mathcal{R}_q + f_b \times \Delta \mathcal{R}_b + f_c \times \Delta \mathcal{R}_c, \end{aligned} \quad (57)$$

where Δ denotes the uncertainty on the individual variables. Since f_b and f_c are fixed here (i.e. without uncertainty), $\Delta f_g = -\Delta f_q$. Also, the uncertainties on the response for the exclusive flavour samples (light quark, gluon, b , and c quarks) are approximately the same as the inclusive jet response uncertainty ($\Delta \mathcal{R}_j$).

The expression can therefore be simplified:

$$\begin{aligned} \Delta \mathcal{R}_s &\approx -\Delta f_q \times (\mathcal{R}_g - 1) + \Delta f_q \times (\mathcal{R}_q - 1) + \\ &+ f_g \times \Delta \mathcal{R}_j + f_q \times \Delta \mathcal{R}_j + f_b \times \Delta \mathcal{R}_j + f_c \times \Delta \mathcal{R}_j = \\ &= \Delta f_q \times (\mathcal{R}_q - \mathcal{R}_g) + (f_g + f_q + f_b + f_c) \times \Delta \mathcal{R}_j \\ &\approx \Delta f_q \times (\mathcal{R}_q - \mathcal{R}_g) + \Delta \mathcal{R}_j. \end{aligned} \quad (58)$$

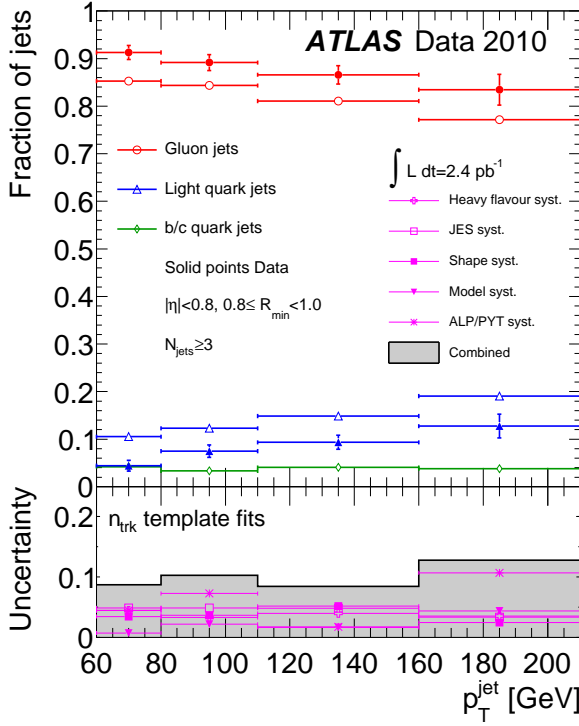
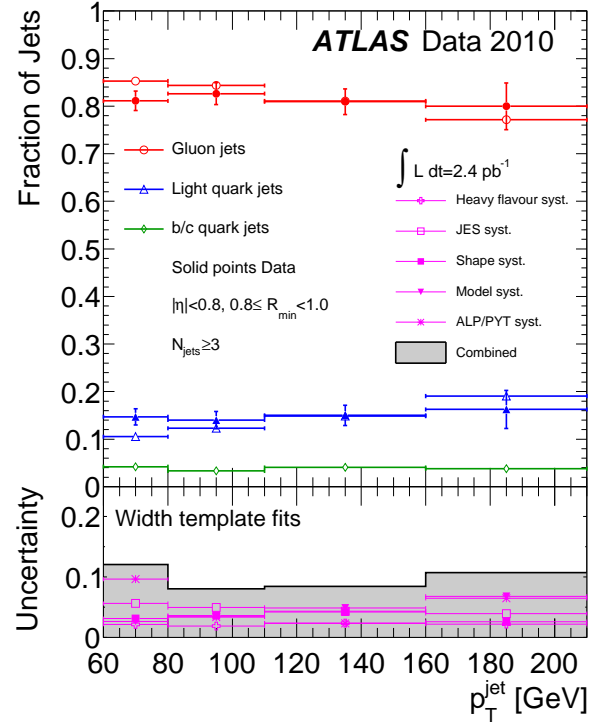
The second term is the inclusive jet energy scale systematic uncertainty, and the first term is the additional flavour dependent contribution.

Dropping the inclusive jet energy scale systematic uncertainty and rewriting Equation 58 as a fractional uncertainty, the flavour dependent contribution becomes:

$$\frac{\Delta \mathcal{R}_s}{\mathcal{R}_s} = \Delta f_q \times \left(\frac{\mathcal{R}_q - \mathcal{R}_g}{\mathcal{R}_s} \right). \quad (59)$$

The uncertainty on the flavour content (Δf_q) and the inclusive response of the sample (\mathcal{R}_s) depends on the specific analysis. The difference in response between light quark and gluon jets depends only on the calibration used, as discussed in Section 18.2.

³⁹ The following equations are strictly speaking only valid for a given bin in p_T and η or in other variables that influence the flavour composition.

(a) Number of tracks n_{trk} template fits

(b) Jet width template fits

Fig. 83: Fitted values of the average light quark and gluon jet fraction in events with three or more jets as a function of p_T^{jet} calculated using the number of tracks n_{trk} templates (a) and the jet width templates (b). Non-isolated anti- k_t jets ($0.8 \leq R_{\text{min}} < 1.0$) with $R = 0.6$ and with $|\eta| < 0.8$ calibrated with the EM+JES scheme are shown. The fraction of heavy quark jets is fixed to that of the Monte Carlo simulation. The flavour fractions obtained in data are shown with closed markers, while the values obtained from the Monte Carlo simulation are shown with open markers. The error bars indicate the statistical uncertainty of the fit. Below each figure the impact of the different systematic effects is shown with markers and the combined systematic uncertainty is indicated by a shaded band.

18.4 Average jet flavour determination

One way of investigating the flavour composition of a sample is to use different MC generators that cover a reasonable range of flavour compositions. However, these different samples may suffer from under- or overcoverage of the uncertainty or from changes in other sample characteristics, e.g. jet p_T spectra, which may result in a poor estimate of the true uncertainty. Another approach, pursued in this section, is to estimate the flavour composition of the samples by using experimental observables that are sensitive to different jet flavours.

As described in Section 18.2, gluon jets tend to have a wider transverse profile and have more particles than light quark jets with the same p_T . The jet width, as defined in Equation 37, and the number of tracks associated to the jet (n_{trk}) are thus expected to be sensitive to the difference between light quark jets and gluon jets. The jet width may have contributions from pile-up interactions. In the following discussion only events with

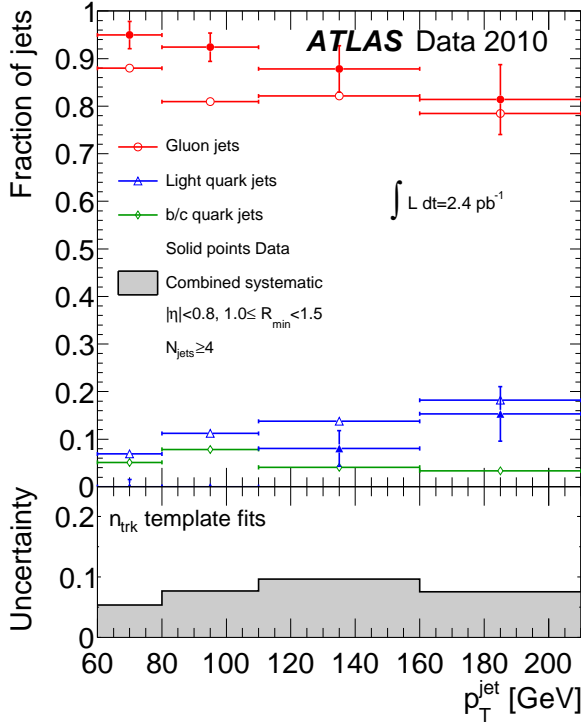
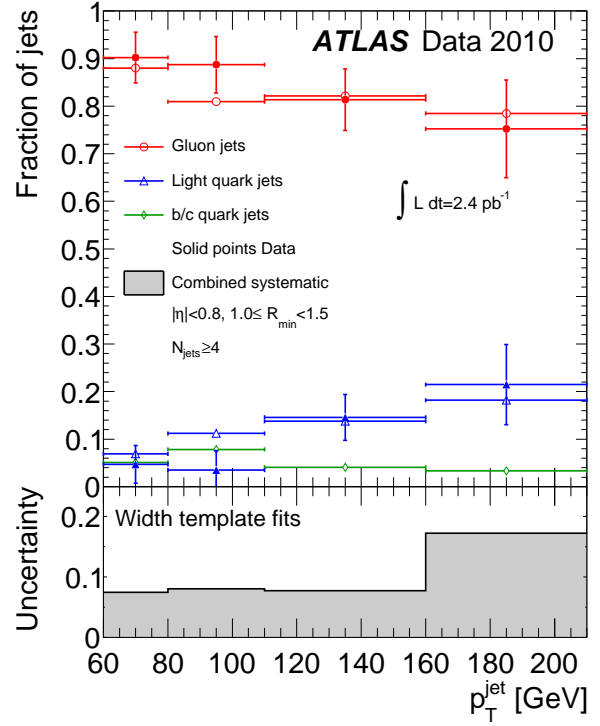
exactly one reconstructed primary vertex enter the jet width distributions⁴⁰.

The number of tracks associated to a jet is defined by counting the tracks with $p_T > 1$ GeV coming from the primary hard scattering vertex with an opening angle between the jet and the track momentum direction $\Delta R < 0.6$. Figure 79 shows the jet width and n_{trk} distributions for isolated light quark and gluon jets with $|\eta| < 0.8$ and $80 \leq p_T < 110$ GeV in the inclusive jet Monte Carlo simulation sample. The gluon jets are broader and have more tracks than light quark jets. For this study anti- k_t jets with $R = 0.6$ calibrated with the EM+JES scheme are used.

Templates are built from the inclusive jet Monte Carlo sample for the jet width and n_{trk} of light quark and gluon jets separately⁴¹, using the flavour tagging algorithm of Section 6.3. The templates are constructed in bins of p_T^{jet} , η , and isolation

⁴⁰ Techniques to correct for these additional interactions are being developed and are discussed in Section 9.7.4.

⁴¹ The n_{trk} and jet width templates are dealt with independently, and the results of their estimates of flavour fraction are not combined.

(a) Number of tracks n_{trk} template fits

(b) Jet width template fits

Fig. 84: Fitted values of the average light quark and gluon jet fraction in events with four or more jets as a function of p_T^{jet} for isolated anti- k_t jets with $R = 0.6$ and with $|\eta| < 0.8$ calibrated with the EM+JES scheme. The fraction of heavy quark jets is fixed from the Monte Carlo simulation. The number of tracks n_{trk} (a) and the jet width (b) template distributions are used in the fits. The flavour fractions obtained in data are shown with closed markers, while the values obtained from the Monte Carlo simulation are shown with open markers. The error bars indicate the statistical uncertainty of the fit. Below each figure the systematic uncertainty is shown as a shaded band.

(ΔR to the nearest jet, R_{min}). Fits to the data are performed with these templates to extract the flavour composition.

Comparisons of the inclusive jet width and n_{trk} distributions in Monte Carlo simulation and data are shown in Figure 80 for isolated jets with $R = 0.6$. The jet width in Monte Carlo simulation is narrower than in the data for the PYTHIA samples, in agreement with other ATLAS analyses [3].

The inclusive n_{trk} and jet width Monte Carlo simulation distributions are reweighted bin-by-bin according to the data distribution. This accounts for the differences observed between the data and Monte Carlo simulation. The same reweighting is applied to the light quark jet and gluon jet distributions. The reweighted n_{trk} and jet width distributions for the various Monte Carlo simulation samples are shown in Figure 81. Since the reweighting is applied to all flavours equally the average flavour content of the sample does not change.

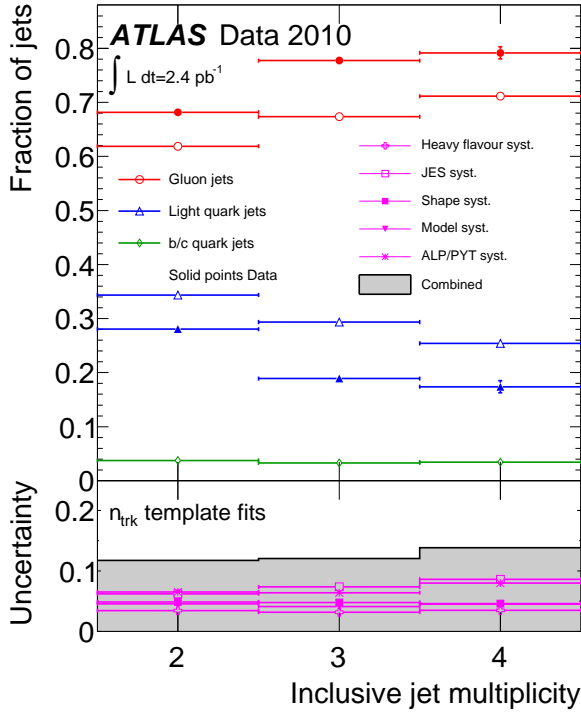
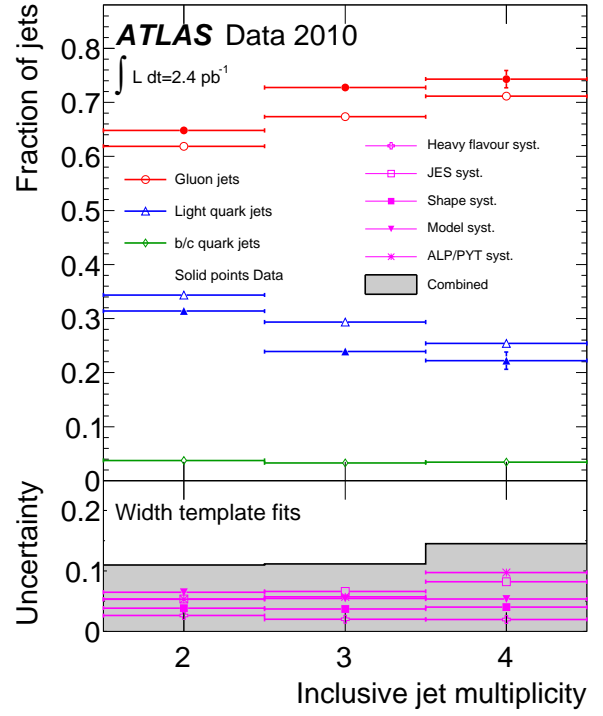
After reweighting, the flavour composition of the dijet sample extracted from the data is consistent with that of the Monte Carlo simulation. The extracted values for two representative jet bins are shown in Table 16. This result is an important closure test and provides some validation of the templates.

18.5 Systematic uncertainties of average flavour composition

Uncertainties on the MC-based templates used in fits to the data result in a systematic uncertainty on the extracted flavour composition. Systematic effects from the Monte Carlo modelling of the jet fragmentation, the jet energy scale and resolution as well as the flavour composition of the sample used to extract the templates are discussed in the following. Since there is no single dominant uncertainty, each is individually considered for the extraction of the flavour composition of a sample of jets.

18.5.1 Monte Carlo modelling of jet width and n_{trk} distributions

Monte Carlo simulation samples generated with PYTHIA with the MC10 and the PERUGIA2010 tunes and HERWIG++ all show reasonable agreement with data (see Figure 80). Therefore, two separate fits with templates obtained from the latter two alternative Monte Carlo simulation samples are performed. Reweighting of these alternate samples is performed

(a) Number of track n_{trk} template fits

(b) Jet width template fits

Fig. 85: Fitted values of the average light quark and gluon jet fraction as a function of inclusive jet multiplicity with total uncertainties on the fit as obtained using the number of tracks n_{trk} (a) and the jet width (b) distributions. The fraction of heavy quark jets is fixed from the Monte Carlo simulation. The flavour fractions obtained in data are shown with closed markers, while the values obtained from the Monte Carlo simulation are shown with open markers. Anti- k_t jets with $R = 0.6$ calibrated with the EM+JES scheme are used. The error bars indicate the statistical uncertainty of the fit. Below each figure the impact of the different systematic effects is indicated by markers, and the combined systematic uncertainty is shown at the bottom of the figure as a shaded band.

in the same manner as for the nominal PYTHIA MC10 sample. The largest of the differences in the flavour fractions with respect to the nominal fits is taken as the uncertainty due to Monte Carlo modelling. This estimate should cover physics effects that may impact light quark and gluon jets differently.

18.5.2 The jet energy scale uncertainty and finite detector resolution

The uncertainties in the jet measurement combined with the rapidly falling jet p_T spectrum, lead to p_T bin migrations that affect the templates. Therefore, the templates are rebuilt with all jet momenta scaled up and down according to the inclusive jet energy scale systematic uncertainty. The difference in the flavour content estimated with the modified templates is taken as a systematic uncertainty.

18.5.3 Flavour composition of the MC simulation

The fraction of heavy quark jets in the data is assumed to be the same as that predicted by the PYTHIA MC10 Monte Carlo simulation in the template fits. The uncertainty associated with this assumption is estimated by increasing and decreasing this Monte Carlo simulation based fraction of heavy quark jets in the template fits by a factor of two and repeating the fits with the light quark and gluon jet templates. The factor of two is taken in order to be conservative in the γ -jet and multijet samples, due to the lack of knowledge of gluon splitting fraction to $b\bar{b}$.

The PYTHIA Monte Carlo simulation was produced using the modified LO parton distribution functions, which may not accurately reproduce the true flavour composition. Particularly in the more forward pseudorapidity bins, this could produce some inherent biases in the fits. In order to estimate this uncertainty, the light quark and gluon jet templates from the standard MC sample are combined according to the flavour content of a jet sample generated using ALPGEN. This Monte Carlo generator also uses a leading order PDF, but produces more

hard partons via multiparton matrix elements. This new combination is then reweighted to match the inclusive distribution in data, and the reweighted templates are used to extract the flavour composition of the samples. The difference between the flavour composition derived in this manner and the flavour composition derived using the nominal PYTHIA Monte Carlo simulation is taken as a systematic uncertainty.

18.6 Flavour composition in a photon-jet sample

The validity of the MC-based templates and fitting method is tested by applying the method to the γ -jet data sample and comparing the extracted flavour compositions with the γ -jet Monte Carlo simulation predictions. This sample should contain a considerably higher fraction of light quark jets than the inclusive dijet sample. Figure 82 shows the fit to the jet width in the γ -jet data for jets with $|\eta| < 0.8$ and $60 \leq p_T^{\text{jet}} < 80$ GeV. The heavy quark jet fractions are fixed to those obtained from the γ -jet Monte Carlo simulation. The extracted light quark and gluon jet fractions are consistent with the true fractions in Monte Carlo simulation, though with large uncertainties, as shown in Table 16.

18.7 Flavour composition in a multijet sample

The template fit method is also useful for fits to multijet events for various jet multiplicities. These events contain additional jets that mainly result from gluon radiation and hence include a larger fraction of gluon jets than does the γ -jet sample.

For this particular analysis, the templates built from the inclusive jet sample are used to determine the flavour content of the n -jet bin. However, the p_T spectrum of the sub-leading jets is more steeply falling than the leading jet p_T . An additional systematic uncertainty is estimated to account for the difference in p_T spectra. This uncertainty is determined by rederiving templates built with a flat p_T distribution and a significantly steeper p_T distribution than that of the dijet sample. The slope of the steeply falling distribution is taken from the p_T of the sixth leading jet in Monte Carlo events with six jets, generated using ALPGEN. The fits are repeated with these modified templates, and the largest difference is assigned as a p_T^{jet} spectrum shape systematic uncertainty.

Figure 83 compares the fractions of light quark and gluon jets obtained with a fit of the jet width and n_{trk} distributions in events with three or more jets in data and Monte Carlo simulation as a function of p_T^{jet} for non-isolated ($0.8 \leq R_{\text{min}} < 1.0$) jets with $|\eta| < 0.8$. The higher gluon jet fractions predicted by the Monte Carlo simulation are reproduced by the fit, and the data and the Monte Carlo simulation are consistent. The total systematic uncertainty on the measurement is below 10% over the measured p_T^{jet} range.

The average flavour fractions obtained from fitting the jet width and n_{trk} distributions in events with four or more jets are shown in Figure 84. In both cases, the extracted fractions are consistent with the Monte Carlo predictions within the systematic uncertainties, and the total systematic uncertainty is similar to the one for the three-jet bin.

The extracted light quark and gluon jet fractions, with the total systematic uncertainty from the width and n_{trk} fits, are summarised in Figure 85 as a function of inclusive jet multiplicity. The fractions differ by 10% between the data and the Monte Carlo simulation, but are consistent within uncertainties. The total systematic uncertainty is around 10% for each multiplicity bin. Thus, for the four-jet bin, the flavour dependent jet energy scale systematic uncertainty can be reduced by a factor of ~ 10 , from about 6% obtained assuming a 100% flavour composition uncertainty to less than 1% after having determined the flavour composition with a 10% accuracy. A summary of the flavour fit results using the jet width templates for the different samples is provided in Table 16.

18.8 Summary of jet response flavour dependence

The flavour dependence of the jet response has been studied, and an additional term to the jet energy scale systematic uncertainty has been derived.

A generic template fit method has been developed to reduce this uncertainty significantly for any given sample of events. Templates derived in dijet events were applied to both γ -jet and multijet events, demonstrating the potential of the method to reduce the systematic uncertainty. The flavour dependent jet energy scale systematic uncertainty can be reduced from $\sim 6\%$ to below 1%.

19 Global sequential calibrated jet response for a quark sample

In this section, the performance of the GS calibration (see Section 11) is tested for a γ -jet sample. The jet energy scale after each GS correction can be verified using the *in situ* techniques such as the direct p_T balance technique in γ -jet events (see Section 10.2), where mainly quark induced jets are tested. The flavour dependence of the GS calibration is tested for jets with $|\eta| < 1.2$.

The measurement is first made with jets calibrated with the EM+JES calibration and is repeated after the application of each of the corrections that form the GS calibration. To maximise the available statistics one pseudorapidity bin is used $|\eta| < 1.2$. The Monte Carlo based GS corrections are applied to both data and Monte Carlo simulation. The systematic uncertainty associated with the GS calibration is evaluated by computing the data to Monte Carlo simulation ratio of the response after the GS calibration relative to that for the EM+JES calibration.

For $25 \leq p_T^{\text{jet}} < 45$ GeV, the agreement between the response in data and Monte Carlo simulation is 3.2% after EM+JES and 4.2% after GS calibration. For $210 \leq p_T^{\text{jet}} < 260$ GeV, the agreement is 5% after EM+JES and 2.5% after GS calibration. Therefore systematic uncertainties derived from the agreement of data and Monte Carlo simulation vary from 1% at $p_T^{\text{jet}} = 25$ GeV to 2.5% for $p_T^{\text{jet}} = 260$ GeV. These results are compatible within the statistical uncertainty with the uncertainty evaluated using inclusive jet events (see Section 12.1.3).

Sample	Selection	Gluon / light / heavy quark jet fraction	
		Data	MC
Dijet	$80 \leq p_T < 110$ GeV, $ \eta < 0.8$, $1.0 \leq R_{\min} < 1.5$	73 / 22 / 5% $\pm 2(\text{stat.}) \pm 9(\text{syst.})\%$	72 / 23 / 5%
Dijet	$80 \leq p_T < 110$ GeV, $2.1 \leq \eta < 2.8$, $1.0 \leq R_{\min} < 1.5$	45 / 52 / 3% $\pm 3(\text{stat.}) \pm 12(\text{syst.})\%$	39 / 58 / 3%
γ -jet	$60 \leq p_T < 80$ GeV, $ \eta < 0.8$, Isolated	16 / 65 / 19% $\pm 10(\text{stat.}) \pm 19(\text{syst.})\%$	6 / 74 / 19%
Multijet	3-jet, $80 \leq p_T < 110$ GeV, $ \eta < 0.8$, $0.8 \leq R_{\min} < 1.0$	83 / 13 / 4% $\pm 2(\text{stat.}) \pm 7(\text{syst.})\%$	84 / 12 / 4%
Multijet	4-jet, $80 \leq p_T < 110$ GeV, $ \eta < 0.8$, $1.0 \leq \Delta R_{\min} < 1.5$	89 / 3 / 8% $\pm 6(\text{stat.}) \pm 8(\text{syst.})\%$	81 / 11 / 8%

Table 16: The results of flavour fits using jet width templates in three data samples: dijet events, γ -jet events, and multijet events. The Monte Carlo simulation flavour predictions are taken from ALPGEN for the dijet and multijet samples and PYTHIA for the γ -jet sample. The first uncertainty listed is statistical and the second uncertainty is systematic, and both apply to the measured gluon and light quark jet fractions. The heavy quark jet fractions in the data are constrained to be the same as those in the MC simulation.

The obtained results indicate that the uncertainty in a sample with a high fraction of light quark jets is about the same as in the inclusive jet sample.

20 JES uncertainties for jets with identified heavy quark components

Heavy flavour jets such as jets induced by bottom (b) quarks (b -jets) play an important role in many physics analyses.

The calorimeter jet response uncertainties for b -jets is evaluated using single hadron response measurements in samples of inclusive dijet and $b\bar{b}$ dijet events. The JES uncertainty arising from the modelling of the b -quark production mechanism and the b -quark fragmentation can be determined from systematic variations of the Monte Carlo simulation.

Finally, the calorimeter p_T^{jet} measurement can be compared to the one from tracks associated to the jets for inclusive jets and identified b -jets. From the comparison of data to Monte Carlo simulation the b -jet energy scale uncertainty relative to the inclusive jet sample is estimated.

20.1 Selection of identified heavy quark jets

Jets are reconstructed using the anti- k_t jet algorithm with $R = 0.4$ and calibrated with the EM+JES scheme. Jets with $p_T^{\text{jet}} > 20$ GeV and $|\eta| < 2.5$ are selected.

A representative sample of identified b -jets is selected by a track-based b -tagging algorithm, called the SV0 tagger [8, 71]. This algorithm iteratively reconstructs a secondary vertex in jets and calculates the decay length with respect to the primary vertex. The decay length significance is assigned to each jet as a tagging weight. A jet is identified as a b -jet if this weight exceeds a threshold of 5.85 as explained in Ref. [71]. To adjust the Monte Carlo simulation to the b -tagging performance in data, a dedicated b -tagging calibration consisting of “scale

factors” [71] is applied to the simulation and systematic uncertainties for the calibration are evaluated. For Monte Carlo studies, a sample of b -jets is selected using a geometrical matching of the jet ($\Delta R < 0.4$) to a *true* B -hadron.

20.2 Calorimeter response uncertainty

The uncertainty of the calorimeter response to identified b -jets has been evaluated using single hadron response measurements *in situ* and in test-beams [49]. The same method as described in Section 9.3 is used to estimate the b -jet response uncertainty in events with top-quark pairs with respect to the one of inclusive jets.

For jets within $|\eta| < 0.8$ and $20 \leq p_T^{\text{jet}} < 250$ GeV the expected difference in the calorimeter response uncertainty of identified b -jets with respect to the one of inclusive jets is less than 0.5%. It is assumed that this uncertainty extends up to $|\eta| < 2.5$.

Parameter	Nominal	Professor	Bowler-Lund
MSTJ(11)	4	5	4
MSTJ(22)	2	2	2
PARJ(41)	0.3	0.49	0.85
PARJ(42)	0.58	1.2	1.03
PARJ(46)	0.75	1.0	0.85
PARJ(54)	−0.07		
PARJ(55)	−0.006		

Table 17: PYTHIA steering parameters for the considered variations of the b -quark fragmentation functions.

20.3 Uncertainties due to Monte Carlo modelling

The following uncertainties for b -jets are studied using systematic variations of the Monte Carlo simulation:

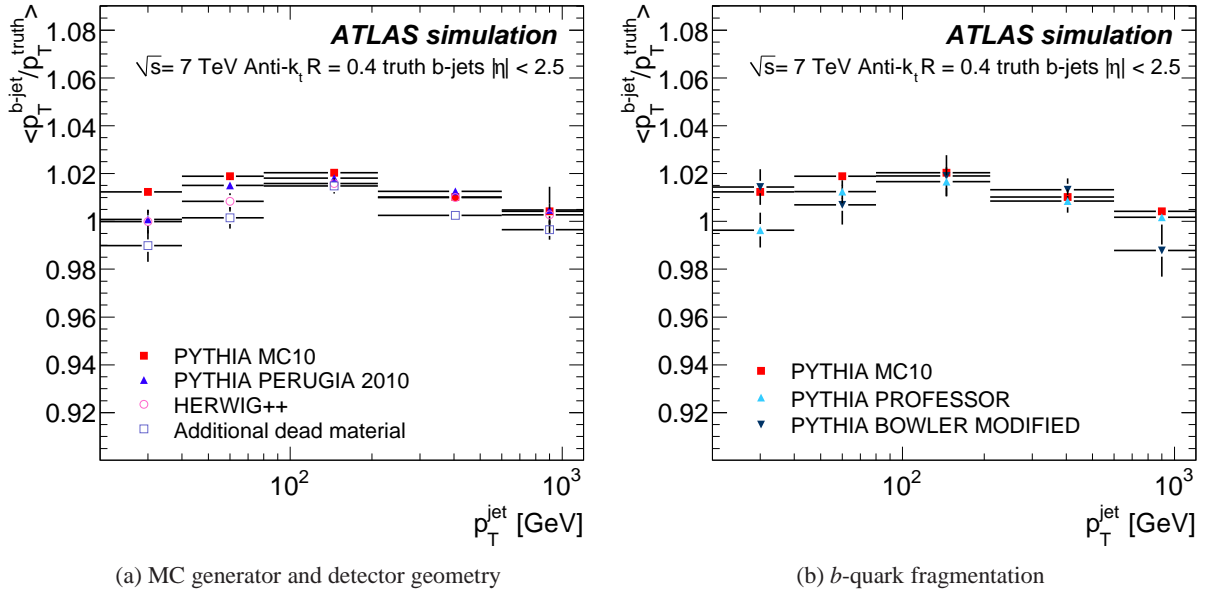


Fig. 86: Average response for b -jets as a function of p_T^{jet} obtained with the Monte Carlo event generators PYTHIA with the MC10 and PERUGIA2010 tunes and HERWIG++ (a) and PYTHIA simulations with additional dead detector material. Average response for b -jets using the PYTHIA Professor tune and the PYTHIA modified Bowler-Lund fragmentation function evaluated with respect to the nominal PYTHIA inclusive jet sample (b). Only statistical uncertainties are shown.

1. Fragmentation and hadronisation modelling uncertainty obtained by comparing the Monte Carlo generators HERWIG vs PYTHIA.
2. Soft physics modelling uncertainty obtained by comparing the PYTHIA MC10 to the PYTHIA PERUGIA2010 tune.
3. Modelling uncertainty of the detector material in front and in between the calorimeters.
4. Modelling uncertainty of the fragmentation of b -quarks.

The event generators PYTHIA and HERWIG++ are used to evaluate the influence of different hadronisation models, different parton showers, as well as differences in the underlying event model (see Section 4). Variations in proton parton density functions are also included.

The influence of the soft physics modelling is estimated by replacing the standard PYTHIA MC10 tune by the PYTHIA PERUGIA2010 tune. The impact of additional dead material is tested following the prescription detailed in Section 9.

The fragmentation function is used to estimate the momentum carried by the B -hadron with respect to that of the b -quark after quark fragmentation. The contribution of the b -quark fragmentation to the JES uncertainty is estimated using Monte Carlo samples generated with different sets of tuning parameters of two fragmentation functions (see Table 17).

The fragmentation function included as default in PYTHIA originates from a detailed study of the b -quark fragmentation function in comparison with OPAL [72] and SLD [73] data. The data are better described using the symmetric Bowler fragmentation function with $r_Q = 0.75$ (PYTHIA PARJ(46)), assuming the same modification for b - and c -quarks. The a (PYTHIA PARJ(41)) and b (PYTHIA PARJ(42)) parameters of the symmetric Lund function were left with the values shown

in Table 17. A more detailed discussion of uncertainties in the b -quark fragmentation function can be found in Refs. [74].

The choice of the fragmentation function for this study is based on comparisons to LEP experimental data, mostly from ALEPH [75] and OPAL [72], as well as from the SLD experiment [73] included in a phenomenological study of the b -quark fragmentation in top-quark decay [76].

To assess the impact of the b -quark fragmentation, the nominal parameters of the PYTHIA fragmentation function are replaced by the values from a recent tune using the Professor framework [77]. In addition, the nominal fragmentation function is replaced by the modified Bowler-Lund fragmentation function [78].

For each effect listed above the b -jet response uncertainty is evaluated from the ratio between the response of b -jets in the Monte Carlo samples with systematic variations to the nominal PYTHIA MC10 b -jet sample. The deviation from unity of this ratio is taken as uncertainty:

$$\text{Uncertainty} = 1 - \left(\frac{\mathcal{R}_{\text{variation}}^{b\text{-jet}}}{\mathcal{R}_{\text{nominal}}^{b\text{-jet}}} \right). \quad (60)$$

The b -jet response obtained with PYTHIA for the MC10 and the PERUGIA2010 tunes, the HERWIG++ Monte Carlo event generator and using a simulation with additional dead material is shown in Figure 86a. Figure 86b shows the variation with various fragmentation functions, i.e. the standard one in the nominal PYTHIA sample versus the ones in the PYTHIA Professor tune sample and the PYTHIA modified Bowler-Lund fragmentation function sample. The response variations are well within about 2%.

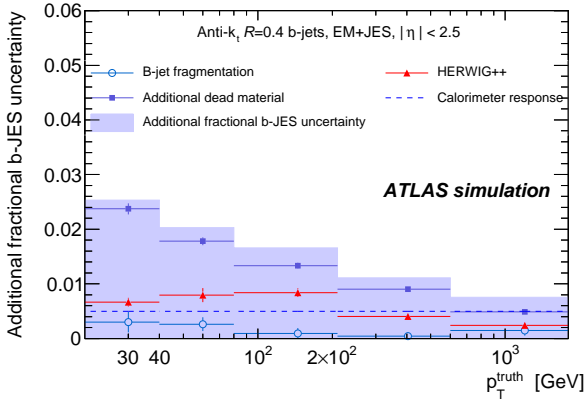


Fig. 87: Additional fractional b -jet JES uncertainty as a function of the truth jet transverse momentum for anti- k_t jets with $R = 0.4$ calibrated with the EM+JES scheme for $|\eta| < 2.5$. Shown are systematic Monte Carlo variations using different modelling of the b -quark fragmentation and physics effects as well as variations in the detector geometry and the uncertainty in the calorimeter response to b -jets as evaluated from single hadron response measurements. Uncertainties on the individual points are statistical only.

20.4 Final bottom quark JES uncertainty

The b -jet JES uncertainty is obtained adding the calorimeter response uncertainty (see Section 20.2 for generator details) and the uncertainties from the systematic Monte Carlo variations (see Section 20.3) in quadrature.

To avoid double counting when combining the b -jet uncertainty with the JES uncertainty of inclusive jets the following effects need to be considered:

1. The uncertainty component due to the PERUGIA2010 tune is not added, since the effect on b -jets is similar to the one on inclusive jets where it is already accounted for.
2. The average uncertainty for inclusive jets due to additional dead detector material is subtracted from the corresponding b -jet uncertainty component. The JES uncertainty due to dead material is smaller for inclusive jets, since *in situ* measurements are used.

The resulting additional JES uncertainty for b -jets is shown in Figure 87. It is about 2% up to $p_T^{\text{jet}} \approx 100$ GeV and below 1% for higher p_T^{jet} . To obtain the overall b -jet uncertainty this uncertainty needs to be added in quadrature to the JES uncertainty for inclusive jets described in Section 9.

20.5 Validation of the heavy quark energy scale using tracks

The validation of the identified b -jet JES uncertainty uses the tracks associated to the b -jet as reference object and closely follows the method described in Section 10.1. The transverse momentum of a jet is compared to the total transverse momentum measured in tracks associated to the jet (see Equation 22).

20.5.1 Method

The double ratio of charged-to-total momentum observed in data to that obtained in Monte Carlo simulation defined in Equation 23 will be referred to as $R_{r_{\text{trk}}, \text{inclusive}}$. In analogy this ratio is studied for b -tagged jets:

$$R_{r_{\text{trk}}, b\text{-jet}} \equiv \frac{[\langle r_{\text{trk}} b\text{-jet} \rangle]_{\text{Data}}}{[\langle r_{\text{trk}} b\text{-jet} \rangle]_{\text{MC}}}. \quad (61)$$

The r_{trk} distributions for all p_T bins are calculated and the mean values of r_{trk} for data and Monte Carlo simulation are derived. The relative response to b -jets relative to inclusive jets, R' , is defined as

$$R' \equiv \frac{R_{r_{\text{trk}}, b\text{-jet}}}{R_{r_{\text{trk}}, \text{inclusive}}}. \quad (62)$$

20.5.2 Systematic uncertainties

The systematic uncertainties arise from the modelling of the b -fragmentation, b -tagging calibration, jet resolution and tracking efficiency. They are assumed to be uncorrelated. The resulting fractional systematic uncertainties are shown on the right part of Figure 88 and are determined as follows:

1. **MC generator:** The r_{trk} distribution is also calculated from HERWIG++ samples. The shift in the distribution is fitted by a constant function. The variations in the data to Monte Carlo simulation ratio are taken as a systematic uncertainty.
2. **b -tagging calibration:** The scale factors are varied correlated within their systematic uncertainty in the Monte Carlo simulation and the ratio is re-evaluated. The resulting shifts are added in quadrature to the systematic uncertainty.
3. **Material description:** The knowledge of the tracking efficiency modelling in Monte Carlo simulation was evaluated in detail in Ref. [64]. The systematic uncertainty on the tracking efficiency for isolated tracks increases from 2% ($|\eta^{\text{track}}| < 1.3$) to 7% ($2.3 \leq |\eta^{\text{track}}| < 2.5$) for tracks with $p_T > 500$ MeV. The resulting effect on r_{trk} is 2% for $|y| < 1.2$, 3.1% for $1.2 \leq |y| < 2.1$ and 5.5% for $2.1 \leq |y| < 2.5$.
4. **Tracking in jet core:** High track densities in the jet core influence the tracking efficiency due to shared hits between tracks, fake tracks and lost tracks. The number of shared hits is well-described in Monte Carlo simulation. The p_T carried by fake tracks is negligible.

A relative systematic uncertainty of 50% on the loss of efficiency is assigned. The shift of r_{trk} due to this uncertainty on the loss of efficiency is evaluated in Monte Carlo simulation on generated charged particles. Monte Carlo pseudo-experiments are generated according to the varied inefficiency. For each jet the ratio of the p_T sum of the associated generated particles (truth tracks) with $p_T^{\text{track}} > 1$ GeV to the p_T sum of those associated truth tracks with $p_T > 1$ GeV which also have a matched reconstructed track with $p_T^{\text{track}} > 1$ GeV, is calculated. In this latter sample a truth track without or with a reconstructed track with $p_T^{\text{track}} > 1$ GeV is added or respectively discarded according to the inefficiency uncertainty. The relative shift in the ratio r_{trk} is added in quadrature to the systematic uncertainty.

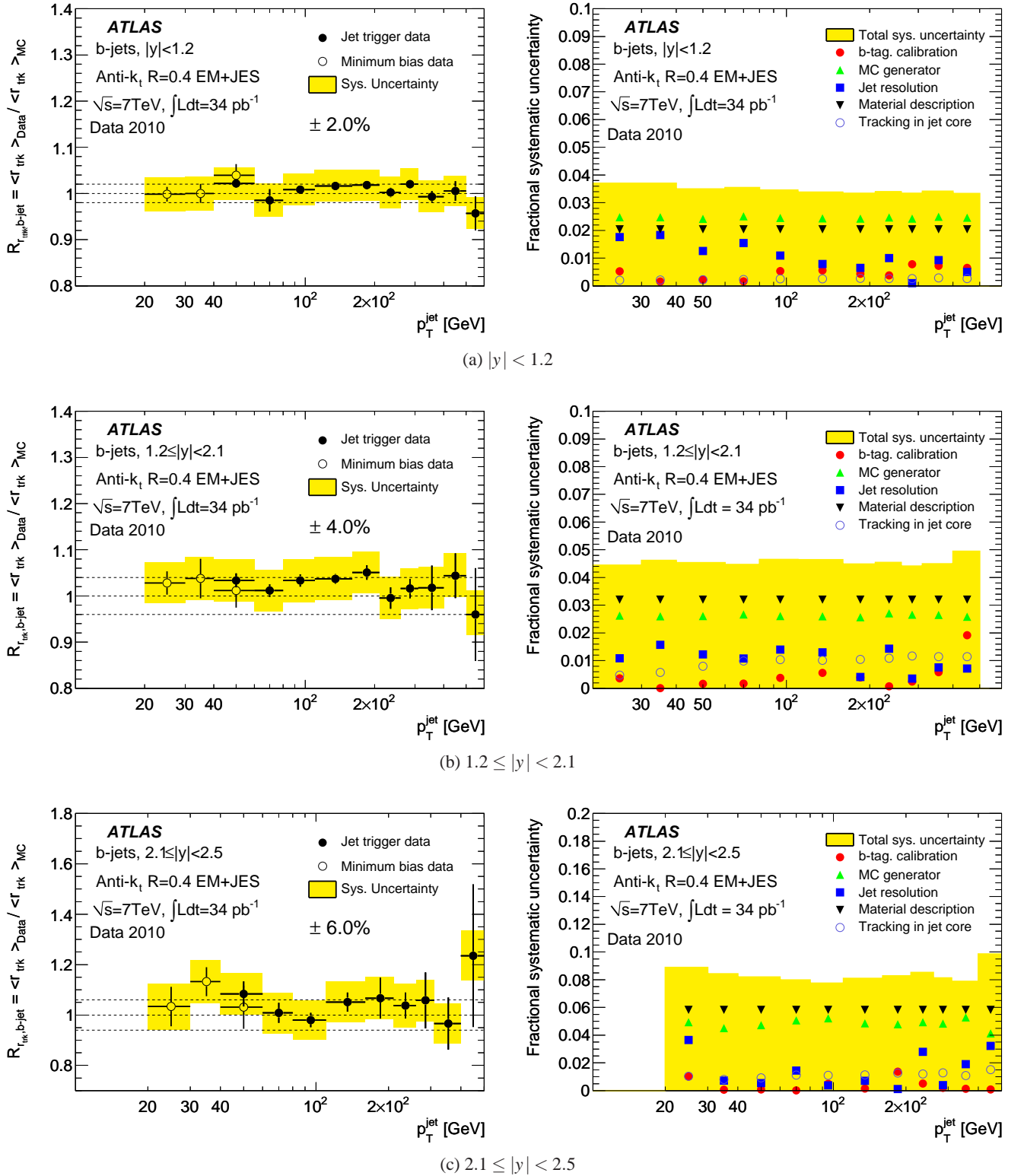


Fig. 88: The ratio of the mean value of r_{trk} in data and Monte Carlo (left) and the fractional systematic uncertainty (right) as a function of p_T^{jet} for $|y| < 1.2$ (a), $1.2 \leq |y| < 2.1$ (b) and $2.1 \leq |y| < 2.5$ (c). Anti- k_t jets with $R = 0.4$ calibrated with the EM+JES scheme are used. The dashed lines indicate the estimated uncertainty from the data and Monte Carlo simulation agreement. Note the changed axis ranges in (c). Only statistical uncertainties are shown on the data points.

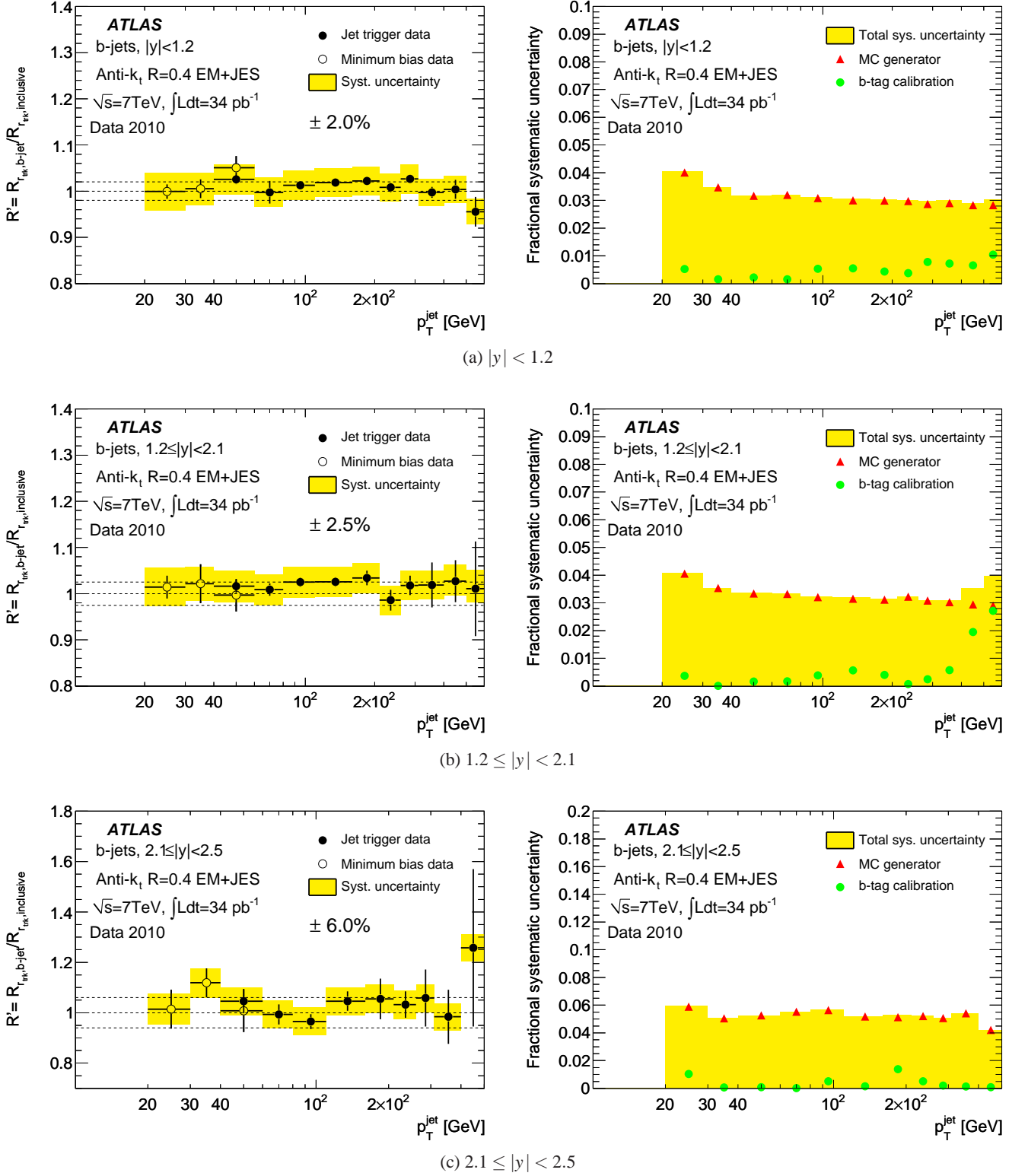


Fig. 89: The ratio R' (see Equation 62) of $R_{r_{\text{tk}}, b\text{-jet}}$ for identified b -jets and $R_{r_{\text{tk}}, \text{inclusive}}$ for inclusive jets (left) and the fractional systematic uncertainty (right) as a function of p_T^{jet} for $|y| < 1.2$ (a), $1.2 \leq |y| < 2.1$ (b) and $2.1 \leq |y| < 2.5$ (c). Anti- k_t jets with $R = 0.4$ calibrated with the EM+JES scheme are used. The dashed lines indicate the estimated uncertainty from the data and Monte Carlo simulation agreement. Only statistical uncertainties are shown on the data points. Note the changed axis ranges in (c).

5. **Jet resolution:** The jet energy resolution in Monte Carlo simulation is degraded. A random energy that corresponds to a resolution smearing of 10% is added to each jet. The resulting shift of the ratio r_{trk} is evaluated and added in quadrature to the overall systematic uncertainty.

The two biggest contributions to the systematic uncertainty are due to the material description and the difference between the r_{trk} distribution for HERWIG++ and PYTHIA.

20.5.3 Results

Figure 88 (left) shows the ratio of data to Monte Carlo simulation. An agreement of the calorimeter to track jet p_T measurements is found within 2% in the bin $|y| < 1.2$, within 4% for $1.2 \leq |y| < 2.1$ and within 6% for $2.1 \leq |y| < 2.5$.

The relative response R' between identified b -jets and inclusive jets is shown in Figure 89 for all y -bins indicating the resulting relative b -jet energy scale uncertainty with respect to the inclusive jets sample. The uncertainty for b -jets is estimated to be 2%, 2.5% and 6% in the range $|y| < 1.2$, $1.2 \leq |y| < 2.1$ and $2.1 \leq |y| < 2.5$, respectively. For the calculation of the systematic uncertainty in R' it is assumed that at first order the uncertainty in the denominator and numerator of R' from the tracking, namely tracking efficiency, material description, are fully correlated and cancel. The p_T^{jet} resolution for inclusive and identified b -jets is considered to be similar. Both assumptions are exactly valid for high p_T jets; for low p_T jets the second order deviations are estimated to be about 0.2%.

The most significant systematic uncertainties on R' are due to the choice of the Monte Carlo generator and the b -tagging calibration. Those independent uncertainties are added in quadrature. The Monte Carlo generator uncertainties from the inclusive sample and from the b -tagged sample are also added in quadrature.

20.5.4 Summary

The jet energy scale for identified b -jets relative to that of inclusive jets is evaluated for anti- k_t jets with $R = 0.4$ for the EM+JES calibration scheme. The resulting relative b -jet energy scale with respect to the inclusive jets sample is derived within 2%, 2.5% and 6% in the range $|y| < 1.2$, $1.2 \leq |y| < 2.1$ and $2.1 \leq |y| < 2.5$, respectively.

21 Study of jet punch-through

For jets at very high transverse momentum it is possible that part of the energy is not deposited in the calorimeter, but leaks out to the detector components beyond the calorimeter. This leads to a systematic reduction in the measured jet energy.

Jets that deposit energy beyond the hadronic Tile calorimeter and in the muon system are called *punch-through* jets. A graphical representation of a candidate for a punch-through jet in data is shown in Figure 90.

In this section the Monte Carlo simulation of energy deposits in the outermost calorimeter layer is tested. Quantitative estimates of the energy lost beyond the calorimeter are obtained using a tag-and-probe technique.

21.1 Event selection for punch-through analysis

Anti- k_t jets with $R = 0.4$ calibrated with the EM+JES scheme are used in this study. Jets in the barrel of the Tile calorimeter with $|\eta| < 1.2$ are used. Events with at least two jets are retained, if the highest p_T jet satisfies $p_T^{j1} > 120$ GeV and the second highest p_T jet satisfies $p_T^{j2} > 80$ GeV. The two leading jets are required to be back-to-back requiring $\Delta\phi > 170^\circ$.

21.2 Energy depositions in the hadronic calorimeter

The energy deposits in the outermost layer of the barrel of the Tile calorimeter are a good indicator of the jet energy depositions beyond the calorimeter. These are shown in Figure 91 for the leading and the sub-leading jet. Most jets deposit only about 3 to 7 GeV energy in the outermost calorimeter layer. The Monte Carlo simulation gives a good description of the data for $p_T^{\text{jet}} < 80$ GeV. For higher p_T^{jet} the data distribution is below the Monte Carlo simulation, but the statistical uncertainties are large.

Figure 92 shows the dependence of the energy deposition in the outermost layer of the Tile calorimeter measured at the EM scale for the leading and sub-leading jet p_T . The energy in the third layer of the Tile calorimeter increases with rising jet p_T . The data are well described by the Monte Carlo simulation in the low p_T^{jet} region. Starting from about 400 GeV the data tend to be 5–10% above the Monte Carlo simulation. For high p_T^{jet} the statistical uncertainties are large.

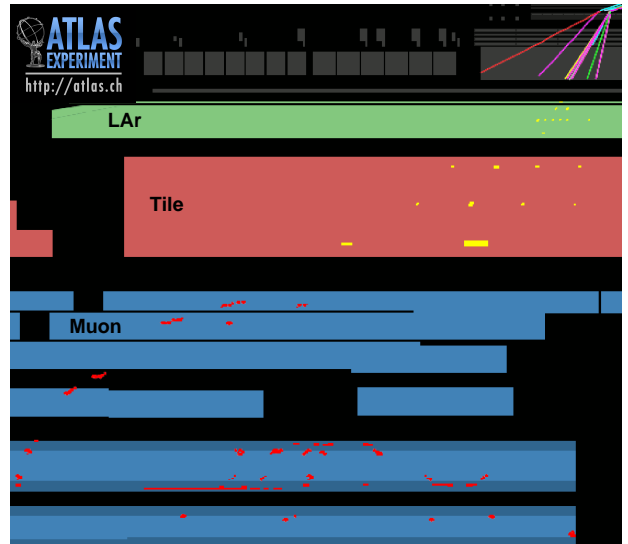


Fig. 90: Graphical representation in a zoomed x - y view of an event candidate with one large transverse momentum jet ($p_T^{\text{jet}} = 176$ GeV) having a large activity in the last Tile calorimeter layer (82 GeV at the EM scale) and in the muon detectors. The tracks in the inner detector are shown as lines in the top right, the energy deposits in the LAr and Tile calorimeters are shown as light boxes. The hits in the muon system are shown as points. There are 128 hits measured in the muon system.

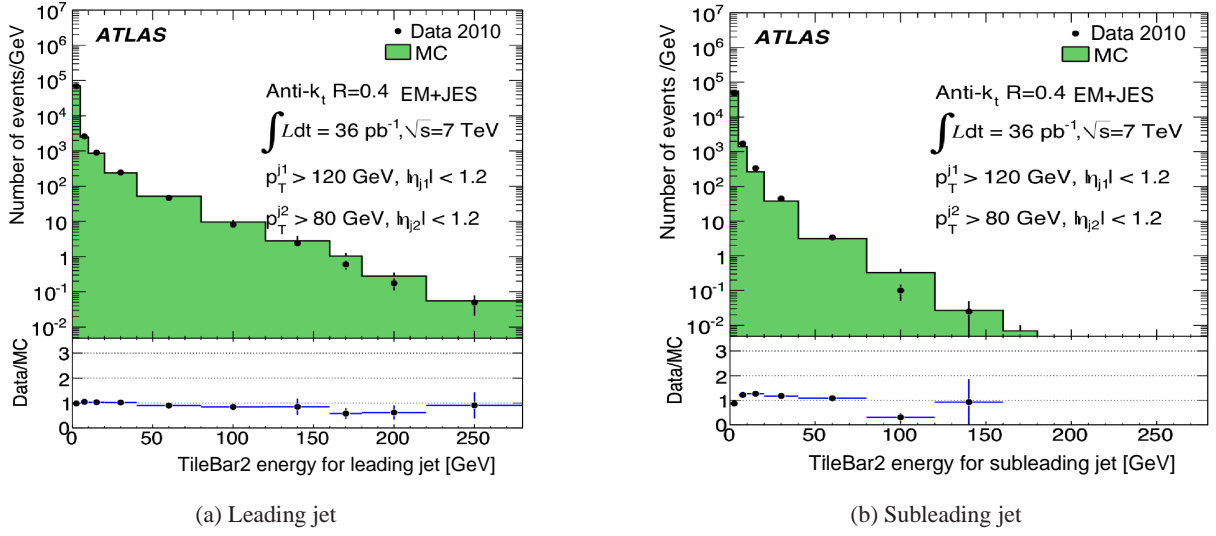


Fig. 91: Distribution of the deposited energy in the outermost layer of the Tile barrel calorimeter measured at the EM-scale for the leading (a) and the subleading (b) jet. Anti- k_t jets with $R = 0.4$ within $|\eta| < 1.2$ and calibrated with the EM+JES scheme are used. The leading jet is required to be above $p_T^{\text{jet}} > 120$ GeV the subleading jet is required to be above $p_T^{\text{jet}} > 80$ GeV. Only statistical uncertainties are shown.

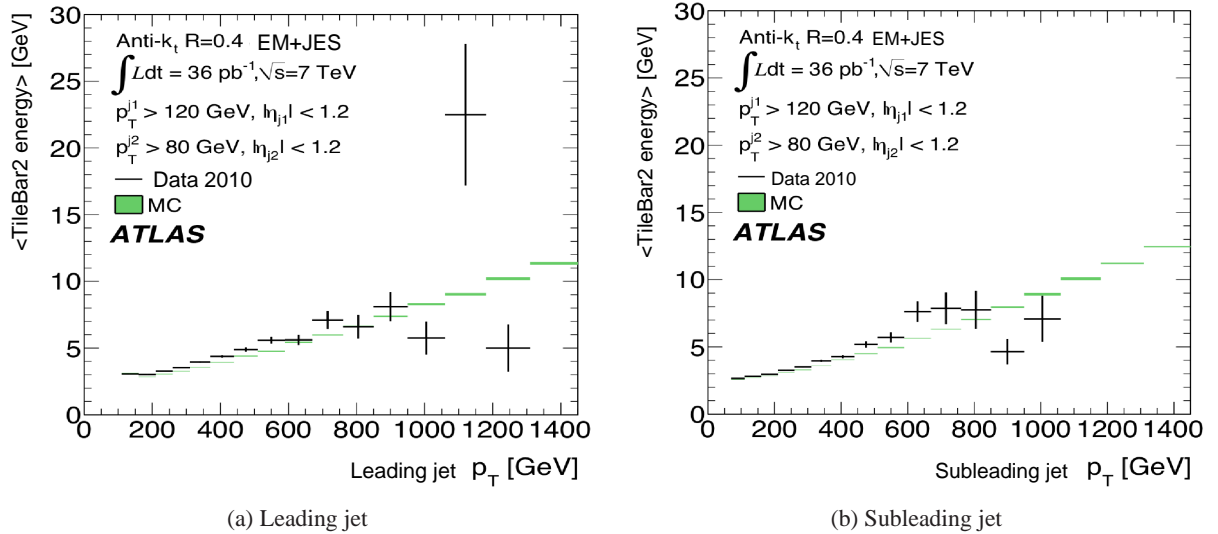


Fig. 92: Average energy deposited in the outermost layer of the Tile barrel calorimeter at the EM-scale for the leading (a) and the subleading jet (b) as a function of the jet transverse momentum. Anti- k_t jets with $R = 0.4$ within $|\eta| < 1.2$ and calibrated with the EM+JES scheme are used. The leading jet is required to be above $p_T^{\text{jet}} > 120$ GeV the subleading jet is required to be above $p_T^{\text{jet}} > 80$ GeV. Only statistical uncertainties are shown.

21.3 Dijet balance as an indication of punch-through

The relative calorimeter response between the two jets in a dijet event can be measured using the dijet p_T balance method. In Section 9.6 the reference jet is chosen as a well-measured object in the central detector region that is used to assess the JES uncertainty of the probe jet in the forward region. However, in the context of punch-through such a distinction cannot

be made. Jet punch-through can occur in any detector pseudo-rapidity region. Fluctuations in the particle composition or in the hadronic shower occur with equal probability for both jets and it is not possible to know *a priori* which of the jets will be affected.

A different approach is therefore employed. The energy lost beyond the calorimeter will create a component of the missing transverse energy E_T^{miss} in the direction of the punch-through

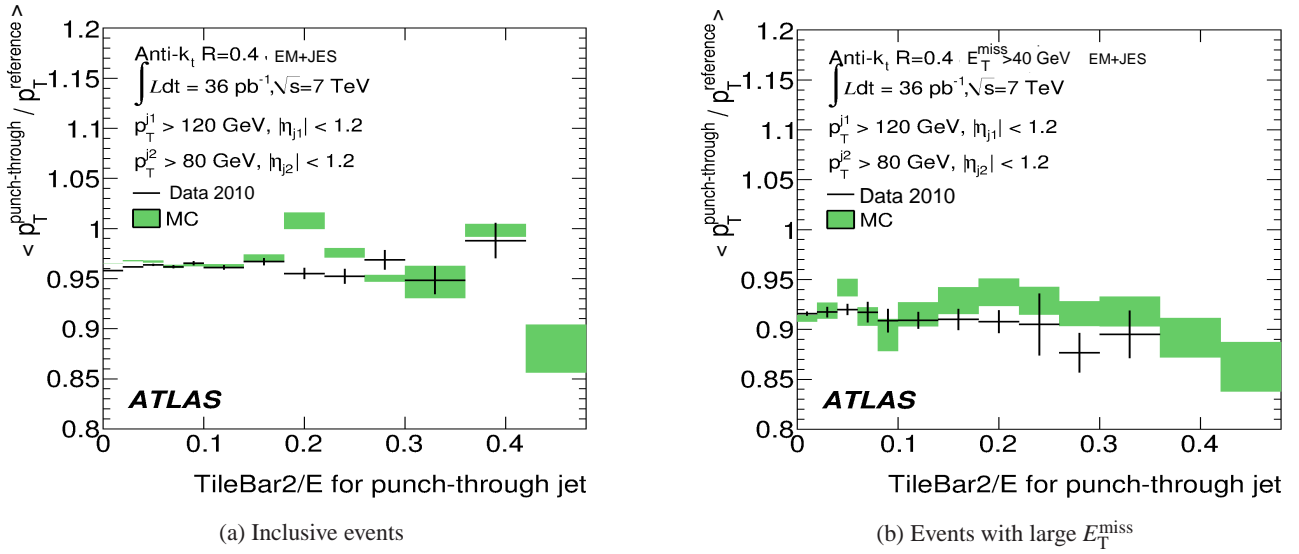


Fig. 93: Average relative jet response as a function of the energy deposited in the outermost layer of the Tile barrel calorimeter at the EM-scale divided by the total jet energy. In (a) the standard event selection is employed, whilst in (b) an extra requirement is placed upon the missing transverse momentum in the event. Anti- k_t jets with $R = 0.4$ within $|\eta| < 1.2$ and calibrated with the EM+JES scheme are used. The leading jet is required to be above $p_T^{\text{jet}} > 120$ GeV the subleading jet is required to be above $p_T^{\text{jet}} > 80$ GeV. Only statistical uncertainties are shown (errors bars for data, shaded band for Monte Carlo simulation).

jet. The punch-through jet can therefore be defined as the one that is closest to the E_T^{miss} ϕ -direction. The asymmetry between the transverse momentum of the reference jet ($p_T^{\text{reference}}$) away from the E_T^{miss} direction and the punch-through jet, acting as probe jet ($p_T^{\text{punch-through}}$), can then be measured as a function of the energy deposition of the jet that is the candidate for punch-through.

Figure 93a show the average ratio of the transverse momentum of the punch-through jet to the one of the reference jet as a function of the energy depositions in the last Tile calorimeter layer measured at the EM-scale with respect to the total jet energy. Figure 93b show the average jet response where $E_T^{\text{miss}} > 40$ GeV is required. This selection enhances possible punch-through effects. The transverse momentum of the punch-through jet is lower than that of the reference jet. This is a bias due to the selection of the punch-through jet as the one pointing to the direction of the missing transverse momentum. There is no dependence on the energy fraction in the outermost layer, indicating that energy losses due to punch-through are small for the jet p_T range considered in this study. The Monte Carlo simulation describes the data within the statistical uncertainties.

21.4 Summary of the jet punch-through study

The energy deposition in the outer layer of the Tile calorimeter and its dependence on the transverse jet energy is described by the Monte Carlo simulation. This indicates that the Monte Carlo simulation is able to describe energy deposited beyond the calorimeter. For the few jets that are potentially affected by

punch-through no additional uncertainty due to punch-through effects is assigned.

22 Summary

The jet energy scale (JES) and its systematic uncertainty for various jet calibration schemes are determined for jets measured with the ATLAS detector in the 2010 data set corresponding to an integrated luminosity of 38 pb^{-1} . Jets produced in proton-proton collisions at the LHC with a centre-of-mass energy of $\sqrt{s} = 7$ TeV are reconstructed with the anti- k_t algorithm with distance parameters $R = 0.4$ or $R = 0.6$. The energy and the direction of the jets are calibrated with simple factors derived from Monte Carlo simulations for transverse jet momenta $p_T^{\text{jet}} \geq 20$ GeV and pseudorapidities $|\eta| < 4.5$ using various jet calibration schemes.

In the simplest calibration scheme (EM+JES), where the JES correction factor is directly applied to the calorimeter measurement at the electromagnetic scale, the JES systematic uncertainty is estimated using the single hadron response measured *in situ* and in test-beams and by studying systematic variations in Monte Carlo simulations. The transverse momentum balance between central and forward jets in dijet events is used to derive the JES uncertainty for forward jets.

In the central region, $|\eta| < 0.8$, the EM+JES uncertainty is lower than 4.6% for all jets with $p_T^{\text{jet}} > 20$ GeV and less than 2.5% for jets with $60 \leq p_T^{\text{jet}} < 800$ GeV. Jets with transverse momenta in the TeV-regime have a JES uncertainty of 3 to 4%. Towards the forward region the EM+JES uncertainty increases, mainly because of differences between the Monte Carlo event generators PYTHIA and HERWIG when deriving the relative

η -intercalibration uncertainty. The largest JES uncertainty of about 14% is found for low p_T jets with $20 \leq p_T^{\text{jet}} < 30$ GeV at $3.6 \leq |\eta| < 4.5$. The jet energy scale uncertainty is found to be similar for jets reconstructed with both jet distance parameters studied: $R = 0.4$ and $R = 0.6$.

The additional energy induced by superimposed events from multiple proton-proton collisions in the same bunch crossing (pile-up) is determined to be 0.5 GeV per additional reconstructed vertex. The JES uncertainty after applying the pile-up correction is estimated as a function of the number of primary vertices. In the case of two primary vertices per event, the uncertainty due to pile-up for jets with $p_T^{\text{jet}} \approx 20$ GeV and $0.3 \leq |\eta| < 0.8$ is about 1%, while it amounts to about 2% for jets with $2.1 \leq |\eta| < 2.8$. For jets with transverse momentum above 200 GeV, the uncertainty due to pile-up is negligible for all jets.

The JES and its uncertainty are validated up to $p_T^{\text{jet}} \lesssim 1$ TeV to the level of a few per cent using several *in situ* techniques by comparing the high p_T jet to a well known reference recoiling against it. These reference objects include the sum of the transverse track momenta associated to the jet, a system of low p_T jets or the photon p_T . The track-based method covers the full p_T^{jet} range and has the highest statistical precision. However, the systematic uncertainty of the method is as large as 6% for very low p_T jets and about 3-4% for $40 \leq p_T^{\text{jet}} < 800$ GeV and somewhat higher for jets outside this p_T^{jet} range. The γ -jet method has a systematic uncertainty of about 1%, but is still statistically limited and reaches only $p_T^{\text{jet}} \lesssim 300$ GeV. Balancing very high p_T jets against a recoil system of lower p_T jets allows the validation of the high p_T jets within 5% up to 1 TeV. In this range the statistical uncertainty is roughly equivalent to, or smaller than, the systematic uncertainty.

The JES uncertainty derived from a combination of *in situ* techniques is compatible to the one derived from the single hadron response measurements over a wide kinematic range, but it is larger for very low and very large p_T^{jet} , where the uncertainties of the *in situ* methods are large.

More sophisticated jet energy calibration schemes based on cell energy density weighting or jet properties are studied. These provide a better jet energy resolution and a reduced flavour dependence of the jet response.

The global sequential jet calibration (GS) based on global properties of the internal jet structure improves the energy resolution and reduces flavour dependence of the EM+JES calibration scheme. The JES uncertainty for the GS jet calibration scheme is given by the sum in quadrature of the EM+JES uncertainty and the uncertainty associated to the GS corrections. The latter is conservatively taken to be 0.5% for $30 \leq p_T < 800$ GeV and $|\eta| < 2.1$ and 1% for $p_T^{\text{jet}} < 30$ GeV and $2.1 < |\eta| < 2.8$. These uncertainties are also supported by *in situ* measurements with the γ -jet and the dijet technique.

The global cell weighting scheme (GCW) derives cell weights by optimising the resolution of reconstructed jets relative to their respective truth jets. The local cluster calibration (LCW) derives energy corrections for calorimeter clusters using single hadron Monte Carlo simulations. The JES uncertainty is obtained from *in situ* techniques. Over a wide kinematic range the JES uncertainties for the various schemes are

similar, except at very low and very high p_T^{jet} where the uncertainty from the *in situ* techniques are larger. The LCW+JES and the GCW+JES scheme show similar performance.

For all jet calibration methods additional uncertainties are derived for close-by jet topologies and for response differences for jets induced by quarks, gluons or heavy flavour quarks. A method to reduce the uncertainty due to uncertainties on the quark and gluon composition in a given event sample is shown. The uncertainty due to close-by jets is largest for low p_T jets, but is at most below 2 to 3%. The JES uncertainty of jets containing B -hadrons is about 2% for low- p_T jets and smaller than 1% for jets with $p_T^{\text{jet}} > 200$ GeV.

The jet reconstruction efficiency is derived using the Monte Carlo simulation and the systematic uncertainty evaluated with a tag-and-probe technique using track jets. The jet reconstruction efficiency is well-described by the Monte Carlo simulation. The associated systematic uncertainty is below 2% for jets with $p_T^{\text{jet}} < 30$ GeV and negligible for higher p_T^{jet} .

The Monte Carlo simulation gives a good description of the main aspects of the data. Detailed studies show that the calorimeter cell energy densities in jets, the calorimeter energy topology induced by jets and track related properties are well-described. This includes the amount of energy deposited in the outermost calorimeter layers from which it is inferred that the JES uncertainty due to energy leaking beyond the calorimeter is small and well-described by the Monte Carlo simulation. No additional uncertainty for punch-through effects is assigned for high- p_T jets.

In summary, the precision of the jet energy measurement with the ATLAS detector has been established using various techniques in the first year of proton-proton collisions at the LHC. In the central detector the jet energy can be measured with a precision of about 2 to 3% over a wide transverse momentum range.

This excellent performance would not have been possible without a very detailed understanding of the detector and sophisticated calorimeter calibration procedures as well as the good description of the ATLAS detector in the Monte Carlo simulation.

Acknowledgement

We thank CERN for the very successful operation of the LHC, as well as the support staff from our institutions without whom ATLAS could not be operated efficiently.

We acknowledge the support of ANPCyT, Argentina; YerPhI, Armenia; ARC, Australia; BMWF, Austria; ANAS, Azerbaijan; SSTC, Belarus; CNPq and FAPESP, Brazil; NSERC, NRC and CFI, Canada; CERN; CONICYT, Chile; CAS, MOST and NSFC, China; COLCIENCIAS, Colombia; MSMT CR, MPO CR and VSC CR, Czech Republic; DNRF, DNSRC and Lundbeck Foundation, Denmark; ARTEMIS, European Union; IN2P3-CNRS, CEA-DSM/IRFU, France; GNAS, Georgia; BMBF, DFG, HGF, MPG and AvH Foundation, Germany; GSRT, Greece; ISF, MINERVA, GIF, DIP and Benoziyo Center, Israel; INFN, Italy; MEXT and JSPS, Japan; CNRST, Morocco; FOM and NWO, Netherlands; RCN, Norway; MNiSW, Poland; GRICES

and FCT, Portugal; MERYS (MECTS), Romania; MES of Russia and ROSATOM, Russian Federation; JINR; MSTD, Serbia; MSSR, Slovakia; ARRS and MVZT, Slovenia; DST/NRF, South Africa; MICINN, Spain; SRC and Wallenberg Foundation, Sweden; SER, SNSF and Cantons of Bern and Geneva, Switzerland; NSC, Taiwan; TAEK, Turkey; STFC, the Royal Society and Leverhulme Trust, United Kingdom; DOE and NSF, United States of America.

The crucial computing support from all WLCG partners is acknowledged gratefully, in particular from CERN and the ATLAS Tier-1 facilities at TRIUMF (Canada), NDGF (Denmark, Norway, Sweden), CC-IN2P3 (France), KIT/GridKA (Germany), INFN-CNAF (Italy), NL-T1 (Netherlands), PIC (Spain), ASGC (Taiwan), RAL (UK) and BNL (USA) and in the Tier-2 facilities worldwide.

References

1. ATLAS Collaboration, *Measurement of inclusive jet and dijet cross sections in proton-proton collisions at 7 TeV centre-of-mass energy with the ATLAS detector*, Eur. Phys. J. C **71** (2011) 1512, [arXiv:1009.5908 \[hep-ex\]](#).
2. ATLAS Collaboration, *Measurement of multijet cross sections in proton-proton collisions at a 7 TeV center-of-mass energy*, submitted to Eur. Phys. J. (2011), [arXiv:1107.2092 \[hep-ex\]](#).
3. ATLAS Collaboration, *Study of jet shapes in inclusive jet production in pp collisions at $\sqrt{s} = 7$ TeV using the ATLAS detector*, Phys. Rev. D **83** (2011) 052003, [arXiv:1101.0070 \[hep-ex\]](#).
4. ATLAS Collaboration, *Measurement of dijet azimuthal decorrelations in pp collisions at $\sqrt{s} = 7$ TeV*, Phys. Rev. Lett. **106** (2011) 172002, [arXiv:1102.2696 \[hep-ex\]](#). ATLAS Collaboration, *Measurement of dijet production with a veto on additional central jet activity in pp collisions at $\sqrt{s} = 7$ TeV using the ATLAS detector*, JHEP **09** (2011) 053, [arXiv:1107.1641 \[hep-ex\]](#).
5. ATLAS Collaboration, *Measurement of the production cross section for W-bosons in association with jets in pp collisions at $\sqrt{s} = 7$ TeV with the ATLAS detector*, Phys. Lett. B **698** (2011) 325–345, [arXiv:1012.5382 \[hep-ex\]](#). ATLAS Collaboration, *Measurement of the cross-section for b-jets produced in association with a Z boson at $\sqrt{s} = 7$ TeV with the ATLAS detector*, [arXiv:1109.1403 \[hep-ex\]](#).
6. ATLAS Collaboration, *Search for quark contact interactions in dijet angular distributions in pp collisions at $\sqrt{s} = 7$ TeV measured with the ATLAS detector*, Phys. Lett. B **694** (2011) 327–345, [arXiv:1009.5069 \[hep-ex\]](#). ATLAS Collaboration, *Search for new particles in two-jet final states in 7 TeV proton-proton collisions with the ATLAS detector at the LHC*, Phys. Rev. Lett. **105** (2010) 161801, [arXiv:1008.2461 \[hep-ex\]](#). ATLAS Collaboration, *Search for new physics in dijet mass and angular distributions in pp collisions at $\sqrt{s} = 7$ TeV measured with the ATLAS Detector*, New J. Phys. **13** (2011) 053044, [arXiv:1103.3864 \[hep-ex\]](#). ATLAS Collaboration, *Search for supersymmetry using final states with one lepton, jets, and missing transverse momentum with the ATLAS detector in $\sqrt{s} = 7$ TeV pp collisions*, Phys. Rev. Lett. **106** (2011) 131802, [arXiv:1102.2357 \[hep-ex\]](#). ATLAS Collaboration, *Search for squarks and gluinos using final states with jets and missing transverse momentum with the ATLAS detector in $\sqrt{s} = 7$ TeV proton-proton collisions*, Phys. Lett. B **701** (2011) 186–203, [arXiv:1102.5290 \[hep-ex\]](#). ATLAS Collaboration, *Search for supersymmetry in pp collisions at $\sqrt{s} = 7$ TeV in final states with missing transverse momentum and b-jets*, Phys. Lett. B **701** (2011) 398–416, [arXiv:1103.4344 \[hep-ex\]](#).
7. M. Cacciari, G. P. Salam, and G. Soyez, *The anti- k_t jet clustering algorithm*, JHEP **04** (2008) 063, [arXiv:0802.1189 \[hep-ph\]](#).
8. ATLAS Collaboration, *Expected performance of the ATLAS experiment - detector, trigger and physics*, CERN, Geneva, September, 2009. [arXiv:0901.0512 \[hep-ex\]](#). CERN-OPEN-2008-020.
9. ATLAS Collaboration, *The ATLAS experiment at the CERN Large Hadron Collider*, JINST **3** (2008) S08003.
10. ATLAS Collaboration, *Performance of the ATLAS trigger system in 2010*, submitted to Eur. Phys. J. (2011), [arXiv:1110.1530 \[hep-ex\]](#).
11. E. Abat et al., *Combined performance studies for electrons at the 2004 ATLAS combined test-beam*, JINST **5** (2010) P11006.
12. M. Aharrouché et al., *Measurement of the response of the ATLAS liquid argon barrel calorimeter to electrons at the 2004 combined test-beam*, Nucl. Instrum. Meth. A **614** (2010) 400–432.
13. J. Colas et al., *Response uniformity of the ATLAS liquid argon electromagnetic calorimeter*, Nucl. Instrum. Meth. A **582** (2007) 429–455, [arXiv:0709.1094 \[physics.ins-det\]](#). M. Aharrouché et al., *Energy linearity and resolution of the ATLAS electromagnetic barrel calorimeter in an electron test-beam*, Nucl. Instrum. Meth. A **568** (2006) 601–623.
14. P. Adragna et al., *Testbeam studies of production modules of the ATLAS Tile calorimeter*, Nucl. Instrum. Meth. A **606** (2009) 362–394.
15. J. Pinfold et al., *Performance of the ATLAS liquid argon endcap calorimeter in the pseudorapidity region $2.5 < |\eta| < 4.0$ in beam tests*, Nucl. Instrum. Meth. A **593** (2008) 324–342.
16. C. Cojocaru et al., *Hadronic calibration of the ATLAS liquid argon end-cap calorimeter in the pseudorapidity region $1.6 < |\eta| < 1.8$ in beam tests*, Nucl. Instrum. Meth. A **531** (2004) 481–514.
17. M. Aharrouché et al., *Study of the response of ATLAS electromagnetic liquid argon calorimeters to muons*, Nucl. Instrum. Meth. A **606** (2009) 419–431.
18. ATLAS Collaboration, *Readiness of the ATLAS Tile calorimeter for LHC collisions*, Eur. Phys. J. C **70** (2010) 1193–1236, [arXiv:1007.5423 \[physics.ins-det\]](#).
19. ATLAS Collaboration, *Electron performance measurements with the ATLAS detector using the 2010 LHC proton-proton collision data*, submitted to Eur. Phys. J. (2011), [arXiv:1110.3174 \[hep-ex\]](#).
20. A. Buckley et al., *General-purpose event generators for LHC physics*, Phys. Rept. **504** (2011) 145–233, [arXiv:1101.2599 \[hep-ph\]](#).
21. T. Sjostrand, S. Mrenna, and P. Z. Skands, *PYTHIA 6.4 physics and manual*, JHEP **0605** (2006) 026, [arXiv:0603175 \[hep-ph\]](#).
22. R. Corke and T. Sjostrand, *Improved Parton Showers at Large Transverse Momenta*, Eur. Phys. J. C **69** (2010) 1–18, [arXiv:1003.2384 \[hep-ph\]](#).
23. T. Sjostrand and P. Z. Skands, *Transverse-momentum-ordered showers and interleaved multiple interactions*, Eur. Phys. J. C **39** (2005) 129–154, [arXiv:0408302 \[hep-ph\]](#).

24. B. Andersson et al., *Parton fragmentation and string dynamics*, Phys. Rep. **97** (1983) 31–145.
25. A. Sherstnev and R. S. Thorne, *Parton distributions for LO generators*, Eur. Phys. J. C **55** (2008) 553–575, [arXiv:0711.2473 \[hep-ph\]](#).
26. ATLAS Collaboration, *Charged particle multiplicities in pp interactions at $\sqrt{s} = 0.9$ and 7 TeV in a diffractive limited phase-space measured with the ATLAS detector at the LHC and new PYTHIA6 tune*, ATLAS-CONF-2010-031, May, 2010.
27. ATLAS Collaboration, *Charged particle multiplicities in p-p interactions for track $p_T > 100$ MeV at $\sqrt{s} = 0.9$ and 7 TeV measured with the ATLAS detector at the LHC*, ATLAS-CONF-2010-046, July, 2010.
28. P. Z. Skands, *Tuning Monte Carlo generators: The Perugia tunes*, Phys. Rev. D **82** (2010) 074018, [arXiv:1005.3457 \[hep-ph\]](#).
29. G. Marchesini et al., *Monte Carlo simulation of general hard processes with coherent QCD radiation*, Nucl. Phys. B **310** (1988) 461. G. Marchesini et al., *A Monte Carlo event generator for simulating hadron emission reactions with interfering gluons*, Comput. Phys. Commun. **67** (1991) 465–508. G. Corcella et al., *HERWIG 6.5 release note*, [arXiv:0210213 \[hep-ph\]](#).
30. B. R. Webber, *A QCD model for jet fragmentation including soft gluon interference*, Nucl. Phys. B **238** (1984) 492.
31. J. M. Butterworth, J. R. Forshaw, and M. H. Seymour, *Multiparton interactions in photoproduction at HERA*, Z. Phys. C **72** (1996) 637–646, [arXiv:9601371 \[hep-ph\]](#).
32. ATLAS Collaboration, *First tuning of HERWIG/JIMMY to ATLAS data*, ATL-PHYS-PUB-2010-014, October, 2010.
33. M. Bahr et al., *Herwig++ physics and manual*, Eur. Phys. J. C **58** (2008) 639–707, [arXiv:0803.0883 \[hep-ph\]](#).
34. M. Bahr, S. Gieseke, and M. H. Seymour, *Simulation of multiple partonic interactions in Herwig++*, JHEP **07** (2008) 076, [arXiv:0803.3633 \[hep-ph\]](#).
35. M. L. Mangano, M. Moretti, F. Piccinini, R. Pittau, and A. D. Polosa, *ALPGEN, a generator for hard multiparton processes in hadronic collisions*, JHEP **07** (2003) 001, [arXiv:0206293 \[hep-ph\]](#).
36. M. L. Mangano, M. Moretti, and R. Pittau, *Multijet matrix elements and shower evolution in hadronic collisions: $Wb\bar{b} + n$ jets as a case study*, Nucl. Phys. B **632** (2002) 343–362, [arXiv:0108069 \[hep-ph\]](#).
37. ATLAS Collaboration, *ATLAS MC tunes for MC09*, ATLAS-PHYS-PUB-2010-002, March, 2010.
38. J. Pumplin et al., *New generation of parton distributions with uncertainties from global QCD analysis*, JHEP **07** (2002) 012, [arXiv:0201195 \[hep-ph\]](#).
39. GEANT4 Collaboration, S. Agostinelli et al., *GEANT4: A simulation toolkit*, Nucl. Instrum. Meth. A **506** (2003) 250–303.
40. ATLAS Collaboration, *The ATLAS simulation infrastructure*, Eur. Phys. J. C **70** (2010) 823–874, [arXiv:1005.4568 \[physics.ins-det\]](#).
41. A. Ribon et al., *Status of Geant4 hadronic physics for the simulation of LHC experiments at the start of the LHC physics program*, CERN-LCGAPP-2010-02, May, 2010.
42. G. Folger and J. Wellisch, *String parton models in GEANT4*, [arXiv:0306007 \[nucl-th\]](#). N. S. Amelin et al., *Transverse flow and collectivity in ultrarelativistic heavy ion collisions*, Phys. Rev. Lett. **67** (1991) 1523–1526. N. S. Amelin, L. P. Csernai, E. F. Staubo, and D. Strottman, *Collectivity in ultrarelativistic heavy ion collisions*, Nucl. Phys. A **544** (1992) 463–466. L. V. Bravina, L. P. Csernai, P. Levai, N. S. Amelin, and D. Strottman, *Fluid dynamics and quark gluon string model: What we can expect for Au + Au collisions at 11.6-A/GeV/c*, Nucl. Phys. A **566** (1994) 461–464. L. V. Bravina, *Scaling violation of transverse flow in heavy ion collisions at AGS energies*, Phys. Lett. B **344** (1995) 49–54.
43. H. W. Bertini, *Intranuclear-cascade calculation of the secondary nucleon spectra from nucleon-nucleus interactions in the energy range 340 to 2900 MeV and comparisons with experiment*, Phys. Rev. A **188** (1969) 1711–1730. M. P. Guthrie, R. G. Alsmiller, and H. W. Bertini, *Calculation of the capture of negative pions in light elements and comparison with experiments pertaining to cancer radiotherapy*, Nucl. Instrum. Meth. **66** (1968) 29–36. M. P. Guthrie and H. W. Bertini, *News item results from medium-energy intranuclear-cascade calculation*, Nucl. Phys. A **169** (1971) 670–672. N. V. Stepanov, *Statistical modeling of fission of excited atomic nuclei. 2. calculation and comparison with experiment*, In Russian, ITEP, Moscow, 1988. [Preprint: ITEP-88-55](#).
44. P. Adragna et al., *Measurement of pion and proton response and longitudinal shower profiles up to 20 nuclear interaction lengths with the ATLAS Tile calorimeter*, Nucl. Instrum. Meth. A **615** (2010) 158–181. E. Abat et al., *Response and shower topology of 2 to 180 GeV pions measured with the ATLAS barrel calorimeter at the CERN test-beam and comparison to Monte Carlo simulations*, ATL-CAL-PUB-2010-001, May, 2010.
45. E. Abat et al., *Study of energy response and resolution of the ATLAS barrel calorimeter to hadrons of energies from 20 GeV to 350 GeV*, Nucl. Instrum. Meth. A **621** (2010) 134–150.
46. E. Abat et al., *Study of the response of the ATLAS central calorimeter to pions of energies from 3 to 9 GeV*, Nucl. Instrum. Meth. A **607** (2009) 372–386.
47. A. E. Kiryunin, H. Oberlack, D. Salihagic, P. Schacht, and P. Strizenec, *GEANT4 physics evaluation with testbeam data of the ATLAS hadronic end-cap calorimeter*, Nucl. Instrum. Meth. A **560** (2006) 278–290.
48. ATLAS Collaboration, *Response of the ATLAS calorimeter to single isolated hadrons produced in proton proton collisions at centre-of-mass energy of $\sqrt{s} = 900$ GeV*, ATLAS-CONF-2010-017, March, 2010.
49. ATLAS Collaboration, *ATLAS calorimeter response to single isolated hadrons and estimation of the calorimeter jet scale uncertainty*, ATLAS-CONF-2011-028, March, 2011.
50. ATLAS Collaboration, *Response of isolated particles identified using resonances in proton-proton collisions at $\sqrt{s} = 7$ TeV with the ATLAS detector*, ATLAS-CONF-2011-019, February, 2011.
51. ATLAS Collaboration, *A measurement of the material in the ATLAS inner detector using secondary hadronic interactions*, [arXiv:1110.6191 \[hep-ex\]](#).
52. ATLAS Collaboration, *Photon conversions at $\sqrt{s} = 900$ GeV measured with the ATLAS detector*, ATLAS-CONF-2010-007, June, 2010.
53. ATLAS Collaboration, *Probing the material in front of the ATLAS electromagnetic calorimeter with energy flow from $\sqrt{s} = 7$ TeV minimum bias events*, ATLAS-CONF-2010-037, July, 2010.
54. ATLAS Collaboration, *Luminosity determination in p-p collisions at $\sqrt{s} = 7$ TeV using the ATLAS detector at the LHC*, Eur. Phys. J. C **71** (2011) 1630, [arXiv:1101.2185 \[hep-ex\]](#).
55. R. Achenbach et al., *The ATLAS Level-1 calorimeter trigger*, ATL-DAQ-PUB-2008-001, January, 2008.

56. M. Cacciari and G. P. Salam, *Dispelling the N^3 myth for the k_T jet-finder*, Phys. Lett. B **641** (2006) 57–61. M. Cacciari, G. P. Salam, and G. Soyez. <http://fastjet.fr/>.
57. W. Lampl et al., *Calorimeter clustering algorithms: description and performance*, ATL-LARG-PUB-2008-002, April, 2008.
58. ATLAS Collaboration, *ATLAS calorimeter response to single isolated hadrons and estimation of the calorimeter jet scale uncertainty*, ATLAS-CONF-2010-052, June, 2010.
59. ATLAS Collaboration, *Study of the material budget in the ATLAS inner detector with K_S^0 decays in collision data at $\sqrt{s}=900$ GeV*, ATLAS-CONF-2010-019, July, 2010. ATLAS Collaboration, *Mapping the material in the ATLAS inner detector using secondary hadronic interactions in 7 TeV collisions*, ATLAS-CONF-2010-058, July, 2010.
60. D0 Collaboration, B. Abbott et al., *Determination of the absolute jet energy scale in the DZERO calorimeters*, Nucl. Instrum. Methods A **424** (1999) 352–394.
61. CDF Collaboration, A. Bhatti et al., *Determination of the jet energy scale at the collider detector at Fermilab*, Nucl. Instrum. Meth. A **566** (2006) 375–412, [arXiv:0510047 \[hep-ex\]](#).
62. ATLAS Collaboration, *Measurement of the jet fragmentation function and transverse profile in proton-proton collisions at a center-of-mass energy of 7 TeV with the ATLAS detector*, Eur. Phys. J. C **71** (2011) 1795, [arXiv:1109.5816 \[hep-ex\]](#).
63. DELPHI Collaboration, P. Abreu et al., *Tuning and test of fragmentation models based on identified particles and precision event shape data*, Z. Phys. C **73** (1996) 11–60.
64. ATLAS Collaboration, *Charged-particle multiplicities in p-p interactions measured with the ATLAS detector at the LHC*, New J.Phys. **13** (2011) 053033, [arXiv:1012.5104 \[hep-ex\]](#).
65. ATLAS Collaboration, *Jet energy resolution from in-situ techniques with the ATLAS detector using proton-proton collisions at a centre of mass energy $\sqrt{s} = 7$ TeV*, ATLAS-CONF-2011-054, July, 2011.
66. ATLAS Collaboration, *Measurement of the inclusive isolated prompt photon cross section in pp collisions at $\sqrt{s} = 7$ TeV with the ATLAS detector*, Phys. Rev. D **83** (2010) 052005, [arXiv:1012.4389 \[hep-ex\]](#).
67. M. Davier, A. Hoecker, B. Malaescu, C. Z. Yuan, and Z. Zhang, *Reevaluation of the hadronic contribution to the muon magnetic anomaly using new $e^+e^- \rightarrow \pi^+\pi^-$ cross section data from BABAR*, Eur. Phys. J. C **66** (2010) 1, [arXiv:0908.4300 \[hep-ex\]](#).
68. D. Lincoln, G. Morrow, and P. Kasper, *A hidden bias in a common calorimeter calibration scheme*, Nucl. Instrum. Meth. A **345** (1994) 449–452.
69. T. Barillari et al., *Local hadronic calibration*, ATL-LARG-PUB-2009-001, December, 2008.
70. OPAL Collaboration, G. Abbiendi et al., *Experimental properties of gluon and quark jets from a point source*, Eur. Phys. J. C **11** (1999) 217–238, [arXiv:9903027v1 \[hep-ex\]](#).
71. ATLAS Collaboration, *Calibrating the b-tag efficiency and mistag rate in 35 pb^{-1} of data with the ATLAS detector*, ATLAS-CONF-2011-089, June, 2011.
72. OPAL Collaboration, G. Abbiendi et al., *Inclusive analysis of the b-quark fragmentation function in Z decays at LEP*, Eur. Phys. J. C **29** (2003) 463–478, [arXiv:0210031 \[hep-ex\]](#).
73. SLD Collaboration, K. Abe et al., *Measurement of the b-quark fragmentation function in Z^0 decays*, Phys. Rev. D **65** (2002) 092006, [arXiv:0202031 \[hep-ex\]](#).
74. T. Carli, V. Chiochia, and K. Klimek, *Definition and calculation of bottom quark cross-sections in deep inelastic scattering at HERA and determination of their uncertainties*, JHEP **09** (2003) 070, [arXiv:0305103 \[hep-ph\]](#).
- M. Cacciari, M. Greco, and P. Nason, *The p_T spectrum in heavy flavour hadroproduction*, JHEP **05** (1998) 007, [arXiv:9803400 \[hep-ph\]](#).
- A. Banfi, G. P. Salam, and G. Zanderighi, *Accurate QCD predictions for heavy quark jets at the Tevatron and LHC*, JHEP **07** (2007) 026, [arXiv:0704.2999 \[hep-ph\]](#).
- R. D. Ball and R. K. Ellis, *Heavy quark production at high energy*, JHEP **05** (2001) 053, [arXiv:0101199 \[hep-ph\]](#).
- M. Cacciari and P. Nason, *Is there a significant excess in bottom hadroproduction at the Tevatron?*, Phys. Rev. Lett. **89** (2002) 122003, [arXiv:0204025 \[hep-ph\]](#).
75. ALEPH Collaboration, A. Heister et al., *Study of the fragmentation of b-quarks into B-mesons at the Z peak*, Phys. Letts. B **512** (2001) 30–48.
76. G. Corcella and F. Mescia, *A phenomenological study of bottom quark fragmentation in top quark decay*, Eur. Phys. J. C **65** (2010) 171–180, [arXiv:0907.5158 \[hep-ph\]](#).
77. A. Buckley, H. Hoeth, H. Lacker, H. Schulz, and J. E. von Seggern, *Systematic event generator tuning for the LHC*, Eur. Phys. J. C **65** (2010) 331–357, [arXiv:0907.2973 \[hep-ph\]](#).
78. M. Bowler, *e^+e^- Production of Heavy Quarks in the String Model*, Z. Phys. C **11** (1981) 169.

The ATLAS Collaboration

G. Aad⁴⁸, B. Abbott¹¹¹, J. Abdallah¹¹, A.A. Abdelalim⁴⁹, A. Abdesselam¹¹⁸, O. Abidinov¹⁰, B. Abi¹¹², M. Abolins⁸⁸, H. Abramowicz¹⁵³, H. Abreu¹¹⁵, E. Acerbi^{89a,89b}, B.S. Acharya^{164a,164b}, D.L. Adams²⁴, T.N. Addy⁵⁶, J. Adelman¹⁷⁵, M. Aderholz⁹⁹, S. Adomeit⁹⁸, P. Adragna⁷⁵, T. Adye¹²⁹, S. Aefsky²², J.A. Aguilar-Saavedra^{124b,a}, M. Aharrouche⁸¹, S.P. Ahlen²¹, F. Ahles⁴⁸, A. Ahmad¹⁴⁸, M. Ahsan⁴⁰, G. Aielli^{133a,133b}, T. Akdogan^{18a}, T.P.A. Åkesson⁷⁹, G. Akimoto¹⁵⁵, A.V. Akimov⁹⁴, A. Akiyama⁶⁷, M.S. Alam¹, M.A. Alam⁷⁶, J. Albert¹⁶⁹, S. Albrand⁵⁵, M. Aleksa²⁹, I.N. Aleksandrov⁶⁵, F. Alessandria^{89a}, C. Alexa^{25a}, G. Alexander¹⁵³, G. Alexandre⁴⁹, T. Alexopoulos⁹, M. Alhroob²⁰, M. Aliev¹⁵, G. Alimonti^{89a}, J. Alison¹²⁰, M. Aliyev¹⁰, P.P. Allport⁷³, S.E. Allwood-Spiers⁵³, J. Almond⁸², A. Aloisio^{102a,102b}, R. Alon¹⁷¹, A. Alonso⁷⁹, M.G. Alvigi^{102a,102b}, K. Amako⁶⁶, P. Amaral²⁹, C. Amelung²², V.V. Ammosov¹²⁸, A. Amorim^{124a,b}, G. Amorós¹⁶⁷, N. Amram¹⁵³, C. Anastopoulos²⁹, L.S. Ancu¹⁶, N. Andari¹¹⁵, T. Andeen³⁴, C.F. Anders²⁰, G. Anders^{58a}, K.J. Anderson³⁰, A. Andreazza^{89a,89b}, V. Andrei^{58a}, M-L. Andrieux⁵⁵, X.S. Anduaga⁷⁰, A. Angerami³⁴, F. Anghinolfi²⁹, N. Anjos^{124a}, A. Annovi⁴⁷, A. Antonaki⁸, M. Antonelli⁴⁷, A. Antonov⁹⁶, J. Antos^{144b}, F. Anulli^{132a}, S. Aoun⁸³, L. Aperio Bella⁴, R. Apolle^{118,c}, G. Arabidze⁸⁸, I. Aracena¹⁴³, Y. Arai⁶⁶, A.T.H. Arce⁴⁴, J.P. Archambault²⁸, S. Arfaoui^{29,d}, J-F. Arguin¹⁴, E. Arik^{18a,*}, M. Arik^{18a}, A.J. Armbruster⁸⁷, O. Arnaez⁸¹, C. Arnault¹¹⁵, A. Artamonov⁹⁵, G. Artoni^{132a,132b}, D. Arutinov²⁰, S. Asai¹⁵⁵, R. Asfandiyarov¹⁷², S. Ask²⁷, B. Åsman^{146a,146b}, L. Asquith⁵, K. Assamagan²⁴, A. Astbury¹⁶⁹, A. Astvatsaturov⁵², G. Atoian¹⁷⁵, B. Aubert⁴, E. Auge¹¹⁵, K. Augsten¹²⁷, M. Auresseau^{145a}, N. Austin⁷³, G. Avolio¹⁶³, R. Avramidou⁹, D. Axen¹⁶⁸, C. Ay⁵⁴, G. Azuelos^{93,e}, Y. Azuma¹⁵⁵, M.A. Baak²⁹, G. Baccaglioni^{89a}, C. Bacci^{134a,134b}, A.M. Bach¹⁴, H. Bachacou¹³⁶, K. Bachas²⁹, G. Bachy²⁹, M. Backes⁴⁹, M. Backhaus²⁰, E. Badescu^{25a}, P. Bagnaia^{132a,132b}, S. Bahinipati², Y. Bai^{32a}, D.C. Bailey¹⁵⁸, T. Bain¹⁵⁸, J.T. Baines¹²⁹, O.K. Baker¹⁷⁵, M.D. Baker²⁴, S. Baker⁷⁷, E. Banas³⁸, P. Banerjee⁹³, Sw. Banerjee¹⁷², D. Banfi²⁹, A. Bangert¹³⁷, V. Bansal¹⁶⁹, H.S. Bansil¹⁷, L. Barak¹⁷¹, S.P. Baranov⁹⁴, A. Barashkou⁶⁵, A. Barbaro Galtieri¹⁴, T. Barber⁴⁸, E.L. Barberio⁸⁶, D. Barberis^{50a,50b}, M. Barbero²⁰, D.Y. Bardin⁶⁵, T. Barillari⁹⁹, M. Barisonzi¹⁷⁴, T. Barklow¹⁴³, N. Barlow²⁷, B.M. Barnett¹²⁹, R.M. Barnett¹⁴, A. Baroncelli^{134a}, G. Barone⁴⁹, A.J. Barr¹¹⁸, F. Barreiro⁸⁰, J. Barreiro Guimarães da Costa⁵⁷, P. Barrillon¹¹⁵, R. Bartoldus¹⁴³, A.E. Barton⁷¹, D. Bartsch²⁰, V. Bartsch¹⁴⁹, R.L. Bates⁵³, L. Batkova^{144a}, J.R. Batley²⁷, A. Battaglia¹⁶, M. Battistin²⁹, G. Battistoni^{89a}, F. Bauer¹³⁶, H.S. Bawa^{143,f}, B. Beare¹⁵⁸, T. Beau⁷⁸, P.H. Beauchemin¹¹⁸, R. Beccherle^{50a}, P. Bechtel⁴¹, H.P. Beck¹⁶, M. Beckingham¹³⁸, K.H. Becks¹⁷⁴, A.J. Beddall^{18c}, A. Beddall^{18c}, S. Bedikian¹⁷⁵, V.A. Bednyakov⁶⁵, C.P. Bee⁸³, M. Begel²⁴, S. Behar Harpaz¹⁵², P.K. Behera⁶³, M. Beimforde⁹⁹, C. Belanger-Champagne⁸⁵, P.J. Bell⁴⁹, W.H. Bell⁴⁹, G. Bella¹⁵³, L. Bellagamba^{19a}, F. Bellina²⁹, M. Bellomo²⁹, A. Belloni⁵⁷, O. Beloborodova¹⁰⁷, K. Belotskiy⁹⁶, O. Beltramello²⁹, S. Ben Ami¹⁵², O. Benary¹⁵³, D. Benchekroun^{135a}, C. Benchouk⁸³, M. Bendel⁸¹, N. Benekos¹⁶⁵, Y. Benhammou¹⁵³, D.P. Benjamin⁴¹, M. Benoit¹¹⁵, J.R. Bensinger²², K. Benslama¹³⁰, S. Bentvelsen¹⁰⁵, D. Berge²⁹, E. Bergeas Kuutmann⁴¹, N. Berger⁴, F. Berghaus¹⁶⁹, E. Berglund⁴⁹, J. Beringer¹⁴, K. Bernadet⁸³, P. Bernat⁷⁷, R. Bernhard⁴⁸, C. Bernius²⁴, T. Berry⁷⁶, A. Bertin^{19a,19b}, F. Bertinelli²⁹, F. Bertolucci^{122a,122b}, M.I. Besana^{89a,89b}, N. Besson¹³⁶, S. Bethke⁹⁹, W. Bhimji⁴⁵, R.M. Bianchi²⁹, M. Bianco^{72a,72b}, O. Biebel⁹⁸, S.P. Bienenk⁷⁷, K. Bierwagen⁵⁴, J. Biesiada¹⁴, M. Biglietti^{134a,134b}, H. Bilokon⁴⁷, M. Bind^{19a,19b}, S. Binet¹¹⁵, A. Bingul^{18c}, C. Bini^{132a,132b}, C. Biscarat¹⁷⁷, U. Bitenc⁴⁸, K.M. Black²¹, R.E. Blair⁵, J.-B. Blanchard^{115,g}, G. Blanchot²⁹, T. Blazek^{144a}, C. Blocker²², J. Blocki³⁸, A. Blondel⁴⁹, W. Blum⁸¹, U. Blumenschein⁵⁴, G.J. Bobbink¹⁰⁵, V.B. Bobrovnikov¹⁰⁷, S.S. Bocchetta⁷⁹, A. Bocci⁴⁴, C.R. Boddy¹¹⁸, M. Boehler⁴¹, J. Boek¹⁷⁴, N. Boelaert³⁵, S. Böser⁷⁷, J.A. Bogaerts²⁹, A. Bogdanchikov¹⁰⁷, A. Bogouch^{90,*}, C. Bohm^{146a}, V. Boisvert⁷⁶, T. Bold³⁷, V. Boldea^{25a}, N.M. Bolnet¹³⁶, M. Bona⁷⁵, V.G. Bondarenko⁹⁶, M. Bondioli¹⁶³, M. Boonekamp¹³⁶, G. Boorman⁷⁶, C.N. Booth¹³⁹, S. Bordini⁷⁸, C. Borer¹⁶, A. Borisov¹²⁸, G. Borissov⁷¹, I. Borjanovic^{12a}, S. Borroni⁸⁷, K. Bos¹⁰⁵, D. Boscherini^{19a}, M. Bosman¹¹, H. Boterenbrood¹⁰⁵, D. Botterill¹²⁹, J. Bouchami⁹³, J. Boudreau¹²³, E.V. Bouhova-Thacker⁷¹, C. Bourdarios¹¹⁵, N. Bousson⁸³, A. Boveia³⁰, J. Boyd²⁹, I.R. Boyko⁶⁵, N.I. Bozhko¹²⁸, I. Bozovic-Jelisavcic^{12b}, J. Bracinik¹⁷, A. Braem²⁹, P. Branchini^{134a}, G.W. Brandenburg⁵⁷, A. Brandt⁷, G. Brandt¹⁵, O. Brandt⁵⁴, U. Bratzler¹⁵⁶, B. Brau⁸⁴, J.E. Brau¹¹⁴, H.M. Braun¹⁷⁴, B. Brelrier¹⁵⁸, J. Bremer²⁹, R. Brenner¹⁶⁶, S. Bressler¹⁷¹, D. Breton¹¹⁵, D. Britton⁵³, F.M. Brochu²⁷, I. Brock²⁰, R. Brock⁸⁸, T.J. Brodbeck⁷¹, E. Brodet¹⁵³, F. Broggi^{89a}, C. Bromberg⁸⁸, G. Brooijmans³⁴, W.K. Brooks^{31b}, G. Brown⁸², H. Brown⁷, P.A. Bruckman de Renstrom³⁸, D. Bruncko^{144b}, R. Bruneliere⁴⁸, S. Brunet⁶¹, A. Bruni^{19a}, G. Bruni^{19a}, M. Bruschi^{19a}, T. Buanes¹³, F. Bucci⁴⁹, J. Buchanan¹¹⁸, N.J. Buchanan², P. Buchholz¹⁴¹, R.M. Buckingham¹¹⁸, A.G. Buckley⁴⁵, S.I. Buda^{25a}, I.A. Budagov⁶⁵, B. Budick¹⁰⁸, V. Büscher⁸¹, L. Bugge¹¹⁷, D. Buira-Clark¹¹⁸, O. Bulekov⁹⁶, M. Bunse⁴², T. Buran¹¹⁷, H. Burckhart²⁹, S. Burdin⁷³, T. Burgess¹³, S. Burke¹²⁹, E. Busato³³, P. Bussey⁵³, C.P. Buszello¹⁶⁶, F. Butin²⁹, B. Butler¹⁴³, J.M. Butler²¹, C.M. Buttar⁵³, J.M. Butterworth⁷⁷, W. Buttinger²⁷, S. Cabrera Urbán¹⁶⁷, D. Caforio^{19a,19b}, O. Cakir^{3a}, P. Calafiura¹⁴, G. Calderini⁷⁸, P. Calfayan⁹⁸, R. Calkins¹⁰⁶, L.P. Caloba^{23a}, R. Caloi^{132a,132b}, D. Calvet³³, S. Calvet³³, R. Camacho Toro³³, P. Camarri^{133a,133b}, M. Cambiaghi^{119a,119b}, D. Cameron¹¹⁷, S. Campana²⁹, M. Campanelli⁷⁷, V. Canale^{102a,102b}, F. Canelli^{30,h}, A. Canepa^{159a}, J. Cantero⁸⁰, L. Capasso^{102a,102b}, M.D.M. Capeans Garrido²⁹, I. Caprini^{25a}, M. Caprini^{25a}, D. Capriotti^{99,g}, M. Capua^{36a,36b}, R. Caputo¹⁴⁸, R. Cardarelli^{133a}, T. Carli²⁹, G. Carlino^{102a}, L. Carminati^{89a,89b}, B. Caron^{159a}, S. Caron⁴⁸, G.D. Carrillo Montoya¹⁷², A.A. Carter⁷⁵, J.R. Carter²⁷, J. Carvalho^{124a,i}, D. Casadei¹⁰⁸, M.P. Casado¹¹, M. Cascella^{122a,122b}, C. Caso^{50a,50b,*}, A.M. Castaneda Hernandez¹⁷², E. Castaneda-Miranda¹⁷², V. Castillo Gimenez¹⁶⁷, N.F. Castro^{124a}, G. Cataldi^{72a}, F. Cataneo²⁹, A. Catinaccio²⁹, J.R. Catmore⁷¹, A. Cattai²⁹, G. Cattani^{133a,133b}, S. Caughron⁸⁸, D. Cauz^{164a,164c}, P. Cavalleri⁷⁸, D. Cavalli^{89a}, M. Cavalli-Sforza¹¹, V. Cavasinni^{122a,122b}, F. Ceradini^{134a,134b}, A.S. Cerqueira^{23a}, A. Cerri²⁹, L. Cerrito⁷⁵, F. Cerutti⁴⁷, S.A. Cetin^{18b}, F. Cevenini^{102a,102b}, A. Chafaq^{135a}, D. Chakraborty¹⁰⁶, K. Chan², B. Chapleau⁸⁵, J.D. Chapman²⁷, J.W. Chapman⁸⁷, E. Chareyre⁷⁸, D.G. Charlton¹⁷, V. Chavda⁸², C.A. Chavez Barajas²⁹, S. Cheatham⁸⁵,

S. Chekanov⁵, S.V. Chekulaev^{159a}, G.A. Chelkov⁶⁵, M.A. Chelstowska¹⁰⁴, C. Chen⁶⁴, H. Chen²⁴, S. Chen^{32c}, T. Chen^{32c}, X. Chen¹⁷², S. Cheng^{32a}, A. Cheplakov⁶⁵, V.F. Chepurinov⁶⁵, R. Cherkaoui El Moursli^{135e}, V. Chernyatin²⁴, E. Cheu⁶, S.L. Cheung¹⁵⁸, L. Chevalier¹³⁶, G. Chiefari^{102a,102b}, L. Chikovani^{51a}, J.T. Childers^{58a}, A. Chilingarov⁷¹, G. Chiodini^{72a}, M.V. Chizhov⁶⁵, G. Choudalakis³⁰, S. Chouridou¹³⁷, I.A. Christidi⁷⁷, A. Christov⁴⁸, D. Chromek-Burckhart²⁹, M.L. Chu¹⁵¹, J. Chudoba¹²⁵, G. Ciapetti^{132a,132b}, K. Ciba³⁷, A.K. Ciftci^{3a}, R. Ciftci^{3a}, D. Cinca³³, V. Cindro⁷⁴, M.D. Ciobotaru¹⁶³, C. Ciocca^{19a}, A. Cicio¹⁴, M. Cirilli⁸⁷, M. Ciubancan^{25a}, A. Clark⁴⁹, P.J. Clark⁴⁵, W. Cleland¹²³, J.C. Clemens⁸³, B. Clement⁵⁵, C. Clement^{146a,146b}, R.W. Clift¹²⁹, Y. Coadou⁸³, M. Cobal^{164a,164c}, A. Coccaro^{50a,50b}, J. Cochran⁶⁴, P. Coe¹¹⁸, J.G. Cogan¹⁴³, J. Coggeshall¹⁶⁵, E. Cogneras¹⁷⁷, C.D. Cojocaru²⁸, J. Colas⁴, A.P. Colijn¹⁰⁵, C. Collard¹¹⁵, N.J. Collins¹⁷, C. Collins-Tooth⁵³, J. Collot⁵⁵, G. Colon⁸⁴, P. Conde Muno^{124a}, E. Coniavitis¹¹⁸, M.C. Conidi¹¹, M. Consonni¹⁰⁴, V. Consorti¹⁴⁸, S. Constantinescu^{25a}, C. Conta^{119a,119b}, F. Conventi^{102a,j}, J. Cook²⁹, M. Cooke¹⁴, B.D. Cooper⁷⁷, A.M. Cooper-Sarkar¹¹⁸, K. Copic³⁴, T. Cornelissen¹⁷⁴, M. Corradi^{19a}, F. Corriveau^{85,k}, A. Cortes-Gonzalez¹⁶⁵, G. Cortiana⁹⁹, G. Costa^{89a}, M.J. Costa¹⁶⁷, D. Costanzo¹³⁹, T. Costin³⁰, D. Cte²⁹, L. Courneyea¹⁶⁹, G. Cowan⁷⁶, C. Cowden²⁷, B.E. Cox⁸², K. Cranmer¹⁰⁸, F. Crescioli^{122a,122b}, M. Cristinziani²⁰, G. Crosetti^{36a,36b}, R. Crupi^{72a,72b}, S. Crp-Renaudin⁵⁵, C.-M. Cuciuc^{25a}, C. Cuenca Almenar¹⁷⁵, T. Cuhadar Donszelmann¹³⁹, M. Curatolo⁴⁷, C.J. Curtis¹⁷, P. Cwetanski⁶¹, H. Czirr¹⁴¹, Z. Czyzula¹⁷⁵, S. D'Auria⁵³, M. D'Onofrio⁷³, A. D'Orazio^{132a,132b}, P.V.M. Da Silva^{23a}, C. Da Via⁸², W. Dabrowski³⁷, T. Dai⁸⁷, C. Dallapiccola⁸⁴, M. Dam³⁵, M. Dameri^{50a,50b}, D.S. Damiani¹³⁷, H.O. Danielsson²⁹, D. Dannheim⁹⁹, V. Dao⁴⁹, G. Darbo^{50a}, G.L. Darlea^{25b}, C. Daum¹⁰⁵, J.P. Dauvergne²⁹, W. Davey²⁰, T. Davidek¹²⁶, N. Davidson⁸⁶, R. Davidson⁷¹, E. Davies^{118,c}, M. Davies⁹³, A.R. Davison⁷⁷, Y. Davygora^{58a}, E. Dawe¹⁴², I. Dawson¹³⁹, J.W. Dawson^{5,*}, R.K. Daya³⁹, K. De⁷, R. de Asmundis^{102a}, S. De Castro^{19a,19b}, P.E. De Castro Faria Salgado²⁴, S. De Cecco⁷⁸, J. de Graat⁹⁸, N. De Groot¹⁰⁴, P. de Jong¹⁰⁵, C. De La Taille¹¹⁵, H. De la Torre⁸⁰, B. De Lotto^{164a,164c}, L. de Mora⁷¹, L. De Nooij¹⁰⁵, D. De Pedis^{132a}, A. De Salvo^{132a}, U. De Sanctis^{164a,164c}, A. De Santo¹⁴⁹, J.B. De Vivie De Regie¹¹⁵, S. Dean⁷⁷, R. Debbe²⁴, D.V. Dedovich⁶⁵, J. Degenhardt¹²⁰, M. Dehchar¹¹⁸, C. Del Papa^{164a,164c}, J. Del Peso⁸⁰, T. Del Prete^{122a,122b}, M. Deliyergiyev⁷⁴, A. Dell'Acqua²⁹, L. Dell'Asta^{89a,89b}, M. Della Pietra^{102a,j}, D. della Volpe^{102a,102b}, M. Delmastro²⁹, P. Delpierre⁸³, N. Delruelle²⁹, P.A. Delsart⁵⁵, C. Deluca¹⁴⁸, S. Demers¹⁷⁵, M. Demichev⁶⁵, B. Demirkoz^{11,l}, J. Deng¹⁶³, S.P. Denisov¹²⁸, D. Derendarz³⁸, J.E. Derkaoui^{135d}, F. Derue⁷⁸, P. Dervan⁷³, K. Desch²⁰, E. Devetak¹⁴⁸, P.O. Deviveiros¹⁵⁸, A. Dewhurst¹²⁹, B. DeWilde¹⁴⁸, S. Dhaliwal¹⁵⁸, R. Dhullipudi^{24,m}, A. Di Ciaccio^{133a,133b}, L. Di Ciaccio⁴, A. Di Girolamo²⁹, B. Di Girolamo²⁹, S. Di Luise^{134a,134b}, A. Di Mattia¹⁷², B. Di Micco²⁹, R. Di Nardo^{133a,133b}, A. Di Simone^{133a,133b}, R. Di Sipio^{19a,19b}, M.A. Diaz^{31a}, F. Diben^{18c}, E.B. Diehl⁸⁷, J. Dietrich⁴¹, T.A. Dietzsch^{58a}, S. Diglio¹¹⁵, K. Dindar Yagci³⁹, J. Dingfelder²⁰, C. Dionisi^{132a,132b}, P. Dita^{25a}, S. Dita^{25a}, F. Dittus²⁹, F. Djama⁸³, T. Djobava^{51b}, M.A.B. do Vale^{23c}, A. Do Valle Wemans^{124a}, T.K.O. Doan⁴, M. Dobbs⁸⁵, R. Dobinson^{29,*}, D. Dobos²⁹, E. Dobson²⁹, M. Dobson¹⁶³, J. Dodd³⁴, C. Doglioni¹¹⁸, T. Doherty⁵³, Y. Doi^{66,*}, J. Dolejsi¹²⁶, I. Dolenc⁷⁴, Z. Dolezal¹²⁶, B.A. Dolgoshein^{96,*}, T. Dohmae¹⁵⁵, M. Donadelli^{23d}, M. Donega¹²⁰, J. Donini⁵⁵, J. Dopke²⁹, A. Doria^{102a}, A. Dos Anjos¹⁷², M. Dosil¹¹, A. Dotti^{122a,122b}, M.T. Dova⁷⁰, J.D. Dowell¹⁷, A.D. Doxiadis¹⁰⁵, A.T. Doyle⁵³, Z. Drasal¹²⁶, J. Drees¹⁷⁴, N. Dressnandt¹²⁰, H. Drevermann²⁹, C. Driouchi³⁵, M. Dris⁹, J. Dubbert⁹⁹, T. Dubbs¹³⁷, S. Dube¹⁴, E. Duchovni¹⁷¹, G. Duckeck⁹⁸, A. Dudarev²⁹, F. Dudziak⁶⁴, M. Dhrssen²⁹, I.P. Duerdoth⁸², L. Duflot¹¹⁵, M.-A. Dufour⁸⁵, M. Dunford²⁹, H. Duran Yildiz^{3b}, R. Duxfield¹³⁹, M. Dwuznik³⁷, F. Dydak²⁹, M. Dren⁵², W.L. Ebenstein⁴⁴, J. Ebke⁹⁸, S. Eckert⁴⁸, S. Eckweiler⁸¹, K. Edmonds⁸¹, C.A. Edwards⁷⁶, N.C. Edwards⁵³, W. Ehrenfeld⁴¹, T. Ehrich⁹⁹, T. Eifert²⁹, G. Eigen¹³, K. Einsweiler¹⁴, E. Eisenhandler⁷⁵, T. Ekelof¹⁶⁶, M. El Kacimi^{135c}, M. Ellert¹⁶⁶, S. Elles⁴, F. Ellinghaus⁸¹, K. Ellis⁷⁵, N. Ellis²⁹, J. Elmsheuser⁹⁸, M. Elsing²⁹, D. Emeliyanov¹²⁹, R. Engelmann¹⁴⁸, A. Engl⁹⁸, B. Epp⁶², A. Eppig⁸⁷, J. Erdmann⁵⁴, A. Ereditato¹⁶, D. Eriksson^{146a}, J. Ernst¹, M. Ernst²⁴, J. Ernwein¹³⁶, D. Errede¹⁶⁵, S. Errede¹⁶⁵, E. Ertel⁸¹, M. Escalier¹¹⁵, C. Escobar¹²³, X. Espinal Curull¹¹, B. Esposito⁴⁷, F. Etienne⁸³, A.I. Etiennevire¹³⁶, E. Etzion¹⁵³, D. Evangelakou⁵⁴, H. Evans⁶¹, L. Fabbri^{19a,19b}, C. Fabre²⁹, R.M. Fakhruddinov¹²⁸, S. Falciano^{132a}, Y. Fang¹⁷², M. Fanti^{89a,89b}, A. Farbin⁷, A. Farilla^{134a}, J. Farley¹⁴⁸, T. Farooque¹⁵⁸, S.M. Farrington¹¹⁸, P. Farthouat²⁹, P. Fassnacht²⁹, D. Fassouliotis⁸, B. Fathollahzadeh¹⁵⁸, A. Favareto^{89a,89b}, L. Fayard¹¹⁵, S. Fazio^{36a,36b}, R. Febbraro³³, P. Federic^{144a}, O.L. Fedin¹²¹, W. Fedorko⁸⁸, M. Fehling-Kaschek⁴⁸, L. Feligioni⁸³, C.U. Felzmann⁸⁶, C. Feng^{32d}, E.J. Feng³⁰, A.B. Fenyuk¹²⁸, J. Ferencei^{144b}, J. Ferland⁹³, W. Fernando¹⁰⁹, S. Ferrag⁵³, J. Ferrando⁵³, V. Ferrara⁴¹, A. Ferrari¹⁶⁶, P. Ferrari¹⁰⁵, R. Ferrari^{119a}, A. Ferrer¹⁶⁷, M.L. Ferrer⁴⁷, D. Ferrere⁴⁹, C. Ferretti⁸⁷, A. Ferretto Parodi^{50a,50b}, M. Fiascaris³⁰, F. Fiedler⁸¹, A. Filipi⁷⁴, A. Filippas⁹, F. Filthaut¹⁰⁴, M. Fincke-Keeler¹⁶⁹, M.C.N. Fiolhais^{124a,i}, L. Fiorini¹⁶⁷, A. Firani³⁹, G. Fischer⁴¹, P. Fischer²⁰, M.J. Fisher¹⁰⁹, S.M. Fisher¹²⁹, M. Flechl¹⁴⁸, I. Fleck¹⁴¹, J. Fleckner⁸¹, P. Fleischmann¹⁷³, S. Fleischmann¹⁷⁴, T. Flick¹⁷⁴, L.R. Flores Castillo¹⁷², M.J. Flowerdew⁹⁹, M. Fokitis⁹, T. Fonseca Martin¹⁶, D.A. Forbush¹³⁸, A. Formica¹³⁶, A. Forti⁸², D. Fortin^{159a}, J.M. Foster⁸², D. Fournier¹¹⁵, A. Foussat²⁹, A.J. Fowler⁴⁴, K. Fowler¹³⁷, H. Fox⁷¹, P. Francavilla^{122a,122b}, S. Franchino^{119a,119b}, D. Francis²⁹, T. Frank¹⁷¹, M. Franklin⁵⁷, S. Franz²⁹, M. Fraternali^{119a,119b}, S. Fratina¹²⁰, S.T. French²⁷, F. Friedrich⁴³, R. Froeschl²⁹, D. Froidevaux²⁹, J.A. Frost²⁷, C. Fukunaga¹⁵⁶, E. Fullana Torregrosa²⁹, J. Fuster¹⁶⁷, C. Gabaldon²⁹, O. Gabizon¹⁷¹, T. Gadfort²⁴, S. Gadomski⁴⁹, G. Gagliardi^{50a,50b}, P. Gagnon⁶¹, C. Galea⁹⁸, E.J. Gallas¹¹⁸, V. Gallo¹⁶, B.J. Gallop¹²⁹, P. Gallus¹²⁵, E. Galyaev⁴⁰, K.K. Gan¹⁰⁹, Y.S. Gao^{143,f}, V.A. Gapienko¹²⁸, A. Gaponenko¹⁴, F. Garbersson¹⁷⁵, M. Garcia-Sciveres¹⁴, C. Garca¹⁶⁷, J.E. Garca Navarro⁴⁹, R.W. Gardner³⁰, N. Garelli²⁹, H. Garitaonandia¹⁰⁵, V. Garonne²⁹, J. Garvey¹⁷, C. Gatti⁴⁷, G. Gaudio^{119a}, O. Gaume⁴⁹, B. Gaur¹⁴¹, L. Gauthier¹³⁶, I.L. Gavrilenko⁹⁴, C. Gay¹⁶⁸, G. Gaycken²⁰, J.-C. Gayde²⁹, E.N. Gazis⁹, P. Ge^{32d}, C.N.P. Gee¹²⁹, D.A.A. Geerts¹⁰⁵, Ch. Geich-Gimbel²⁰, K. Gellerstedt^{146a,146b}, C. Gemme^{50a}, A. Gemmell⁵³, M.H. Genest⁹⁸, S. Gentile^{132a,132b}, M. George⁵⁴, S. George⁷⁶, P. Gerlach¹⁷⁴, A. Gershon¹⁵³, C. Geweniger^{58a}, H. Ghazlane^{135b}, N. Ghodbane³³, B. Giacobbe^{19a}, S. Giagu^{132a,132b},

V. Giakoumopoulou⁸, V. Giangiobbe^{122a,122b}, F. Gianotti²⁹, B. Gibbard²⁴, A. Gibson¹⁵⁸, S.M. Gibson²⁹, L.M. Gilbert¹¹⁸, V. Gilevsky⁹¹, D. Gillberg²⁸, A.R. Gillman¹²⁹, D.M. Gingrich^{2,e}, J. Ginzburg¹⁵³, N. Giokaris⁸, M.P. Giordani^{164c}, R. Giordano^{102a,102b}, F.M. Giorgi¹⁵, P. Giovannini⁹⁹, P.F. Giraud¹³⁶, D. Giugni^{89a}, M. Giunta⁹³, P. Giusti^{19a}, B.K. Gjelsten¹¹⁷, L.K. Gladilin⁹⁷, C. Glasman⁸⁰, J. Glatzer⁴⁸, A. Glazov⁴¹, K.W. Glitza¹⁷⁴, G.L. Glonti⁶⁵, J. Godfrey¹⁴², J. Godlewski²⁹, M. Goebel⁴¹, T. Göpfert⁴³, C. Goeringer⁸¹, C. Gössling⁴², T. Göttfert⁹⁹, S. Goldfarb⁸⁷, T. Golling¹⁷⁵, S.N. Golovina¹²⁸, A. Gomes^{124a,b}, L.S. Gomez Fajardo⁴¹, R. Gonçalves⁷⁶, J. Goncalves Pinto Firmino Da Costa⁴¹, L. Gonella²⁰, A. Gonidec²⁹, S. Gonzalez¹⁷², S. González de la Hoz¹⁶⁷, M.L. Gonzalez Silva²⁶, S. Gonzalez-Sevilla⁴⁹, J.J. Goodson¹⁴⁸, L. Goossens²⁹, P.A. Gorbounov⁹⁵, H.A. Gordon²⁴, I. Gorelov¹⁰³, G. Gorfine¹⁷⁴, B. Gorini²⁹, E. Gorini^{72a,72b}, A. Gorišek⁷⁴, E. Gornicki³⁸, S.A. Gorokhov¹²⁸, V.N. Goryachev¹²⁸, B. Gosdzik⁴¹, M. Gosselink¹⁰⁵, M.I. Gostkin⁶⁵, I. Gough Eschrich¹⁶³, M. Gouighri^{135a}, D. Goujdami^{135c}, M.P. Goulette⁴⁹, A.G. Goussiou¹³⁸, C. Goy⁴, I. Grabowska-Bold^{163,n}, P. Grafström²⁹, C. Grah¹⁷⁴, K.-J. Grahn⁴¹, F. Grancagnolo^{72a}, S. Grancagnolo¹⁵, V. Grassi¹⁴⁸, V. Gratchev¹²¹, N. Grau³⁴, H.M. Gray²⁹, J.A. Gray¹⁴⁸, E. Graziani^{134a}, O.G. Grebenyuk¹²¹, D. Greenfield¹²⁹, T. Greenshaw⁷³, Z.D. Greenwood^{24,m}, K. Gregersen³⁵, I.M. Gregor⁴¹, P. Grenier¹⁴³, J. Griffiths¹³⁸, N. Grigalashvili⁶⁵, A.A. Grillo¹³⁷, S. Grinstein¹¹, Y.V. Grishkevich⁹⁷, J.-F. Grivaz¹¹⁵, M. Groh⁹⁹, E. Gross¹⁷¹, J. Grosse-Knetter⁵⁴, J. Groth-Jensen¹⁷¹, K. Grybel¹⁴¹, V.J. Guarino⁵, D. Guest¹⁷⁵, C. Guicheney³³, A. Guida^{72a,72b}, S. Guindon⁵⁴, H. Guler^{85,o}, J. Gunther¹²⁵, B. Guo¹⁵⁸, J. Guo³⁴, A. Gupta³⁰, Y. Gusakov⁶⁵, V.N. Gushchin¹²⁸, A. Gutierrez⁹³, P. Gutierrez¹¹¹, N. Guttman¹⁵³, O. Gutzwiller¹⁷², C. Guyot¹³⁶, C. Gwenlan¹¹⁸, C.B. Gwilliam⁷³, A. Haas¹⁴³, S. Haas²⁹, C. Haber¹⁴, R. Hackenburg²⁴, H.K. Hadavand³⁹, D.R. Hadley¹⁷, P. Haefner⁹⁹, F. Hahn²⁹, S. Haider²⁹, Z. Hajduk³⁸, H. Hakobyan¹⁷⁶, J. Haller⁵⁴, K. Hamacher¹⁷⁴, P. Hamal¹¹³, A. Hamilton⁴⁹, S. Hamilton¹⁶¹, H. Han^{32a}, L. Han^{32b}, K. Hanagaki¹¹⁶, M. Hance¹⁴, C. Handel⁸¹, P. Hanke^{58a}, J.R. Hansen³⁵, J.B. Hansen³⁵, J.D. Hansen³⁵, P.H. Hansen³⁵, P. Hansson¹⁴³, K. Hara¹⁶⁰, G.A. Hare¹³⁷, T. Harenberg¹⁷⁴, S. Harkusha⁹⁰, D. Harper⁸⁷, R.D. Harrington⁴⁵, O.M. Harris¹³⁸, K. Harrison¹⁷, J. Hartert⁴⁸, F. Hartjes¹⁰⁵, T. Haruyama⁶⁶, A. Harvey⁵⁶, S. Hasegawa¹⁰¹, Y. Hasegawa¹⁴⁰, S. Hassani¹³⁶, M. Hatch²⁹, D. Hauff⁹⁹, S. Haug¹⁶, M. Hauschild²⁹, R. Hauser⁸⁸, M. Havranek²⁰, B.M. Hawes¹¹⁸, C.M. Hawkes¹⁷, R.J. Hawking²⁹, D. Hawkins¹⁶³, T. Hayakawa⁶⁷, T. Hayashi¹⁶⁰, D. Hayden⁷⁶, H.S. Hayward⁷³, S.J. Haywood¹²⁹, E. Hazen²¹, M. He^{32d}, S.J. Head¹⁷, V. Hedberg⁷⁹, L. Heelan⁷, S. Heim⁸⁸, B. Heinemann¹⁴, S. Heisterkamp³⁵, L. Helary⁴, M. Heller²⁹, S. Hellman^{146a,146b}, D. Hellmich²⁰, C. Helsen¹¹, R.C.W. Henderson⁷¹, M. Henke^{58a}, A. Henrichs⁵⁴, A.M. Henriques Correia²⁹, S. Henrot-Versille¹¹⁵, F. Henry-Couannier⁸³, C. Hensel⁵⁴, T. Henß¹⁷⁴, C.M. Hernandez⁷, Y. Hernández Jiménez¹⁶⁷, R. Herrberg¹⁵, A.D. Hershenhorn¹⁵², G. Herten⁴⁸, R. Hertenberger⁹⁸, L. Hervas²⁹, N.P. Hessey¹⁰⁵, A. Hidvegi^{146a}, E. Higón-Rodríguez¹⁶⁷, D. Hill^{5,*}, J.C. Hill²⁷, N. Hill⁵, K.H. Hiller⁴¹, S. Hillert²⁰, S.J. Hillier¹⁷, I. Hinchliffe¹⁴, E. Hines¹²⁰, M. Hirose¹¹⁶, F. Hirsch⁴², D. Hirschbuehl¹⁷⁴, J. Hobbs¹⁴⁸, N. Hod¹⁵³, M.C. Hodgkinson¹³⁹, P. Hodgson¹³⁹, A. Hoecker²⁹, M.R. Hoferkamp¹⁰³, J. Hoffman³⁹, D. Hoffmann⁸³, M. Hohlfield⁸¹, M. Holder¹⁴¹, S.O. Holmgren^{146a}, T. Holy¹²⁷, J.L. Holzbauer⁸⁸, Y. Homma⁶⁷, T.M. Hong¹²⁰, L. Hooft van Huysduynen¹⁰⁸, T. Horazdovsky¹²⁷, C. Horn¹⁴³, S. Horner⁴⁸, K. Horton¹¹⁸, J.-Y. Hostachy⁵⁵, S. Hou¹⁵¹, M.A. Houlden⁷³, A. Hoummada^{135a}, J. Howarth⁸², D.F. Howell¹¹⁸, I. Hristova¹⁵, J. Hrivnac¹¹⁵, I. Hruska¹²⁵, T. Hryn'ova⁴, P.J. Hsu¹⁷⁵, S.-C. Hsu¹⁴, G.S. Huang¹¹¹, Z. Hubacek¹²⁷, F. Hubaut⁸³, F. Huegging²⁰, T.B. Huffman¹¹⁸, E.W. Hughes³⁴, G. Hughes⁷¹, R.E. Hughes-Jones⁸², M. Huhtinen²⁹, P. Hurst⁵⁷, M. Hurwitz¹⁴, U. Husemann⁴¹, N. Huseynov^{65,p}, J. Huston⁸⁸, J. Huth⁵⁷, G. Iacobucci⁴⁹, G. Iakovidis⁹, M. Ibbotson⁸², I. Ibragimov¹⁴¹, R. Ichimiya⁶⁷, L. Iconomidou-Fayard¹¹⁵, J. Idarraga¹¹⁵, P. Iengo^{102a,102b}, O. Igonkina¹⁰⁵, Y. Ikegami⁶⁶, M. Ikeno⁶⁶, Y. Ilchenko³⁹, D. Iliadis¹⁵⁴, D. Imbault⁷⁸, M. Imori¹⁵⁵, T. Ince²⁰, J. Inigo-Golfín²⁹, P. Ioannou⁸, M. Iodice^{134a}, A. Irls Quiles¹⁶⁷, A. Ishikawa⁶⁷, M. Ishino⁶⁸, R. Ishmukhametov³⁹, C. Issever¹¹⁸, S. Istin^{18a}, A.V. Ivashin¹²⁸, W. Iwanski³⁸, H. Iwasaki⁶⁶, J.M. Izen⁴⁰, V. Izzo^{102a}, B. Jackson¹²⁰, J.N. Jackson⁷³, P. Jackson¹⁴³, M.R. Jaekel²⁹, V. Jain⁶¹, K. Jakobs⁴⁸, S. Jakobsen³⁵, J. Jakubek¹²⁷, D.K. Jana¹¹¹, E. Jankowski¹⁵⁸, E. Jansen⁷⁷, A. Jantsch⁹⁹, M. Janus²⁰, G. Jarlskog⁷⁹, L. Jeanty⁵⁷, K. Jelen³⁷, I. Jen-La Plante³⁰, P. Jenni²⁹, A. Jeremie⁴, P. Jež³⁵, S. Jézéquel⁴, M.K. Jha^{19a}, H. Ji¹⁷², W. Ji⁸¹, J. Jia¹⁴⁸, Y. Jiang^{32b}, M. Jimenez Belenguer⁴¹, G. Jin^{32b}, S. Jin^{32a}, O. Jinnouchi¹⁵⁷, M.D. Joergensen³⁵, D. Joffe³⁹, L.G. Johansen¹³, M. Johansen^{146a,146b}, K.E. Johansson^{146a}, P. Johansson¹³⁹, S. Johnert⁴¹, K.A. Johns⁶, K. Jon-And^{146a,146b}, G. Jones⁸², R.W.L. Jones⁷¹, T.W. Jones⁷⁷, T.J. Jones⁷³, O. Jonsson²⁹, C. Joram²⁹, P.M. Jorge^{124a}, J. Joseph¹⁴, T. Jovin^{12b}, X. Ju¹³⁰, C.A. Jung⁴², V. Juranek¹²⁵, P. Jussel⁶², A. Juste Rozas¹¹, V.V. Kabachenko¹²⁸, S. Kabana¹⁶, M. Kaci¹⁶⁷, A. Kaczmarska³⁸, P. Kadlecik³⁵, M. Kado¹¹⁵, H. Kagan¹⁰⁹, M. Kagan⁵⁷, S. Kaiser⁹⁹, E. Kajomovitz¹⁵², S. Kalinin¹⁷⁴, L.V. Kalinovskaya⁶⁵, S. Kama³⁹, N. Kanaya¹⁵⁵, M. Kaneda²⁹, T. Kanno¹⁵⁷, V.A. Kantserov⁹⁶, J. Kanzaki⁶⁶, B. Kaplan¹⁷⁵, A. Kapliy³⁰, J. Kaplon²⁹, D. Kar⁴³, M. Karagoz¹¹⁸, M. Karnevskiy⁴¹, K. Karr⁵, V. Kartvelishvili⁷¹, A.N. Karyukhin¹²⁸, L. Kashif¹⁷², A. Kasmi³⁹, R.D. Kass¹⁰⁹, A. Kastanas¹³, M. Kataoka⁴, Y. Kataoka¹⁵⁵, E. Katsoufis⁹, J. Katzy⁴¹, V. Kaushik⁶, K. Kawagoe⁶⁷, T. Kawamoto¹⁵⁵, G. Kawamura⁸¹, M.S. Kayl¹⁰⁵, V.A. Kazanin¹⁰⁷, M.Y. Kazarinov⁶⁵, J.R. Keates⁸², R. Keeler¹⁶⁹, R. Kehoe³⁹, M. Keil⁵⁴, G.D. Kekelidze⁶⁵, M. Kelly⁸², J. Kennedy⁹⁸, C.J. Kenney¹⁴³, M. Kenyon⁵³, O. Kepka¹²⁵, N. Kerschen²⁹, B.P. Kerševan⁷⁴, S. Kersten¹⁷⁴, K. Kessoku¹⁵⁵, C. Ketterer⁴⁸, J. Keung¹⁵⁸, M. Khakzad²⁸, F. Khalil-zada¹⁰, H. Khandanyan¹⁶⁵, A. Khanov¹¹², D. Kharchenko⁶⁵, A. Khodinov⁹⁶, A.G. Kholodenko¹²⁸, A. Khomich^{58a}, T.J. Khoo²⁷, G. Khoriali²⁰, A. Khoroshilov¹⁷⁴, N. Khovanskiy⁶⁵, V. Khovanskiy⁹⁵, E. Khramov⁶⁵, J. Khubua^{51b}, H. Kim⁷, M.S. Kim², P.C. Kim¹⁴³, S.H. Kim¹⁶⁰, N. Kimura¹⁷⁰, O. Kind¹⁵, B.T. King⁷³, M. King⁶⁷, R.S.B. King¹¹⁸, J. Kirk¹²⁹, L.E. Kirsch²², A.E. Kiryunin⁹⁹, T. Kishimoto⁶⁷, D. Kisielewska³⁷, T. Kittelmann¹²³, A.M. Kiver¹²⁸, E. Kladiva^{144b}, J. Klaiber-Lodewigs⁴², M. Klein⁷³, U. Klein⁷³, K. Kleinknecht⁸¹, M. Klemetti⁸⁵, A. Klier¹⁷¹, A. Klimentov²⁴, R. Klingenberg⁴², E.B. Klinkby^{35,g}, T. Klioutchnikova²⁹, P.F. Klok¹⁰⁴, S. Klous¹⁰⁵, E.-E. Kluge^{58a}, T. Kluge⁷³, P. Kluit¹⁰⁵, S. Kluth⁹⁹, N.S. Knecht¹⁵⁸, E. Kneringer⁶², J. Knobloch²⁹, E.B.F.G. Knoop⁸³, A. Knue⁵⁴, B.R. Ko⁴⁴, T. Kobayashi¹⁵⁵, M. Kobel⁴³, M. Kocian¹⁴³,

A. Kocnar¹¹³, P. Kodys¹²⁶, K. Köneke²⁹, A.C. König¹⁰⁴, S. Koenig⁸¹, L. Köpke⁸¹, F. Koetsveld¹⁰⁴, P. Koevesarki²⁰, T. Koffas²⁸, E. Koffeman¹⁰⁵, F. Kohn^{54,g}, Z. Kohout¹²⁷, T. Kohriki⁶⁶, T. Koi¹⁴³, T. Kokott²⁰, G.M. Kolachev¹⁰⁷, H. Kolanoski¹⁵, V. Kolesnikov⁶⁵, I. Koletsou^{89a}, J. Koll⁸⁸, D. Kollar²⁹, M. Kollefrath⁴⁸, S.D. Kolya⁸², A.A. Komar⁹⁴, Y. Komori¹⁵⁵, T. Kondo⁶⁶, T. Kono^{41,q}, A.I. Kononov⁴⁸, R. Konoplich^{108,r}, N. Konstantinidis⁷⁷, A. Kootz¹⁷⁴, S. Koperny³⁷, S.V. Kopikov¹²⁸, K. Korcyl³⁸, K. Kordas¹⁵⁴, V. Koreshev¹²⁸, A. Korn¹¹⁸, A. Korol¹⁰⁷, I. Korolkov¹¹, E.V. Korolkova¹³⁹, V.A. Korotkov¹²⁸, O. Kortner⁹⁹, S. Kortner⁹⁹, V.V. Kostyukhin²⁰, M.J. Kotamäki²⁹, S. Kotov⁹⁹, V.M. Kotov⁶⁵, A. Kotwal⁴⁴, C. Kourkoumelis⁸, V. Kouskoura¹⁵⁴, A. Koutsman¹⁰⁵, R. Kowalewski¹⁶⁹, T.Z. Kowalski³⁷, W. Kozanecki¹³⁶, A.S. Kozhin¹²⁸, V. Kral¹²⁷, V.A. Kramarenko⁹⁷, G. Kramberger⁷⁴, M.W. Krasny⁷⁸, A. Krasznahorkay¹⁰⁸, J. Kraus⁸⁸, J.K. Kraus²⁰, A. Kreisel¹⁵³, F. Krejci¹²⁷, J. Kretzschmar⁷³, N. Krieger⁵⁴, P. Krieger¹⁵⁸, K. Kroeninger⁵⁴, H. Kroha⁹⁹, J. Kroll¹²⁰, J. Kroseberg²⁰, J. Krstic^{12a}, U. Kruchonak⁶⁵, H. Krüger²⁰, T. Kruker¹⁶, Z.V. Krumshcheyn⁶⁵, A. Kruth²⁰, T. Kubota⁸⁶, S. Kuehn⁴⁸, A. Kugel^{58c}, T. Kuhl⁴¹, D. Kuhn⁶², V. Kukhtin⁶⁵, Y. Kulchitsky⁹⁰, S. Kuleshov^{31b}, C. Kummer⁹⁸, M. Kuna⁷⁸, N. Kundu¹¹⁸, J. Kunkle¹²⁰, A. Kupco¹²⁵, H. Kurashige⁶⁷, M. Kurata¹⁶⁰, Y.A. Kurochkin⁹⁰, V. Kus¹²⁵, M. Kuze¹⁵⁷, P. Kuzhir⁹¹, J. Kvita²⁹, R. Kwee¹⁵, A. La Rosa¹⁷², L. La Rotonda^{36a,36b}, L. Labarga⁸⁰, J. Labbe⁴, S. Lablak^{135a}, C. Lacasta¹⁶⁷, F. Lacava^{132a,132b}, H. Lacker¹⁵, D. Lacour⁷⁸, V.R. Lacuesta¹⁶⁷, E. Ladygin⁶⁵, R. Lafaye⁴, B. Laforge⁷⁸, T. Lagouri⁸⁰, S. Lai⁴⁸, E. Laisne⁵⁵, M. Lamanna²⁹, C.L. Lampen⁶, W. Lampl⁶, E. Lancon¹³⁶, U. Landgraf⁴⁸, M.P.J. Landon⁷⁵, H. Landsman¹⁵², J.L. Lane⁸², C. Lange⁴¹, A.J. Lankford¹⁶³, F. Lanni²⁴, K. Lantzsch¹⁷⁴, S. Laplace⁷⁸, C. Lapoire²⁰, J.F. Laporte¹³⁶, T. Lari^{89a}, A.V. Larionov¹²⁸, A. Larner¹¹⁸, C. Lasseur²⁹, M. Lassnig²⁹, P. Laurelli⁴⁷, W. Lavrijsen¹⁴, P. Laycock⁷³, A.B. Lazarev⁶⁵, O. Le Dortz⁷⁸, E. Le Guirrec⁸³, C. Le Maner¹⁵⁸, E. Le Menedeu^{136,g}, C. Lebel⁹³, T. LeCompte⁵, F. Ledroit-Guillon⁵⁵, H. Lee¹⁰⁵, J.S.H. Lee¹¹⁶, S.C. Lee¹⁵¹, L. Lee¹⁷⁵, M. Lefebvre¹⁶⁹, M. Legendre¹³⁶, A. Leger⁴⁹, B.C. LeGeyt¹²⁰, F. Legger⁹⁸, C. Leggett¹⁴, M. Lehmann²⁰, G. Lehmann Miotto²⁹, X. Lei⁶, M.A.L. Leite^{23d}, R. Leitner¹²⁶, D. Lellouch¹⁷¹, M. Leltchouk³⁴, B. Lemmer⁵⁴, V. Lendemann^{58a}, K.J.C. Leney^{145b}, G. Lenzen¹⁰⁵, R. Lenzi¹⁷⁴, B. Lenzi²⁹, K. Leonhardt⁴³, S. Leontsinis⁹, C. Leroy⁹³, J.-R. Lessard¹⁶⁹, J. Lesser^{146a}, C.G. Lester²⁷, A. Leung Fook Cheong¹⁷², J. Levêque⁴, D. Levin⁸⁷, L.J. Levinson¹⁷¹, M.S. Levitski¹²⁸, M. Lewandowska²¹, A. Lewis¹¹⁸, G.H. Lewis¹⁰⁸, A.M. Leyko²⁰, M. Leyton¹⁵, B. Li⁸³, H. Li¹⁷², S. Li^{32b,d}, X. Li⁸⁷, Z. Liang³⁹, Z. Liang^{118,s}, H. Liao³³, B. Liberti^{133a}, P. Lichard²⁹, M. Lichtnecker⁹⁸, K. Lie¹⁶⁵, W. Liebig¹³, R. Lifshitz¹⁵², J.N. Lilley¹⁷, C. Limbach²⁰, A. Limosani⁸⁶, M. Limper⁶³, S.C. Lin^{151,t}, F. Linde¹⁰⁵, J.T. Linnemann⁸⁸, E. Lipeles¹²⁰, L. Lipinsky¹²⁵, A. Lipniacka¹³, T.M. Liss¹⁶⁵, D. Lissauer²⁴, A. Lister⁴⁹, A.M. Litke¹³⁷, C. Liu²⁸, D. Liu^{151,u}, H. Liu⁸⁷, J.B. Liu⁸⁷, M. Liu^{32b,g}, S. Liu², Y. Liu^{32b}, M. Livan^{119a,119b}, S.S.A. Livermore¹¹⁸, A. Lleres⁵⁵, J. Llorente Merino⁸⁰, S.L. Lloyd⁷⁵, E. Lobodzinska⁴¹, P. Loch⁶, W.S. Lockman¹³⁷, T. Loddienkoetter²⁰, F.K. Loebinger⁸², A. Loginov¹⁷⁵, C.W. Loh¹⁶⁸, T. Lohse¹⁵, K. Lohwasser⁴⁸, M. Lokajicek¹²⁵, J. Loken¹¹⁸, V.P. Lombardo⁴, R.E. Long⁷¹, L. Lopes^{124a,b}, D. Lopez Mateos⁵⁷, M. Losada¹⁶², P. Loscutoff¹⁴, F. Lo Sterzo^{132a,132b}, M.J. Losty^{159a}, X. Lou⁴⁰, A. Lounis¹¹⁵, K.F. Loureiro¹⁶², J. Love²¹, P.A. Love⁷¹, A.J. Lowe^{143,f}, F. Lu^{32a}, H.J. Lubatti¹³⁸, C. Luci^{132a,132b}, A. Lucotte⁵⁵, A. Ludwig⁴³, D. Ludwig⁴¹, I. Ludwig⁴⁸, J. Ludwig⁴⁸, F. Luehring⁶¹, G. Luijckx¹⁰⁵, D. Lumb⁴⁸, L. Luminari^{132a}, E. Lund¹¹⁷, B. Lund-Jensen¹⁴⁷, B. Lundberg⁷⁹, J. Lundberg^{146a,146b}, J. Lundquist³⁵, M. Lungwitz⁸¹, A. Lupi^{122a,122b}, G. Lutz⁹⁹, D. Lynn²⁴, J. Lys¹⁴, E. Lytken⁷⁹, H. Ma²⁴, L.L. Ma¹⁷², J.A. Macana Goia⁹³, G. Maccarrone⁴⁷, A. Macchiolo⁹⁹, B. Maček⁷⁴, J. Machado Miguens^{124a}, R. Mackeprang³⁵, R.J. Madaras¹⁴, W.F. Mader⁴³, R. Maenner^{58c}, T. Maeno²⁴, P. Mättig¹⁷⁴, S. Mättig⁴¹, L. Magnoni²⁹, E. Magradze⁵⁴, Y. Mahalalel¹⁵³, K. Mahboubi⁴⁸, G. Mahout¹⁷, C. Maiani^{132a,132b}, C. Maidantchik^{23a}, A. Maio^{124a,b}, S. Majewski²⁴, Y. Makida⁶⁶, N. Makovec¹¹⁵, P. Mal⁶, B. Malaescu²⁹, Pa. Malecki³⁸, P. Malecki³⁸, V.P. Maleev¹²¹, F. Malek⁵⁵, U. Mallik⁶³, D. Malon⁵, C. Malone¹⁴³, S. Maltezos⁹, V. Malyshev¹⁰⁷, S. Malyukov²⁹, R. Mameghani⁹⁸, J. Mamuzic^{12b}, A. Manabe⁶⁶, L. Mandelli^{89a}, I. Mandić⁷⁴, R. Mandrysch¹⁵, J. Maneira^{124a}, P.S. Mangedard⁸⁸, I.D. Manjavidze⁶⁵, A. Mann⁵⁴, P.M. Manning¹³⁷, A. Manousakis-Katsikakis⁸, B. Mansoulie¹³⁶, A. Manz⁹⁹, A. Mapelli²⁹, L. Mapelli²⁹, L. March⁸⁰, J.F. Marchand²⁹, F. Marchese^{133a,133b}, G. Marchiori⁷⁸, M. Marcisovsky^{125,g}, A. Marin^{21,*}, C.P. Marino¹⁶⁹, F. Marroquim^{23a}, R. Marshall⁸², Z. Marshall²⁹, F.K. Martens¹⁵⁸, S. Marti-Garcia¹⁶⁷, A.J. Martin¹⁷⁵, B. Martin²⁹, B. Martin⁸⁸, F.F. Martin¹²⁰, J.P. Martin⁹³, Ph. Martin⁵⁵, T.A. Martin¹⁷, V.J. Martin⁴⁵, B. Martin dit Latour⁴⁹, S. Martin-Haugh¹⁴⁹, M. Martinez¹¹, V. Martinez Outschoorn⁵⁷, A.C. Martyniuk⁸², M. Marx⁸², F. Marzano^{132a}, A. Marzin¹¹¹, L. Masetti⁸¹, T. Mashimo¹⁵⁵, R. Mashinistov⁹⁴, J. Masik⁸², A.L. Maslennikov¹⁰⁷, I. Massa^{19a,19b}, G. Massaro¹⁰⁵, N. Massol⁴, P. Mastrandrea^{132a,132b}, A. Mastroberardino^{36a,36b}, T. Masubuchi¹⁵⁵, M. Mathes²⁰, P. Matricon¹¹⁵, H. Matsumoto¹⁵⁵, H. Matsunaga¹⁵⁵, T. Matsushita⁶⁷, C. Mattheyses^{118,c}, J.M. Maugain²⁹, S.J. Maxfield⁷³, D.A. Maximov¹⁰⁷, E.N. May⁵, A. Mayne¹³⁹, R. Mazini¹⁵¹, M. Mazur²⁰, M. Mazzanti^{89a}, E. Mazzoni^{122a,122b}, S.P. Mc Kee⁸⁷, A. McCarn¹⁶⁵, R.L. McCarthy¹⁴⁸, T.G. McCarthy²⁸, N.A. McCubbin¹²⁹, K.W. McFarlane⁵⁶, J.A. McFayden¹³⁹, H. McGlone⁵³, G. Mchedlidze^{51b}, R.A. McLaren²⁹, T. McLaughlan¹⁷, S.J. McMahon¹²⁹, R.A. McPherson^{169,k}, A. Meade⁸⁴, J. Mechnich¹⁰⁵, M. Mechtel¹⁷⁴, M. Medinnis⁴¹, R. Meera-Lebbai¹¹¹, T. Meguro¹¹⁶, R. Mehdiyev⁹³, S. Mehlhase³⁵, A. Mehta⁷³, K. Meier^{58a}, J. Meinhardt⁴⁸, B. Meirose⁷⁹, C. Melachrinou³⁰, B.R. Mellado Garcia¹⁷², L. Mendoza Navas¹⁶², Z. Meng^{151,u}, A. Mengarelli^{19a,19b}, S. Menke⁹⁹, C. Menot²⁹, E. Meoni¹¹, K.M. Mercurio⁵⁷, P. Mermod¹¹⁸, L. Merola^{102a,102b}, C. Meroni^{89a}, F.S. Merritt³⁰, A. Messina²⁹, J. Metcalfe¹⁰³, A.S. Mete⁶⁴, C. Meyer⁸¹, J.-P. Meyer¹³⁶, J. Meyer¹⁷³, J. Meyer⁵⁴, T.C. Meyer²⁹, W.T. Meyer⁶⁴, J. Miao^{32d}, S. Michal²⁹, L. Micu^{25a}, R.P. Middleton¹²⁹, P. Miele²⁹, S. Migas⁷³, L. Mijović⁴¹, G. Mikenberg¹⁷¹, M. Mikestikova¹²⁵, M. Mikuž⁷⁴, D.W. Miller³⁰, R.J. Miller⁸⁸, W.J. Mills¹⁶⁸, C. Mills⁵⁷, A. Milov¹⁷¹, D.A. Milstead^{146a,146b}, D. Milstein¹⁷¹, A.A. Minaenko¹²⁸, M. Miñano Moya¹⁶⁷, I.A. Minashvili⁶⁵, A.I. Mincer¹⁰⁸, B. Mindur³⁷, M. Mineev⁶⁵, Y. Ming¹³⁰, L.M. Mir¹¹, G. Mirabelli^{132a}, L. Miralles Verge¹¹, A. Misiejuk⁷⁶, J. Mitrevski¹³⁷, G.Y. Mitrofanov¹²⁸, V.A. Mitsou¹⁶⁷, S. Mitsui⁶⁶, P.S. Miyagawa¹³⁹, K. Miyazaki⁶⁷, J.U. Mjörnmark⁷⁹, T. Moa^{146a,146b}, P. Mockett¹³⁸, S. Moed⁵⁷,

V. Moeller²⁷, K. Mönig⁴¹, N. Möser²⁰, S. Mohapatra¹⁴⁸, W. Mohr⁴⁸, S. Mohrdieck-Möck⁹⁹, A.M. Moiseev^{128,*}, R. Moles-Valls¹⁶⁷, J. Molina-Perez²⁹, J. Monk⁷⁷, E. Monnier⁸³, S. Montesano^{89a,89b}, F. Monticelli⁷⁰, S. Monzani^{19a,19b}, R.W. Moore², G.F. Moorhead⁸⁶, C. Mora Herrera⁴⁹, A. Moraes⁵³, N. Morange¹³⁶, J. Morel⁵⁴, G. Morello^{36a,36b}, D. Moreno⁸¹, M. Moreno Llácer¹⁶⁷, P. Morettini^{50a}, M. Morii⁵⁷, J. Morin⁷⁵, A.K. Morley²⁹, G. Mornacchi²⁹, S.V. Morozov⁹⁶, J.D. Morris⁷⁵, L. Morvaj¹⁰¹, H.G. Moser⁹⁹, M. Mosidze^{51b}, J. Moss¹⁰⁹, R. Mount¹⁴³, E. Mountricha^{136,g}, S.V. Mouraviev⁹⁴, E.J.W. Moyse⁸⁴, M. Mudrinic^{12b}, F. Mueller^{58a}, J. Mueller¹²³, K. Mueller²⁰, T.A. Müller⁹⁸, D. Muenstermann²⁹, A. Muir¹⁶⁸, Y. Munwes¹⁵³, W.J. Murray¹²⁹, I. Mussche¹⁰⁵, E. Musto^{102a,102b}, A.G. Myagkov¹²⁸, J. Nadal¹¹, K. Nagai¹⁶⁰, K. Nagano⁶⁶, Y. Nagasaka⁶⁰, A.M. Nairz²⁹, Y. Nakahama²⁹, K. Nakamura¹⁵⁵, T. Nakamura¹⁵⁵, I. Nakano¹¹⁰, G. Nanava²⁰, A. Napier¹⁶¹, M. Nash^{77,c}, N.R. Nation²¹, T. Nattermann²⁰, T. Naumann⁴¹, G. Navarro¹⁶², H.A. Neal⁸⁷, E. Nebot⁸⁰, P.Yu. Nechaeva⁹⁴, A. Negri^{119a,119b}, G. Negri²⁹, S. Nektarijevic⁴⁹, A. Nelson¹⁶³, S. Nelson¹⁴³, T.K. Nelson¹⁴³, S. Nemecek¹²⁵, P. Nemethy¹⁰⁸, A.A. Nepomuceno^{23a}, M. Nessi^{29,v}, S.Y. Nesterov¹²¹, M.S. Neubauer¹⁶⁵, A. Neusiedl⁸¹, R.M. Neves¹⁰⁸, P. Nevski²⁴, P.R. Newman¹⁷, V. Nguyen Thi Hong^{136,g}, R.B. Nickerson¹¹⁸, R. Nicolaidou¹³⁶, L. Nicolas¹³⁹, B. Nicquevert²⁹, F. Niedercorn¹¹⁵, J. Nielsen¹³⁷, T. Niinikoski²⁹, N. Nikiforou³⁴, A. Nikiforov¹⁵, V. Nikolaenko¹²⁸, K. Nikolaev⁶⁵, I. Nikolic-Audit⁷⁸, K. Nikolics⁴⁹, K. Nikolopoulos²⁴, H. Nilsen⁴⁸, P. Nilsson⁷, Y. Ninomiya¹⁵⁵, A. Nisati^{132a}, T. Nishiyama⁶⁷, R. Nisius⁹⁹, L. Nodulman⁵, M. Nomachi¹¹⁶, I. Nomidis¹⁵⁴, M. Nordberg²⁹, B. Nordkvist^{146a,146b}, P.R. Norton¹²⁹, J. Novakova¹²⁶, M. Nozaki⁶⁶, L. Nozka¹¹³, I.M. Nugent^{159a}, A.-E. Nuncio-Quiroz²⁰, G. Nunes Hanninger⁸⁶, T. Nunnemann⁹⁸, E. Nurse⁷⁷, T. Nyman²⁹, B.J. O'Brien⁴⁵, S.W. O'Neill^{17,*}, D.C. O'Neil¹⁴², V. O'Shea⁵³, F.G. Oakham^{28,e}, H. Oberlack⁹⁹, J. Ocariz⁷⁸, A. Ochi⁶⁷, S. Oda¹⁵⁵, S. Odaka⁶⁶, J. Odier⁸³, H. Ogren⁶¹, A. Oh⁸², S.H. Oh⁴⁴, C.C. Ohm^{146a,146b}, T. Ohshima¹⁰¹, H. Ohshita¹⁴⁰, T. Ohsugi⁵⁹, S. Okada⁶⁷, H. Okawa¹⁶³, Y. Okumura¹⁰¹, T. Okuyama¹⁵⁵, M. Olcese^{50a}, A.G. Olchevski⁶⁵, M. Oliveira^{124a,i}, D. Oliveira Damazio²⁴, E. Oliver Garcia¹⁶⁷, D. Olivito¹²⁰, A. Olszewski³⁸, J. Olszowska³⁸, C. Omachi⁶⁷, A. Onofre^{124a,w}, P.U.E. Onyisi³⁰, C.J. Oram^{159a}, M.J. Oreglia³⁰, Y. Oren¹⁵³, D. Orestano^{134a,134b}, I. Orlov¹⁰⁷, C. Oropeza Barrera⁵³, R.S. Orr¹⁵⁸, B. Osculati^{50a,50b}, R. Ospanov¹²⁰, C. Osuna¹¹, G. Otero y Garzon²⁶, J.P. Ottersbach¹⁰⁵, M. Ouchrif^{135d}, F. Ould-Saada¹¹⁷, A. Ouraou¹³⁶, Q. Ouyang^{32a}, M. Owen⁸², S. Owen^{139,g}, V.E. Ozcan^{18a}, N. Ozturk⁷, A. Pacheco Pages¹¹, C. Padilla Aranda¹¹, S. Pagan Griso¹⁴, E. Paganis¹³⁹, F. Paige²⁴, K. Pajchel¹¹⁷, G. Palacino^{159b}, C.P. Paleari⁶, S. Palestini²⁹, D. Pallin³³, A. Palma^{124a}, J.D. Palmer¹⁷, Y.B. Pan¹⁷², E. Panagiotopoulou⁹, B. Panes^{31a}, N. Panikashvili⁸⁷, S. Panitkin²⁴, D. Pantea^{25a}, M. Panuskova¹²⁵, V. Paolone¹²³, A. Papadellis^{146a}, Th.D. Papadopolou⁹, A. Paramonov⁵, W. Park^{24,x}, M.A. Parker²⁷, F. Parodi^{50a,50b}, J.A. Parsons³⁴, U. Parzefall⁴⁸, E. Pasqualucci^{132a}, A. Passeri^{134a}, F. Pastore^{134a,134b}, Fr. Pastore⁷⁶, G. Pásztor^{49,y}, S. Pataria¹⁷⁴, N. Patel¹⁵⁰, J.R. Pater⁸², S. Patricelli^{102a,102b}, T. Pauly²⁹, M. Pecsly^{144a}, M.I. Pedraza Morales¹⁷², S.V. Peleganchuk¹⁰⁷, H. Peng^{32b}, R. Pengo²⁹, A. Penson³⁴, J. Penwell⁶¹, M. Perantoni^{23a,g}, K. Perez^{34,z}, T. Perez Cavalcanti⁴¹, E. Perez Codina¹¹, M.T. Pérez García-Están¹⁶⁷, V. Perez Reale³⁴, L. Perini^{89a,89b}, H. Pernegger²⁹, R. Perrino^{72a}, P. Perrodo⁴, S. Persema^{3a}, V.D. Peshekhonov⁶⁵, B.A. Petersen²⁹, J. Petersen²⁹, T.C. Petersen³⁵, E. Petit⁸³, A. Petridis¹⁵⁴, C. Petridou¹⁵⁴, E. Petrolo^{132a}, F. Petrucci^{134a,134b}, D. Petschall⁴¹, M. Petteni¹⁴², R. Pezoa^{31b}, A. Phan⁸⁶, A.W. Phillips²⁷, P.W. Phillips¹²⁹, G. Piacquadio²⁹, E. Piccaro⁷⁵, M. Piccinini^{19a,19b}, A. Pickford⁵³, S.M. Piec⁴¹, R. Piegaia²⁶, J.E. Pilcher³⁰, A.D. Pilkington⁸², J. Pina^{124a,b}, M. Pinamonti^{164a,164c}, A. Pinder¹¹⁸, J.L. Pinfold², J. Ping^{32c}, B. Pinto^{124a,b}, O. Pirotte²⁹, C. Pizio^{89a,89b}, R. Placakyte⁴¹, M. Plamondon¹⁶⁹, M.-A. Pleier²⁴, A.V. Pleskach¹²⁸, A. Poblaguev²⁴, S. Poddar^{58a}, F. Podlyski³³, L. Poggioni¹¹⁵, T. Poghosyan²⁰, M. Pohl⁴⁹, F. Polci⁵⁵, G. Polesello^{119a}, A. Policicchio¹³⁸, A. Polini^{19a}, J. Poli⁷⁵, V. Polychronakos²⁴, D.M. Pomarede¹³⁶, D. Pomeroy²², K. Pommès²⁹, L. Pontecorvo^{132a}, B.G. Pope⁸⁸, G.A. Popeneciu^{25a}, D.S. Popovic^{12a}, A. Poppleton²⁹, X. Portell Bueso²⁹, C. Posch²¹, G.E. Pospelov⁹⁹, S. Pospisil¹²⁷, I.N. Potrap⁹⁹, C.J. Potter¹⁴⁹, C.T. Potter¹¹⁴, G. Poulard²⁹, J. Poveda¹⁷², R. Prabhu⁷⁷, P. Pralavorio⁸³, S. Prasad⁵⁷, R. Pravahan⁷, S. Prell⁶⁴, K. Pretzl¹⁶, L. Pribyl²⁹, D. Price⁶¹, L.E. Price⁵, M.J. Price²⁹, P.M. Prichard⁷³, D. Prieur¹²³, M. Primavera^{72a}, K. Prokofiev¹⁰⁸, F. Prokoshin^{31b}, S. Protopopescu²⁴, J. Proudfoot⁵, X. Prudent⁴³, H. Przysiezniak⁴, S. Psoroulas²⁰, E. Ptacek¹¹⁴, E. Pueschel⁸⁴, J. Purdham⁸⁷, M. Purohit^{24,x}, P. Puzo¹¹⁵, Y. Pylypchenko¹¹⁷, J. Qian⁸⁷, Z. Qian⁸³, Z. Qin⁴¹, A. Quadt⁵⁴, D.R. Quarrie¹⁴, W.B. Quayle¹⁷², F. Quinonez^{31a}, M. Raas¹⁰⁴, V. Radescu^{58b}, B. Radics²⁰, T. Rador^{18a}, F. Ragusa^{89a,89b}, G. Rahal¹⁷⁷, A.M. Rahimi¹⁰⁹, D. Rahm²⁴, S. Rajagopalan²⁴, M. Rammensee⁴⁸, M. Rammes¹⁴¹, M. Ramstedt^{146a,146b}, A.S. Randle-Conde^{39,g}, K. Randrianarivony²⁸, P.N. Ratoff⁷¹, F. Rauscher⁹⁸, E. Rauter⁹⁹, M. Raymond²⁹, A.L. Read¹¹⁷, D.M. Rebuzzi^{119a,119b}, A. Redelbach¹⁷³, G. Redlinger²⁴, R. Reece¹²⁰, K. Reeves⁴⁰, A. Reichold¹⁰⁵, E. Reinherz-Aronis¹⁵³, A. Reinsch¹¹⁴, I. Reisinger⁴², D. Reljic^{12a}, C. Rembser²⁹, Z.L. Ren¹⁵¹, A. Renaud¹¹⁵, P. Renkel³⁹, M. Rescigno^{132a}, S. Resconi^{89a}, B. Resende¹³⁶, P. Reznicek⁹⁸, R. Rezvani¹⁵⁸, A. Richards⁷⁷, R. Richter⁹⁹, E. Richter-Was^{4,aa}, M. Ridel⁷⁸, S. Rieke⁸¹, M. Rijpstra¹⁰⁵, M. Rijssenbeek¹⁴⁸, A. Rimoldi^{119a,119b}, L. Rinaldi^{19a}, R.R. Rios³⁹, I. Riu¹¹, G. Rivoltella^{89a,89b}, F. Rizatdinova¹¹², E. Rizvi⁷⁵, S.H. Robertson^{85,k}, A. Robichaud-Veronneau¹¹⁸, D. Robinson²⁷, J.E.M. Robinson⁷⁷, M. Robinson¹¹⁴, A. Robson⁵³, J.G. Rocha de Lima¹⁰⁶, C. Roda^{122a,122b}, D. Roda Dos Santos²⁹, S. Rodier⁸⁰, D. Rodriguez¹⁶², A. Roe⁵⁴, S. Roe²⁹, O. Røhne¹¹⁷, V. Rojo¹, S. Rolli¹⁶¹, A. Romaniouk⁹⁶, M. Romano^{19a,19b}, V.M. Romanov⁶⁵, G. Romeo²⁶, L. Roos⁷⁸, E. Ros¹⁶⁷, S. Rosati^{132a,132b}, K. Rosbach⁴⁹, A. Rose¹⁴⁹, M. Rose⁷⁶, G.A. Rosenbaum¹⁵⁸, E.I. Rosenberg⁶⁴, P.L. Rosendahl¹³, O. Rosenthal¹⁴¹, L. Rosselet⁴⁹, V. Rossetti¹¹, E. Rossi^{132a,132b}, L.P. Rossi^{50a}, L. Rossi^{89a,89b}, M. Rotaru^{25a}, I. Roth¹⁷¹, J. Rothberg¹³⁸, D. Rousseau¹¹⁵, C.R. Royon¹³⁶, A. Rozanov⁸³, Y. Rozen¹⁵², X. Ruan¹¹⁵, I. Rubinskiy⁴¹, B. Ruckert⁹⁸, N. Ruckstuhl¹⁰⁵, V.I. Rud⁹⁷, C. Rudolph⁴³, G. Rudolph⁶², F. Rühr⁶, F. Ruggieri^{134a,134b}, A. Ruiz-Martinez⁶⁴, E. Rulikowska-Zarebska³⁷, V. Rumiantsev^{91,*}, L. Rummyantsev⁶⁵, K. Runge⁴⁸, O. Runolfsson²⁰, Z. Rurikova⁴⁸, N.A. Rusakovich⁶⁵, D.R. Rust⁶¹, J.P. Rutherford⁶, C. Ruwiedel¹⁴, P. Ruzicka¹²⁵, Y.F. Ryabov¹²¹, V. Ryadovikov¹²⁸, P. Ryan⁸⁸, M. Rybar¹²⁶, G. Rybkin¹¹⁵, N.C. Ryder¹¹⁸, S. Rzaeva¹⁰, A.F. Saavedra¹⁵⁰,

I. Sadeh¹⁵³, H.F.-W. Sadrozinski¹³⁷, R. Sadykov⁶⁵, F. Safai Tehrani^{132a,132b}, H. Sakamoto¹⁵⁵, G. Salamanna⁷⁵, A. Salamon^{133a}, M. Saleem¹¹¹, D. Salihagic⁹⁹, A. Salnikov¹⁴³, J. Salt¹⁶⁷, B.M. Salvachua Ferrando⁵, D. Salvatore^{36a,36b}, F. Salvatore¹⁴⁹, A. Salvucci¹⁰⁴, A. Salzburger²⁹, D. Sampsonidis¹⁵⁴, B.H. Samset¹¹⁷, A. Sanchez^{102a,102b}, H. Sandaker¹³, H.G. Sander⁸¹, M.P. Sanders⁹⁸, M. Sandhoff¹⁷⁴, T. Sandoval²⁷, C. Sandoval¹⁶², R. Sandstroem⁹⁹, S. Sandvoss¹⁷⁴, D.P.C. Sankey¹²⁹, A. Sansoni⁴⁷, C. Santamarina Rios⁸⁵, C. Santoni³³, R. Santonico^{133a,133b}, H. Santos^{124a}, J.G. Saraiva^{124a}, T. Sarangi¹⁷², E. Sarkisyan-Grinbaum⁷, F. Sarri^{122a,122b}, G. Sartisohn¹⁷⁴, O. Sasaki⁶⁶, T. Sasaki⁶⁶, N. Sasao⁶⁸, I. Satsounkevitch⁹⁰, G. Sauvage⁴, E. Sauvan⁴, J.B. Sauvan¹¹⁵, P. Savard^{158,e}, V. Savinov¹²³, D.O. Savu²⁹, P. Savva⁹, L. Sawyer^{24,m}, D.H. Saxon⁵³, L.P. SAYS³³, C. Sbarra^{19a}, A. Sbrizzi^{19a,19b}, O. Scallan⁹³, D.A. Scannicchio¹⁶³, J. Schaarschmidt¹¹⁵, P. Schacht⁹⁹, U. Schäfer⁸¹, S. Schaepe²⁰, S. Schaezel^{58b}, A.C. Schaffer¹¹⁵, D. Schaile⁹⁸, R.D. Schamberger¹⁴⁸, A.G. Schamov¹⁰⁷, V. Scharf^{58a}, V.A. Schegelsky¹²¹, D. Scheirich⁸⁷, M. Schernau¹⁶³, M.I. Scherzer¹⁴, C. Schiavi^{50a,50b}, J. Schieck⁹⁸, M. Schioppa^{36a,36b}, S. Schlenker²⁹, J.L. Schlereth⁵, E. Schmidt⁴⁸, K. Schmieden²⁰, C. Schmitt⁸¹, S. Schmitt^{58b}, M. Schmitz²⁰, A. Schöning^{58b}, M. Schott²⁹, D. Schouten^{159a}, J. Schovancova¹²⁵, M. Schram⁸⁵, C. Schroeder⁸¹, N. Schroer^{58c}, S. Schuh²⁹, G. Schuler²⁹, J. Schultes¹⁷⁴, H.-C. Schultz-Coulon^{58a}, H. Schulz¹⁵, J.W. Schumacher²⁰, M. Schumacher⁴⁸, B.A. Schumm¹³⁷, Ph. Schune¹³⁶, C. Schwanenberger⁸², A. Schwartzman¹⁴³, Ph. Schwemling⁷⁸, R. Schwienhorst⁸⁸, R. Schwierz⁴³, J. Schwindling¹³⁶, T. Schwindt²⁰, W.G. Scott¹²⁹, J. Searcy¹¹⁴, G. Sedov⁴¹, E. Sedykh¹²¹, E. Segura¹¹, S.C. Seidel¹⁰³, A. Seiden¹³⁷, F. Seifert⁴³, J.M. Seixas^{23a}, G. Sekhniadze^{102a}, D.M. Seliverstov¹²¹, B. Sellden^{146a}, G. Sellers⁷³, M. Seman^{144b}, N. Semprini-Cesari^{19a,19b}, C. Serfon⁹⁸, L. Serin¹¹⁵, R. Seuster⁹⁹, H. Severini¹¹¹, M.E. Sevir⁸⁶, A. Sfyrla²⁹, E. Shabalina⁵⁴, M. Shamim¹¹⁴, L.Y. Shan^{32a}, J.T. Shank²¹, Q.T. Shao⁸⁶, M. Shapiro¹⁴, P.B. Shatalov⁹⁵, L. Shaver⁶, K. Shaw^{164a,164c}, D. Sherman¹⁷⁵, P. Sherwood⁷⁷, A. Shibata¹⁰⁸, H. Shichi¹⁰¹, S. Shimizu²⁹, M. Shimojima¹⁰⁰, T. Shin⁵⁶, A. Shmeleva⁹⁴, M.J. Shochet³⁰, D. Short¹¹⁸, M.A. Shupe⁶, P. Sicho¹²⁵, A. Sidoti^{132a,132b}, A. Siebel¹⁷⁴, F. Siegert⁴⁸, Dj. Sijacki^{12a}, O. Silbert¹⁷¹, J. Silva^{124a,b}, Y. Silver¹⁵³, D. Silverstein¹⁴³, S.B. Silverstein^{146a}, V. Simak¹²⁷, O. Simard¹³⁶, Lj. Simic^{12a}, S. Simion¹¹⁵, B. Simmons⁷⁷, M. Simonyan³⁵, P. Sinervo¹⁵⁸, N.B. Sinev¹¹⁴, V. Sipica¹⁴¹, G. Siragusa¹⁷³, A. Sircar²⁴, A.N. Sisakyan⁶⁵, S.Yu. Sivoklov⁹⁷, J. Sjölin^{146a,146b}, T.B. Sjrursen¹³, L.A. Skinnari¹⁴, H.P. Skottowe⁵⁷, K. Skovpen¹⁰⁷, P. Skubic¹¹¹, N. Skvorodnev²², M. Slater¹⁷, T. Slavicek¹²⁷, K. Sliwa¹⁶¹, J. Sloper²⁹, V. Smakhtin¹⁷¹, S.Yu. Smirnov⁹⁶, L.N. Smirnova⁹⁷, O. Smirnova⁷⁹, B.C. Smith⁵⁷, D. Smith¹⁴³, K.M. Smith⁵³, M. Smizanska⁷¹, K. Smolek¹²⁷, A.A. Snesarev⁹⁴, S.W. Snow⁸², J. Snow¹¹¹, J. Snuverink¹⁰⁵, S. Snyder²⁴, M. Soares^{124a}, R. Sobie^{169,k}, J. Sodomka¹²⁷, A. Soffer¹⁵³, C.A. Solans¹⁶⁷, M. Solar¹²⁷, E. Soldatov⁹⁶, U. Soldevila¹⁶⁷, E. Solfaroli Camillocci^{132a,132b}, A.A. Solodkov¹²⁸, O.V. Solovyanov¹²⁸, J. Sondericker²⁴, N. Soni², V. Sopko¹²⁷, B. Sopko¹²⁷, M. Sorbi^{89a,89b}, M. Sosebee⁷, R. Soualah^{164a,164c}, A. Soukharev¹⁰⁷, S. Spagnolo^{72a,72b}, F. Spano⁷⁶, R. Spighi^{19a}, G. Spigo²⁹, F. Spila^{132a,132b}, E. Spiriti^{134a}, R. Spiwoks²⁹, M. Spousta¹²⁶, T. Spreitzer¹⁵⁸, B. Spurlock⁷, R.D. St. Denis⁵³, T. Stahl¹⁴¹, J. Stahlman¹²⁰, R. Stamen^{58a}, E. Stanecka²⁹, R.W. Stanek⁵, C. Stancu^{134a}, S. Stapnes¹¹⁷, E.A. Starchenko¹²⁸, J. Stark⁵⁵, P. Staroba¹²⁵, P. Starovoitov⁹¹, A. Staude⁹⁸, P. Stavina^{144a}, G. Stavropoulos¹⁴, G. Steele⁵³, P. Steinbach⁴³, P. Steinberg²⁴, I. Stekl¹²⁷, B. Stelzer¹⁴², H.J. Stelzer⁸⁸, O. Stelzer-Chilton^{159a}, H. Stenzel⁵², K. Stevenson⁷⁵, G.A. Stewart²⁹, J.A. Stillings²⁰, T. Stockmanns²⁰, M.C. Stockton²⁹, K. Stoerig⁴⁸, G. Stoicea^{25a}, S. Stonjek⁹⁹, P. Strachota¹²⁶, A.R. Stradling⁷, A. Straessner⁴³, J. Strandberg¹⁴⁷, S. Strandberg^{146a,146b}, A. Strandlie¹¹⁷, M. Strang¹⁰⁹, E. Strauss¹⁴³, M. Strauss¹¹¹, P. Strizenec^{144b}, R. Ströhmer¹⁷³, D.M. Strom¹¹⁴, J.A. Strong^{76,*}, R. Stroynowski³⁹, J. Stube¹²⁹, B. Stugu¹³, I. Stumer^{24,*}, J. Stupak¹⁴⁸, P. Sturm¹⁷⁴, D.A. Soh^{151,s}, D. Su¹⁴³, H.S. Subramania², A. Succurro¹¹, Y. Sugaya¹¹⁶, T. Sugimoto¹⁰¹, C. Suhr¹⁰⁶, K. Suita⁶⁷, M. Suk¹²⁶, V.V. Sulin⁹⁴, S. Sultansoy^{3d}, T. Sumida²⁹, X. Sun⁵⁵, J.E. Sundermann⁴⁸, K. Suruliz¹³⁹, S. Sushkov¹¹, G. Susinno^{36a,36b}, M.R. Sutton¹⁴⁹, Y. Suzuki⁶⁶, Y. Suzuki⁶⁷, M. Svatos¹²⁵, Yu.M. Sviridov¹²⁸, S. Swedish¹⁶⁸, I. Sykora^{144a}, T. Sykora¹²⁶, B. Szeless²⁹, J. Sánchez¹⁶⁷, D. Ta¹⁰⁵, K. Tackmann⁴¹, A. Taffard¹⁶³, R. Tafirout^{159a}, N. Taiblum¹⁵³, Y. Takahashi¹⁰¹, H. Takai²⁴, R. Takashima⁶⁹, H. Takeda⁶⁷, T. Takeshita¹⁴⁰, M. Talby⁸³, A. Talyshv¹⁰⁷, M.C. Tamsett²⁴, J. Tanaka¹⁵⁵, R. Tanaka¹¹⁵, S. Tanaka¹³¹, S. Tanaka⁶⁶, Y. Tanaka¹⁰⁰, K. Tani⁶⁷, N. Tannoury⁸³, G.P. Tappern²⁹, S. Tapprogge⁸¹, D. Tardif¹⁵⁸, S. Tarem¹⁵², F. Tarrade²⁸, G.F. Tartarelli^{89a}, P. Tas¹²⁶, M. Tasevsky¹²⁵, E. Tassi^{36a,36b}, M. Tatarkhanov¹⁴, Y. Tayalati^{135d}, C. Taylor⁷⁷, F.E. Taylor⁹², G.N. Taylor⁸⁶, W. Taylor^{159b}, M. Teinturier¹¹⁵, M. Teixeira Dias Castanheira⁷⁵, P. Teixeira-Dias⁷⁶, K.K. Temming⁴⁸, H. Ten Kate²⁹, P.K. Teng¹⁵¹, S. Terada⁶⁶, K. Terashi¹⁵⁵, J. Terron⁸⁰, M. Terwort^{41,q}, M. Testa⁴⁷, R.J. Teuscher^{158,k}, J. Thadome¹⁷⁴, J. Therhaag²⁰, T. Theveneaux-Pelzer⁷⁸, M. Thioye¹⁷⁵, S. Thoma⁴⁸, J.P. Thomas¹⁷, E.N. Thompson³⁴, P.D. Thompson¹⁵⁸, A.S. Thompson⁵³, E. Thomson¹²⁰, M. Thomson²⁷, R.P. Thun⁸⁷, F. Tian³⁴, T. Tic¹²⁵, V.O. Tikhomirov⁹⁴, Y.A. Tikhonov¹⁰⁷, C.J.W.P. Timmermans¹⁰⁴, P. Tipton¹⁷⁵, F.J. Tique Aires Viegas²⁹, S. Tisserant⁸³, J. Tobias⁴⁸, B. Toczec³⁷, T. Todorov⁴, S. Todorova-Nova¹⁶¹, B. Toggerson¹⁶³, J. Tojo⁶⁶, S. Tokár^{144a}, K. Tokunaga⁶⁷, K. Tokushuku⁶⁶, K. Tollefson⁸⁸, M. Tomoto¹⁰¹, L. Tompkins¹⁴, K. Toms¹⁰³, G. Tong^{32a}, A. Tonoyan¹³, C. Topfel¹⁶, N.D. Topilin⁶⁵, I. Torchiani²⁹, E. Torrence¹¹⁴, H. Torres⁷⁸, E. Torró Pastor¹⁶⁷, J. Toth^{83,y}, F. Touchard⁸³, D.R. Tovey¹³⁹, D. Traynor⁷⁵, T. Trefzger¹⁷³, L. Tremblet²⁹, A. Tricoli²⁹, I.M. Trigger^{159a}, S. Trincas-Duvold⁷⁸, T.N. Trinh⁷⁸, M.F. Tripiana⁷⁰, W. Trischuk¹⁵⁸, A. Trivedi^{24,x}, B. Trocme⁵⁵, C. Troncon^{89a}, M. Trotter-McDonald¹⁴², A. Trzupek³⁸, C. Tsarouchas²⁹, J.C.-L. Tseng¹¹⁸, M. Tsiakiris¹⁰⁵, P.V. Tsiarehka⁹⁰, D. Tsionou⁴, G. Tsipolitis⁹, V. Tsiskaridze⁴⁸, E.G. Tskhadadze^{51a}, I.I. Tsukerman⁹⁵, V. Tsulaia¹⁴, J.-W. Tsung²⁰, S. Tsuno⁶⁶, D. Tsybychev¹⁴⁸, A. Tua¹³⁹, A. Tudorache^{25a,g}, V. Tudorache^{25a,g}, J.M. Tuggle³⁰, M. Turala³⁸, D. Turecek¹²⁷, I. Turk Cakir^{3e}, E. Turlay¹⁰⁵, R. Turra^{89a,89b}, P.M. Tuts³⁴, A. Tykhonov⁷⁴, M. Tylmad^{146a,146b}, M. Tyndel¹²⁹, H. Tyrvalinen²⁹, G. Tzanakos⁸, K. Uchida²⁰, I. Ueda¹⁵⁵, R. Ueno²⁸, M. Ugland¹³, M. Uhlenbrock²⁰, M. Uhrmacher⁵⁴, F. Ukegawa¹⁶⁰, G. Unal²⁹, D.G. Underwood⁵, A. Undrus²⁴, G. Unei¹⁶³, Y. Unno⁶⁶, D. Urbaniec³⁴, E. Urkovsky¹⁵³, P. Urrejola^{31a}, G. Usai⁷, M. Uslenghi^{119a,119b}, L. Vacavant⁸³, V. Vacek¹²⁷, B. Vachon⁸⁵, S. Vahsen¹⁴, J. Valenta¹²⁵, P. Valente^{132a}, S. Valentini^{19a,19b}, S. Valkar¹²⁶, E. Valladolid Gallego¹⁶⁷,

S. Vallecorsa¹⁵², J.A. Valls Ferrer¹⁶⁷, H. van der Graaf¹⁰⁵, E. van der Kraaij¹⁰⁵, R. Van Der Leeuw¹⁰⁵, E. van der Poel¹⁰⁵, D. van der Ster²⁹, N. van Eldik⁸⁴, P. van Gemmeren⁵, Z. van Kesteren¹⁰⁵, I. van Vulpen¹⁰⁵, M. Vanadia⁹⁹, W. Vandelli²⁹, G. Vandoni²⁹, A. Vaniachine⁵, P. Vankov⁴¹, F. Vannucci⁷⁸, F. Varela Rodriguez²⁹, R. Vari^{132a}, D. Varouchas¹⁴, A. Vartapetian⁷, K.E. Varvell¹⁵⁰, V.I. Vassilakopoulos⁵⁶, F. Vazeille³³, G. Vegni^{89a,89b}, J.J. Veillet¹¹⁵, C. Vellidis⁸, F. Veloso^{124a}, R. Veness²⁹, S. Veneziano^{132a}, A. Ventura^{72a,72b}, D. Ventura¹³⁸, M. Venturi⁴⁸, N. Venturi¹⁶, V. Vercesi^{119a}, M. Verducci¹³⁸, W. Verkerke¹⁰⁵, J.C. Vermeulen¹⁰⁵, A. Vest⁴³, M.C. Vetterli^{142,e}, I. Vichou¹⁶⁵, T. Vickey^{145b,ab}, O.E. Vickey Boeriu^{145b}, G.H.A. Viehhauser¹¹⁸, S. Viel¹⁶⁸, M. Villa^{19a,19b}, M. Villaplana Perez¹⁶⁷, E. Vilucchi⁴⁷, M.G. Vincker²⁸, E. Vinek²⁹, V.B. Vinogradov⁶⁵, M. Virchaux^{136,*}, J. Virzi¹⁴, O. Vitells¹⁷¹, M. Viti⁴¹, I. Vivarelli⁴⁸, F. Vives Vaquer², S. Vlachos⁹, D. Vladoiu⁹⁸, M. Vlasak¹²⁷, N. Vlasov²⁰, A. Vogel²⁰, P. Vokac¹²⁷, G. Volpi⁴⁷, M. Volpi⁸⁶, G. Volpini^{89a}, H. von der Schmitt⁹⁹, J. von Loeben⁹⁹, H. von Radziewski⁴⁸, E. von Toerne²⁰, V. Vorobel¹²⁶, A.P. Vorobiev¹²⁸, V. Vorwerk¹¹, M. Vos¹⁶⁷, R. Voss²⁹, T.T. Voss¹⁷⁴, J.H. Vossebeld⁷³, N. Vranjes^{12a}, M. Vranjes Milosavljevic¹⁰⁵, V. Vrba¹²⁵, M. Vreeswijk¹⁰⁵, T. Vu Anh⁸¹, R. Vuillermet²⁹, M. Vujicic²⁸, I. Vukotic¹¹⁵, W. Wagner¹⁷⁴, P. Wagner¹²⁰, H. Wahlen¹⁷⁴, J. Wakabayashi¹⁰¹, J. Walbersloh⁴², S. Walch⁸⁷, J. Walder⁷¹, R. Walker⁹⁸, W. Walkowiak¹⁴¹, R. Wall¹⁷⁵, P. Waller⁷³, C. Wang⁴⁴, H. Wang¹⁷², H. Wang^{32b,ac}, J. Wang¹⁵¹, J. Wang^{32d}, J.C. Wang¹³⁸, R. Wang¹⁰³, S.M. Wang¹⁵¹, A. Warburton⁸⁵, C.P. Ward²⁷, M. Warsinsky⁴⁸, P.M. Watkins¹⁷, A.T. Watson¹⁷, M.F. Watson¹⁷, G. Watts¹³⁸, S. Watts⁸², A.T. Waugh¹⁵⁰, B.M. Waugh⁷⁷, J. Weber⁴², M. Weber¹²⁹, M.S. Weber¹⁶, P. Weber⁵⁴, A.R. Weidberg¹¹⁸, P. Weigell⁹⁹, J. Weingarten⁵⁴, C. Weiser⁴⁸, H. Wellenstein²², P.S. Wells²⁹, M. Wen⁴⁷, T. Wenaus²⁴, S. Wendler¹²³, Z. Weng^{151,s}, T. Wengler²⁹, S. Wenig²⁹, N. Wermes²⁰, M. Werner⁴⁸, P. Werner²⁹, M. Werth¹⁶³, M. Wessels^{58a}, C. Weydert⁵⁵, K. Whalen²⁸, S.J. Wheeler-Ellis¹⁶³, S.P. Whitaker²¹, A. White⁷, M.J. White⁸⁶, S.R. Whitehead¹¹⁸, D. Whiteson¹⁶³, D. Whittington⁶¹, F. Wicek¹¹⁵, D. Wicke¹⁷⁴, F.J. Wickens¹²⁹, W. Wiedenmann¹⁷², M. WIELERS¹²⁹, P. Wienemann²⁰, C. Wiglesworth⁷⁵, L.A.M. Wiik⁴⁸, P.A. Wijeratne⁷⁷, A. Wildauer¹⁶⁷, M.A. Wildt^{41,q}, I. Wilhelm¹²⁶, H.G. Wilkens²⁹, J.Z. Will⁹⁸, E. Williams³⁴, H.H. Williams¹²⁰, W. Willis³⁴, S. Willocq⁸⁴, J.A. Wilson¹⁷, M.G. Wilson¹⁴³, A. Wilson⁸⁷, I. Wingerter-Seez⁴, S. Winkelmann⁴⁸, F. Winklmeier²⁹, M. Wittgen¹⁴³, M.W. Wolter³⁸, H. Wolters^{124a,i}, W.C. Wong⁴⁰, G. Wooden⁸⁷, B.K. Wosiek³⁸, J. Wotschack²⁹, M.J. Woudstra⁸⁴, K. Wraight⁵³, C. Wright⁵³, M. Wright⁵³, B. Wrona⁷³, S.L. Wu¹⁷², X. Wu⁴⁹, Y. Wu^{32b,ad}, E. Wulf³⁴, R. Wunstorff⁴², B.M. Wynne⁴⁵, L. Xaplanteris⁹, S. Xella³⁵, S. Xie⁴⁸, Y. Xie^{32a}, C. Xu^{32b,ae}, D. Xu¹³⁹, G. Xu^{32a}, B. Yabsley¹⁵⁰, S. Yacoub^{145b}, M. Yamada⁶⁶, H. Yamaguchi¹⁵⁵, A. Yamamoto⁶⁶, K. Yamamoto⁶⁴, S. Yamamoto¹⁵⁵, T. Yamamura¹⁵⁵, T. Yamanaka¹⁵⁵, J. Yamaoka⁴⁴, T. Yamazaki¹⁵⁵, Y. Yamazaki⁶⁷, Z. Yan²¹, H. Yang⁸⁷, U.K. Yang⁸², Y. Yang⁶¹, Y. Yang^{32a}, Z. Yang^{146a,146b}, S. Yanush⁹¹, Y. Yao¹⁴, Y. Yasu⁶⁶, G.V. Ybeles Smit¹³⁰, J. Ye³⁹, S. Ye²⁴, M. Yilmaz^{3c}, R. Yoosoofmiya¹²³, K. Yorita¹⁷⁰, R. Yoshida⁵, C. Young¹⁴³, S. Youssef²¹, D. Yu²⁴, J. Yu⁷, J. Yu¹¹², L. Yuan^{32a,af}, A. Yurkewicz¹⁴⁸, V.G. Zaets¹²⁸, R. Zaidan⁶³, A.M. Zaitsev¹²⁸, Z. Zajacova²⁹, Yo.K. Zalite¹²¹, L. Zanello^{132a,132b}, P. Zarzhitsky³⁹, A. Zaytsev¹⁰⁷, C. Zeitnitz¹⁷⁴, M. Zeller¹⁷⁵, M. Zeman¹²⁵, A. Zemla³⁸, C. Zendler²⁰, O. Zenin¹²⁸, T. Ženis^{144a}, Z. Zenonos^{122a,122b}, S. Zenz¹⁴, D. Zerwas¹¹⁵, G. Zevi della Porta⁵⁷, Z. Zhan^{32d}, D. Zhang^{32b,ac}, H. Zhang⁸⁸, J. Zhang⁵, X. Zhang^{32d}, Z. Zhang¹¹⁵, L. Zhao¹⁰⁸, T. Zhao¹³⁸, Z. Zhao^{32b}, A. Zhemchugov⁶⁵, S. Zheng^{32a}, J. Zhong^{151,ag}, B. Zhou⁸⁷, N. Zhou¹⁶³, Y. Zhou¹⁵¹, C.G. Zhu^{32d}, H. Zhu⁴¹, J. Zhu⁸⁷, Y. Zhu^{32b}, X. Zhuang⁹⁸, V. Zhuravlov⁹⁹, D. Zieminska⁶¹, R. Zimmermann²⁰, S. Zimmermann²⁰, S. Zimmermann⁴⁸, M. Ziolkowski¹⁴¹, R. Zitoun⁴, L. Živković³⁴, V.V. Zmouchko^{128,*}, G. Zobernig¹⁷², A. Zoccoli^{19a,19b}, Y. Zolnierowski⁴, A. Zsenei²⁹, M. zur Nedden¹⁵, V. Zutshi¹⁰⁶, L. Zwalinski²⁹.

¹ University at Albany, Albany NY, United States of America

² Department of Physics, University of Alberta, Edmonton AB, Canada

³ (a) Department of Physics, Ankara University, Ankara; (b) Department of Physics, Dumlupinar University, Kutahya;

(c) Department of Physics, Gazi University, Ankara; (d) Division of Physics, TOBB University of Economics and Technology, Ankara; (e) Turkish Atomic Energy Authority, Ankara, Turkey

⁴ LAPP, CNRS/IN2P3 and Université de Savoie, Annecy-le-Vieux, France

⁵ High Energy Physics Division, Argonne National Laboratory, Argonne IL, United States of America

⁶ Department of Physics, University of Arizona, Tucson AZ, United States of America

⁷ Department of Physics, The University of Texas at Arlington, Arlington TX, United States of America

⁸ Physics Department, University of Athens, Athens, Greece

⁹ Physics Department, National Technical University of Athens, Zografou, Greece

¹⁰ Institute of Physics, Azerbaijan Academy of Sciences, Baku, Azerbaijan

¹¹ Institut de Física d'Altes Energies and Departament de Física de la Universitat Autònoma de Barcelona and ICREA, Barcelona, Spain

¹² (a) Institute of Physics, University of Belgrade, Belgrade; (b) Vinca Institute of Nuclear Sciences, Belgrade, Serbia

¹³ Department for Physics and Technology, University of Bergen, Bergen, Norway

¹⁴ Physics Division, Lawrence Berkeley National Laboratory and University of California, Berkeley CA, United States of America

¹⁵ Department of Physics, Humboldt University, Berlin, Germany

¹⁶ Albert Einstein Center for Fundamental Physics and Laboratory for High Energy Physics, University of Bern, Bern, Switzerland

¹⁷ School of Physics and Astronomy, University of Birmingham, Birmingham, United Kingdom

- ¹⁸ ^(a)Department of Physics, Bogazici University, Istanbul; ^(b)Division of Physics, Dogus University, Istanbul; ^(c)Department of Physics Engineering, Gaziantep University, Gaziantep; ^(d)Department of Physics, Istanbul Technical University, Istanbul, Turkey
- ¹⁹ ^(a)INFN Sezione di Bologna; ^(b)Dipartimento di Fisica, Università di Bologna, Bologna, Italy
- ²⁰ Physikalisches Institut, University of Bonn, Bonn, Germany
- ²¹ Department of Physics, Boston University, Boston MA, United States of America
- ²² Department of Physics, Brandeis University, Waltham MA, United States of America
- ²³ ^(a)Universidade Federal do Rio De Janeiro COPPE/EE/IF, Rio de Janeiro; ^(b)Federal University of Juiz de Fora (UFJF), Juiz de Fora; ^(c)Federal University of Sao Joao del Rei (UFSJ), Sao Joao del Rei; ^(d)Instituto de Fisica, Universidade de Sao Paulo, Sao Paulo, Brazil
- ²⁴ Physics Department, Brookhaven National Laboratory, Upton NY, United States of America
- ²⁵ ^(a)National Institute of Physics and Nuclear Engineering, Bucharest; ^(b)University Politehnica Bucharest, Bucharest; ^(c)West University in Timisoara, Timisoara, Romania
- ²⁶ Departamento de Física, Universidad de Buenos Aires, Buenos Aires, Argentina
- ²⁷ Cavendish Laboratory, University of Cambridge, Cambridge, United Kingdom
- ²⁸ Department of Physics, Carleton University, Ottawa ON, Canada
- ²⁹ CERN, Geneva, Switzerland
- ³⁰ Enrico Fermi Institute, University of Chicago, Chicago IL, United States of America
- ³¹ ^(a)Departamento de Física, Pontificia Universidad Católica de Chile, Santiago; ^(b)Departamento de Física, Universidad Técnica Federico Santa María, Valparaíso, Chile
- ³² ^(a)Institute of High Energy Physics, Chinese Academy of Sciences, Beijing; ^(b)Department of Modern Physics, University of Science and Technology of China, Anhui; ^(c)Department of Physics, Nanjing University, Jiangsu; ^(d)High Energy Physics Group, Shandong University, Shandong, China
- ³³ Laboratoire de Physique Corpusculaire, Clermont Université and Université Blaise Pascal and CNRS/IN2P3, Aubiere Cedex, France
- ³⁴ Nevis Laboratory, Columbia University, Irvington NY, United States of America
- ³⁵ Niels Bohr Institute, University of Copenhagen, Kobenhavn, Denmark
- ³⁶ ^(a)INFN Gruppo Collegato di Cosenza; ^(b)Dipartimento di Fisica, Università della Calabria, Arcavata di Rende, Italy
- ³⁷ Faculty of Physics and Applied Computer Science, AGH-University of Science and Technology, Krakow, Poland
- ³⁸ The Henryk Niewodniczanski Institute of Nuclear Physics, Polish Academy of Sciences, Krakow, Poland
- ³⁹ Physics Department, Southern Methodist University, Dallas TX, United States of America
- ⁴⁰ Physics Department, University of Texas at Dallas, Richardson TX, United States of America
- ⁴¹ DESY, Hamburg and Zeuthen, Germany
- ⁴² Institut für Experimentelle Physik IV, Technische Universität Dortmund, Dortmund, Germany
- ⁴³ Institut für Kern- und Teilchenphysik, Technical University Dresden, Dresden, Germany
- ⁴⁴ Department of Physics, Duke University, Durham NC, United States of America
- ⁴⁵ SUPA - School of Physics and Astronomy, University of Edinburgh, Edinburgh, United Kingdom
- ⁴⁶ Fachhochschule Wiener Neustadt, Johannes Gutenbergstrasse 3 2700 Wiener Neustadt, Austria
- ⁴⁷ INFN Laboratori Nazionali di Frascati, Frascati, Italy
- ⁴⁸ Fakultät für Mathematik und Physik, Albert-Ludwigs-Universität, Freiburg i.Br., Germany
- ⁴⁹ Section de Physique, Université de Genève, Geneva, Switzerland
- ⁵⁰ ^(a)INFN Sezione di Genova; ^(b)Dipartimento di Fisica, Università di Genova, Genova, Italy
- ⁵¹ ^(a)E.Andronikashvili Institute of Physics, Georgian Academy of Sciences, Tbilisi; ^(b)High Energy Physics Institute, Tbilisi State University, Tbilisi, Georgia
- ⁵² II Physikalisches Institut, Justus-Liebig-Universität Giessen, Giessen, Germany
- ⁵³ SUPA - School of Physics and Astronomy, University of Glasgow, Glasgow, United Kingdom
- ⁵⁴ II Physikalisches Institut, Georg-August-Universität, Göttingen, Germany
- ⁵⁵ Laboratoire de Physique Subatomique et de Cosmologie, Université Joseph Fourier and CNRS/IN2P3 and Institut National Polytechnique de Grenoble, Grenoble, France
- ⁵⁶ Department of Physics, Hampton University, Hampton VA, United States of America
- ⁵⁷ Laboratory for Particle Physics and Cosmology, Harvard University, Cambridge MA, United States of America
- ⁵⁸ ^(a)Kirchhoff-Institut für Physik, Ruprecht-Karls-Universität Heidelberg, Heidelberg; ^(b)Physikalisches Institut, Ruprecht-Karls-Universität Heidelberg, Heidelberg; ^(c)ZITI Institut für technische Informatik, Ruprecht-Karls-Universität Heidelberg, Mannheim, Germany
- ⁵⁹ Faculty of Science, Hiroshima University, Hiroshima, Japan
- ⁶⁰ Faculty of Applied Information Science, Hiroshima Institute of Technology, Hiroshima, Japan
- ⁶¹ Department of Physics, Indiana University, Bloomington IN, United States of America
- ⁶² Institut für Astro- und Teilchenphysik, Leopold-Franzens-Universität, Innsbruck, Austria

- ⁶³ University of Iowa, Iowa City IA, United States of America
- ⁶⁴ Department of Physics and Astronomy, Iowa State University, Ames IA, United States of America
- ⁶⁵ Joint Institute for Nuclear Research, JINR Dubna, Dubna, Russia
- ⁶⁶ KEK, High Energy Accelerator Research Organization, Tsukuba, Japan
- ⁶⁷ Graduate School of Science, Kobe University, Kobe, Japan
- ⁶⁸ Faculty of Science, Kyoto University, Kyoto, Japan
- ⁶⁹ Kyoto University of Education, Kyoto, Japan
- ⁷⁰ Instituto de Física La Plata, Universidad Nacional de La Plata and CONICET, La Plata, Argentina
- ⁷¹ Physics Department, Lancaster University, Lancaster, United Kingdom
- ⁷² ^(a) INFN Sezione di Lecce; ^(b) Dipartimento di Fisica, Università del Salento, Lecce, Italy
- ⁷³ Oliver Lodge Laboratory, University of Liverpool, Liverpool, United Kingdom
- ⁷⁴ Department of Physics, Jožef Stefan Institute and University of Ljubljana, Ljubljana, Slovenia
- ⁷⁵ School of Physics and Astronomy, Queen Mary University of London, London, United Kingdom
- ⁷⁶ Department of Physics, Royal Holloway University of London, Surrey, United Kingdom
- ⁷⁷ Department of Physics and Astronomy, University College London, London, United Kingdom
- ⁷⁸ Laboratoire de Physique Nucléaire et de Hautes Energies, UPMC and Université Paris-Diderot and CNRS/IN2P3, Paris, France
- ⁷⁹ Fysiska institutionen, Lunds universitet, Lund, Sweden
- ⁸⁰ Departamento de Física Teórica C-15, Universidad Autónoma de Madrid, Madrid, Spain
- ⁸¹ Institut für Physik, Universität Mainz, Mainz, Germany
- ⁸² School of Physics and Astronomy, University of Manchester, Manchester, United Kingdom
- ⁸³ CPPM, Aix-Marseille Université and CNRS/IN2P3, Marseille, France
- ⁸⁴ Department of Physics, University of Massachusetts, Amherst MA, United States of America
- ⁸⁵ Department of Physics, McGill University, Montreal QC, Canada
- ⁸⁶ School of Physics, University of Melbourne, Victoria, Australia
- ⁸⁷ Department of Physics, The University of Michigan, Ann Arbor MI, United States of America
- ⁸⁸ Department of Physics and Astronomy, Michigan State University, East Lansing MI, United States of America
- ⁸⁹ ^(a) INFN Sezione di Milano; ^(b) Dipartimento di Fisica, Università di Milano, Milano, Italy
- ⁹⁰ B.I. Stepanov Institute of Physics, National Academy of Sciences of Belarus, Minsk, Republic of Belarus
- ⁹¹ National Scientific and Educational Centre for Particle and High Energy Physics, Minsk, Republic of Belarus
- ⁹² Department of Physics, Massachusetts Institute of Technology, Cambridge MA, United States of America
- ⁹³ Group of Particle Physics, University of Montreal, Montreal QC, Canada
- ⁹⁴ P.N. Lebedev Institute of Physics, Academy of Sciences, Moscow, Russia
- ⁹⁵ Institute for Theoretical and Experimental Physics (ITEP), Moscow, Russia
- ⁹⁶ Moscow Engineering and Physics Institute (MEPhI), Moscow, Russia
- ⁹⁷ Skobeltsyn Institute of Nuclear Physics, Lomonosov Moscow State University, Moscow, Russia
- ⁹⁸ Fakultät für Physik, Ludwig-Maximilians-Universität München, München, Germany
- ⁹⁹ Max-Planck-Institut für Physik (Werner-Heisenberg-Institut), München, Germany
- ¹⁰⁰ Nagasaki Institute of Applied Science, Nagasaki, Japan
- ¹⁰¹ Graduate School of Science, Nagoya University, Nagoya, Japan
- ¹⁰² ^(a) INFN Sezione di Napoli; ^(b) Dipartimento di Scienze Fisiche, Università di Napoli, Napoli, Italy
- ¹⁰³ Department of Physics and Astronomy, University of New Mexico, Albuquerque NM, United States of America
- ¹⁰⁴ Institute for Mathematics, Astrophysics and Particle Physics, Radboud University Nijmegen/Nikhef, Nijmegen, Netherlands
- ¹⁰⁵ Nikhef National Institute for Subatomic Physics and University of Amsterdam, Amsterdam, Netherlands
- ¹⁰⁶ Department of Physics, Northern Illinois University, DeKalb IL, United States of America
- ¹⁰⁷ Budker Institute of Nuclear Physics (BINP), Novosibirsk, Russia
- ¹⁰⁸ Department of Physics, New York University, New York NY, United States of America
- ¹⁰⁹ Ohio State University, Columbus OH, United States of America
- ¹¹⁰ Faculty of Science, Okayama University, Okayama, Japan
- ¹¹¹ Homer L. Dodge Department of Physics and Astronomy, University of Oklahoma, Norman OK, United States of America
- ¹¹² Department of Physics, Oklahoma State University, Stillwater OK, United States of America
- ¹¹³ Palacký University, RCPTM, Olomouc, Czech Republic
- ¹¹⁴ Center for High Energy Physics, University of Oregon, Eugene OR, United States of America
- ¹¹⁵ LAL, Univ. Paris-Sud and CNRS/IN2P3, Orsay, France
- ¹¹⁶ Graduate School of Science, Osaka University, Osaka, Japan
- ¹¹⁷ Department of Physics, University of Oslo, Oslo, Norway
- ¹¹⁸ Department of Physics, Oxford University, Oxford, United Kingdom
- ¹¹⁹ ^(a) INFN Sezione di Pavia; ^(b) Dipartimento di Fisica Nucleare e Teorica, Università di Pavia, Pavia, Italy
- ¹²⁰ Department of Physics, University of Pennsylvania, Philadelphia PA, United States of America

- ¹²¹ Petersburg Nuclear Physics Institute, Gatchina, Russia
- ¹²² (a) INFN Sezione di Pisa; (b) Dipartimento di Fisica E. Fermi, Università di Pisa, Pisa, Italy
- ¹²³ Department of Physics and Astronomy, University of Pittsburgh, Pittsburgh PA, United States of America
- ¹²⁴ (a) Laboratório de Instrumentação e Física Experimental de Partículas - LIP, Lisboa, Portugal; (b) Departamento de Física Teórica y del Cosmos and CAFPE, Universidad de Granada, Granada, Spain
- ¹²⁵ Institute of Physics, Academy of Sciences of the Czech Republic, Praha, Czech Republic
- ¹²⁶ Faculty of Mathematics and Physics, Charles University in Prague, Praha, Czech Republic
- ¹²⁷ Czech Technical University in Prague, Praha, Czech Republic
- ¹²⁸ State Research Center Institute for High Energy Physics, Protvino, Russia
- ¹²⁹ Particle Physics Department, Rutherford Appleton Laboratory, Didcot, United Kingdom
- ¹³⁰ Physics Department, University of Regina, Regina SK, Canada
- ¹³¹ Ritsumeikan University, Kusatsu, Shiga, Japan
- ¹³² (a) INFN Sezione di Roma I; (b) Dipartimento di Fisica, Università La Sapienza, Roma, Italy
- ¹³³ (a) INFN Sezione di Roma Tor Vergata; (b) Dipartimento di Fisica, Università di Roma Tor Vergata, Roma, Italy
- ¹³⁴ (a) INFN Sezione di Roma Tre; (b) Dipartimento di Fisica, Università Roma Tre, Roma, Italy
- ¹³⁵ (a) Faculté des Sciences Ain Chock, Réseau Universitaire de Physique des Hautes Energies - Université Hassan II, Casablanca; (b) Centre National de l'Energie des Sciences Techniques Nucleaires, Rabat; (c) Université Cadi Ayyad, Faculté des sciences Semlalia Département de Physique, B.P. 2390 Marrakech 40000; (d) Faculté des Sciences, Université Mohamed Premier and LPTPM, Oujda; (e) Faculté des Sciences, Université Mohammed V, Rabat, Morocco
- ¹³⁶ DSM/IRFU (Institut de Recherches sur les Lois Fondamentales de l'Univers), CEA Saclay (Commissariat à l'Energie Atomique), Gif-sur-Yvette, France
- ¹³⁷ Santa Cruz Institute for Particle Physics, University of California Santa Cruz, Santa Cruz CA, United States of America
- ¹³⁸ Department of Physics, University of Washington, Seattle WA, United States of America
- ¹³⁹ Department of Physics and Astronomy, University of Sheffield, Sheffield, United Kingdom
- ¹⁴⁰ Department of Physics, Shinshu University, Nagano, Japan
- ¹⁴¹ Fachbereich Physik, Universität Siegen, Siegen, Germany
- ¹⁴² Department of Physics, Simon Fraser University, Burnaby BC, Canada
- ¹⁴³ SLAC National Accelerator Laboratory, Stanford CA, United States of America
- ¹⁴⁴ (a) Faculty of Mathematics, Physics & Informatics, Comenius University, Bratislava; (b) Department of Subnuclear Physics, Institute of Experimental Physics of the Slovak Academy of Sciences, Kosice, Slovak Republic
- ¹⁴⁵ (a) Department of Physics, University of Johannesburg, Johannesburg; (b) School of Physics, University of the Witwatersrand, Johannesburg, South Africa
- ¹⁴⁶ (a) Department of Physics, Stockholm University; (b) The Oskar Klein Centre, Stockholm, Sweden
- ¹⁴⁷ Physics Department, Royal Institute of Technology, Stockholm, Sweden
- ¹⁴⁸ Department of Physics and Astronomy, Stony Brook University, Stony Brook NY, United States of America
- ¹⁴⁹ Department of Physics and Astronomy, University of Sussex, Brighton, United Kingdom
- ¹⁵⁰ School of Physics, University of Sydney, Sydney, Australia
- ¹⁵¹ Institute of Physics, Academia Sinica, Taipei, Taiwan
- ¹⁵² Department of Physics, Technion: Israel Inst. of Technology, Haifa, Israel
- ¹⁵³ Raymond and Beverly Sackler School of Physics and Astronomy, Tel Aviv University, Tel Aviv, Israel
- ¹⁵⁴ Department of Physics, Aristotle University of Thessaloniki, Thessaloniki, Greece
- ¹⁵⁵ International Center for Elementary Particle Physics and Department of Physics, The University of Tokyo, Tokyo, Japan
- ¹⁵⁶ Graduate School of Science and Technology, Tokyo Metropolitan University, Tokyo, Japan
- ¹⁵⁷ Department of Physics, Tokyo Institute of Technology, Tokyo, Japan
- ¹⁵⁸ Department of Physics, University of Toronto, Toronto ON, Canada
- ¹⁵⁹ (a) TRIUMF, Vancouver BC; (b) Department of Physics and Astronomy, York University, Toronto ON, Canada
- ¹⁶⁰ Institute of Pure and Applied Sciences, University of Tsukuba, 1-1-1 Tennodai, Tsukuba, Ibaraki 305-8571, Japan
- ¹⁶¹ Science and Technology Center, Tufts University, Medford MA, United States of America
- ¹⁶² Centro de Investigaciones, Universidad Antonio Narino, Bogota, Colombia
- ¹⁶³ Department of Physics and Astronomy, University of California Irvine, Irvine CA, United States of America
- ¹⁶⁴ (a) INFN Gruppo Collegato di Udine; (b) ICTP, Trieste; (c) Dipartimento di Chimica, Fisica e Ambiente, Università di Udine, Udine, Italy
- ¹⁶⁵ Department of Physics, University of Illinois, Urbana IL, United States of America
- ¹⁶⁶ Department of Physics and Astronomy, University of Uppsala, Uppsala, Sweden
- ¹⁶⁷ Instituto de Física Corpuscular (IFIC) and Departamento de Física Atómica, Molecular y Nuclear and Departamento de Ingeniería Electrónica and Instituto de Microelectrónica de Barcelona (IMB-CNM), University of Valencia and CSIC, Valencia, Spain
- ¹⁶⁸ Department of Physics, University of British Columbia, Vancouver BC, Canada

- ¹⁶⁹ Department of Physics and Astronomy, University of Victoria, Victoria BC, Canada
- ¹⁷⁰ Waseda University, Tokyo, Japan
- ¹⁷¹ Department of Particle Physics, The Weizmann Institute of Science, Rehovot, Israel
- ¹⁷² Department of Physics, University of Wisconsin, Madison WI, United States of America
- ¹⁷³ Fakultät für Physik und Astronomie, Julius-Maximilians-Universität, Würzburg, Germany
- ¹⁷⁴ Fachbereich C Physik, Bergische Universität Wuppertal, Wuppertal, Germany
- ¹⁷⁵ Department of Physics, Yale University, New Haven CT, United States of America
- ¹⁷⁶ Yerevan Physics Institute, Yerevan, Armenia
- ¹⁷⁷ Domaine scientifique de la Doua, Centre de Calcul CNRS/IN2P3, Villeurbanne Cedex, France
- ^a Also at Laboratório de Instrumentação e Física Experimental de Partículas - LIP, Lisboa, Portugal
- ^b Also at Faculdade de Ciências and CFNUL, Universidade de Lisboa, Lisboa, Portugal
- ^c Also at Particle Physics Department, Rutherford Appleton Laboratory, Didcot, United Kingdom
- ^d Also at CPPM, Aix-Marseille Université and CNRS/IN2P3, Marseille, France
- ^e Also at TRIUMF, Vancouver BC, Canada
- ^f Also at Department of Physics, California State University, Fresno CA, United States of America
- ^g null
- ^h Also at Fermilab, Batavia IL, United States of America
- ⁱ Also at Department of Physics, University of Coimbra, Coimbra, Portugal
- ^j Also at Università di Napoli Parthenope, Napoli, Italy
- ^k Also at Institute of Particle Physics (IPP), Canada
- ^l Also at Department of Physics, Middle East Technical University, Ankara, Turkey
- ^m Also at Louisiana Tech University, Ruston LA, United States of America
- ⁿ Also at Faculty of Physics and Applied Computer Science, AGH-University of Science and Technology, Krakow, Poland
- ^o Also at Group of Particle Physics, University of Montreal, Montreal QC, Canada
- ^p Also at Institute of Physics, Azerbaijan Academy of Sciences, Baku, Azerbaijan
- ^q Also at Institut für Experimentalphysik, Universität Hamburg, Hamburg, Germany
- ^r Also at Manhattan College, New York NY, United States of America
- ^s Also at School of Physics and Engineering, Sun Yat-sen University, Guanzhou, China
- ^t Also at Academia Sinica Grid Computing, Institute of Physics, Academia Sinica, Taipei, Taiwan
- ^u Also at High Energy Physics Group, Shandong University, Shandong, China
- ^v Also at Section de Physique, Université de Genève, Geneva, Switzerland
- ^w Also at Departamento de Física, Universidade de Minho, Braga, Portugal
- ^x Also at Department of Physics and Astronomy, University of South Carolina, Columbia SC, United States of America
- ^y Also at KFKI Research Institute for Particle and Nuclear Physics, Budapest, Hungary
- ^z Also at California Institute of Technology, Pasadena CA, United States of America
- ^{aa} Also at Institute of Physics, Jagiellonian University, Krakow, Poland
- ^{ab} Also at Department of Physics, Oxford University, Oxford, United Kingdom
- ^{ac} Also at Institute of Physics, Academia Sinica, Taipei, Taiwan
- ^{ad} Also at Department of Physics, The University of Michigan, Ann Arbor MI, United States of America
- ^{ae} Also at DSM/IRFU (Institut de Recherches sur les Lois Fondamentales de l'Univers), CEA Saclay (Commissariat à l'Energie Atomique), Gif-sur-Yvette, France
- ^{af} Also at Laboratoire de Physique Nucléaire et de Hautes Energies, UPMC and Université Paris-Diderot and CNRS/IN2P3, Paris, France
- ^{ag} Also at Department of Physics, Nanjing University, Jiangsu, China
- * Deceased